UNSW
AUSTRALIA

Climate Change Research Centre

University of New South Wales

Interhemispheric Asymmetry of Global Warming: The Role of Ocean Dynamics

David Karel Hutchinson

December 31, 2015

Supervisors: Prof. Matthew H. England,
Dr. Andrew McC. Hogg.

A thesis submitted in fulfillment of the requirements for the degree of Doctor of Philosophy.

THE UNIVERSITY OF NEW SOUTH WALES
Thesis/Dissertation Sheet

Surname: HUTCHINSON

First name: DAVID Other name: KAREL

Abbreviation for degree as given in the University calendar: PhD

School: BIOLOGICAL, EARTH AND ENVIRONMENTAL SCIENCES Faculty: SCIENCE

Title:
INTERHEMISPHERIC ASYMMETRY OF GLOBAL WARMING: THE ROLE OF OCEAN DYNAMICS

Abstract

Global surface air temperature is increasing due to rising greenhouse gases. This warming has occurred at a faster rate in the Northern Hemisphere (NH) than the Southern Hemisphere (SH) and the asymmetry of warming between hemispheres is predicted to continue throughout the 21st Century. Several factors contribute to this interhemispheric asymmetry, including the greater proportion of land in the NH and the northward transport of heat by the ocean. This thesis focuses on the role of ocean dynamics in setting the warming asymmetry, using several modelling approaches. Firstly the impact of the Antarctic Circumpolar Current (ACC) on the interhemispheric warming asymmetry is investigated. The role of the ACC is isolated by comparing warming experiments in a global coupled climate model with and without a land barrier across Drake Passage (DP). With DP closed, the asymmetry in sea surface temperature (SST) warming is reduced, due to the presence of a subpolar gyre, and a lower Antarctic sea ice extent. Secondly the asymmetry of warming is examined when moving from coarse (1°) to eddy-permitting (0.25°) ocean resolution. We use an idealised coupled model with a 60° sector ocean domain, comprising one basin with Atlantic-like bathymetry and an ACC channel. A larger high latitude SST asymmetry develops in the 0.25° model than the 1° model, both in control runs and in warming scenarios. The larger warming asymmetry in the 0.25° model is caused by stronger boundary current heat transport and reduced NH sea ice. The SH warming is less sensitive to the resolution change, since eddy heat transport differences between the models are small compared with mean flow heat transport differences. When SH westerly winds are enhanced, the warming asymmetry increases, with greater upwelling of cool water in the Southern Ocean and greater warming in the NH. Finally the impact of realistic bathymetry is explored in the sector climate model. The Atlantic-like sector model is compared with a flat bottom rectangular model in similar experiments. The Atlantic and rectangular models have similar control climates, however the rectangular models have a stronger subpolar gyre in the NH in the absence of bathymetry. In warming experiments, the rectangular models develop warming and cooling regions in the NH, while the Atlantic models have no significant cooling regions. The Atlantic models exhibit greater sensitivity of ACC transport to wind forcing.

Originality Statement

I hereby declare that this submission is my own work and to the best of my knowledge it contains no materials previously published or written by another person, or substantial proportions of material which have been accepted for the award of any other degree or diploma at UNSW or any other educational institution, except where due acknowledgment is made in the thesis. Any contribution made to the research by others, with whom I have worked at UNSW or elsewhere, is explicitly acknowledged in the thesis. I also declare that the intellectual content of this thesis is the product of my own work, except to the extent that assistance from others in the projects design and conception or in style, presentation and linguistic expression is acknowledged.

Signed: .....

Date: .....

Copyright Statement

Signed: .....

Date: .....

Authenticity Statement

I certify that the Library deposit digital copy is a direct equivalent of the final officially approved version of my thesis. No emendation of content has occurred and if there are any minor variations in formatting, they are the result of the conversion to digital format.

Signed: .....

Date: .....

Abstract

Global surface air temperature is increasing due to rising greenhouse gases. This warming has occurred at a faster rate in the Northern Hemisphere (NH) than the Southern Hemisphere (SH) and the asymmetry of warming between hemispheres is predicted to continue throughout the 21st Century. Several factors contribute to this interhemispheric asymmetry, including the greater proportion of land in the NH and the northward transport of heat by the ocean. This thesis focuses on the role of ocean dynamics in setting the warming asymmetry, using several modelling approaches.

Firstly the impact of the Antarctic Circumpolar Current (ACC) on the interhemispheric warming asymmetry is investigated. The role of the ACC is isolated by comparing warming experiments in a global coupled climate model with and without a land barrier across Drake Passage (DP). With DP closed, the asymmetry in sea surface temperature (SST) warming is reduced, due to the presence of a subpolar gyre, and a lower Antarctic sea ice extent.

Secondly the asymmetry of warming is examined when moving from coarse (1°) to eddy-permitting (0.25°) ocean resolution. We use an idealised coupled model with a 60° sector ocean domain, comprising one basin with Atlantic-like bathymetry and an ACC channel. A larger high latitude SST asymmetry develops in the 0.25° model than the 1° model, both in control runs and in warming scenarios. The larger warming asymmetry in the 0.25° model is caused by stronger boundary current heat transport and reduced NH sea ice. The SH warming is less sensitive to the resolution change, since eddy heat transport differences between the models are small compared with mean flow heat transport differences. When SH westerly winds are enhanced, the warming asymmetry increases, with greater upwelling of cool water in the Southern Ocean and greater warming in the NH.

Finally the impact of realistic bathymetry is explored in the sector climate model. The Atlantic-like sector model is compared with a flat bottom rectangular model in similar experiments. The Atlantic and rectangular models have similar control climates, however the rectangular models have a stronger subpolar gyre in the NH in the absence of bathymetry. In warming experiments, the rectangular models develop warming and cooling regions in the NH, while the Atlantic models have no significant cooling regions. The Atlantic models exhibit greater sensitivity of ACC transport to wind forcing.

Acknowledgments

I am deeply grateful to my supervisor, Matt England, for his vision, enthusiasm, advice and encouragement over the duration of my PhD. He was always a source of great energy and insight, and supported me in developing key ideas and strategic directions for the project. He also worked tirelessly behind the scenes to ensure that I had the resources and funding to pursue my project to its fullest extent, and to attend summer schools, winter schools, conferences, workshops and a research expedition; places where I gained valuable contacts, new ideas and inspiration. I also deeply thank my co-supervisor Andy Hogg, who gave me many key insights, ideas, strategy and advice which were absolutely vital during this project. I also thank Andy for generously hosting me at ANU on multiple occasions, and for enabling me to make strong connections with his research group in Canberra.

Thanks very much to Agus Santoso for providing great modelling assistance at the beginning of my project and collaborating on the first paper, Kate Snow for allowing me to use her hard-won topography configuration and collaborating on the second paper, Marshall Ward for making my introduction to MOM as efficient as possible, Riccardo Farneti for supplying code and advice on the Intermediate Complexity Coupled Model and for hosting my visit to ICTP, Trieste, Steve Phipps for advice on CSIRO Mk3L and all others who have contributed their time and energy to helping me during my project. I also thank Chris Turney and Chris Fogwill for having me on the Australasian Antarctic Expedition to the Sub-Antarctic Islands of New Zealand, which was a wonderful experience, and for collaborating with me on two paleoclimate papers.

I am very grateful to the ARC Centre of Excellence for Climate Systems Science, who have generously supported me financially and provided great winter schools

and workshops, Matt England's ARC Laureate Fellowship which provided my PhD scholarship, the Climate Change Research Centre for giving me a top-up scholarship, and for supporting me in many capacities through my project. Special thanks go to the professional staff of the CCRC, who do an outstanding job of managing the Centre and make life a lot easier for us.

I would like to thank my beautiful partner Sam Dawson for her love and support through these years, she has shared the journey with me through good times and bad, held me together in the critical moments, and deserves to celebrate the finish as much as me. I also thank my mum, dad and brother Henry for their love and support and for their many visits to Sydney. I would like to thank all of my friends at the CCRC, though I cannot do them justice by trying to name all the people, past and present, who have made work a fun place to be, and shared in so many great experiences outside of work. I also thank my running coach Deano and the running team, for keeping me (relatively) sane throughout.

Contents

List of Figures

List of Tables

Supporting Publications

Hutchinson, D. K., M. H. England, A. Santoso and A. McC. Hogg, 2013. Interhemispheric asymmetry in transient global warming: The role of Drake Passage. *Geophysical Research Letters*, **40**, 1587-1593, doi:10.1002/grl.50341

Hutchinson, D. K., M. H. England, A. McC. Hogg and K. Snow, 2015. Interhemispheric asymmetry of warming in an eddy permitting coupled sector model. *Journal of Climate*, **28**, 7385-7406. doi:10.1175/JCLI-D-15-0014.1

Hutchinson, D. K., M. H. England and A. McC. Hogg, 2015. Impacts of Realistic Bathymetry and Eddy-Permitting Ocean Resolution in a Sector Climate Model, *In preparation.*

England, M. H., **D. K. Hutchinson**, A. Santoso and W. P. Sijp, 2015. Ice-atmosphere feedbacks dominate the response of the climate system to Drake Passage closure. *Journal of Climate*, submitted.

Preface

Motivation

The Northern Hemisphere (NH) is warming at a faster rate than the Southern Hemisphere (SH), as documented by many observational datasets. This interhemispheric asymmetry has long been predicted by climate models, and is a prominent feature of end of 21st Century climate projections. There is more than twice as much land surface in the NH than the SH, and it warms faster than the ocean due to lower evaporative cooling and heat capacity, providing a simple explanation for some of the asymmetry. However, the ocean circulation is also asymmetric, with the zonally unbounded Antarctic Circumpolar Current (ACC) in the SH contrasting with gyres and associated boundary currents in the same latitudes of the NH. These contrasting circulation features create large differences in the heat transported towards the high latitudes by the ocean. Nevertheless, the ocean's contribution to the interhemispheric asymmetry of warming is difficult to isolate from the land-ocean warming contrast, or the differential aerosol and ozone forcing between the hemispheres.

Apart from the horizontal circulation, the meridional overturning circulation (MOC) in the ocean is also strongly asymmetric. In particular, the sinking of North Atlantic Deep Water (NADW) draws a significant amount of warm water northwards in the upper layers of the Atlantic Ocean, while cold water is returned southward at depth. This strong overturning cell creates a northward zonal mean heat transport at all latitudes of the Atlantic Ocean, which creates a further ocean temperature asymmetry. The NADW cell partly resurfaces in the Southern Ocean, along the steeply sloping isopycnals in the zonally unbounded latitudes of the ACC.

This overturning circulation is caused by the interplay of wind-forced upwelling, buoyancy-forced sinking and interior mixing in the deep ocean, and its structure is strongly shaped by the geometry of the worlds ocean basins. The MOC therefore represents an important component of the ocean's contribution to the warming asymmetry across hemispheres, and forms a significant focus of this thesis.

This thesis seeks to better understand the ocean's contribution to the warming asymmetry within coupled climate models, using several different modelling approaches to isolate features of the ocean circulation. We examine a global climate model where the ACC is removed from the system, with all other features left unchanged. We then construct an idealized sector climate model using a single ocean basin, which has near-symmetric landmasses but retains the asymmetry of a circumpolar flow in the SH and gyres in the NH. This sector model is simulated at coarse (1°) resolution with parameterized eddies, and at eddy-permitting (0.25°) ocean resolution where mesoscale eddies are partially resolved and no eddy parameterization is used. The sector model is simulated with Atlantic bathymetry, in order to capture flow features that are constrained by bathymetry, and using a flat bottom configuration. These scenarios allow us to probe features of the ocean circulation that are controlled by topography, as well as features that are captured without realistic bathymetry.

While we focus on transient warming in response to increasing greenhouse gases, the equilibrium surface climate is also warmer in the NH in the present-day system. Thus, there is already a baseline interhemispheric asymmetry in mean surface climate of the earth, a result of the asymmetry of landmasses as average incoming solar insolation is virtually identical across hemispheres. Ocean dynamics play a significant role in setting both the equilibrium temperature asymmetry and its transient warming asymmetry by transporting vast amounts of heat into the North Atlantic and limiting heat transport across the Southern Ocean. Due to this baseline interhemispheric asymmetry, we also examine asymmetries in the control climate state,

and how differences in the equilibrium states in turn have a major impact on the warming asymmetries found in each of the models.

Thesis Structure and Objectives

This thesis is divided into three main parts, corresponding to the three lead-authored publications listed in the Supporting Publications (Page xxix), while the co-authored publication is included as an Appendix. Each part consists of a complete scientific article, including an abstract, introduction, methods, results, discussion and conclusion. The original manuscripts have been extended with additional figures and analysis, including the integration of published supplementary material into the main body of the manuscript in Part 1. While each part is largely self-contained, the references for each part are compiled into a single bibliography at the end of the thesis. The aims of each part are introduced below.

Part 1

Part 1 investigates the influence of the Antarctic Circumpolar Current (ACC) upon the interhemispheric warming asymmetry. We use a global coupled climate model with a realistic continental configuration, and simulate experiments with and without a land bridge across Drake Passage. The model has coarse ($\sim 2^\circ$) resolution with parameterized ocean eddies. Using the Drake Passage land bridge isolates the impact of the ACC on the climate, while making a negligible direct change to surface properties such as land area, and ice-albedo. The interhemispheric asymmetry of warming in sea surface temperature (SST) and surface air temperature (SAT) are examined with and without Drake Passage. We quantify the reduction in asymmetry found when Drake Passage is closed. Major changes to the meridional overturning circulation occur in response to the closure of Drake Passage. Furthermore, we examine the importance of the ACC in maintaining sea ice around Antarctica, and

how the presence of sea ice influences SST warming in the high latitudes of the Southern Hemisphere.

Part 2

Part 2 examines the interhemispheric warming asymmetry in an intermediate complexity climate model. The ocean is simulated at coarse (1°) and eddy-permitting (0.25°) resolution, since eddy and boundary current heat fluxes are expected to change when moving to higher resolution. The model is configured to be near symmetric in its land-ocean cover between the hemispheres, with a single ocean basin and an ACC-like channel in the SH. The ocean basin uses realistic Atlantic-like bathymetry, spanning a 60°-wide sector domain, and the atmosphere consists of 120°-wide sector, with land outside the ocean domain. The near-symmetry of landmasses isolates the role of the ocean currents in setting the interhemispheric asymmetry. Sea ice plays a critical role in setting the high latitude asymmetry, and we particularly focus on differences in the NH sea ice response between the resolutions. We further examine the impact of a poleward shift and intensification of the SH westerly winds upon the asymmetry. Increases in Southern Ocean wind forcing may cause changes to the meridional overturning circulation, and we examine this effect upon the interhemispheric warming asymmetry, both separately and together with radiative forcing.

Part 3

Part 3 explores the influence of bathymetry in an idealized sector climate model, comparing the mean climate and sensitivity to forcing between the Atlantic model used in Part 2, and a flat bottom rectangular model with no bathymetry. This comparison is motivated by many recent studies that have employed sector ocean models with little or no topographic features. We examine the control climates

and circulation features of each model, focusing on features that are constrained by the bathymetry and coastlines in the Atlantic model. These models are simulated at coarse (1°) and eddy-permitting (0.25°) ocean resolution, as in Part 2. We explore differences in the warming patterns between the models, and the circulation response to enhanced SH wind forcing. The structure of the NH subpolar and subtropical gyres are closely examined, including the differing vertical structure of motion when bathymetry is included. Topography also has a major influence on the ACC transport, and we examine differences in its sensitivity to warming and wind perturbations when topography is removed.

As each of these parts contains a discussion and conclusion of the results presented, the final part of the thesis consists of concluding remarks (page 105), providing a brief summary of the key findings of the thesis. Recommendations for future research based on this work are presented in the final section of the concluding remarks.

Part 1

Interhemispheric Asymmetry in Transient Global Warming: The Role of Drake Passage

Abstract

Climate models predict that the Northern Hemisphere (NH) will warm faster than the Southern Hemisphere (SH) in response to increasing greenhouse gases, and observations show that this trend has already begun to occur. This interhemispheric asymmetry has largely been attributed to land-ocean differences between the hemispheres and ice-albedo feedbacks from Arctic sea ice melt, while the role of ocean currents in setting this asymmetry is less well understood. This study isolates the impact of an open Southern Ocean gateway upon the interhemispheric asymmetry in transient global warming by forcing a fully-coupled climate model with an increasing CO_2 scenario with and without a land bridge across Drake Passage (DP). It is found that over the transient warming period the NH-SH surface warming asymmetry is reduced in the DP closed case, by approximately 41% for sea surface temperature and approximately 6% for surface air temperature. In the DP open case, sea ice extent is far greater in the SH than in the DP closed case, whereas the sea ice response to warming in the NH is insensitive to whether or not DP is closed. These results illustrate that part of the interhemispheric asymmetry in surface warming is due to the ACC thermally isolating Antarctica. The ACC limits ocean heat transport across the DP latitudes and allows a much greater coverage of sea ice in the Southern Ocean than would be the case in the absence of a circumpolar ocean.

1.1 Introduction

Global climate models show a strong interhemispheric asymmetry in the transient response of surface air temperature (SAT) to CO_2, with the Northern Hemisphere (NH) warming considerably faster than the Southern Hemisphere (SH) (Meehl et al., 2007). This result has been well established through several decades of climate modelling (e.g. Bryan et al., 1988; Manabe et al., 1991; Flato and Boer, 2001), and has

been found to be largely attributed to the greater coverage of ocean in the SH; yielding a higher effective heat capacity of the SH compared to the NH. Higher evaporative cooling over the oceans implies that warming is more rapid over land, further enhancing the interhemispheric asymmetry independently of ocean circulation differences. Yet ocean circulation differs markedly across the hemispheres, with the land mass geometry enabling a circumpolar flow around Antarctica, which could impact the warming response to rising greenhouse gases. This study focuses on the role of an open Southern Ocean gateway in regulating the hemisphere-scale response to global warming in a coupled climate model.

Observations of warming in recent decades have confirmed that this warming asymmetry has already begun to occur. The HADCRUT4 dataset (Morice et al., 2012) has shown a steady trend from 1980 onward exhibiting much faster warming in the NH compared to the SH. Furthermore, the spatial pattern of SAT warming in the last two decades is broadly consistent with earlier global climate model predictions (Manabe et al., 2011). Observations of ocean warming have also indicated greater warming of sea surface temperature (SST) in the NH compared to the SH, though the magnitude of asymmetry is somewhat less than that in the SAT (Levitus et al., 2012). The Levitus et al. (2012) data also indicate that the ocean heat uptake and its asymmetry towards greater NH warming are largest in the Atlantic Ocean. The Pacific and Indian Oceans make smaller contributions to the net interhemispheric asymmetry. Lee et al. (2011) used simulations of 20th Century warming to show that the North Atlantic Ocean heat content increase is more dependent on remote heating of the global ocean than local heating of the Atlantic. This result suggests that advection of heat into the North Atlantic by ocean currents is playing a major role in setting the asymmetry of SST warming.

A further cause of warming asymmetry is the difference in polar climates. Antarctic sea ice trends have been non-uniform in recent decades, with a decline west of the Antarctic Peninsula and growth over the Ross Sea region (Simpkins

et al., 2012). By contrast, seasonal melting of Arctic sea ice appears to be accelerating (Wang and Overland, 2009), allowing a strong ice-albedo positive feedback that exacerbates the warming and thus the asymmetry between hemispheres. Sea ice can also alter the polar warming response by insulating the air from warmer ocean temperatures below the ice.

There are several additional factors which may influence the interhemispheric asymmetry of global warming. Sulfate aerosols are expected to cool the NH more than the SH (Dufresne et al., 2005), and therefore reduce the warming asymmetry. Ozone may also play a role in the asymmetry, as the anthropogenic ozone hole has caused a trend towards the high-index polarity of the Southern Annular Mode (Thompson et al., 2011), contributing to cooling over high southern latitudes. In the present study, no aerosols are included and ozone concentrations are prescribed from observations and fixed in time (Wang et al., 1995); thus we focus on ocean heat transport and heat capacity effects on the asymmetry, and the specific role of the Drake Passage (DP) gap.

The Antarctic Circumpolar Current (ACC) provides a further possible mechanism for slowing global warming at high southern latitudes. The vigorous re-entrant flow of the ACC prevents any net upper ocean meridional geostrophic flow across DP, causing Antarctica to be 3-4°C cooler than it would otherwise be if DP were closed (Toggweiler and Bjornsson, 2000; Sijp and England, 2004). Although the impacts of the ACC upon the climate have been investigated previously in ocean-only models (Cox, 1989; Toggweiler and Samuels, 1995), in intermediate complexity climate models (Sijp and England, 2004; Sijp et al., 2009) and in idealized continental geometries (Enderton and Marshall, 2009), the DP effect has not been explored in a coupled climate model with realistic continental geometry. Here we investigate the hypothesis that the ocean, and particularly the ACC, plays a major role in controlling the interhemispheric asymmetry during transient global warming. We compare climate simulations with an open and closed DP under transient warming

to demonstrate the influence of the ACC on this interhemispheric asymmetry.

1.2 Climate Model and Experimental Design

This study implements the Commonwealth Scientific and Industrial Research Organisation Mark version 3L climate model (CSIRO Mk3L) Earth system model, comprising fully interactive ocean, atmosphere, land and sea ice sub-models (Phipps, 2010). CSIRO Mk3L is designed for millennial climate simulations with ocean model resolution of 1.6° latitude x 2.8° longitude x 21 levels, and atmospheric model resolution of 3.2° latitude x 5.6° longitude x 18 pressure levels. The version used in this study includes an updated configuration of the Indonesian Archipelago as implemented by Santoso et al. (2012).

Two sets of 6-member ensemble simulations were run. The first set uses the standard coastline configuration, and the second set includes an extra land bridge to close the Drake Passage (DP), referred to respectively as the DP_{open} and DP_{clsd} simulations. The land bridge reduces the ocean surface area of the SH by only 0.2%, and therefore makes negligible *direct* change to hemisphere-averaged surface properties such as albedo and heat capacity. Indirect changes can occur, for example via differing sea ice distributions across the hemispheres. The DP_{open} simulations were initiated from a 3000 year pre-industrial control simulation with an atmospheric CO_2 concentration of 280 ppm. The DP_{clsd} control simulation was also initiated from this state, and equilibrated for a further 2000 years with the DP land bridge included. A 6-member ensemble was generated at the end of each control run, using the model restart configuration at the end of six consecutive years. Each ensemble member was then perturbed with increasing atmospheric CO_2 concentration following the SRES A2 forcing scenario (Nakicenovic and Swart, 2000) from nominal year 1781 until 2100. From the year 2100 onwards, CO_2 was held fixed at 856 ppm. While the initial spread between these ensemble members is small, within a few years the

asymmetry indices become highly uncorrelated. Thus, the ensemble members can be considered sufficiently independent. Subsequently the models have 220 years to diverge before the 21st Century, at which point we analyse the results.

The control simulations and warming experiments were initially conducted with and without flux adjustments in single-member experiments. The flux adjustments were set in order to restore the DP_{open} simulation towards a modern climatology in the control state. The same set of flux adjustments were applied to the DP_{clsd} simulation for comparison. While the flux adjustments improved the climatology of the DP_{open} simulation, they produced spurious trends in the warming scenarios of the DP_{clsd} simulation. Since the DP_{clsd} simulation has a very different ocean circulation in the SH, the flux adjustments derived from the DP_{open} simulation restored the DP_{clsd} simulation towards a different mean state. Ensemble simulations were therefore run without flux adjustments to ensure a physically meaningful comparison between the two sets of simulations; their results are presented here.

1.3 Results

1.3.1 Interhemispheric Asymmetry

The interhemispheric asymmetry in temperature anomaly (defined as the NH minus SH mean temperature anomaly) is plotted in Figure 1.1a, showing the SAT and SST asymmetry for both ensembles over the period 1781-2300. The SST asymmetry is higher in the DP_{open} ensemble than the DP_{clsd} ensemble, with an average asymmetry of 0.37°C from 2081-2100 in the DP_{open} ensemble, compared to 0.22°C in the DP_{clsd} ensemble. Using a bootstrap resampling method to obtain a 95% confidence interval, the SST asymmetry ensembles become statistically different from year 2072 onwards, marked by the vertical dashed line in Figure 1.1a. This threshold of significance is a crude estimate, since the sample size of 6 ensemble members is small. The

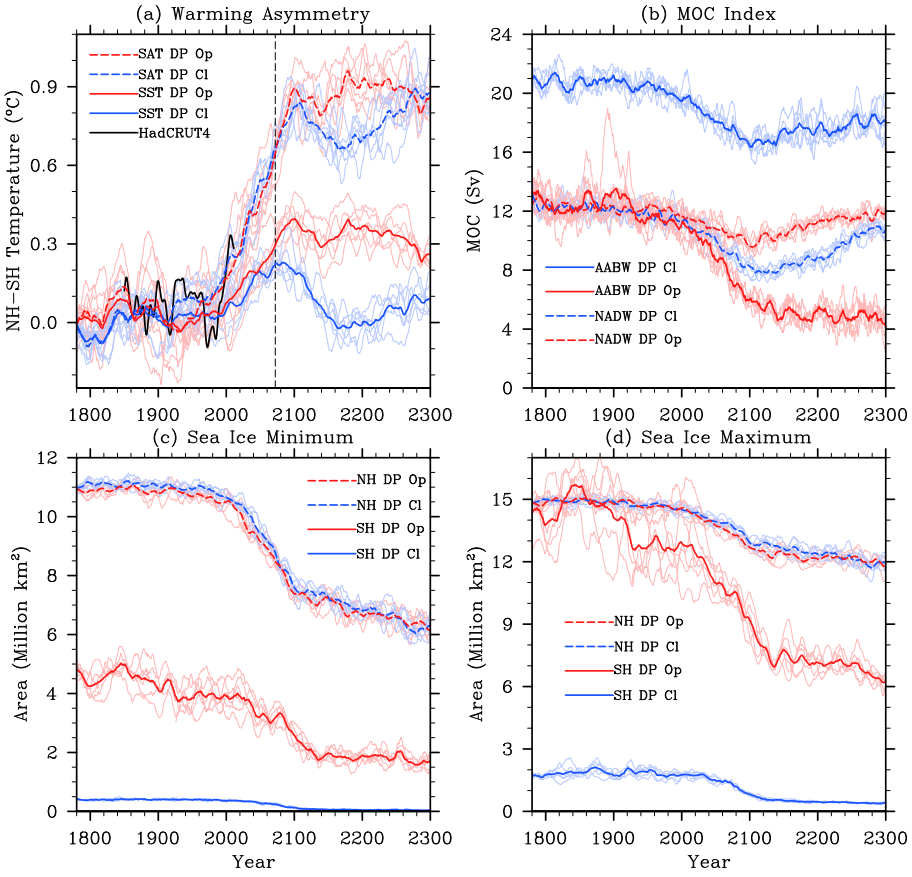

Figure 1.1: (a) Northern Hemisphere - Southern Hemisphere (NH-SH) temperature anomaly relative to the pre-industrial 100 year mean, showing the asymmetry in surface air temperature (SAT) anomalies (dashed lines), sea surface temperature (SST) anomalies (solid lines) and the HadCRUT4 observational dataset (Morice et al., 2012). The vertical dashed line marks the year after which the SST asymmetry trends become statistically different. (b) MOC index calculated as the annual mean formation of Antarctic Bottom Water (AABW - solid lines) and North Atlantic Deep Water (NADW - dashed lines); (c) sea ice minimum extent, measured as the area where sea ice concentration is greater than 0.15 (NH - dashed lines, SH - solid lines); (d) as in (c) but the sea ice maximum. In all plots, the bold lines represent ensemble means and the fine lighter colored lines are the ensemble members. All model trends have been filtered using an 11 year running average.

asymmetry is mainly due to the reduced warming around the coast of Antarctica when DP is open (Figure 1.2c).

The spatial pattern and magnitude of asymmetry in SAT is more robust across the two ensembles (Figure 1.3); from 2081-2100, SAT asymmetry is 0.82°C in the DP_{open} ensemble compared to 0.77°C in the DP_{clsd} ensemble. The land-ocean warming contrast dominates the SAT asymmetry, especially in the mid-latitudes where the NH has large continents whereas the SH is mostly ocean. The differences in

SST asymmetry are significant; however when combining these changes with the land surface, which is twice as large in the NH than the SH, the differences in SAT asymmetry become smaller. The SAT asymmetry is thus more robust to the change induced by closing DP, suggesting that the differences in surface heat capacity and evaporative cooling effects are dominant in setting the SAT asymmetry. Nevertheless, the SAT asymmetry is reduced by 6% compared to the DP_{open} case, while the SST asymmetry is reduced by 41% compared to the DP_{open} case.

1.3.2 Surface Warming

In the transient warming runs, SST anomalies around Antarctica remain considerably cooler in the DP_{open} ensemble over the Ross Sea and South Pacific sectors (Figure 1.2). The slower warming of SST around DP and in the Pacific sector of the Southern Ocean is likely due to the thermal isolation created by the ACC. There is also a region of enhanced warming in the Weddell Gyre to the east of DP, which warms faster in the DP_{open} ensemble. This region is associated with enhanced sea ice melt (see Supplementary Figure 1g). When DP is closed, this warmer region of the Weddell Gyre is spread across a larger area by the enhanced subpolar gyre that forms in the absence of the DP throughflow. The SST anomalies in the Arctic Ocean are very similar in both ensembles, showing relatively weak warming over most of the Arctic due to persistent sea ice coverage. There is also a localized region of very strong warming between Svalbard and Scandinavia, associated with sea ice melt. This 'hotspot' is present in both ensembles, and therefore appears to have little dependence on the DP changes in this experiment.

The SAT changes show a similar pattern of polar amplification to that typical of IPCC AR4 simulations (Meehl et al., 2007). Figure 1.3 shows the SAT ensemble mean anomaly during 2081-2100 relative to the pre-industrial 100 year mean, as in Figure 1.2. Both ensembles show amplified warming in the high latitudes of the NH, especially in the Arctic, and stronger warming over land than ocean. SAT changes

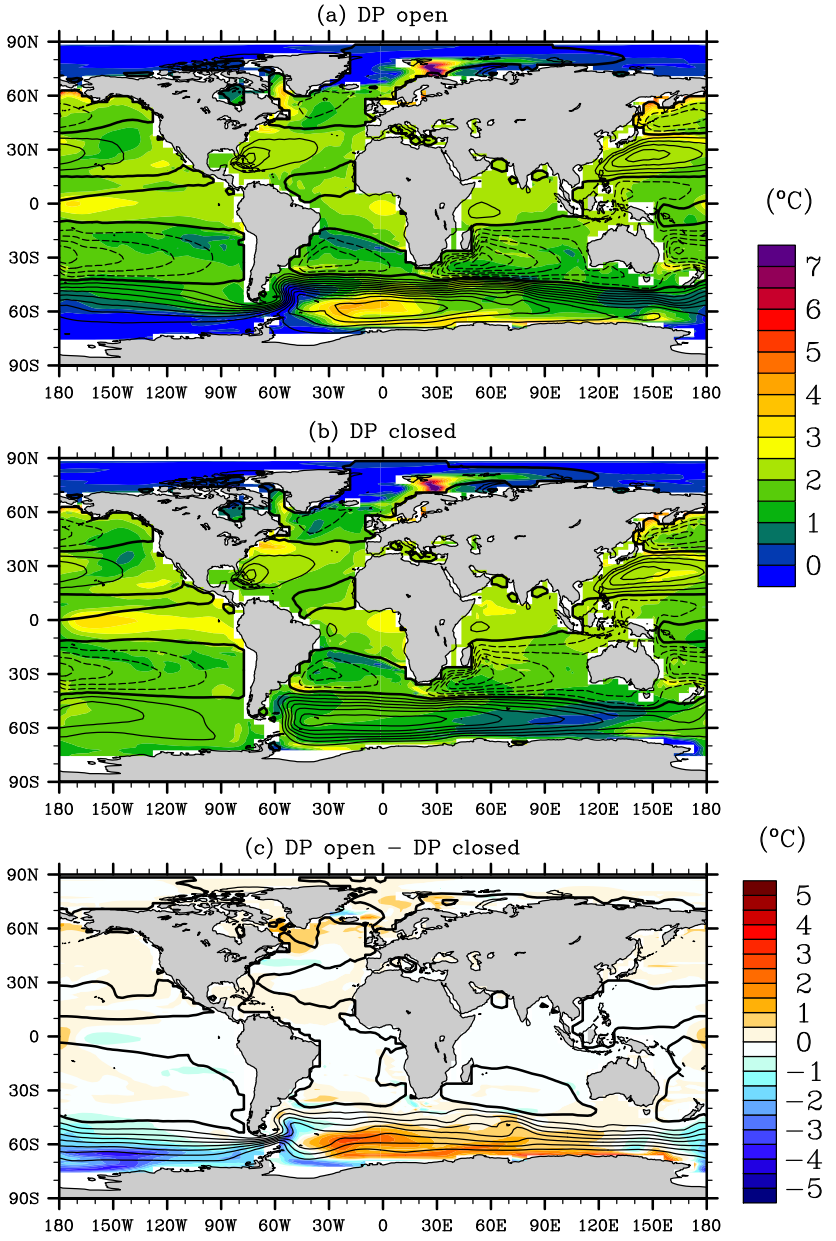

Figure 1.2: Sea surface temperature (SST) ensemble mean anomaly (colored contours) during 2081-2100 relative to the final 100 years of the pre-industrial simulation for (a) DP_{open}, (b) DP_{clsd} and (c) the difference DP_{open} - DP_{clsd}. The respective barotropic streamfunctions during 2081-2100 are overlaid (black contours) on (a)-(b) and the difference in streamfunctions overlaid on (c). The streamfunction contour interval is 10 Sv, solid lines are positive, dashed lines are negative and the zero contour is bold.

over the ocean reflect the SST patterns in most regions, except in the Arctic where there is little change in SST but a large increase in SAT. The SAT trends over the Arctic are broadly consistent with IPCC AR4 projections Meehl et al. (2007), while the SST warming in the Arctic is limited by persistent sea ice coverage, discussed

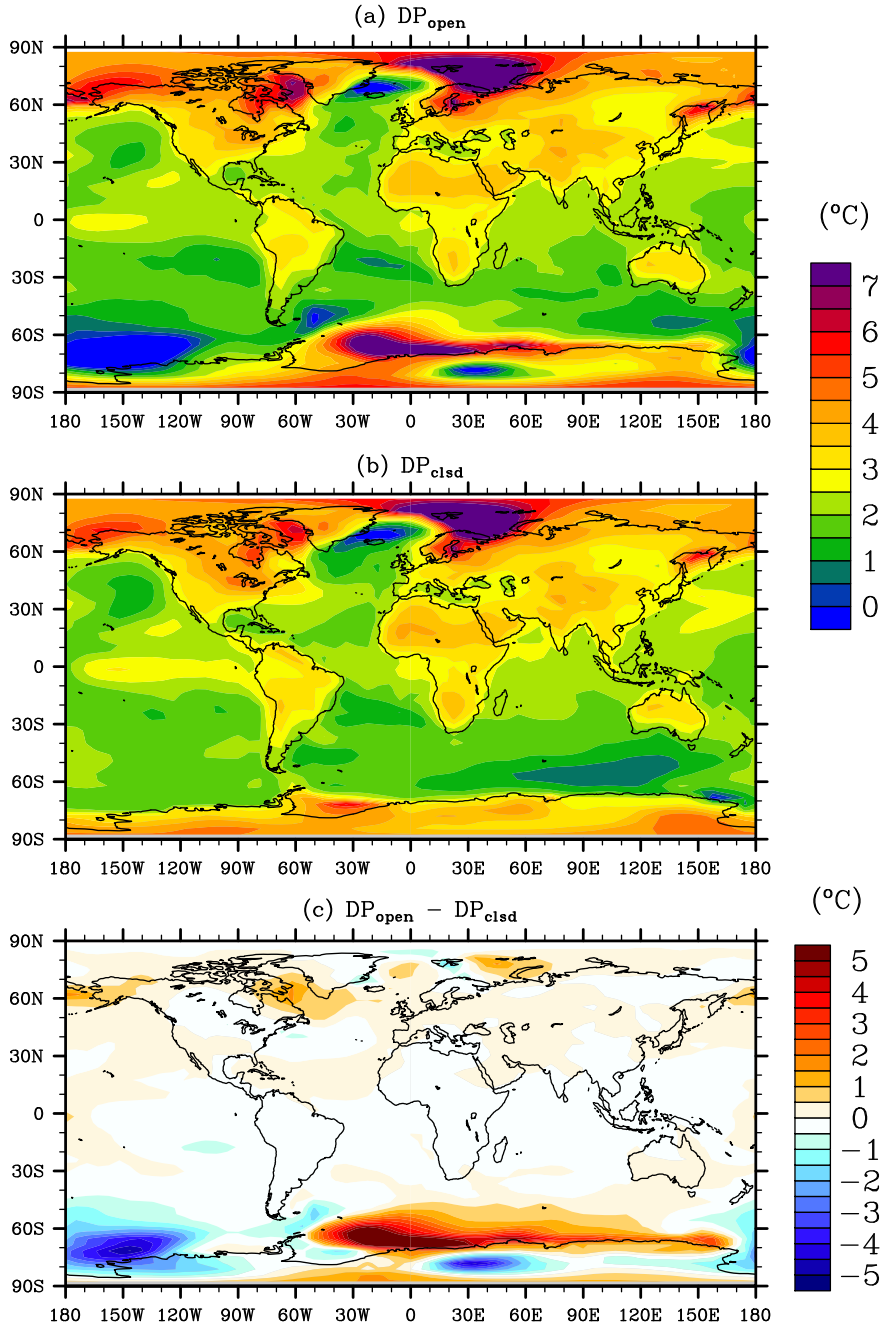

Figure 1.3: Surface air temperature anomaly during 2081-2100 relative to pre-industrial 100 year mean for (a) DP_{open}, (b) DP_{clsd} and (c) the difference DP_{open} - DP_{clsd}.

further in Section 1.3.4.

1.3.3 Deep Warming and Overturning Changes

Figure 1.4 shows the zonally-averaged ocean temperature anomaly for each ensemble, plotted as a function of latitude and depth during 2081-2100 relative to the pre-industrial 100 year mean. In the DP_{open} ensemble (Figure 1.4a), Southern Ocean warming is substantially weaker, especially adjacent to the coast of Antarctica. In the DP_{clsd} ensemble (Figure 1.4b), ocean warming persists through to the highest latitudes of the Southern Ocean, extending to approximately 1500 m depth. There is a reversal of this trend below 1500 m depth, with the DP_{open} ensemble warming more than the DP_{clsd} ensemble. This warming at depth can be explained by the shallower penetration of AABW in the DP_{clsd} ensemble, discussed below.

The meridional overturning circulation (MOC) streamfunction, calculated in density coordinates and re-projected back to latitude-depth space, during 2081-2100 is overlaid on the temperature anomalies in Figures 1.4a,b, with the difference in streamfunctions shown in Figure 1.4c. The rate of Antarctic Bottom Water (AABW) formation is higher in the DP_{clsd} ensemble, however its density is reduced due to the warmer Antarctic climate. The lower density of the AABW mass causes it to penetrate to shallower depths, and the NADW mass becomes the dominant source of the abyssal ocean in this case. In the DP_{open} ensemble, by contrast, the AABW mass dominates the abyssal ocean. Therefore AABW ventilation can more rapidly transfer any surface warming signal to the deep Southern Ocean in the DP_{open} ensemble, as seen in Figure 1.4c.

Figure 1.1b shows a time series of NADW and AABW formation, calculated from the MOC streamfunction in latitude-density coordinates. The domain of the water masses is defined as having potential density of $\sigma_2 > 35$ kg m^{-3}, and poleward of 50° N and 50° S for NADW and AABW, respectively. Weakening of AABW relative to NADW formation in the DP_{open} ensemble slows the advection of heat across the DP latitudes. By contrast, the steady formation of AABW in the DP_{clsd}

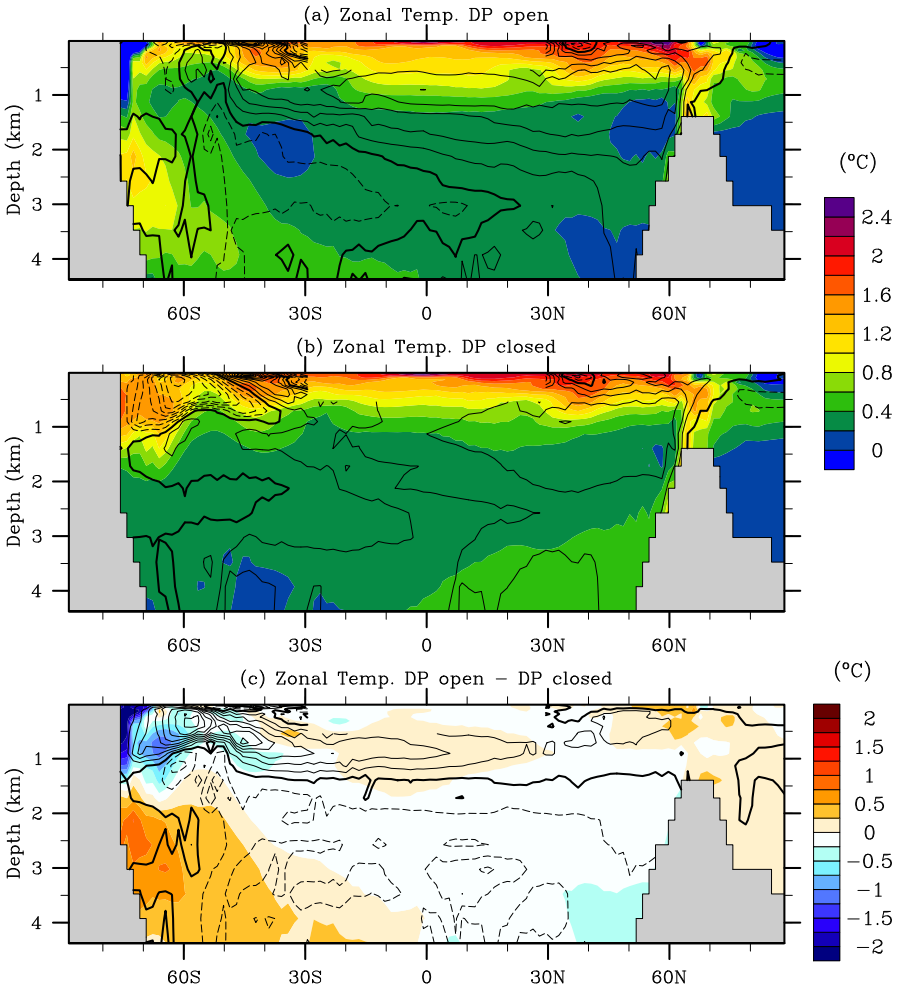

Figure 1.4: Zonal-averaged ocean temperature anomaly (colored contours) during 2081-2100 relative to pre-industrial 100 year mean, for (a) DP_{open}, (b) DP_{clsd} and (c) DP_{open} - DP_{clsd}. The meridional overturning circulation during 2081-2100, calculated in density coordinates and re-projected back to latitude-depth space, is shown in black contours (2 Sv interval; solid lines are positive, dashed lines are negative and the zero contour is bold). The tropical overturning cells are masked out in the domain $\pm 30°$ latitude and < 500 m depth in order to show the near surface temperature trend.

ensemble allows the high latitude Southern Ocean to warm more rapidly in that experiment set.

It is worth noting that the NADW formation is very similar between the two control simulations, and does not appear to depend strongly on the DP throughflow, in contrast to previous studies that used models with idealized continental geometries (e.g. Toggweiler and Bjornsson, 2000; Enderton and Marshall, 2009) or a non-interactive atmosphere (Sijp and England, 2004). The realistic land-mass

with topography and the fully-interactive atmosphere in our model, complete with a hydrological cycle, appear to play an important role in regulating the heat and freshwater budgets of the Altantic MOC (Sinha et al., 2012). Nonetheless, our result is consistent with Rahmstorf and England (1997), who showed that the rate of NADW formation is much less sensitive to Southern Ocean wind forcing when atmospheric thermal feedbacks are included.

1.3.4 Sea Ice Changes

Differences in the Southern Ocean SST response of the two ensemble sets are strongly linked to sea ice patterns. The sea ice minima for both the NH and SH, measured respectively as the September and March sea ice extent (the area where sea ice concentration exceeds 0.15) are shown in Figure 1.1c. In the DP_{open} ensemble, the Arctic sea ice minimum is 11.0M km^2 in pre-industrial conditions, and declines to approximately 7.8M km^2 by 2081-2100. The DP_{clsd} ensemble shows a similar trend, covering 11.1M km^2 in pre-industrial conditions and declining to 8.0M km^2 by 2081-2100. The Arctic sea ice maxima (Figure 1.1d) show a weaker decline over the same period, from 15.0M to 13.0M km^2 in the DP_{open} ensemble and 14.9M to 13.3M km^2 in the DP_{clsd} ensemble. Although the initial extent of the sea ice minimum is larger than satellite estimates (8.2M km^2 for the 1980-1999 average), the magnitude of the decline in these simulations is consistent with IPCC AR4 projections (Figure 10.13 of Meehl et al., 2007).

In the DP_{open} ensemble there is a substantial coverage of SH sea ice, and though it decreases over the warming period, there remains a substantial coverage providing insulation to the sea surface despite ongoing global warming. The SH sea ice maximum declines from a pre-industrial level of 14.6M to 9.7M km^2 by 2081-2100, and the minimum declines from 4.4M to 2.9M km^2 over the same period, consistent with Meehl et al. (2007). By contrast, the DP_{clsd} ensemble begins with almost no SH sea ice even in winter, with a pre-industrial maximum of 1.8M km^2 declining to 1.0M

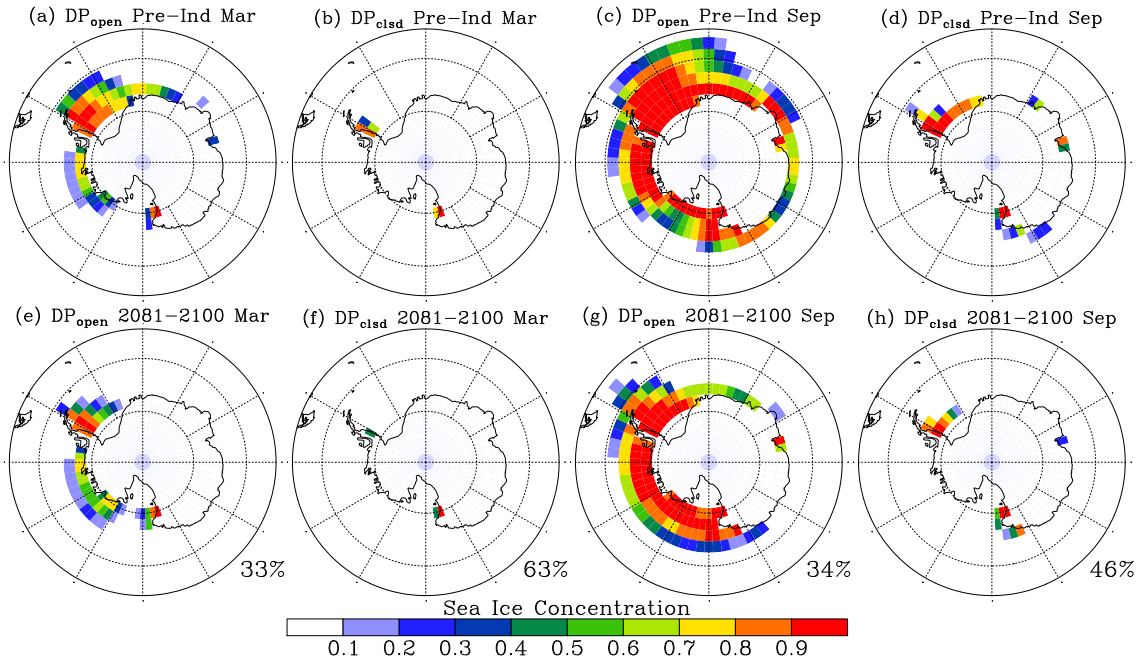

Figure 1.5: Mean sea ice concentration in the Southern Hemisphere, showing the last 100 years of the control simulation for (a) DP_{open} in March, (b) DP_{clsd} in March, (c) DP_{open} in September and (d) DP_{clsd} in September; and the 2081-2100 mean for (e) DP_{open} in March, (f) DP_{clsd} in March, (g) DP_{open} in September and (h) DP_{clsd} in September. In parts (e)-(h), the percent reduction in sea ice extent is shown in the bottom right.

km^2 by 2081-2100, and a minimum declining from 0.4M to 0.2M km^2 over the same period. Recent observations show that Arctic sea ice is melting more rapidly than IPCC AR4 projections (Wang and Overland, 2009), and therefore warming of SST in the Arctic is likely to be higher than our model suggests. Thus, our model may underestimate the asymmetry of warming in SST, due to a weak trend in the Arctic. Nevertheless, the trends in Arctic sea ice are very similar between the DP_{open} and DP_{clsd} ensembles, and therefore our experiments can still isolate the impact of the ACC on the warming asymmetry.

Figure 1.5 shows the sea ice concentration at September maximum and March minimum for the SH during the last 100 years of the control simulation (a-d) and during 2081-2100 (e-h). In the DP_{open} ensemble, sea ice coverage shows a strong seasonal cycle with circumpolar coverage in September, with high concentrations in the Ross and Weddell Seas and in the South Pacific sector. Substantial melting occurs in summer with the Eastern hemisphere becoming virtually sea ice free, and

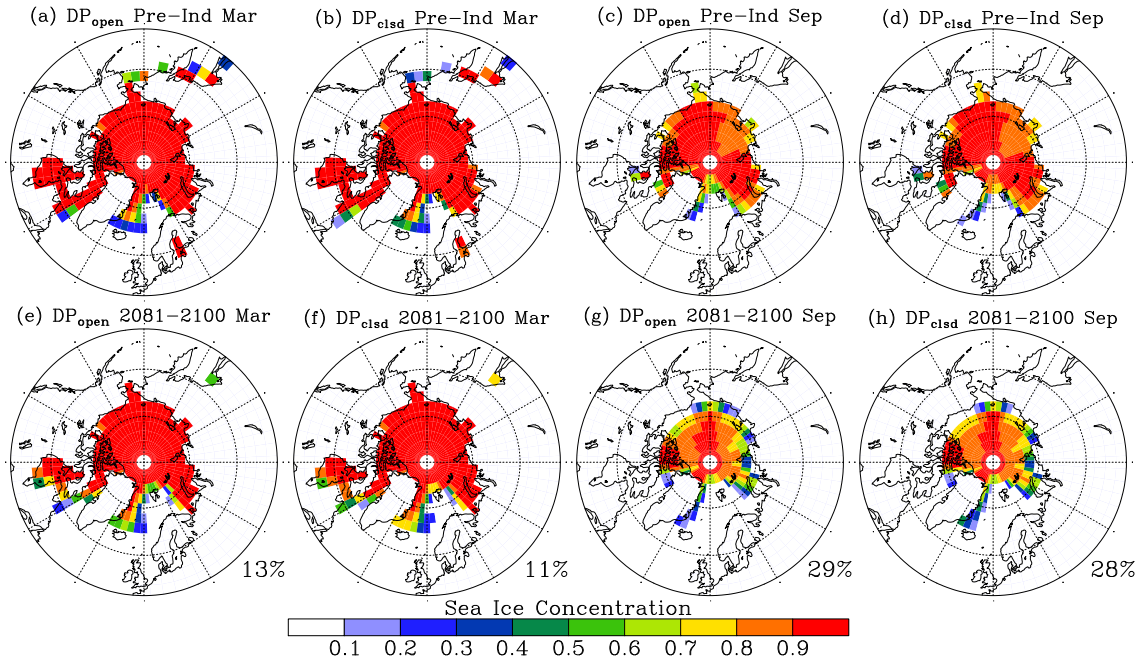

Figure 1.6: Same as Figure 1.5 but for the Northern Hemisphere.

the western sector declining markedly. These sea ice patterns are broadly consistent with observations and IPCC AR4 models (Meehl et al., 2007). By contrast, the DP_{clsd} ensemble is close to ice free all year round, with only a modest increase in sea ice extent in winter. This enables greater radiative fluxes into the oceans surrounding Antarctica and thereby a faster SST warming in the Southern Ocean.

Figure 1.6 shows the sea ice concentration at March maximum and September minimum for the NH, as in Figure 1.5. The DP_{open} and DP_{clsd} ensembles are very similar in their sea ice coverage. There is a clear seasonal cycle with greater coverage and concentration in March than in September. In both cases the decline in sea ice is modest over the warming period, and observations suggest that this decline is underestimated (Wang and Overland, 2009). However, the model's NH sea ice coverage and response to global warming are both consistent with the IPCC AR4 projections (Meehl et al., 2007). The similarity between the two DP scenarios indicates that the ensembles do isolate the impact of opening and closing DP upon the interhemispheric asymmetry, with little impact over the Arctic.

The sea ice differences indicate that when the ACC is replaced by polar gyres in

the presence of a land bridge, the increased advection of heat into the far Southern Ocean prevents much of the present day sea ice from forming. Sea ice, enabled by the presence of the ACC, provides insulation to the ocean from both incoming shortwave and outgoing longwave radiation. Furthermore, heat loss from the ocean to the atmosphere is suppressed in the presence of sea ice. However, our results suggest that the primary impact of this sea ice is to reduce the warming effect of the shortwave radiation, thus slowing the warming response of the SH sufficiently to increase the interhemispheric asymmetry of both SST and SAT.

1.4 Summary and Conclusions

The results presented here have further implications for detecting a CO_2 warming footprint in observed temperature trends. By comparing two sets of ensemble global warming simulations with an open and a closed DP we demonstrate the importance of the ACC in limiting the rate of warming in the Southern Ocean. This effect would not be captured in climate models with simplified representations of the ocean, such as a uniform slab ocean or an aquaplanet. Furthermore, given the faster rate of warming in the NH and the lower proportion of observations available in the high southern latitudes, care needs to be taken when inferring global trends from an asymmetric set of observations.

This study has demonstrated the importance of the ACC in determining the climate response to global warming, and highlights the need to improve its representation in climate models. While the impact of the DP has been analyzed in ocean-only, intermediate complexity and idealized coupled climate models, this study is the first to demonstrate its impact in a fully coupled climate model with realistic continents and a complete representation of the hydrological cycle. The present model relies upon sub-grid scale eddy parameterizations, however the Southern Ocean climate may respond differently when eddies are explicitly resolved (Hallberg and Gnanade-

sikan, 2006). Investigating the interhemispheric asymmetry of global warming in eddy-permitting and eddy-resolving models will be the focus of a follow-up study.

Transient global warming experiments with the DP closed reveal that a significant fraction of warming asymmetry in SST can be attributed to the thermal isolation provided the ACC. The ACC enables a much greater presence of sea ice and reduced poleward heat transport in the SH, causing the Southern Ocean as a whole to warm more slowly in response to strong CO_2 forcing. Previous discussions of the interhemispheric asymmetry have emphasised the role of heat capacity differences between the hemispheres, heat uptake in the deep mixed layers of the Southern Ocean, and ice-albedo feedback in the Arctic. This study has shown that the ACC provides a further mechanism to slow global warming in the high southern latitudes, contributing to a substantial proportion of the asymmetry compared to the scenario of a blocked circumpolar flow around the Southern Hemisphere.

Part 2

Interhemispheric Asymmetry of Warming in an Eddy Permitting Coupled Sector Model

Abstract

Climate model projections and observations show a faster rate of warming in the Northern Hemisphere (NH) than the Southern Hemisphere (SH). This asymmetry is partly due to faster rates of warming over the land than the ocean, and partly due to the ocean circulation redistributing heat towards the NH. This study examines the interhemispheric asymmetry of warming in an intermediate complexity coupled climate model with eddy-permitting (0.25°) ocean resolution, and results are compared with a similar model with coarse (1°) ocean resolution. The models use a pole-to-pole 60°-wide sector domain in the ocean and a 120°-wide sector in the atmosphere, with Atlantic-like bathymetry and a simple land model. There is a larger high-latitude ocean temperature asymmetry in the 0.25° model compared with the 1° model, both in equilibrated control runs and in response to greenhouse warming. The larger warming asymmetry is caused by greater melting of NH sea ice in the 0.25° model, associated with faster, less viscous boundary currents transporting heat northwards. The SH sea ice and heat transport response is relatively insensitive to the resolution change, since the eddy heat transport differences between the models are small compared with the mean flow heat transport. When a wind shift and intensification is applied in these warming scenarios, the warming asymmetry is further enhanced, with greater upwelling of cool water in the Southern Ocean and enhanced warming in the NH. Surface air temperatures show a substantial but lesser degree of high latitude warming asymmetry, reflecting the sea surface warming patterns over the ocean but warming more symmetrically over the land regions.

2.1 Introduction

Global climate models predict greater warming in the Northern Hemisphere (NH) than the Southern Hemisphere (SH) over the 21st Century in response to increasing

greenhouse gases (Friedman et al., 2013). Observations of sea surface temperature (SST) warming show a high degree of interhemispheric asymmetry (Morice et al., 2012), which is reflected in the rapid melting of Arctic sea ice in contrast to a lack of melting of Antarctic sea ice (Blunden and Arndt, 2014). This asymmetry has long been established (Stouffer et al., 1989; Manabe et al., 1991; Flato and Boer, 2001), and is due in large part to differences in the land surface area of each hemisphere, since the NH is 39% land-covered while the SH is only 19% (National Geophysical Data Center, 2006). The ocean's large heat capacity and its high evaporative cooling imply that it should warm more slowly than the land surface (Sutton et al., 2007; Byrne and O'Gorman, 2013) and thus create a warming asymmetry. The asymmetry is reinforced by the Antarctic Circumpolar Current (Part 1), which limits ocean heat transport towards the high southern latitudes.

Marshall et al. (2014, 2015) recently argued that much of the asymmetry of sea surface temperature (SST) warming predicted in the Coupled Model Intercomparison Project Phase 5 (CMIP5) models can be explained by ocean circulation. They applied a globally uniform warming flux of 4 W m^{-2} over a 100 year simulation using a global ocean-only model and found a global SST anomaly pattern with striking similarity to the CMIP5 average. It therefore seems likely that the interhemispheric asymmetry of warming is caused in large part by both ocean circulation and faster warming over land. Marshall et al. (2014) also found that ozone forcing causes a temporary cooling of the Southern Ocean due to wind-driven upwelling, whereas in the latter half of the 21st Century stronger wind forcing creates warming in the Southern Ocean. This transient cooling trend may be enhanced at eddy-permitting ocean resolution (Morrison et al., 2013) due to the fast response of the vertical eddy heat flux induced by stronger winds.

Global climate models suitable for equilibrium integrations remain restricted to the resolution of parameterized ocean eddies, of order 1° resolution as in most of the CMIP5 models. There is a growing body of evidence that permitting or

resolving eddies will alter the climate's response to atmospheric forcing (Farneti et al., 2010; Spence et al., 2013; Zhang and Vallis, 2013). Furthermore, key oceanic processes that regulate Earth's climate, such as western boundary currents and inter-ocean exchange, are better resolved in high-resolution ocean models. Thus we are motivated to examine the impact of a higher resolution ocean model on the interhemispheric asymmetry of warming, since the response of eddies, stronger boundary currents and sea ice may depend upon resolution.

Recent progress has been made in simulating a fully coupled climate system at high resolution for greater than 100 years, allowing $2\times CO_2$ warming experiments at 0.25° resolution in the eddy-permitting regime (Delworth et al., 2012), and at 0.1° resolution in the eddy-resolving regime (Kirtman et al., 2012; Bryan et al., 2014; Griffies et al., 2015). These cutting-edge simulations have come at a high computational expense, and were not tuned to the same degree as their low resolution equivalents, nor were they run to equilibrium. Yet, the higher resolution models have shown strikingly different climate states to their lower resolution counterparts, raising questions about how these differences can be explained or reconciled between resolutions.

A key difference highlighted by these high resolution simulations is the sea ice climatology. Kirtman et al. (2012) found a lower sea ice concentration and coverage in the NH at 0.1° resolution than the 1° model, which had a more realistic sea ice climatology. SH sea ice coverage was very similar between the resolutions, leading to a greater degree of asymmetry between the polar climates at high resolution. By contrast, the Delworth et al. (2012) model showed a greater coverage of sea ice at 0.25° resolution. However, parameter changes such as zero prescribed background vertical diffusion and increased ice albedo may have weakened the meridional overturning circulation (MOC), and increased sea ice extent.

A recent ocean-only study (Zhang and Vallis, 2013) examined differences in the MOC between coarse, eddy-permitting and eddy-resolving resolutions (2°, 0.25° and

0.125° respectively). They found a decreased heat transport across the Southern Ocean in the eddy-permitting model, resulting in overly steep isopycnals and a weaker AABW cell. By contrast, the eddy-resolving simulation had a more realistic stratification and lower overturning cell, as did the coarse model. However, their domain was a flat-bottomed 60° pole-to-pole sector, with idealized temperature forcing and uniform salinity. Our study examines resolution dependence in a similar domain, however we include realistic bathymetry and couple the ocean with sea ice, atmosphere and land components.

While pole-to-pole sector domains are often used in ocean models to make higher resolution modelling more tractable, the same approach is less common in coupled models of the climate system, where global dynamics are important. One climate model that uses a sector configuration is the Intermediate Complexity Climate Model (ICCM) of Farneti and Vallis (2009), with a 60°-wide sector ocean coupled to a 120° sector atmosphere. This model was designed as a fast-running coarse resolution climate model to explore a wide range of parameters (Farneti and Vallis, 2011), but also provides a useful framework for reducing the computational load in a high resolution coupled climate model. A further benefit is that it allows a comparison between ocean-only sector models (e.g. Zhang and Vallis, 2013) and fully coupled climate models that cannot be easily adapted to sector domains.

In this study we use different configurations of the Farneti and Vallis (2009) ICCM to explore the gap between ocean-only sector models and global coupled climate models, at two different horizontal ocean model resolutions. This configuration allows us to simulate the ocean at eddy-permitting (0.25°) resolution for 500 year control runs. This spin-up time is longer than many recent eddy-permitting global climate models, and therefore results in reduced drift prior to the perturbation experiments. We compare our results to a coarse resolution 1° model, with parameterized eddies. We investigate the impact of resolution on the interhemispheric temperature asymmetry and its response to greenhouse warming. We further examine the

impact of a poleward shift and intensification of the SH westerly winds upon the asymmetry.

2.2 Climate Model and Experiments

2.2.1 Model Description

The experiments presented here use the Intermediate Complexity Climate Model (ICCM) developed by Farneti and Vallis (2009) with several modifications outlined below. The ocean component is the Modular Ocean Model (MOM) Version 5.0.2 (Griffies, 2012), in a 60°-wide sector domain, spanning from 78°S to 75°N. The ocean is simulated at two different resolutions, 1° and 0.25° longitudinal spacing, using a Mercator grid refinement in the latitudinal spacing. Both resolutions use z^* vertical coordinates, given by:

$$z^* = H\left(\frac{z-\eta}{H+\eta}\right) \tag{2.1}$$

where z is the geopotential height, H is the ocean depth, and η is the sea surface height. Both resolutions use 50 levels to a depth of 5500 m and varying vertical resolution from 10 m at the surface to 210 m at depth.

The ocean coastlines and bathymetry use a modified Atlantic-like topography, derived from a realistic global ocean model, as described in Snow et al. (2015). The bathymetry is constructed via dilation and contraction of terrain contained within two piecewise linear boundaries to fit a 60°-wide sector. The boundaries are chosen to be mainly over land bordering the Atlantic ocean, producing sidewalls everywhere except for a zonally unbounded channel through Drake Passage to allow a flow analogous to the Antarctic Circumpolar Current (ACC). The sea ice model is the Sea Ice Simulator in the standard MOM distribution, and uses the same horizontal grid as the ocean model.

The atmosphere is a B-grid dynamical model, spanning a 120° sector and latitudes from 84°S to 84°N, with a horizontal resolution of 2° latitude × 2° longitude and 7 vertical levels. The atmosphere employs a simplified grey radiation model, with no seasonal or diurnal cycle, and no explicit greenhouse gas or cloud schemes. Outside of the ocean sector, a simple land model is coupled to the atmosphere. As described in Farneti and Vallis (2009), the land model uses a 'bucket' soil water scheme, with constant values of water availability and heat capacity. When precipitation exceeds the water capacity, idealized rivers redistribute runoff back into the ocean using a basin map. This scheme allows closure of the water budget within the coupled model. There is no orography, and all precipitated water stays in liquid form. Coupling of the model components is implemented through the Geophysical Fluid Dynamics Laboratory Flexible Modelling System. A schematic diagram of the ICCM sector domain is shown in Figure 2.1, reproduced from Farneti and Vallis (2009).

The different horizontal resolutions allow a comparison of coupled climate simulations between parameterized and permitted ocean eddies. In the 1° model, we use the Gent and McWilliams (1990) eddy parameterization as implemented by Griffies (1998), using a constant coefficient of 600 $m^2\ s^{-1}$, while in the 0.25° model, no eddy parameterization is used. For the horizontal viscosity we use a biharmonic Smagorinsky viscosity (Griffies and Hallberg, 2000), where the viscosity varies according to the grid length and the ocean state. Using the Griffies and Hallberg (2000) scheme, we set the dimensionless scaling parameter to $C = 3$ in the 1° models and $C = 2$ in the 0.25° models. Laplacian viscosity is used in the bottom grid cells, in order to improve stability in thin partial cells. The coarse resolution model must be run with a higher viscosity due to numerical stability issues. While it is possible to run the higher resolution model with high viscosity, this would greatly reduce the benefit of running at higher resolution, namely, the more realistic eddy field and sharper gradients in the velocity fields.

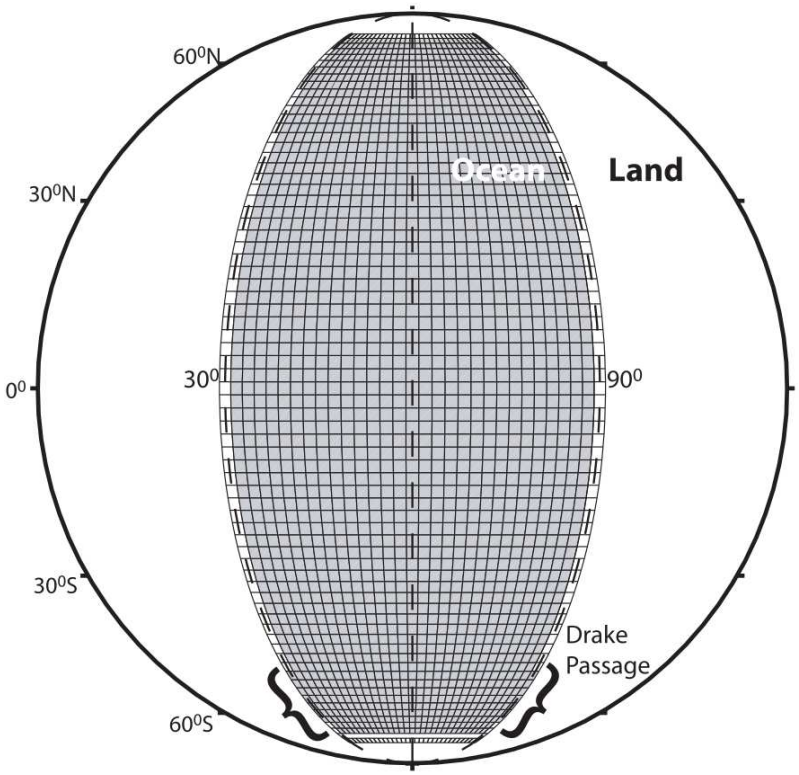

Figure 2.1: Schematic diagram of the Intermediate Complexity Coupled Model (ICCM), reproduced from Figure 1 of Farneti and Vallis (2009). The atmosphere and land components span the longitudes of 0-120°E, while the ocean and sea ice components span the longitudes of 30-90°E, while a periodic boundary condition in the ocean enables an ACC-like flow.

In the mixed layer at both resolutions, we use the sub-mesoscale eddy parameterization of Fox-Kemper et al. (2008) and the KPP boundary layer mixing scheme of Large et al. (1994). We use the interior gravity wave-induced mixing scheme of Simmons et al. (2004) and the coastal tide mixing scheme of Lee et al. (2006). The background vertical diffusivity is set to 5×10^{-5} m^2 s^{-1}, which is higher than estimates from observations, but forces an overturning circulation similar in magnitude to that of the global ocean (Section 2.3.5). For a discussion on the sensitivity of the ICCM to vertical diffusivity, see Farneti and Vallis (2009).

2.2.2 Calibration of Radiative Forcing

Due to the grey radiation scheme used in the ICCM, no explicit representation of greenhouse gases is possible. To emulate the effects of increasing greenhouse gases,

we adjust the infrared optical depth as a proxy for greenhouse gas radiative forcing. The model contains an analytic profile of longwave optical depth (Frierson et al., 2006), where the dimensionless surface optical depth τ_0 is given by

$$\tau_0 = \tau_{0e} + (\tau_{0p} - \tau_{0e}) \sin^2(\theta), \tag{2.2}$$

$\tau_{0e} = 6.0$ and $\tau_{0p} = 1.5$ are the surface values at the equator and pole respectively, and θ is the latitude. The vertical structure of optical depth is given by

$$\tau = \tau_0 \left[f_l \left(\frac{p}{p_s} \right) + (1 - f_l) \left(\frac{p}{p_s} \right)^4 \right], \tag{2.3}$$

where p and p_s are the pressure at the model level and the surface respectively, and $f_l = 0.1$ is a parameter that allows shorter relaxation times in the stratosphere.

This optical depth profile is designed to represent the greenhouse effect of water vapour in the atmosphere, which is strongest in the tropics, decreases towards the poles, and decays rapidly with height (Frierson et al., 2006). We implemented radiative forcing by increasing τ_{0e} and τ_{0p} in proportion to their original values, which keeps the shape of the optical depth profile the same. The rationale for this choice is that although greenhouse gases cause global radiative forcing, the water vapour feedback follows a similar profile to the original distribution.

To achieve the equivalent radiative forcing of a $2\times CO_2$ scenario, we calibrated the optical depth parameters to give an increase in radiative forcing of 8 W m^{-2}. This value was chosen to represent 4 W m^{-2} of direct radiative forcing from doubling CO_2 concentration, plus a further 4 W m^{-2} to represent the water vapour feedback (Myhre et al., 2013), which would otherwise be missing in this model. To calibrate this forcing, a set of five perturbation tests were initiated from a spun-up state and run for 1 day with increases in the optical depth of 0, 5, 10, 15 and 20%. In each case, the global mean outgoing longwave radiation (OLR) was computed and the anomaly from the 0% case is shown in Figure 2.2. The near-instantaneous deficit

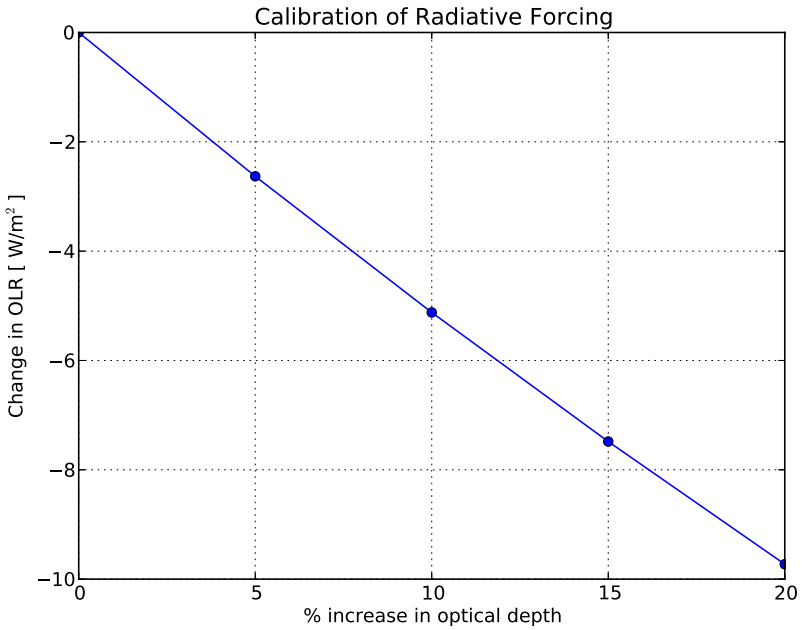

Figure 2.2: Calibration of the optical depth parameter to achieve a radiative forcing of 8 W m^{-2}. The drop in OLR after 1 day is approximately equal to the radiative forcing of the optical depth change.

in OLR approximately equals the radiative forcing from the optical depth change (e.g. Pierrehumbert, 2010). The percentage change associated with an 8 W m^{-2} forcing was found to be 16.2% using linear regression. Finally, to emulate a 1% per year increase in CO_2, the optical depth was increased by 0.215% per year, so that it reached the $2\times CO_2$ value of 16.2% at year 70, after which it was held fixed.

2.2.3 Wind Stress Forcing

The default configuration of the ICCM yields midlatitude westerly winds that are nearly symmetric about the equator, being too weak in the Southern Hemisphere and with an equatorward bias compared with observations (Farneti and Vallis, 2009). This wind stress profile was partially corrected in this model by adjusting the land surface roughness in the SH. A shorter roughness length results in a lower drag coefficient, as given by Equations 12-14 of Frierson et al. (2006). We used a land surface roughness length of $z_0 = 0.1$ m everywhere in the domain, except between the latitudes of 40°S to 70°S where the roughness length was lowered to $z_0 = 1.0 \times 10^{-4}$

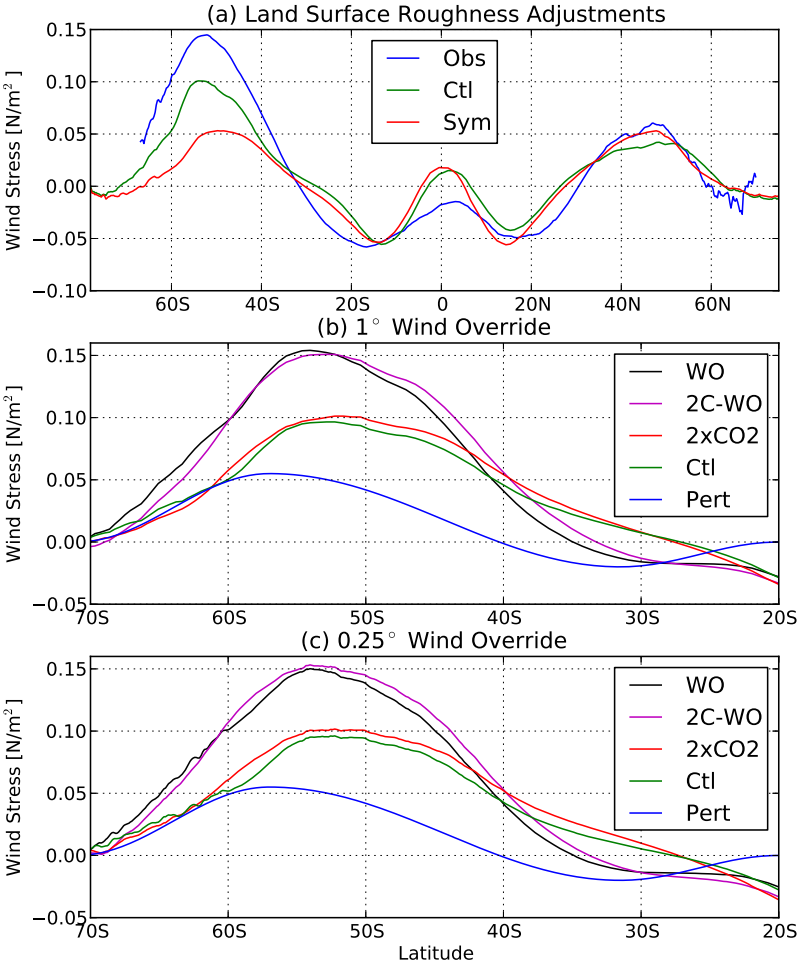

Figure 2.3: (a) Zonal mean wind stress (N m^{-2}) comparison between the observational dataset of Risien and Chelton (2008) (blue), the default ICCM wind stress (red) and the wind stress with land surface roughness adjustments (green). (b) Zonal mean wind stress in the 1° Control, 2×CO_2, wind override (WO) and 2×CO_2 wind override (2C-WO) experiments, with the perturbation pattern (Pert) from year 70 onwards. (c) As in (b), but for the 0.25° model. The experiment definitions are given in Section 2.2.4.

m. The lowered roughness in these latitudes provides an analogue to a global model, where the SH westerly winds are stronger due to lower friction over the ocean than over the corresponding NH continents. This adjustment yielded a more realistic position and strength of the SH surface westerly winds, though the peak magnitude is still lower than observed values. The improved wind stress profile is shown in Figure 2.3a, compared with the default symmetric profile and an observational dataset.

In the warming experiments presented here, we found that the midlatitude SH westerly wind stress peak increased by 5% and 6% in the 1° and 0.25° models

respectively. In the 1° model the peak location shifted equatorward from 52.3°S to 51.6°S, while in the 0.25° model the peak location remained steady at 52.3°S. This evolution does not agree with the poleward wind shift found in most global climate model projections (Barnes and Polvani, 2013). The difference is partly due to the grey radiation scheme employed here, which does not include ozone or an explicit representation of greenhouse gases. Ozone depletion and CO_2 forcing can both cause cooling of the polar stratosphere, which in turn leads to a poleward shift of the westerly winds (Polvani and Kushner, 2002; Barnes and Polvani, 2013). These effects are not captured by the radiative forcing method we have used to emulate a CO_2 perturbation in the troposphere. Nevertheless, there remains uncertainty over the relative roles of greenhouse gases and ozone in the observed and projected poleward shift of the westerly winds (Kidston and Gerber, 2010; Thompson et al., 2011). It is therefore useful to examine warming scenarios both with and without a poleward shift and intensification of the westerly winds.

In order to simulate the impact of a poleward shift of the westerly winds on the ocean circulation, we apply a correction to the wind stress field as shown in Figure 2.3b,c. This correction is referred to as a 'wind override', and consists of a perturbation in the Southern Hemisphere only, with a zonally uniform pattern, which increases the peak zonal mean wind stress from approximately 0.1 N m^{-2} to 0.15 N m^{-2} (a similar perturbation to Delworth and Zeng, 2008). The wind override is applied both with and without radiative forcing. In the 1° model, the wind override shifts the wind stress peak southward from 52.3°S to 54.1°S in the control case, and from 51.6°S to 52.9°S in the $2\times CO_2$ case. In the 0.25° model, the wind stress peak shifts from 52.3°S to 54.1°S in both the control and $2\times CO_2$ cases. The position of the wind stress maximum cannot be explicitly controlled, since the winds are freely evolving. However, the wind override experiments provide a much larger change to the Southern Ocean wind stress than the differences between the control and $2\times CO_2$ runs, as shown in Figure 2.3b,c.

2.2.4 Summary of Experiments

The 1° model was equilibrated for 1000 years after the model parameters were finalized. The ocean temperature and salinity restart file at year 500 was interpolated onto the 0.25° grid and spun up from zero velocity for a further 500 years. These equilibrated states were used to initiate perturbation experiments and parallel control runs. In each case we subtract the control run from the perturbation run to remove model drift.

We present four experiments at each resolution, and define shorthand for these experiments below. All experiments are initiated from the same equilibrated state, and run for 90 years: (i) Control (no perturbation); (ii) $2\times CO_2$: where our equivalent CO_2 was increased at 1% per year until doubling at year 70 and then held fixed; (iii) wind override: a wind shift and intensification perturbation, with a linearly increasing magnitude until year 70 and then held fixed; and (iv) $2\times CO_2$ wind override: combined perturbations of the $2\times CO_2$ and wind override experiments. We add the prefix 1° or 0.25° to this shorthand to denote the ocean model resolution.

2.3 Warming Response

2.3.1 Control Climates

The control states of both the 1° and 0.25° model have a substantial interhemispheric temperature asymmetry. The land-ocean ratio is very similar between the hemispheres; the NH and SH are 61% and 59% land covered respectively. The land distribution and the largely symmetric atmosphere forcing ensure that the ocean circulation is the key mechanism that creates the asymmetry. The interhemispheric temperature (NH-SH) difference is 2.19°C and 1.25°C for SST and surface air temperature (SAT) respectively in the 1° control run, and 2.72° and 1.95°C for SST and

SAT in the 0.25° control run. This asymmetry compares with an interhemispheric SST difference of 3.63°C from an observational climatology (Locarnini et al., 2010).

A comparison of the control run surface climates is shown in Figure 2.4. There is a significant increase in the interhemispheric temperature asymmetry when moving from 1° to 0.25° ocean resolution. The difference is greatest in the northern high latitudes, where warmer SST penetrates further towards the poles. The SAT difference is greatest over the northern edge of the ocean basin, but there is also a warmer SAT over the mid and high latitude land regions. The Southern Hemisphere SST and SAT are more similar between the resolutions. These differences are closely linked to sea ice differences between the models, which are discussed in Section 2.3.3. The asymmetries we present in the perturbation runs are in addition to a substantial asymmetry in the mean state.

The warmer NH high latitude ocean in the 0.25° model is in large part caused by differences in the boundary currents. In the 0.25° model, the boundary currents are narrower and more closely confined to the coastlines than in the 1° model, leading to an increase in poleward heat transport. The separation of the Gulf Stream from the coast is not well captured in these models, due to distortions in the coastline geometry and changes in the wind forcing over this basin. However, the latitude of the Gulf Stream separation is slightly closer to observations in the 1° model. Apart from the separation point, the velocities and widths of the boundary currents are more realistic at 0.25°, and the presence of eastern boundary currents (especially north of 60°N) give the 0.25° model a better overall representation of boundary current heat transport.

2.3.2 Surface and Deep Warming

Both the 1° and the 0.25° simulations show a strong asymmetry of warming in the Atlantic configuration. Figure 2.5 shows the SST and SAT anomaly pattern

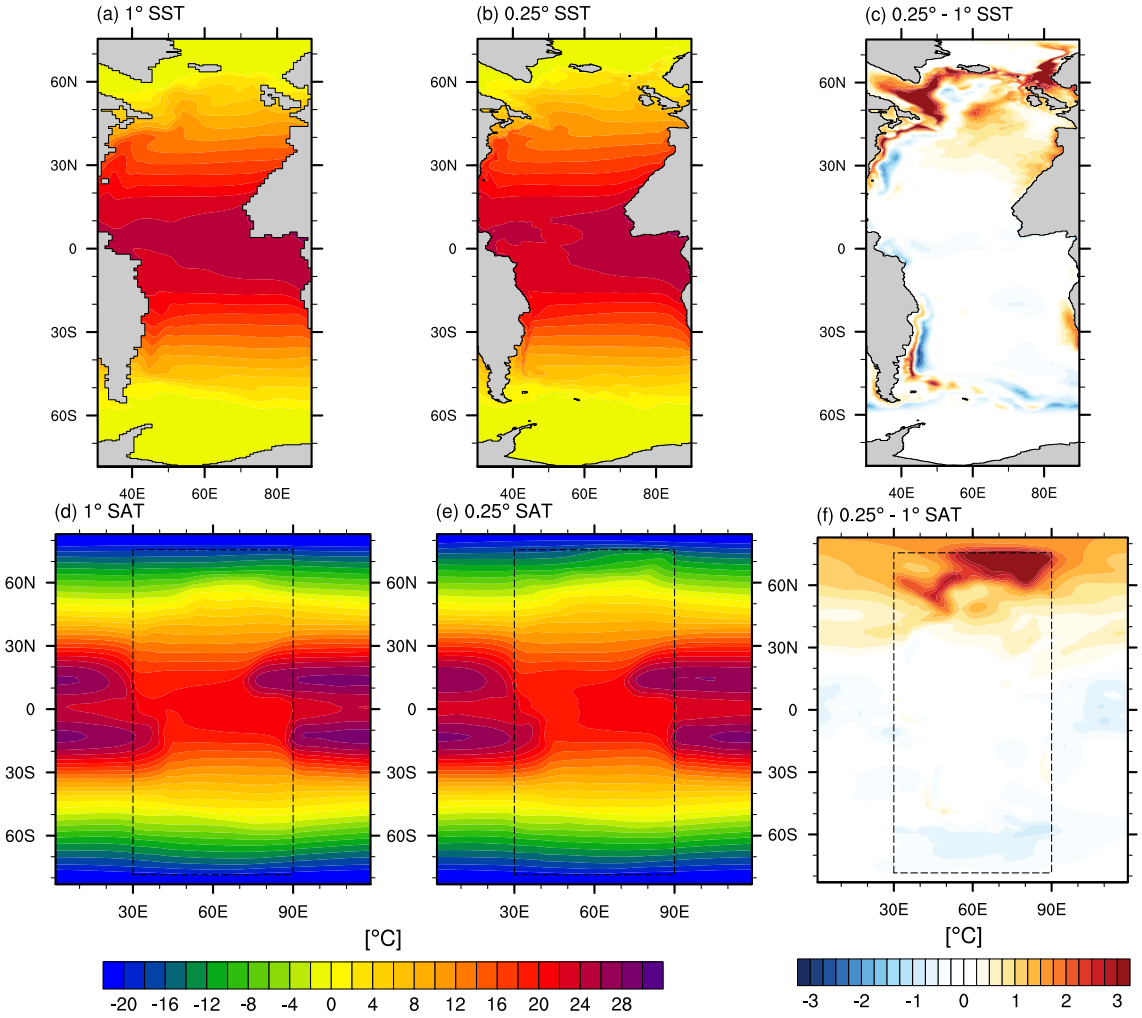

Figure 2.4: Control run climates, showing sea surface temperature (SST; °C) in the (a) 1° model and (b) 0.25° model, and (c) difference 0.25° - 1°; and surface air temperature (SAT; °C) in the (d) 1° model and (e) 0.25° model, and (f) difference 0.25° - 1°. The ocean domain is denoted by the dashed box in parts (d-f).

in years 71-90 of the $2\times CO_2$ run, differenced from the same period of the control run. In the 1° model there is a region around 60°N where SST warms by up to 5°C (Figure 2.5a). This warming is associated with a high rate of melting of Arctic sea ice. North of approximately 65°N there is a region of suppressed warming, where sea ice persists in the $2\times CO_2$ state. The 0.25° SST (Figure 2.5b) shows a similar pattern of warming in most regions, except that the warming extends throughout nearly all of the North Atlantic. The patterns of SST warming project strongly onto the northern high latitude SAT warming patterns (Figure 2.5d,e). SAT warming is enhanced over the Arctic in the 0.25° model compared with the 1° model, due to the greater sea ice melting and high latitude SST warming. Differences in SST and

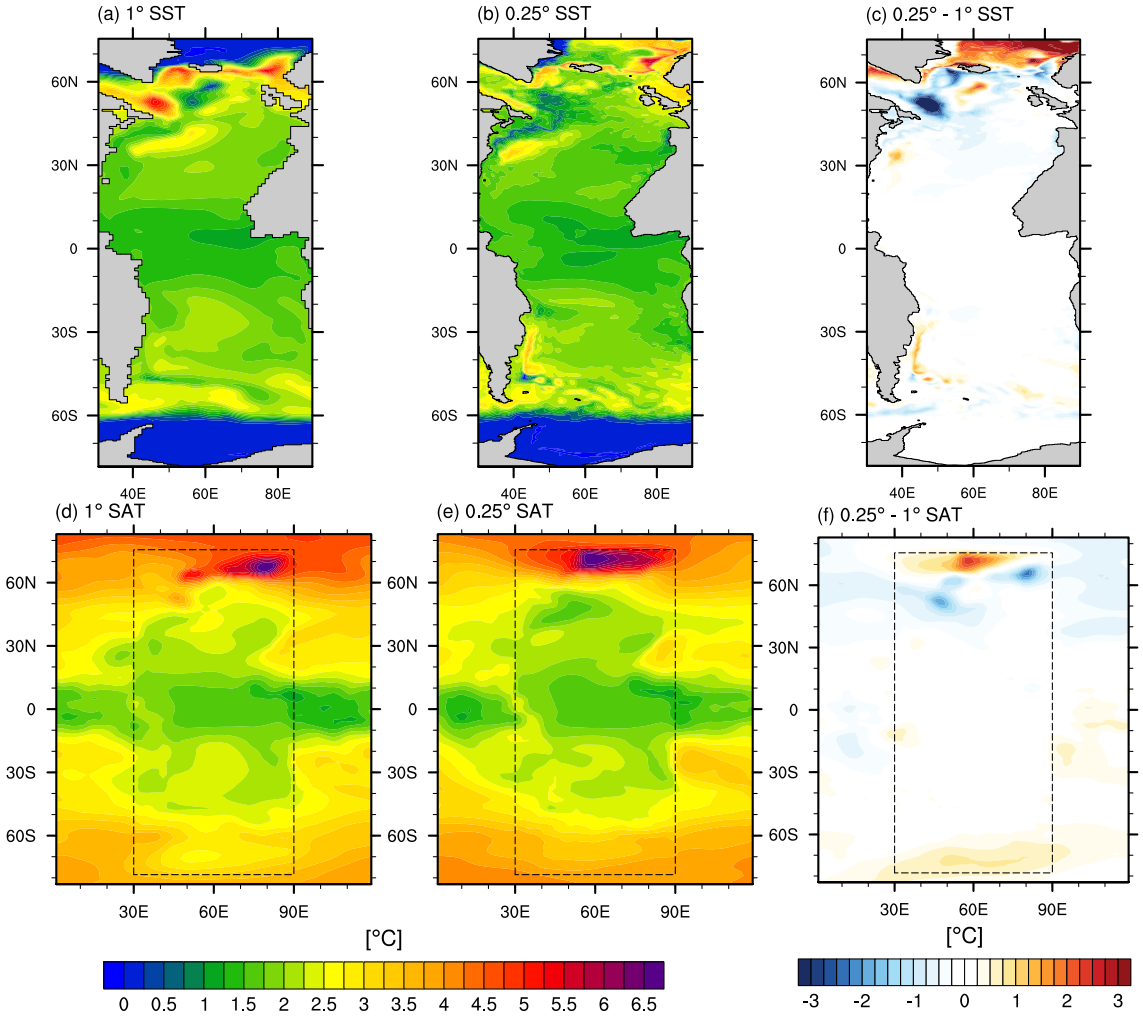

Figure 2.5: SST anomaly (°C) in the (a) 1° model, (b) 0.25° model and (c) the difference; SAT anomaly (°C) in the (d) 1° model, (e) 0.25° model and (f) the difference. The anomaly is the average from years 71-90 of the 2×CO_2 run, minus the same period from the control run. The ocean domain is indicated by the dashed box in parts (d-f).

SAT warming between the resolutions are shown in Figure 2.5c,f.

The Antarctic warming is markedly lower than the Arctic warming in both simulations. Sea ice melt in the SH is relatively low through the 2×CO_2 runs and there is very little (∼0.1°C) warming of SST poleward of 60°S in either scenario. There remains polar amplification of the SH SAT warming pattern, however its magnitude is 3°C lower over the Southern Ocean than over the NH ocean at the same latitudes. The SH warming pattern is relatively insensitive to the change in resolution. This result suggests that the parameterized and permitted eddy regimes perform similarly well in simulating the surface warming of the Southern Ocean.

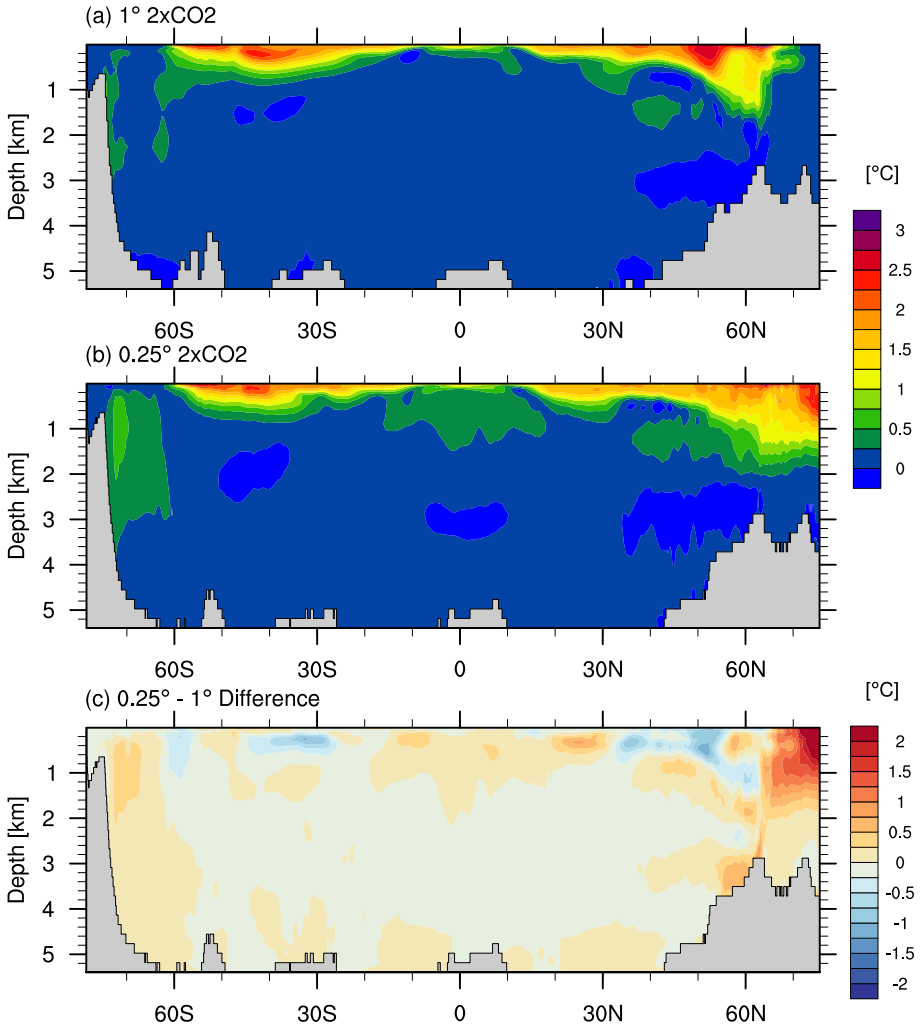

Figure 2.6: Zonal mean temperature anomaly (°C) in the (a) 1° and (b) 0.25° $2\times CO_2$ runs; and (c) the difference 0.25° - 1°. The anomaly is the average from years 71-90 of the $2\times CO_2$ run, minus the same period from the control run.

The zonal mean temperature anomaly at depth in each of the models is shown in Figure 2.6. The warming anomaly is generally less than 0.5°C below the top 1 km, except in the northern high latitude deep water formation region. The enhanced warming in the northern high latitudes extends to the edge of the domain in the 0.25° model, whereas in the 1° model the warming signal becomes weaker north of 65°N. In addition, there is a stronger warming signal in the top 500 m at around 50-55°N in the 1° model, associated with the melting of sea ice at lower latitudes in this model. Deep warming south of 60°S is slightly stronger in the 0.25° model, but is generally less than 0.5°C at all depths.

Deep water formation regions, as measured by deeper mixed layers (Figure

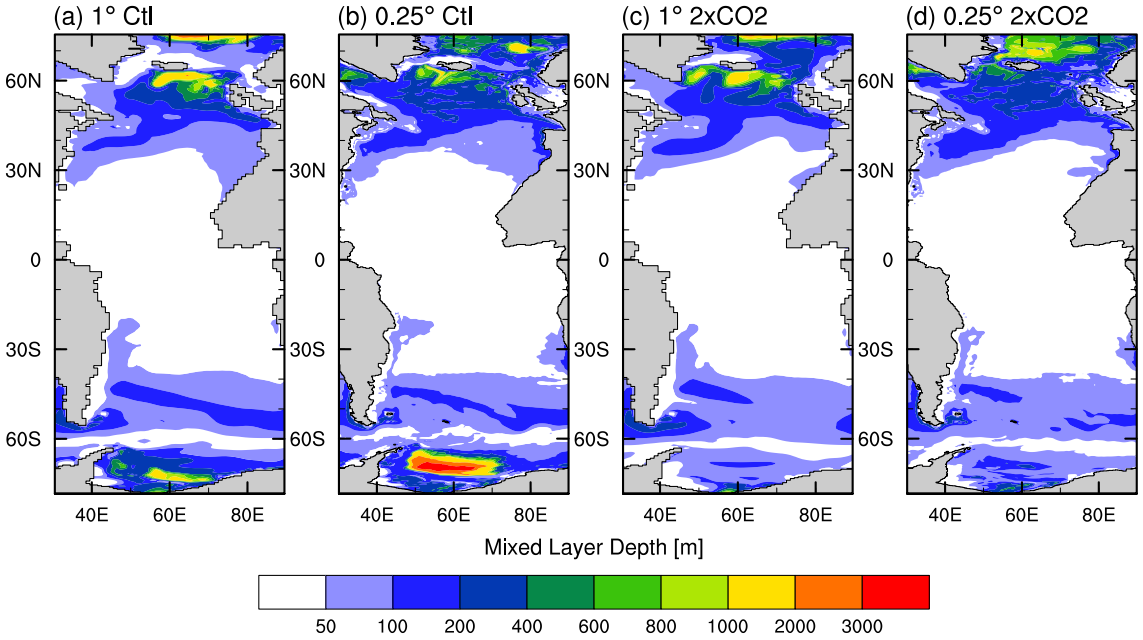

Figure 2.7: Mixed layer depth (m) averaged over years 71-90 in the (a) 1° and (b) 0.25° control runs; and the (c) 1° and (d) 0.25° 2×CO_2 runs.

2.7), also reveal differences between the coarse and eddy-permitting models. The 1° control run has a major sinking region near the southern coast of Iceland, which remains the primary NH sinking region in 2×CO_2 run. The 1° model also exhibits significant sinking along the northern edge of the domain, where a vertical sidewall enhances convection. In the 0.25° control run, the sinking region south of Iceland is also present but covers a smaller area, however this sinking region largely disappears by the end of the 2×CO_2 run. Instead, the sinking region shifts north and becomes centered around 70°N in the 0.25° 2×CO_2 run. The more northern location of sinking is associated with a northward shift of the sea ice edge, since ice formation greatly enhances the local density of seawater through brine rejection. This northward shift of the NADW formation draws surface heat further north in the 0.25° model, enhancing the warming asymmetry. Mixed layer depths in the Southern Ocean show a major decline due to warming in both models. This decrease in the sinking depth is associated with a major weakening of AABW formation, discussed further in Section 2.3.5.

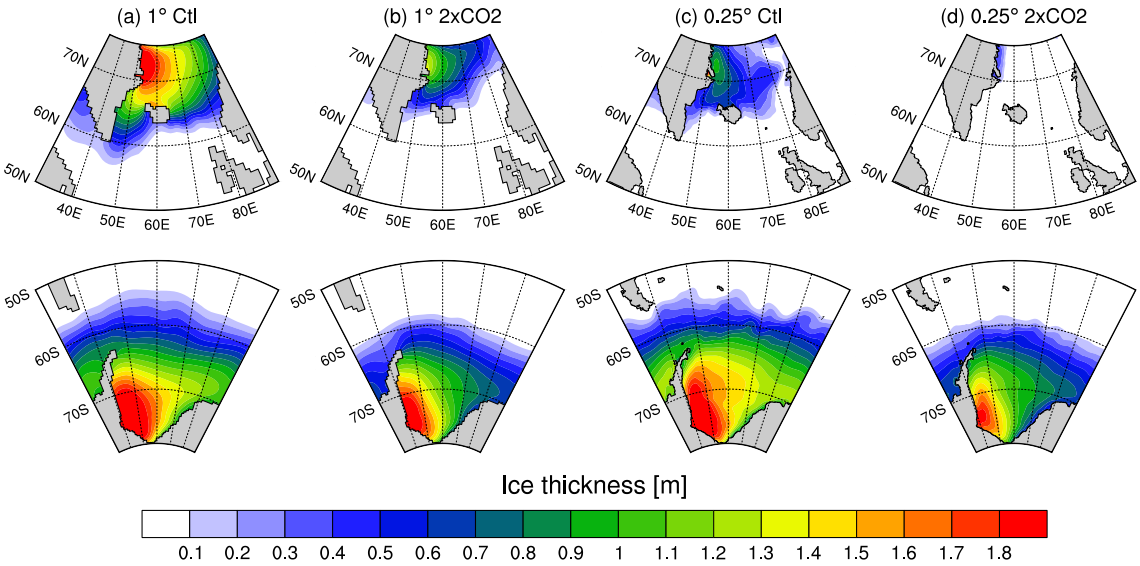

Figure 2.8: Sea ice thickness (m) in the (a) 1° control run, (b) 1° 2×CO_2 run, (c) 0.25° control run and (d) 0.25° 2×CO_2 run averaged from years 71-90.

2.3.3 Sea Ice Response

The sea ice climatology is sensitive to the change in resolution (Figure 2.8). In the 1° model, the NH sea ice is thicker and covers a greater area than in the 0.25° model in the control simulation. By contrast, the SH sea ice distribution and thickness is similar at both resolutions, with a moderate melt back of SH sea ice at the end of the 2×CO_2 run. By the end of the 2×CO_2 run, NH sea ice in the 0.25° model melts almost completely (Figure 2.8d). This in turn leads to increased radiative forcing of the high latitude ocean and a larger SST response. In contrast, NH sea ice in the 1° model melts to a lesser extent (Figure 2.8b), and most of the ocean north of 65°N remains covered by ice. The NH sea ice extent at the end of the 1° 2×CO_2 run is similar to that of the 0.25° control run.

Due to the major role sea ice plays in the asymmetric warming response, additional experiments are performed in an attempt to decouple the feedback from ice melting. In these experiments, sea ice from the control run is output at monthly resolution for the 90 year period analysed here, and additional runs based on the control and 2×CO_2 runs are performed in which sea ice is restored towards the control run sea ice evolution. This restoring perturbs the circulation of both runs,

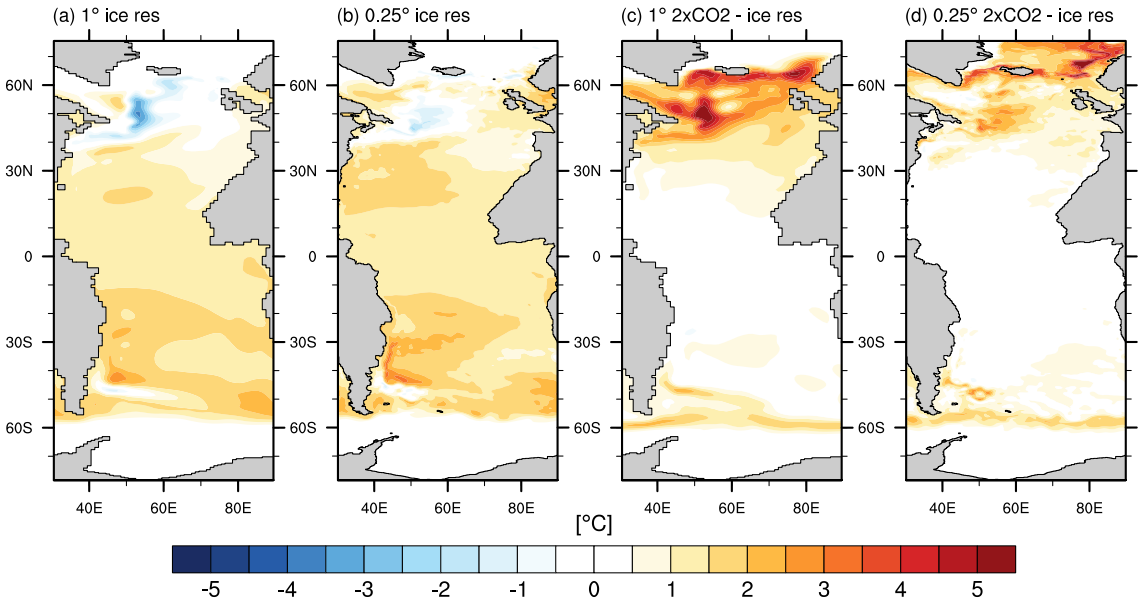

Figure 2.9: SST anomalies (°C) from the (a) 1° and (b) 0.25° ice restored warming runs, and the difference between the SST anomaly of the $2\times CO_2$ runs (Figure 2.5a,b) minus the ice-restored warming runs (Figure 7a,b) for the (c) 1° and (d) 0.25° models.

with NADW and AABW formation weakening due to the altered fluxes at their formation regions. Figure 2.9 shows the SST warming response of the ice-restored $2\times CO_2$ run minus the ice-restored control run. We also show the difference between the $2\times CO_2$ warming anomaly (shown in Figure 2.5) and the ice restored $2\times CO_2$ anomaly.

With sea ice restoring, the polar warming of SST is greatly damped, especially in the NH. In the region of the Gulf Stream, there is a cooling of up to 2°C (Figure 2.9a,b), which is likely due to a large reduction of NADW formation in the ice restored warming run. The strong warming signal poleward of 50°N in the $2\times CO_2$ run largely disappears. In the SH, the warming signal is also damped by the ice restoring, but since the change in SH sea ice extent is much smaller, the SH warming signal is less perturbed by the ice restoring. Away from the ice region, the warming signal is largely unchanged, with around 1.5°C warming of SST between 40°N and 40°S.

The ice restoring results contrast with Marshall et al. (2014, 2015), who found a strong SST asymmetry in warming simulations where sea ice was not allowed to

melt. However, they used an ocean-only model in which sea ice was held fixed, and equilibrated their model in that state. Our configuration differs in that sea ice continues to evolve and is simultaneously restored towards a control state. In our model, the restoring damps any warming that is advected into the ice region, and greater warming results in stronger damping. Nevertheless, the ice restoring results confirm that sea ice melting is of first order importance in setting the high latitude asymmetry. We argue that the heat transported by warm boundary currents is the underlying cause of asymmetry between the NH and SH sea ice responses.

2.3.4 Boundary Currents

The Southern Ocean's response to external forcing is expected to change at higher resolution, due to effects such as eddy compensation and eddy saturation (Farneti et al., 2010; Morrison and Hogg, 2013; Munday et al., 2013). However, we find that the Southern Ocean SST and sea ice respond similarly between the resolutions. Rather than transient eddy effects, our results suggest that better resolution of the mean boundary currents causes the greatest change. Figure 2.10 shows 20 year averages of the ocean surface speed in the North Atlantic region for the (a) 1° model and (b) 0.25° model control runs. In the 0.25° model, the boundary currents are faster on average and more tightly confined to the edge of the basins, while in the 1° simulation they are broader, slower and more viscous. These boundary currents penetrate further north in the high latitudes of the domain in the 0.25° model, bringing warm water further into the ice region and enhancing sea ice melt.

Figure 2.10c shows a comparison of surface currents with observations, using the 1993-2014 mean from the 1/3° resolution Ocean Surface Current Analyses - Real time (OSCAR) dataset (Bonjean and Lagerloef, 2002). These observations demonstrate the greater fidelity of the 0.25° model velocities, though some features such as the boundary currents around the south of Greenland and the Labrador Sea are still weaker than observed values. We compare the poleward heat transport

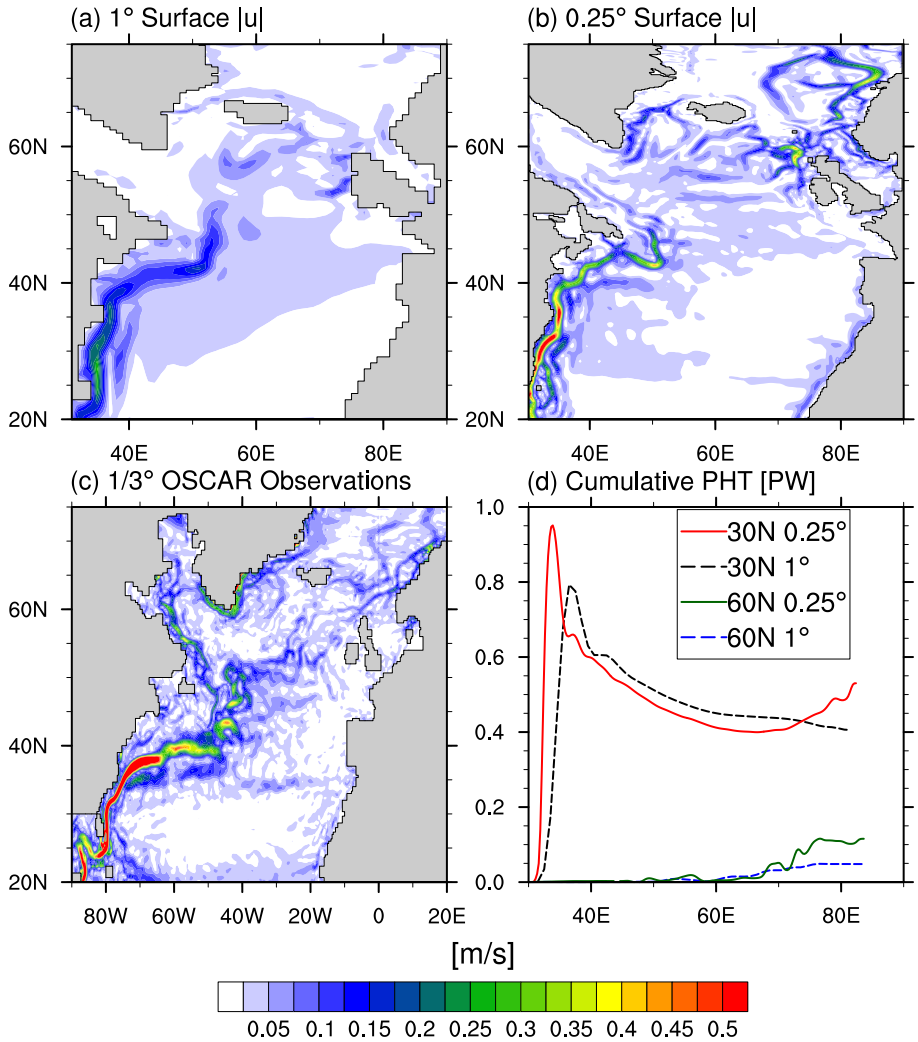

Figure 2.10: 20 year mean surface speed (m s^{-1}) in the North Atlantic for the (a) 1° control, (b) 0.25° control run and (c) 1/3° OSCAR observations of surface currents, showing the 22 year mean from 5-daily observations from 1993-2014 (Bonjean and Lagerloef, 2002). Grid points in (c) were masked out if more than half the time steps were missing. (d) Cumulative integrals from west to east of poleward heat transport (PW) in the top 200 m, at 30°N (red: 0.25°, black dashed: 1°) and 60°N (green: 0.25°, blue dashed: 1°) for each model.

(PHT) of the boundary currents between the resolutions by calculating cumulative integrals of PHT from west to east at 30°N and 60°N, in the top 200 m (Figure 2.10d). These integrals reveal that the western boundary current at 30°N has a larger peak value of PHT in the 0.25° model (0.95 PW) than the 1° model (0.79 PW), and that the heat transported by the eastern boundary currents is larger in the 0.25° model at both 30°N and 60°N. An alternative method of comparing the heat transport between the resolutions is to calculate the PHT per unit length, so that their differences can be directly compared. This difference (not shown) confirms

that the faster, narrower boundary currents at 0.25° resolution transport more heat polewards compared to the equivalent 1° model runs.

2.3.5 Meridional Overturning Circulation

The meridional overturning circulation (MOC) in the control and 2×CO_2 runs is shown for both models in Figure 2.11. The MOC has been computed online in latitude-density coordinates, and then re-projected to latitude-depth coordinates. This method removes the Deacon Cell component of the MOC to give a clearer picture of the residual circulation. The structure of the MOC is similar between the simulations, however the magnitude of overturning in both the North Atlantic Deep Water (NADW) cell and the Antarctic Bottom Water (AABW) cell are greater in the 0.25° model. In the control runs, NADW penetrates deeper in the 1° model than the 0.25° model (about 2.5 km compared with 1.5 km). This deeper penetration occurs at around 60°N, before returning to less than 2 km southward of 50°N. In the 2×CO_2 runs, NADW formation shoals in both the 1° and 0.25° models, as shown in the MOC difference plots of Figure 2.11c,f.

In the 1° model the peak value of NADW formation is 12.0 Sv in the control and remains steady at the same value in the 2×CO_2 run, while in the 0.25° model, NADW weakens from 15.0 Sv to 13.5 Sv in the 2×CO_2 run. The sensitivity of NADW formation to warming is weaker than in most CMIP5 models (Drijfhout et al., 2012), though there is considerable inter-model spread across the CMIP5 ensemble. There are several mechanisms that may cause this weak sensitivity. The AMOC has been identified as a thermally indirect cell, in that its circulation cannot draw kinetic energy from the stratification (Zika et al., 2013b). Compared to the abyss, the AMOC fluxes relatively warm, salty water downwards, while its upwelling branch is cooler and fresher. This kind of circulation requires mechanical energy to drive its circulation, supplied by wind upwelling and mixing processes through the interior. Our models prescribe a relatively strong vertical diffusivity, which

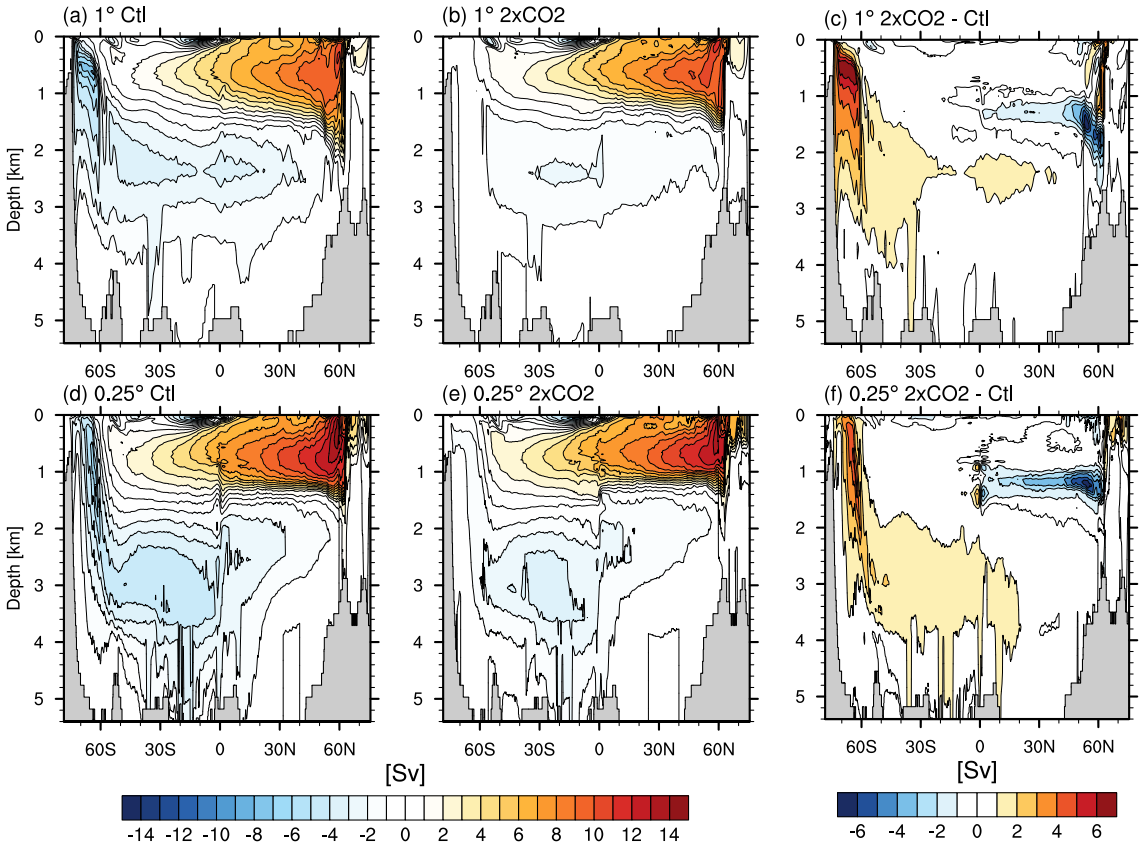

Figure 2.11: Meridional overturning circulation (1 Sv contours) in the 1° model for the (a) control run, (b) 2×CO_2 run and (c) the difference 2×CO_2 - control; and in the 0.25° model for the (d) control run, (e) 2×CO_2 run and (f) the difference 2×CO_2 - control. The circulation is calculated online in latitude-density coordinates and reprojected to latitude-depth space.

maintains the strength of the AMOC, even with a decrease in the buoyancy forcing at the surface. This result is consistent with the warming experiments of Zika et al. (2015), who found the thermally indirect upper cell overturning became shallower but maintained a similar magnitude. Another possible mechanism for differences to the lack of other ocean basins, since the Atlantic Ocean heat budget is influenced by thermal forcing from other basins (e.g. Lee et al., 2011).

Unlike NADW, there is a strong decrease in AABW, from 8.8 Sv to 1.9 Sv in the 1° model and from 6.9 Sv to 2.7 Sv in the 0.25° model. The AABW cell entails downwelling of cold dense water and upwelling of warmer buoyant water through the interior. This kind of cell is known as thermally direct (Zika et al., 2013b), since kinetic energy can be drawn from this circulation. Warming of the surface waters

reduces the buoyancy forcing available to this cell, resulting in a marked decrease in AABW formation, consistent with Zika et al. (2015). There is also an increase in Southern Ocean upwelling of NADW in the $2\times CO_2$ run.

The MOC plots presented in Figure 2.11 have been filtered to reduce noise near the equator. Without this filtering, the MOC contained small cells of 1-2 Sv of alternating orientation within a few degrees of the equator. These alternating cells are sensitive to the number of density bins used in the online overturning diagnostic calculation. We use 160 density bins compared with only 50 vertical levels in the model, in order to better resolve the AABW cell, whereas the apparent noise is reduced when only 80 bins are used. We applied a 3-point mean filter along the density coordinate within $\pm 20^\circ$ latitude, between the density bins corresponding to depths of approximately 200 m to 3000 m. The cells may be partly due to weak computational upwelling modes as in Weaver and Sarachik (1990), since the vertical velocities are relatively high about the equator and there is no enhancement of the horizontal or vertical viscosity in this region. The noise might be reduced by either imposing a higher viscosity about the equator, or by enhancing the vertical resolution. Several recent studies have also found sharp gradients in the MOC near the equator at eddy-permitting or resolving resolution (Farneti et al., 2010; Delworth et al., 2012; Zhang and Vallis, 2013). Since this study is mainly focused on the high latitude response of the climate, the MOC presented here is suitable for this purpose.

2.3.6 Poleward Heat Transport

Poleward heat transport (PHT) for the atmosphere and ocean are shown in Figure 2.12, with the atmosphere and ocean components marked as AHT and OHT respectively. In the control simulations of both models, the total PHT is greater in the NH (peak of 1.7-1.8 PW) than in the SH (peak of 1.4-1.5 PW). The OHT is strongly northward in the NH (0.5-0.6 PW), and slightly southward (< 0.1 PW) in the SH. The AHT partly compensates for this difference in OHT, as the AHT is about 0.2

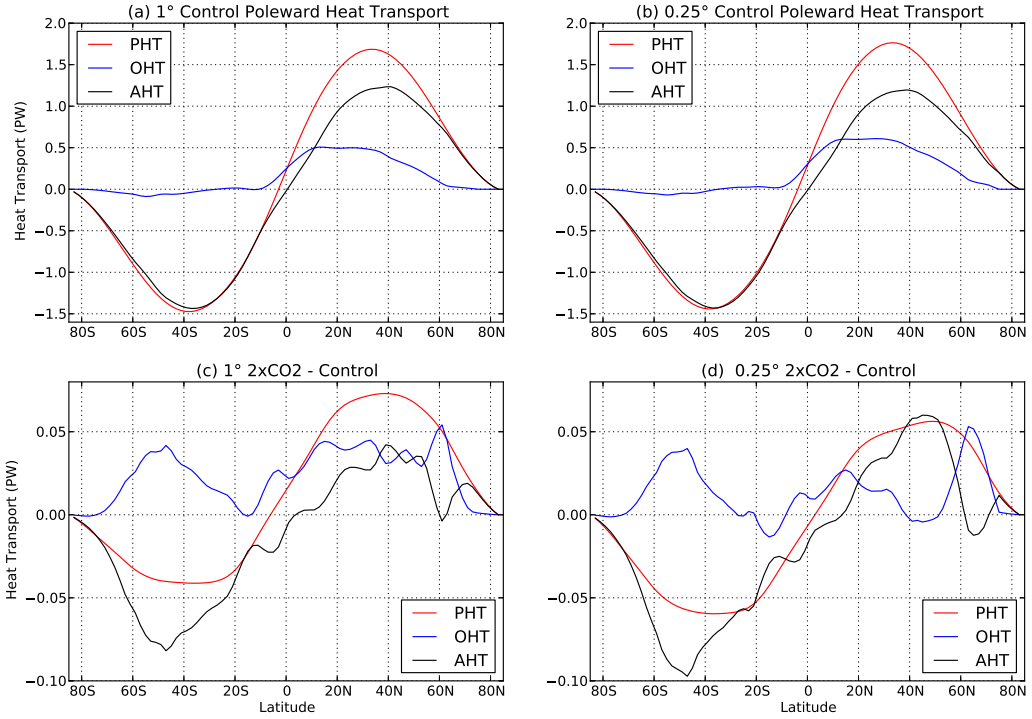

Figure 2.12: Poleward heat transport (PW) in the (a) 1° and (b) 0.25° control runs showing the total (PHT; red), ocean component (OHT; blue) and atmosphere component (AHT; black). The difference between the 2×CO_2 run and the control run is shown for the (c) 1° model and (d) 0.25° model.

PW stronger in the SH than the NH. This compensation is not total, implying that OHT is a major factor in the asymmetry of the control climate.

In the 2×CO_2 runs, the asymmetry in OHT increases at both resolutions, as shown in the Fig 2.12c,d. The change in OHT is positive at all latitudes in the 1° model, and almost all latitudes in the 0.25° model. The AHT change in the 2×CO_2 run is of opposite sign and greater magnitude in the SH. The peak changes in PHT in the 1° model are 0.07 PW in the NH and -0.04 PW in the SH; whereas in the 0.25° model the peak changes are 0.06 PW in the NH and -0.06 PW in the SH. Thus the overall asymmetry in PHT increases in the 1° model but remains steady in the 0.25° model in response to radiative forcing.

Ocean poleward heat transport is decomposed into its mean and eddy components in Figure 2.13. In the 1° model, the eddy component consists of the parameterized eddy heat transport terms. Eddy heat transport is smaller than the mean flow component throughout most of the ocean. It is only in the Southern Ocean

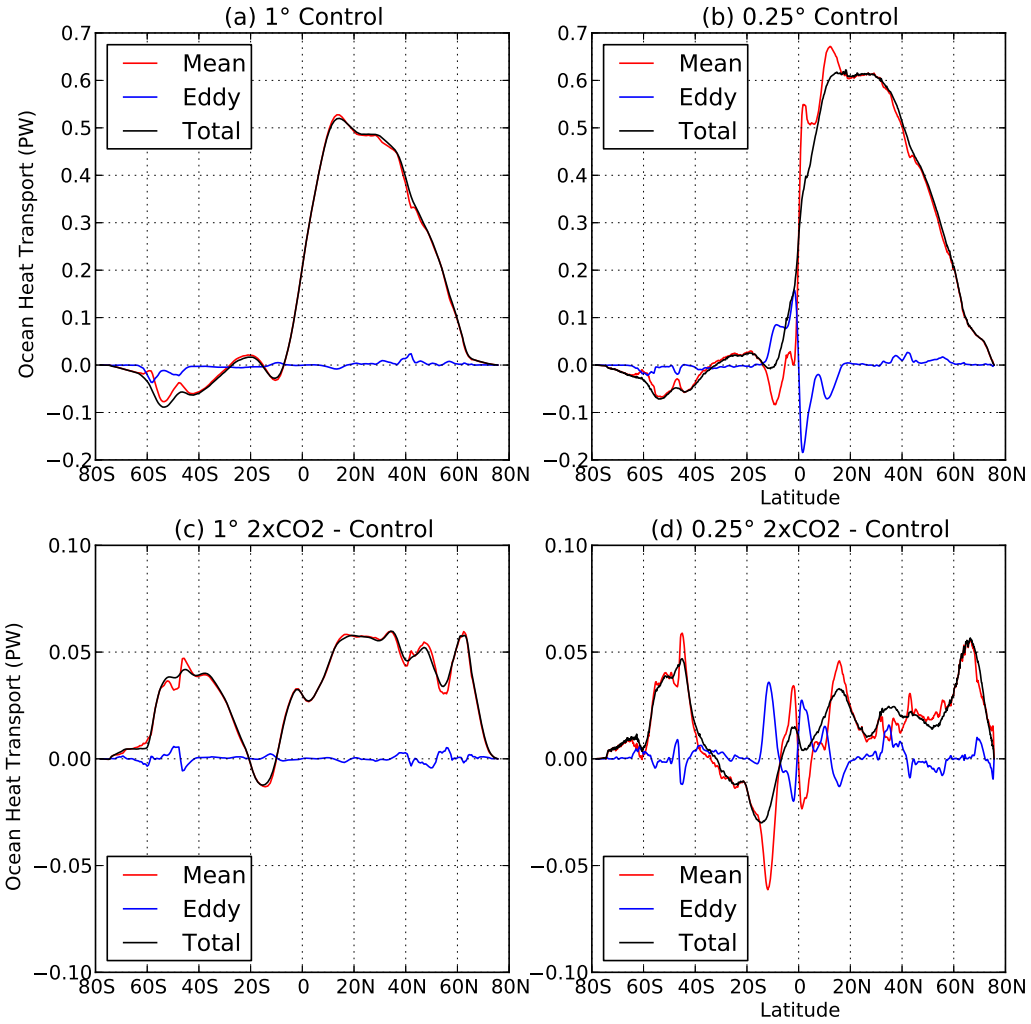

Figure 2.13: The ocean poleward heat transport (OHT; PW) for the (a) 1° control and (b) 0.25° control runs, showing the total (black), the mean flow component (red) and the eddy component (blue). The difference between the $2\times CO_2$ run and the control run is shown for the (c) 1° model and (d) 0.25° model.

from about 50-60°S that the eddy component is comparable in size to the advective component. In the NH midlatitudes there is also a local maximum of poleward eddy heat flux, however it is small compared to the advective component in that region.

The 0.25° model has explicit (albeit partially resolved) eddy heat fluxes and no eddy parameterization, so we derive the eddy heat transport from the velocity and temperature fields directly. We calculate the mean heat transport from the annual average, and the eddy component from the residual anomaly transport calculated from 5-day averages of temperature and velocity. This decomposition treats standing eddies and jets as part of the mean flow, and only the transient eddies contribute

to the eddy heat flux. Eddy heat transport in the 0.25° model is similar to that of the 1° model, except in the tropical band within ±15° latitude. Outside this region, eddy heat transport in the 0.25° is generally smaller in magnitude than the 1° model, and follows a similar latitudinal structure. Although our model does not fully resolve eddies, these results are consistent with Bryan et al. (2014), who found that the main differences in heat transport between their coarse and eddy-resolving models were due to the mean flow rather than transient eddies. The increase in OHT in both simulations consists mainly of the mean flow.

The key difference in OHT between the simulations is in the northern mid- to high-latitudes. The overall pattern of OHT is similar at both resolutions, while its peak value, centered around 10-30°N, is approximately 0.1 PW higher in the 0.25° model than the 1° model. The OHT in the 1° model is close to zero (<0.01 PW) northward of about 65°N, whereas it remains above 0.05 PW up to around 71°N in the 0.25° model, and only falls to near zero values at the edge of the domain. These differences in the high latitude OHT are largely due to stronger boundary currents at the higher resolution, which result in considerable differences in the sea ice climatology.

2.4 Wind Override Response

In this section we present the results of experiments with a transient wind override applied. Although several previous studies have applied a wind perturbation as a step change (Delworth and Zeng, 2008; Marshall et al., 2014), we aim to emulate the effects of a transient change to the wind field. The perturbation patterns are linearly increased from year 1 to year 70 and held fixed thereafter, in line with the transient increase in radiative forcing applied over the same period. The perturbation pattern is shown with the zonal wind stress from the control and $2\times CO_2$ runs in Figure 2.3b,c.

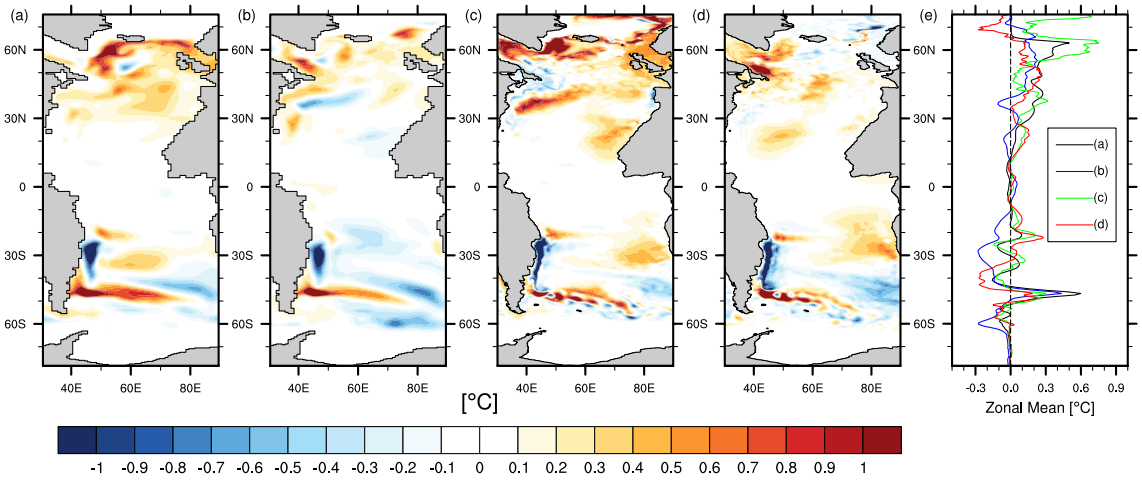

Figure 2.14: Additional SST anomaly (°C) in years 71-90 in the 1° model for the (a) wind override and (b) $2\times CO_2$ wind override, and in the 0.25° model for the (c) wind override and (d) $2\times CO_2$ wind override. In plots (a) and (c), the control run temperature has been subtracted, while in plots (b) and (d) the $2\times CO_2$ temperature has been subtracted. (e) Zonal mean of plots (a-d).

2.4.1 Surface and Deep Warming

We show the SST anomaly induced by the wind override both with and without the $2\times CO_2$ radiative forcing in Figure 2.14. In the wind override run, there is a clear warming trend through most of the North Atlantic, especially around 50-60°N. This remote warming is likely due to the wind-induced increase in the MOC, which draws warm salty water into the North Atlantic. The wind-induced changes to the MOC are discussed further in Section 2.4.3. In the SH midlatitudes, there are both positive and negative signals. There is a cooling trend along the western boundary current of the SH subtropical gyre, and a warming trend on the southern edge of this boundary current. These trends are likely due to the intensification and southward shift of the gyre in response to the wind override. The warming signal at the southern edge of the boundary current extends east into the interior of the basin, due to the ACC transporting the warmer water eastwards. There is also a cooling signal in the south-eastern corner of the domain, which we attribute to greater upwelling and Ekman transport in the Southern Ocean, bringing deep water to the surface and exporting cool water northwards.

In the $2\times CO_2$ wind override runs, the pattern is similar to that of the wind override runs, with warming of the North Atlantic and similar alternate signal trends in the SH. The main differences in the $2\times CO_2$ wind override runs are that the NH warming perturbation (compared to the $2\times CO_2$ run) is weaker and the SH cooling trend is stronger. There appears to be a larger region of the Southern Ocean that is cooled by enhanced Ekman transport, and the warming trend in the NH high latitudes is reduced. However, the wind override increases the temperature asymmetry both with and without radiative forcing.

The zonal mean temperature anomaly at depth induced by the wind override is shown in Figure 2.15, with the anomalies in plots (a-d) derived in the same manner as in Figure 2.14. In the 1° cases, there is a strong cooling signature in the top 1 km from 50-60°S, of order 1°C in the wind override and 0.5°C in the $2\times CO_2$ wind override run. This cooling is likely due to the enhanced upwelling and northward export of cooler water. Poleward of 50°S there is a weaker cooling trend extending to full depth. The North Atlantic shows a warming trend mainly in the top 1 km, which is stronger in the wind override run but also present in the $2\times CO_2$ wind override run. Most of the ocean below 1 km north of 40°S warms slightly (0-0.1°C), which is likely due to an increase in Southern Ocean upwelling (Section 2.4.3).

The 0.25° model shows similar patterns of high latitude deep warming to the 1° model. The North Atlantic warms in the top 1 km, and the Southern Ocean cools throughout the ocean depth poleward of 60°S. The cooling signal in the top 1 km of the Southern Ocean is weaker than in the 1° model. This weakening may be due to partial eddy compensation in the 0.25° model, while the effect is weaker in the 1° model. In the $2\times CO_2$ run, there is a reduced deep warming in the top 1 km north of 65°N, which is also reflected in the SST response (Figure 2.14).

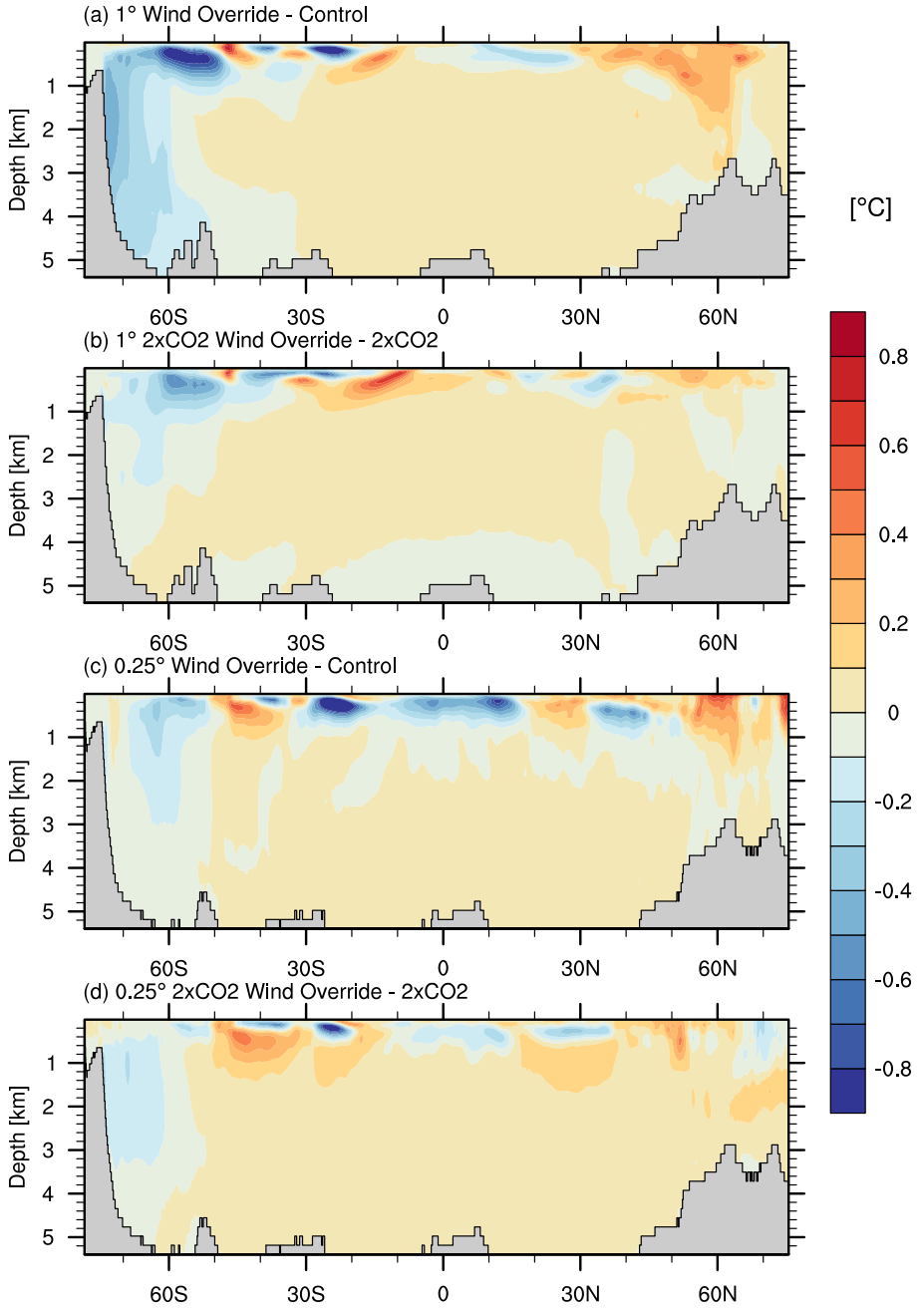

Figure 2.15: Zonal mean temperature anomaly (°C) in the 1° model for the (a) wind override and (b) $2\times CO_2$ wind override and in the 0.25° model for the (c) wind override and (d) $2\times CO_2$ wind override. In plots (a) and (c) the control run temperature has been subtracted while in plots (b) and (d) the $2\times CO_2$ run temperature has been subtracted.

2.4.2 Sea Ice Response

The sea ice response to the wind override is shown in Figure 2.16. In both the 1° and 0.25° wind override runs, there is a reduction of up to 0.3 m ice thickness

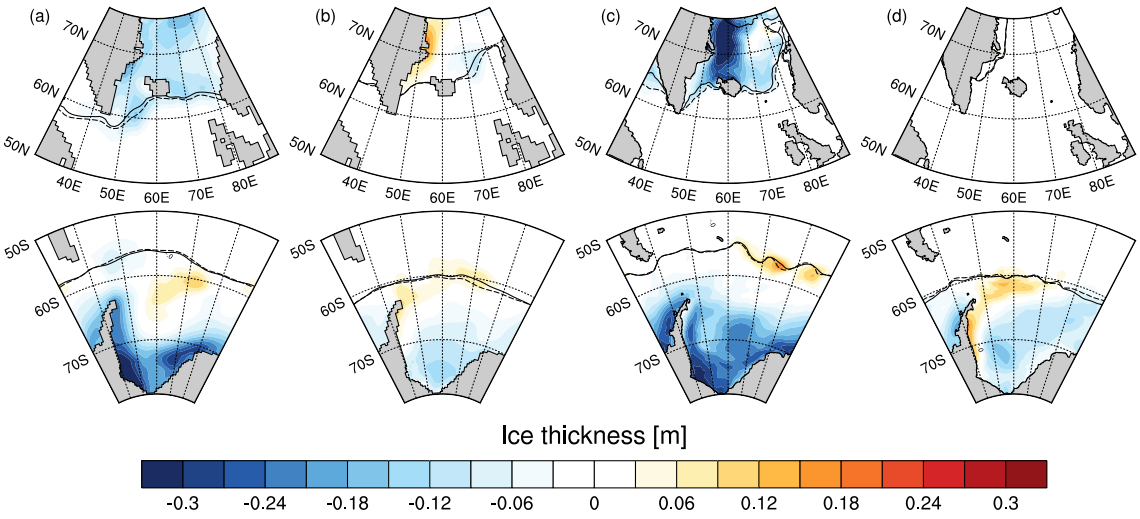

Figure 2.16: Change in sea ice thickness in the 1° model for the (a) wind override and (b) $2\times CO_2$ wind override, and in the 0.25° model for the (c) wind override and (d) $2\times CO_2$ wind override. In plots (a) and (c) the control run ice thickness has been subtracted while in plots (b) and (d) the $2\times CO_2$ run ice thickness has been subtracted. The sea ice edge, as defined by the contour of 0.15 ice concentration, is indicated by the solid contour for the wind override runs, and by the dashed contour for the (a,c) control and (b,d) $2\times CO_2$ cases.

near the coast of Antarctica, and an increase of up to 0.1 m around 60°S. However, the SH sea ice extent (indicated by the black contours in Figure 2.16) is largely unchanged by these changes in thickness, since the changes occur mainly away from the ice edge. These changes in ice thickness are likely due to enhanced northward Ekman transport of the sea ice in the Southern Ocean, drawing thicker ice away from Antarctica and increasing the ice thickness further north.

In the NH, there is a reduction in sea ice thickness in the wind override runs, which is of greater magnitude in the 0.25° model (0.3-0.5 m) than the 1° model (0.1 m). The NH sea ice extent reduces slightly in these scenarios, leading to an ice-albedo feedback. In the $2\times CO_2$ wind override runs, ice thickness reduces near the Antarctic coast, to a lesser extent than in the wind override runs. In the NH, there is almost no change in sea ice thickness in the $2\times CO_2$ wind override runs compared with the $2\times CO_2$ runs.

2.4.3 Meridional Overturning Circulation

The MOC in the wind override runs is shown in Figure 2.17, reprojected from latitude-density space into latitude-depth space as in Figure 2.11. The 1° wind override run has an enhanced AABW cell compared with the control run with an increase of about 5.5 Sv in peak magnitude south of 55°S. In the $2\times CO_2$ wind override run, AABW formation is reduced, but remains 0.7 Sv stronger than in the $2\times CO_2$ run. In the 0.25° wind override run, AABW formation is enhanced by 1.5 Sv compared with the control run, while in the $2\times CO_2$ wind override run AABW weakens, but is approximately 0.4 Sv stronger than in the $2\times CO_2$ run. AABW formation is therefore less sensitive to the wind override in our eddy permitting model than in the parameterized eddy regime.

The increase in AABW in the 1° model is likely a result of Ekman transport increasing the isopycnal slope, combined with enhanced upwelling of the lower cell of the MOC, consistent with Delworth and Zeng (2008). The reduced sensitivity of AABW formation in the 0.25° model may be due to eddy compensation, whereby the northward Ekman transport induced by the wind override is partially compensated by a southward eddy-induced transport. In the 1° model we do not employ a spatially variable eddy parameterization, which can enhance eddy compensation in coarse resolution models (Farneti and Gent, 2011). Despite this difference, the surface temperature anomaly patterns in response to the wind override are similar between the resolutions.

NADW is enhanced in the wind override runs, but retains a similar magnitude and structure. In the 1° wind override run, NADW peak magnitude north of 45°N is 1.2 Sv stronger than in the control run, whereas in the $2\times CO_2$ wind override run it is 0.1 Sv weaker than in the $2\times CO_2$ run. In the 0.25° wind override run, NADW peak magnitude is 0.6 Sv stronger than in the control run, while in the $2\times CO_2$ wind override run it is 0.5 Sv stronger than in the $2\times CO_2$ run. When the

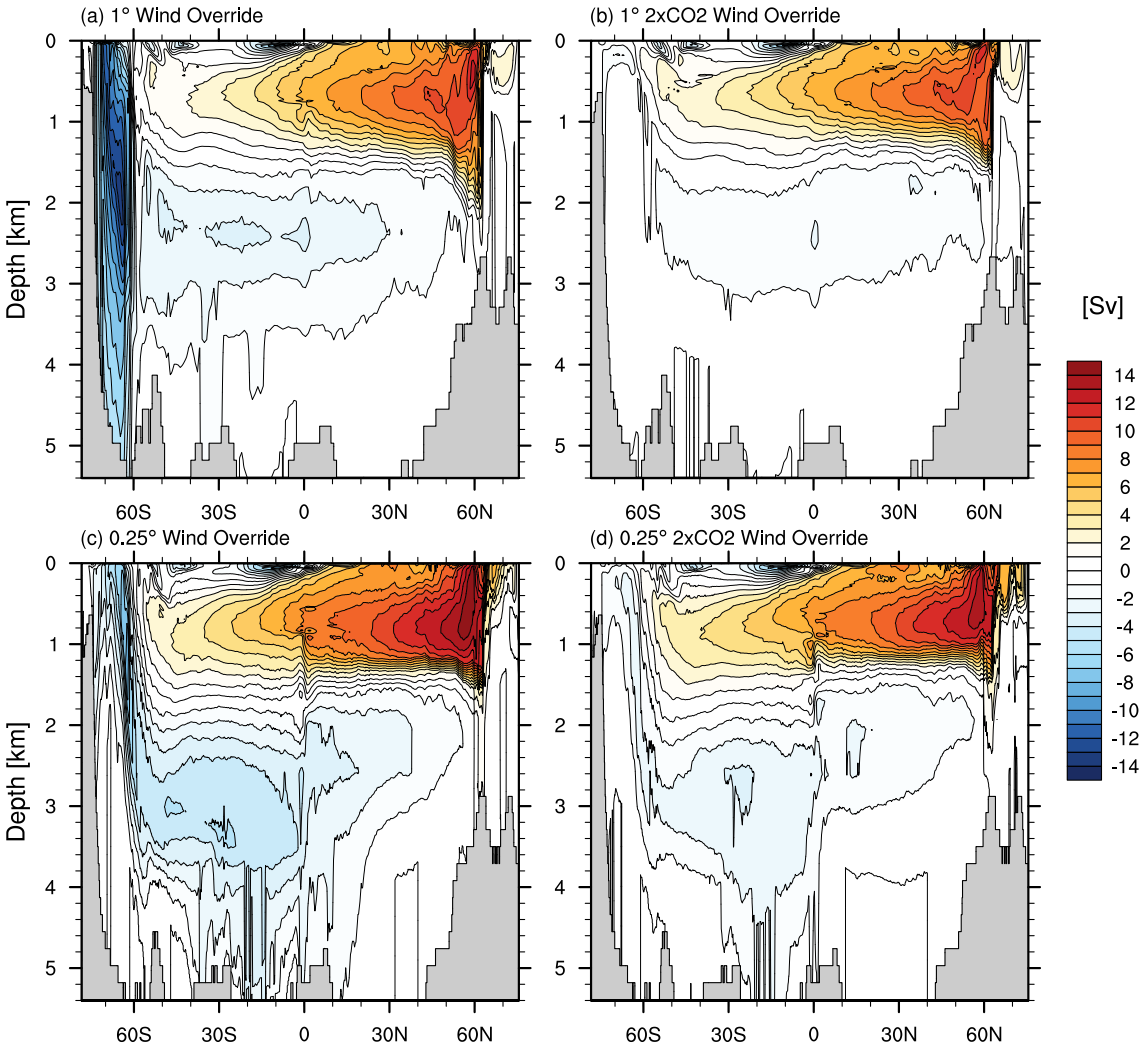

Figure 2.17: Meridional overturning circulation (1 Sv contours) in latitude-density coordinates, re-projected into latitude-depth coordinates, showing the 1° model in the (a) wind override and (b) $2\times CO_2$ wind override runs, and the 0.25° model in the (c) wind override and (d) $2\times CO_2$ wind override runs.

MOC is measured in latitude-depth space (not shown), NADW formation is about 1 Sv stronger in the wind override runs than in the control and $2\times CO_2$ runs, and the Southern Ocean Deacon Cell is enhanced by about 2 Sv. The strengthening of NADW formation and enhanced Southern Ocean upwelling causes some of the enhanced warming asymmetry in the wind override runs.

2.4.4 Poleward Heat Transport

The additional poleward heat transport in the wind override and $2\times CO_2$ wind override runs is shown in Figure 2.18. In the 1° wind override run, OHT becomes more southward through the SH midlatitudes, with a peak difference of about -0.05 PW around 50°S. There is also a smaller southward shift of OHT in the NH. The AHT more than compensates the southward change in the SH, with a peak change of about 0.1 PW around 50°S, creating an overall northward shift of poleward heat transport in the SH. In the NH, the AHT change is of the same sign and similar magnitude as the OHT change, creating an overall southward shift of PHT. The $2\times CO_2$ wind override shows a smaller change compared with the $2\times CO_2$, with an overall northward shift of OHT and a partially compensated southward shift of AHT. The overall change in PHT is northward change through most of the domain of less than 0.01 PW.

In the 0.25° model, the wind override run shows a very different pattern to the 1° model. The largest change in OHT is a northward shift in the NH midlatitudes, with a peak magnitude of around 0.05 PW around 50°N. There is little compensation of AHT in the NH, leading to an overall more northward PHT in the NH, whereas in the SH, the OHT and AHT changes are both smaller in magnitude, leading to a near zero change in PHT. There is a very small southward shift of OHT between 40-70°S with peak magnitude around -0.01 PW, unlike the large change in the 1° model. The 0.25° $2\times CO_2$ wind override PHT change is similar to the 1° model, with a northward shift in OHT partially compensated by AHT, leading to a very small (< 0.01 PW) northward shift of PHT.

2.4.5 Summary of Asymmetry

We derive indices of the interhemispheric temperature asymmetry, by taking the hemisphere mean temperature difference, and the ±45°-to-pole and ±60°-to-pole

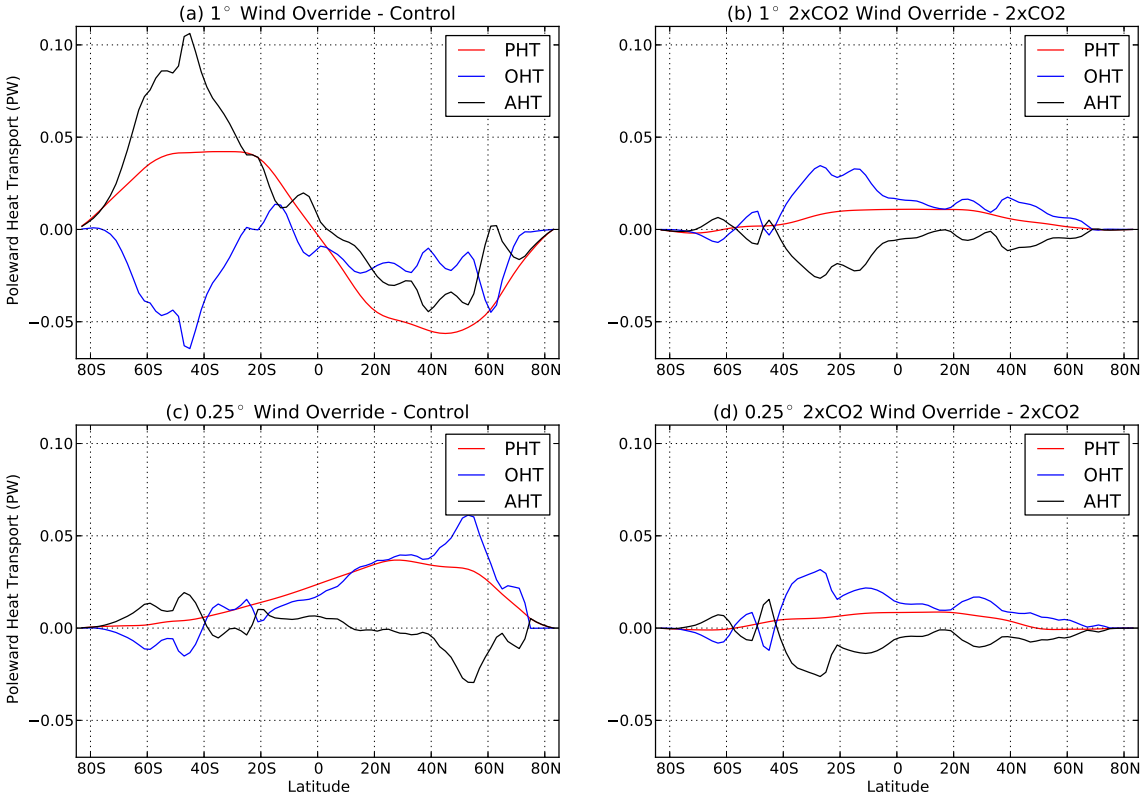

Figure 2.18: The additional poleward heat transport in the 1° model for the (a) wind override and (b) $2\times CO_2$ wind override run; and in the 0.25° model for the (c) wind override and (d) $2\times CO_2$ wind override run. In plots (a) and (c) the control run data have been subtracted while in plots (b) and (d) the $2\times CO_2$ run data have been subtracted. Total poleward heat transport (PHT) is shown in red, the ocean component in blue (OHT) and the atmosphere component is shown in black (AHT).

mean differences, for SST and SAT. Time series of the ±45°-to-pole and ±60°-to-pole indices are plotted in Figure 2.19, showing a strong warming asymmetry in the high-latitude SST response at both resolutions. There is also a strong asymmetry in SAT warming at high latitudes in the 1° case, but less so in the 0.25° case. The smaller signal of high latitude SAT asymmetry is likely due to the near-symmetric land-masses, and the compensation of atmospheric poleward heat transport against the increased ocean poleward heat transport. Each of these indices have had the corresponding control run index subtracted, and the result filtered using a 9-year running average to focus on the low frequency signal. The hemisphere-wide asymmetry (not shown) is weaker, since the tropical warming response is largely symmetric, and covers a larger surface area than the ±45° to pole region.

To summarize these indices, the time-averaged temperature asymmetry indices

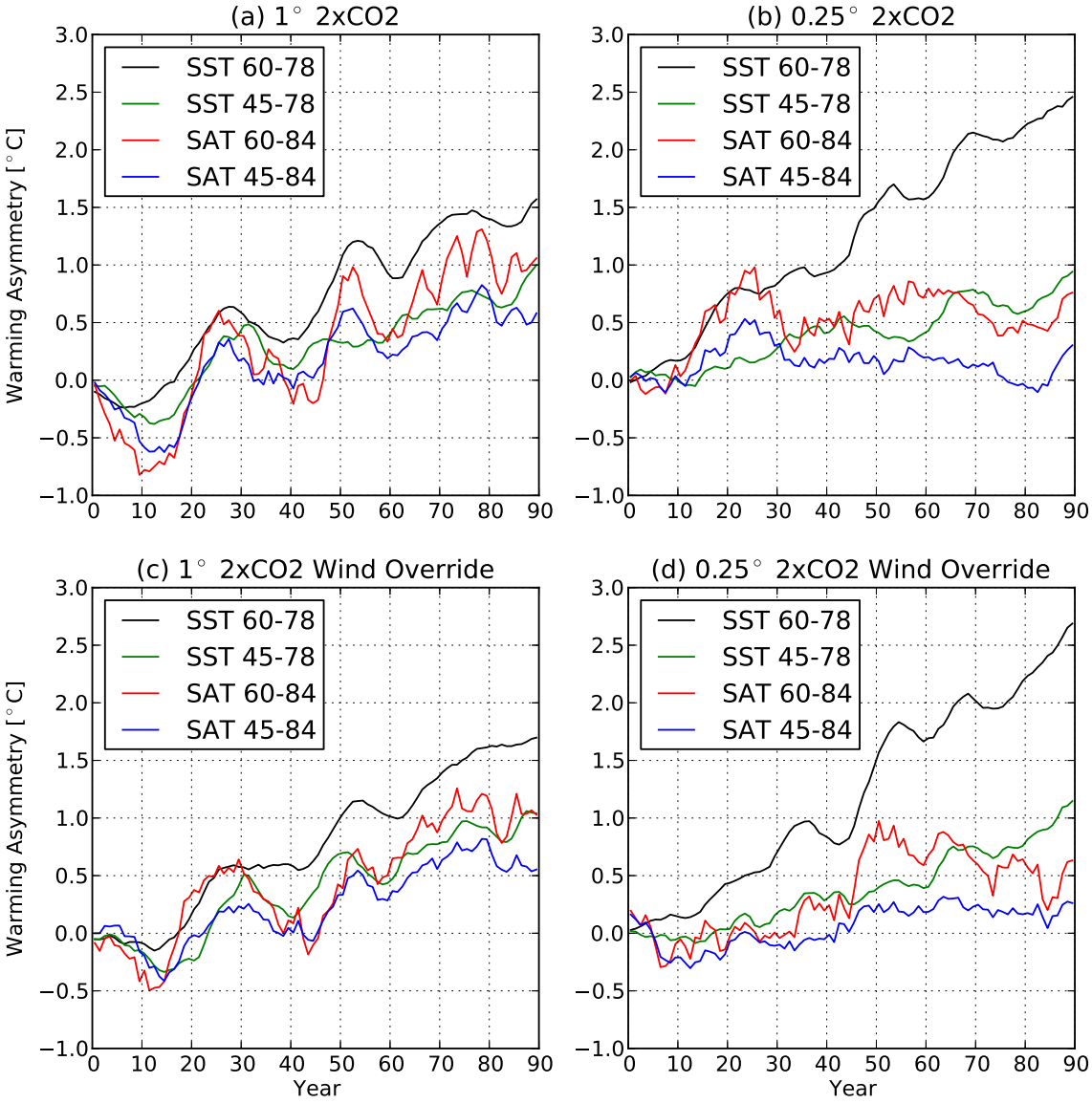

Figure 2.19: Warming asymmetry (°C) showing the 45°-pole and 60°-pole mean difference for SST and SAT in the (a) 1° 2×CO_2 run, (b) 0.25° 2×CO_2 run, (c) 1° 2×CO_2 wind override run and (d) 0.25° 2×CO_2 wind override run. In each case the control run has been subtracted, and the time series then filtered using a 9-year running mean.

from the control and perturbation runs are shown in Figure 2.20. The radiative forcing and wind override both increase the asymmetry in the high latitude warming, while radiative forcing has a significantly larger effect than the wind override. These indices also highlight the major interhemispheric temperature asymmetries in the control runs, which are larger in the 0.25° model than in the 1° model.

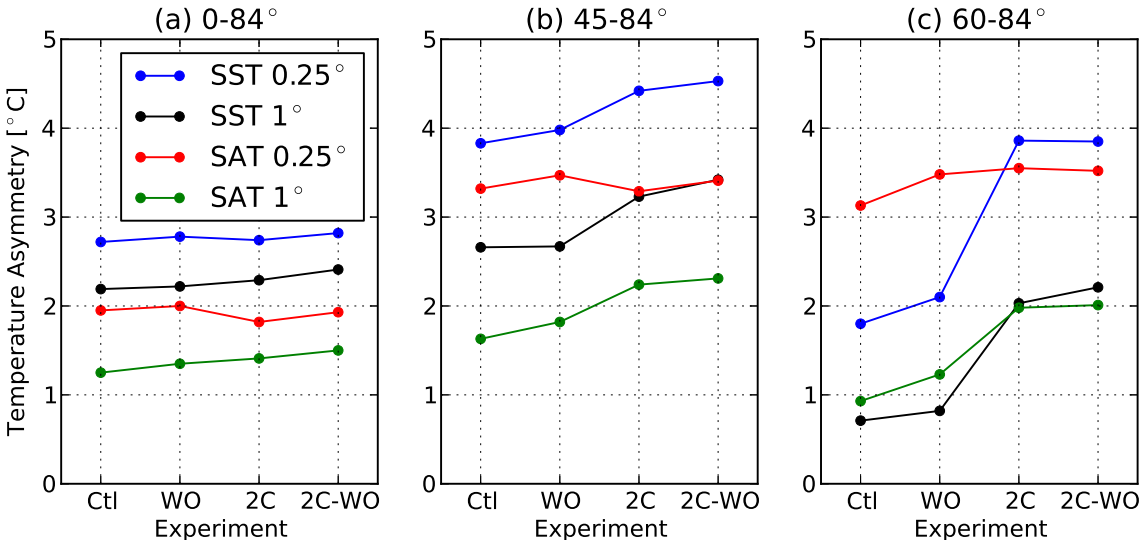

Figure 2.20: Temperature asymmetry (°C) indices from (a) 0-84°, (b) 45-84° and (c) 60-84° latitude, showing SST and SAT at each resolution. The shorthand for the experiments are Ctl: control, WO: wind override, 2C: $2\times CO_2$ and 2C-WO: $2\times CO_2$ wind override. The control run was averaged over the full 90 years, while the perturbation runs were averaged for the last 20 years only.

2.5 Discussion

In all of the experiments presented here, we find a strong interhemispheric asymmetry in high latitude warming. In this model the land-ocean ratio is approximately the same at all latitudes, and the atmospheric forcing is largely symmetric, due to the simplified grey radiation scheme. Thus the primary source of asymmetry is the existence of an ACC in the Southern Ocean, versus the gyre circulation in the NH. We infer that the asymmetry of warming in this model is governed by ocean circulation. This result agrees with the findings of Marshall et al. (2014), who found that most of the interhemispheric asymmetry of SST warming predicted in CMIP5 models can be explained by the ocean circulation redistributing a uniform heat flux perturbation.

One of the aims of this study was to establish whether the inclusion of explicit eddy heat fluxes, especially in the Southern Ocean, would substantially change the pattern of warming found in the coarse resolution model. We found that poleward eddy heat fluxes were generally small compared to the mean flow, and that the

Southern Ocean warming pattern was not sensitive to the resolution change. While our model does not fully resolve eddies, the insensitivity of heat fluxes in the Southern Ocean to the resolution change is consistent with the eddy-resolving model of Bryan et al. (2014). However, we did find a substantial sensitivity to resolution in the heat fluxes of boundary currents. The 0.25° simulations had stronger warming and sea ice melt in the North Atlantic, which was likely caused by higher velocities and better resolved boundary currents.

The stronger boundary currents in the 0.25° model created a large difference in the NH sea ice response. We found that in the eddy-permitting regime, NH sea ice was thinner and covered a smaller area in the control simulations, and melted almost completely by the end of the $2\times CO_2$ run. By contrast in the 1° model, NH sea ice covered a larger area in the control runs, and a substantial amount of ice remained at the end of the $2\times CO_2$ run. The SH sea ice was greater in extent and thickness, and exhibited less melting in response to radiative forcing. This result was robust across the different resolutions, suggesting that the SH climate response was well captured at the coarser resolution. The resolution sensitivity of sea ice between our 1° and 0.25° models is similar to that found in an eddy-resolving coupled climate model (Kirtman et al., 2012; Bryan et al., 2014), where the decline in Arctic sea ice was greater in the 0.1° model compared with a 1° resolution ocean model, but there was little dependence on resolution of the SH sea ice response.

Sea ice differences between the resolutions could perhaps be reduced by tuning the sea ice albedo. For example Delworth et al. (2012) raised the ice albedo and lowered the vertical diffusion when moving from coarse to eddy-permitting ocean resolution to obtain a more realistic sea ice climatology. While this kind of tuning might have made the NH sea ice extent more comparable between our 1° and 0.25° models, such a change would likely increase the SH sea ice extent, thereby creating a new disparity between the resolutions. Our study is focused on processes that differ between the resolutions, rather than obtaining the most realistic climatology,

so tuning of the ice albedo and vertical diffusion are beyond the scope of this study.

Our model allows us to compare warming scenarios both with and without a poleward shift of the westerly winds, due to the nearly steady position of the westerly winds under radiative forcing perturbations. Adding a wind shift and intensification to the model leads to cooling of the surface Southern Ocean, and warming of the North Atlantic (consistent with Toggweiler and Samuels, 1998; Delworth and Zeng, 2008; Sijp et al., 2009), leading to an overall greater magnitude of interhemispheric warming asymmetry. The wind override causes a larger change in temperature asymmetry when no radiative forcing is applied. In particular, AABW formation is substantially increased when the wind override is applied to the control state, but in the $2\times CO_2$ state AABW weakens both with and without the wind override.

This wind stress profile in the ICCM contrasts with that of Enderton and Marshall (2009), who used an aquaplanet model with narrow land barriers to simulate the effect of a Drake Passage throughflow in an otherwise symmetric world. In their case, having an open Drake Passage versus a closed basin created a stronger and more poleward SH westerly wind stress and a significant reduction in surface air temperature (SAT). However, in their aquaplanet model the SAT closely mirrors the SST at all locations, and therefore the thermal wind balance of the atmosphere is strongly constrained by lower SST in the SH high latitudes. Our model's SAT is also influenced by the land surface, which has limited interhemispheric asymmetry and allows the atmosphere temperature to be more symmetric than in the Enderton and Marshall (2009) model.

There remain uncertainties over how the westerly wind position will evolve, despite the consistent poleward shift found in CMIP5 projections (Barnes and Polvani, 2013). Idealized atmosphere experiments (Butler et al., 2010) show that tropical warming and polar stratospheric cooling tend to shift the jets poleward, while polar surface warming shifts the jets equatorwards. Furthermore, models with an equatorward bias of the westerly winds in their control state have a greater poleward

shift under warming scenarios (Kidston and Gerber, 2010). Our results imply that the future evolution of the SH westerly wind position will have a significant impact on the interhemispheric asymmetry of warming.

When applying our results to the global climate system, several caveats must be considered. First, there is no seasonal cycle in our model, which has an important influence on sea ice dynamics. Although our goal was to examine the long-term annual mean climate response, we do not know whether a seasonally varying model with otherwise similar forcing would yield the same results in its annual mean. However, the similarities in sea ice evolution between our model and the Kirtman et al. (2012) model support our annual-mean forcing as a useful coupled model scenario. Our results show that predictions of the ocean-sea ice response to rising CO_2 may change substantially as models move to finer resolution. Given the apparent underestimation of NH sea ice melting in CMIP5 models compared with observations (Collins et al., 2013), improving the resolution of the ocean and sea ice components of climate models may help to improve their NH sea ice predictions.

The simplified grey radiation scheme used in our atmosphere model provides some limitation, since the water vapour in the model is hard-wired through the optical depth profile. However, this scheme significantly reduces the computational expense of the atmosphere component of the model. This model does not include ozone or aerosols, however the wind override scenarios provide an analogue of the poleward shift of the SH westerly winds due to ozone depletion (Thompson et al., 2011). Lastly, the domain of the model has only one ocean basin and an ACC-like channel, which pushes our warming results to be more Atlantic-like. The global ocean also comprises the Pacific and Indian Ocean basins with no northern deep sinking regions, which reduces the asymmetry of meridional heat transport from the overturning circulation compared with a one basin model. In the global model of Part 1, the SST anomaly showed a much stronger warming response in the Atlantic sector than in the Pacific sector of the Southern Ocean (Figure 1.2a). The sector

models used here in contrast cannot capture this zonal asymmetry. Testing the asymmetric warming results found here in an eddy-permitting global climate model therefore remains an important future research priority. Nonetheless we propose that the processes leading to asymmetry of warming in our model are relevant to the global climate system, even if the signal is stronger than expected in a global setting.

2.6 Conclusion

We have shown that the ocean circulation causes a substantial proportion of the interhemispheric temperature asymmetry, both in the control runs and in $2\times CO_2$ warming experiments. In this model the land-ocean ratio and atmosphere forcing are similar between the hemispheres, therefore the asymmetry cannot be due to faster warming over land. Yet the ocean geometry is fundamentally asymmetric, with a zonally unbounded channel in the SH mid-latitudes and sidewalls everywhere in the NH. The high latitude warming asymmetry is enhanced when moving from 1° to 0.25° ocean resolution, due to reduced sea ice cover and faster melting in the Arctic region. This major difference in sea ice response appears to be caused by enhanced boundary currents at the eddy-permitting resolution; most of the poleward heat transport in the ocean model is carried by the mean flow rather than transient eddies. By contrast the Southern Ocean poleward heat transport and Antarctic sea ice cover appear to be insensitive to the resolution change. As in the NH, the mean flow dominates the poleward heat transport rather than transient eddies, in both the eddy-permitting model and the parameterized eddy model. When a poleward wind shift and intensification is added to this warming scenario, the warming asymmetry is enhanced and Southern Ocean warming suppressed. The wind override enhances the upper limb of the MOC, leading to greater subduction of heat in the NH and more upwelling of cool deep water in the SH. The asymmetry caused by doubling CO_2 is greater in magnitude than that caused by the wind override, but both perturbations

increase the asymmetry when imposed both separately and together.

Part 3

Impacts of Realistic Bathymetry and Eddy-Permitting Ocean Resolution in a Sector Climate Model

Abstract

High resolution ocean models often use regional domains to reduce the computational burden of resolving mesoscale eddies. A commonly used domain is a near pole-to-pole sector containing a re-entrant channel in the south, with flat bottom bathymetry and rectangular boundaries. The ocean circulation and climate impacts of including more realistic bathymetry remain untested in these sector models. Here we examine the influence of bathymetry and continental outlines in a coupled climate model with a sector domain. The model is configured in two geometries: one with Atlantic-like bathymetry and coastlines, and a second employing an idealized flat-bottom rectangular set-up. These two configurations are implemented at both coarse (1°) and eddy-permitting (0.25°) resolution. While the two configurations are similar in their mean surface climates, the flat bottom models exhibit a broader subpolar gyre in the Northern Hemisphere (NH), which is in contrast more constrained by bathymetry in the Atlantic models. In a warming scenario with $2\times CO_2$ concentration, the Atlantic models have a strong warming signal in the northern high latitudes, while the flat bottom models have both warming and cooling regions. In addition, when the models are simulated at eddy-permitting resolution, the warming signal is increased in the NH, due to better resolved boundary currents carrying more heat northwards. The Antarctic Circumpolar Current (ACC) transport significantly decreases in $2\times CO_2$ scenarios in all configurations. Due to a barotropic free mode mechanism, the Atlantic-like models show greater ACC transport sensitivity to Southern Ocean wind stress forcing than the flat bottom models.

3.1 Introduction

The Coupled Model Intercomparison Project Phase 5 (CMIP5) models have mostly O(1°) ocean resolution, with parameterized eddies. Recent progress has been made

towards simulating climate models at eddy-permitting (Delworth et al., 2012) or eddy-resolving ocean resolution (Kirtman et al., 2012; Bryan et al., 2014; Griffies et al., 2015). These high resolution models have been restricted to short (100-200 year) equilibration runs, however at 0.1° ocean resolution, the deep ocean has been found to drift less from observed climatology than lower resolution models (Griffies et al., 2015). It is important to better understand the climatic simulations of these different models, as the ocean circulation and its uptake of heat under global warming are expected to behave differently when eddies are permitted or resolved (e.g. Morrison et al., 2013; Zhang and Vallis, 2013).

The response of the North Atlantic gyres and meridional overturning circulation (MOC) to buoyancy forcing is also sensitive to model resolution (Spence et al., 2008). Higher resolution ocean models contain faster and more tightly confined surface boundary currents (Treguier et al., 2012; Marzocchi et al., 2015), giving a more realistic representation of heat transported by ocean gyres. Deep boundary currents also show a richer structure at higher resolution (Spence et al., 2012), and their pathways are better defined by better resolved bathymetry. Lévy et al. (2010) examined an idealized double gyre system in a high resolution (2 km) flat bottom domain, and found that the total northward heat transport decreased with higher resolution. As their resolution increased, the northward mean flow heat transport increased, with an opposing increase in southward eddy heat transport. Yet this study was undertaken in a flat-bottom model; further research is needed to examine resolution impacts in more realistic bathymetry settings.

Model resolution has a large impact on the ACC, and its response to wind and buoyancy perturbations (Morrison and Hogg, 2013). Eddy permitting and eddy resolving models have shown a weaker sensitivity to wind stress perturbations than coarse resolution models (e.g. Meredith and Hogg, 2006; Hallberg and Gnanadesikan, 2006; Farneti et al., 2010; Munday et al., 2013), suggesting that these models are either eddy saturated (Straub, 1993), or close to this limit. While ACC transport

was found to be uncorrelated with wind stress changes in CMIP3 (Sen Gupta et al., 2009) and CMIP5 models (Downes and Hogg, 2013), almost all of these simulations employ coarse grid ocean models with parameterized eddies. By contrast to the wind response, increases in heat and freshwater fluxes over the Southern Ocean correlated significantly with decreases in ACC transport in CMIP5 models (Downes and Hogg, 2013), suggesting that buoyancy gain will dominate over wind stress in future changes to the ACC transport. Recent observations indicate a steady (Böning et al., 2008; Meredith et al., 2011) or slightly weakening ACC transport (Hogg et al., 2015) in recent decades. Interactions with topography have been found to have an important influence on the sensitivity of ACC transport to wind forcing (Hughes et al., 1999; Zika et al., 2013a; Langlais et al., 2015); here we examine this sensitivity and its climatic context when moving from flat bottom to realistic bathymetry in a sector domain.

Many ocean model studies have employed pole-to-pole sector domains to develop theories of the overturning circulation and its response to surface wind and buoyancy forcing (e.g. Wolfe and Cessi, 2009, 2011; Jones et al., 2011; Shakespeare and Hogg, 2012; Morrison and Hogg, 2013; Munday et al., 2013; Fučkar et al., 2013). These regional sector domains reduce the computational load of permitting or resolving eddies, while retaining the essential structure of the global overturning. Sector models enable a wide range of external forcing and parameter sensitivity experiments, and are set to remain valuable tools for ocean and climate modelers for the foreseeable future. In most cases, these models use rectangular coastlines, with a zonally unbounded channel in the Southern Ocean, and with little or no bathymetry except for a Drake Passage sill in some cases. Some models include simplified continental shelf regions or sloping sidewalls, but realistic bathymetry and coastlines are not included. The impact of these simplifications remains largely untested; this forms the main goal of the present study.

Details of the ocean domain can have a significant impact on the Southern Ocean

response to wind perturbations. For example, Hogg and Munday (2014) showed that extending a sector model from $\pm 60^\circ$ to $\pm 70^\circ$ latitude and introducing a high latitude shelf region increased the sensitivity of the Antarctic Circumpolar Current (ACC) transport and the meridional overturning circulation (MOC) to wind forcing. The domain extension and the inclusion of shelves largely explained why the ACC was sensitive to wind forcing in the Shakespeare and Hogg (2012) model, but was insensitive in the Munday et al. (2013) configuration (notwithstanding other differences in model parameters). This sensitivity to domain choice raises questions about the robustness of results from sector model studies investigating ACC, MOC and ocean general circulation sensitivities, and whether similar results are expected in climate models containing realistic topography. This study examines an intermediate case; we employ a sector geometry climate model to investigate sensitivities in the ocean circulation and climate response that are due to bathymetry, realistic continental outlines and eddy-permitting resolution.

3.2 Model and Experiments

This study uses the Intermediate Complexity Climate Model (ICCM) of Farneti and Vallis (2009), with modifications as described in Part 2. Here we briefly outline the model components, and describe new aspects presented in this study. We assessed the various sector models analyzed in this study within coupled ocean-atmosphere-ice configurations as we wish to document the merits and shortcomings of each configuration with regard to coupled climate processes; i.e. with fully interacting sea ice and atmospheric components. Running in an ocean-only configuration would enable controlled forcing of the ocean across all models, but without any amplifying feedbacks that are possible in a coupled configuration.

3.2.1 Model Description

The ocean component is the Modular Ocean Model (MOM) Version 5.0.2 (Griffies, 2012) spanning a 60° sector domain from near pole-to-pole. The atmosphere is a B-grid dynamical model, spanning a 120° sector and latitudes from 84°S to 84°N, with a horizontal resolution of 2° latitude × 2° longitude and 7 vertical levels. The atmosphere employs a simplified grey radiation model, with no seasonal or diurnal cycle, and no explicit greenhouse gas or cloud schemes. The sea ice model is the Sea Ice Simulator in the standard MOM distribution, while the land surface employs a simple bucket model. Coupling of the model components is implemented through the Geophysical Fluid Dynamics Laboratory Flexible Modeling System.

The ocean model uses two different resolutions, 1° and 0.25° longitudinal spacing, using a Mercator grid refinement in the latitudinal spacing. The ocean has a periodic zonal boundary condition, with sidewalls everywhere in the domain except in the Southern Ocean. Two different versions of bathymetry and coastlines are implemented: an 'Atlantic' model and a 'Rectangular' model. The Atlantic model uses bathymetry derived from the Atlantic basin spanning the latitudes of 78°S to 75°N as used in Part 2. For a full description of how the bathymetry was generated and an illustration of the sidewalls along the periodic boundary, see Figure 4 of Snow et al. (2015). The Atlantic model uses 50 vertical levels with a maximum depth of 5500 m, varying from 10 m thickness at the surface to 210 m thickness at the bottom of the ocean.

The Rectangular model uses straight coastlines and flat-bottom bathymetry spanning the latitudes 72.7°S to 72.7°N. The Rectangular model has 40 vertical levels and a depth of 4000 m (approximating the mean depth of the Atlantic model), varying from 10 m at the surface to 190 m at the bottom. All ocean grid points extend to full depth except for a sill of depth 2500 m in the model's Drake Passage to provide topographic form stress for the circumpolar flow. Figure 3.1 illustrates

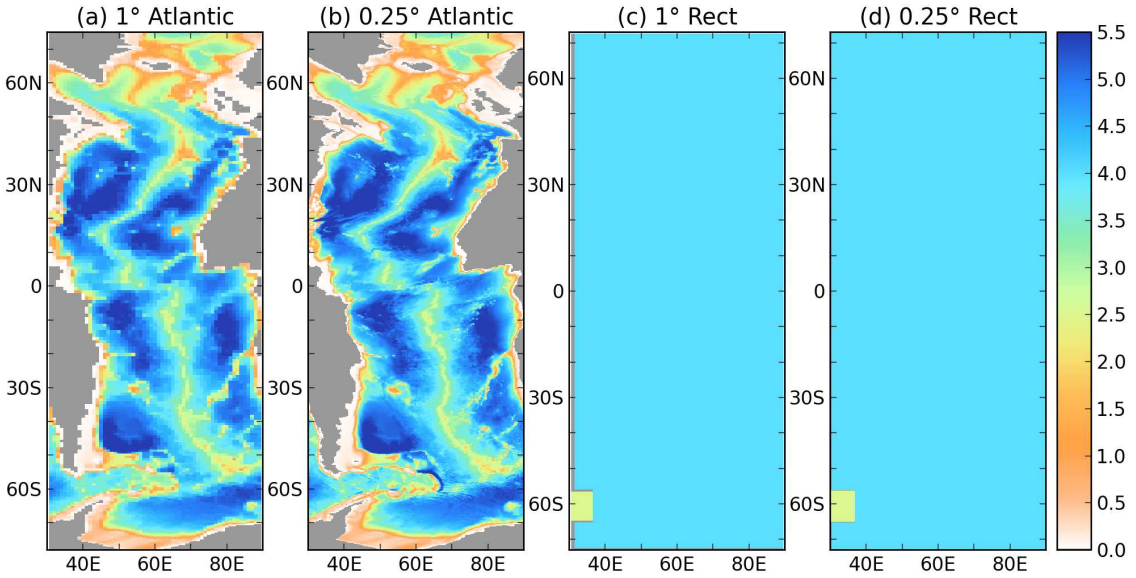

Figure 3.1: Depth of grid cells (km) in the (a) 1° Atlantic, (b) 0.25° Atlantic, (c) 1° Rectangular (Rect) and (d) 0.25° Rectangular models. Descriptions of the 'Atlantic' and 'Rectangular' models are given in Section 3.2.1.

the bathymetry in each model. Partial bottom cells are used to enable the precise depths of the Atlantic models to be well represented.

As in Part 2, the different horizontal resolutions allow a comparison of coupled climate simulations between parameterized and permitted ocean eddies. In the 1° models, we use the Gent and McWilliams (1990) eddy parameterization as implemented by Griffies (1998), using a constant coefficient of 600 m^2s^{-1}, while in the 0.25° models, no eddy parameterization is used. If an eddy parameterization were used at 0.25° resolution, it would have to be made weaker in order to avoid artificially strong mixing, since eddies are partially resolved. Our preference to use no eddy parameterization at this resolution is consistent with recent model studies (e.g. Delworth et al., 2012). For the horizontal viscosity we use a biharmonic Smagorinsky viscosity (Griffies and Hallberg, 2000), where the viscosity varies according to the grid length and the ocean state. Using the Griffies and Hallberg (2000) scheme, we set the dimensionless scaling parameter to $C = 3$ in the 1° models and $C = 2$ in the 0.25° models. Laplacian viscosity is used in the bottom grid cells, in order to improve stability in thin partial cells.

The land model consists of a 'bucket' soil water scheme with constant values of water availability and heat capacity. When precipitation exceeds the water capacity, idealized rivers redistribute runoff back into the ocean using a basin map. This scheme allows closure of the water budget within the coupled model. Since the land had no topography, the runoff map was adjusted manually, and was designed to make the North Atlantic saltier and the Southern Ocean fresher. Due to the different coastlines of the models, the runoff scheme is necessarily different between the Atlantic and Rectangular models.

For the Atlantic models, the runoff map was tuned to approximate the CORE annual forcing (Griffies et al., 2009) for the equivalent Atlantic domain. This tuning was performed by the following method: (i) The CORE runoff field was normalised over the domain so that the runoff into each grid cell was represented as a fraction of the total. This became the target runoff. (ii) A preliminary model run was used to output a map of precipitation over the land. This was also normalised so that each grid cell represented a fraction of the total precipitation. (iii) An a priori river basin map was used to aggregate the land precipitation values to their coastal runoff destinations, creating an synthetic estimated runoff showing the fraction of the total runoff at each grid point. (iv) The synthetic runoff estimate was compared to the target runoff and the river basin map was manually adjusted to create better agreement. Steps (iii) and (iv) were iterated until differences between the target and synthetic runoff were minimised. In the Rectangular model, no such corresponding CORE dataset is available, so the runoff follows a more idealized pathway redirecting freshwater towards the coast.

3.2.2 Vertical Diffusivity

In the mixed layer at both resolutions, we use the sub-mesoscale eddy parameterization of Fox-Kemper et al. (2008) and the KPP boundary layer mixing scheme of Large et al. (1994). In the Atlantic models we use the interior gravity wave-induced

mixing scheme of Simmons et al. (2004) and the coastal tide mixing scheme of Lee et al. (2006), whereas in the Rectangular models these schemes were switched off, since they represent mixing due to topographic roughness. All of the models use the non-linear equation of state of Jackett et al. (2006).

The vertical diffusivity was tuned independently between the Atlantic and Rectangular models, to ensure appropriate representation of the most climatically important ocean circulation features of each model. The Atlantic model was initially tested with a background vertical diffusivity of 1×10^{-5} m^2 s^{-1}, with enhanced mixing in regions of rough topography. This initial configuration led to a weak MOC, with only 1 Sv of North Atlantic Deep Water (NADW) formation. The background vertical diffusivity was then increased to 5×10^{-5} m^2 s^{-1}, which increased NADW formation rate to approximately 12 Sv in the 1° Atlantic model and 15 Sv in the 0.25° Atlantic model.

In the Rectangular model, the same vertical diffusivity settings led to similar NADW formation rates of 13 Sv in both the 1° and 0.25° models, but resulted in an almost total loss of sea ice in the NH. The presence of sea ice and its response to radiative forcing play an important role in the NH climate sensitivity. To ensure a comparable latitudinal extent of sea ice in the NH between the models, a Bryan-Lewis vertical diffusivity scheme (Bryan and Lewis, 1979) was used in the Rectangular model. The Bryan-Lewis scheme enhances mixing at depths greater than 2500 m, and hence no bottom roughness mixing was required. With these diffusivity settings, the NADW formation rate is approximately 6 Sv in the 1° and 9 Sv in the 0.25° Rectangular models.

The Bryan-Lewis diffusivity was also tested in the Atlantic model, but this resulted in a less realistic MOC, and noisy trends in the near surface temperature and salinity fields. Thus the control run vertical diffusivity settings in the Atlantic model were set to include a background 5×10^{-5} m^2 s^{-1} diffusion rate with enhanced topographic mixing, while the Bryan-Lewis scheme was used in the Rectangular model.

The upper cell of the MOC is weaker in the Rectangular model than the Atlantic model under these settings, while the latitudinal extent of sea ice is comparable between the two models, which provides an important feedback in the climate response to increased CO_2. We examine the robustness of the circulation sensitivities presented here to this change in vertical diffusivity.

3.2.3 Description of Experiments

The top of atmosphere insolation S is set according to:

$$S = \frac{S_0}{4}\left(1 + \Delta_{\text{sol}}\frac{1 - 3\sin^2\theta}{4}\right), \tag{3.1}$$

where $S_0 = 1360$ W m^{-2} is the solar constant, $\Delta_{\text{sol}} = 1.2$ is the meridional gradient parameter and θ is the latitude. The ocean albedo is set to 0.25, land albedo is set to 0.4 and sea ice albedo is set to 0.43.

The model's grey radiation atmosphere has no explicit greenhouse gas scheme. Instead the infrared optical depth is used as a proxy for greenhouse gas radiative forcing (e.g. Pierrehumbert, 2010). Optical depth is specified using an analytical profile that approximates the greenhouse effect of water vapor with latitude and pressure (Frierson et al., 2006). In order to achieve a $2\times CO_2$ perturbation, we increased the model's optical depth at all points by 16.2%, which gives a radiative forcing of 8 W m^{-2}. This value represents 4 W m^{-2} of direct forcing from a doubling of CO_2, plus a further 4 W m^{-2} to represent the water vapor feedback which would otherwise be missing from the model. For further details of how this perturbation was calibrated, see Part 2.

Both the Atlantic and Rectangular models were equilibrated for 1000 years at 1° resolution. The ocean temperature and salinity restart file at year 500 was interpolated onto the 0.25° grid and spun up (from zero velocity) for a further 500 years. These model states were then used to initiate 90 year transient radiative

forcing runs, where the equivalent CO_2 was increased by 1% per year until reaching $2\times CO_2$ at year 70, after which it was held fixed until year 90. We simulated parallel control runs for the same 90 year period, and subtracted the control run from the $2\times CO_2$ runs in each case.

In the $2\times CO_2$ runs, we found a slight equatorward shift of the westerly winds on the order of 1° latitude, except in the 0.25° Atlantic run where it remained steady. Most climate models instead show a poleward shift of the westerly winds in response to increased CO_2 (e.g. Barnes and Polvani, 2013; Bracegirdle et al., 2013). Therefore we ran additional 'wind override' experiments in which the SH westerly winds were perturbed to shift poleward and intensify. The perturbation was applied with a linear increase from zero to its full magnitude at year 70, so that it followed the same transient increase pattern as the radiative forcing experiments. These wind override experiments were run both separately and together with the $2\times CO_2$ transient forcing experiments.

The pattern of the perturbation and the zonal mean SH wind stress of the Atlantic models are shown in Figure 3.2, as in Part 2. The perturbation is implemented using a similar method to Delworth and Zeng (2008), with only the zonal momentum flux into the ocean affected by the perturbations. Since the winds are freely evolving, we cannot directly control their position, so that each model configuration possesses a slightly different wind stress position. Table 3.1 indicates the position and magnitude of the zonal mean SH westerly wind stress in each of the model runs. There is a small increase in the SH winds in response to warming, and a larger intensification and poleward shift in the wind override scenarios.

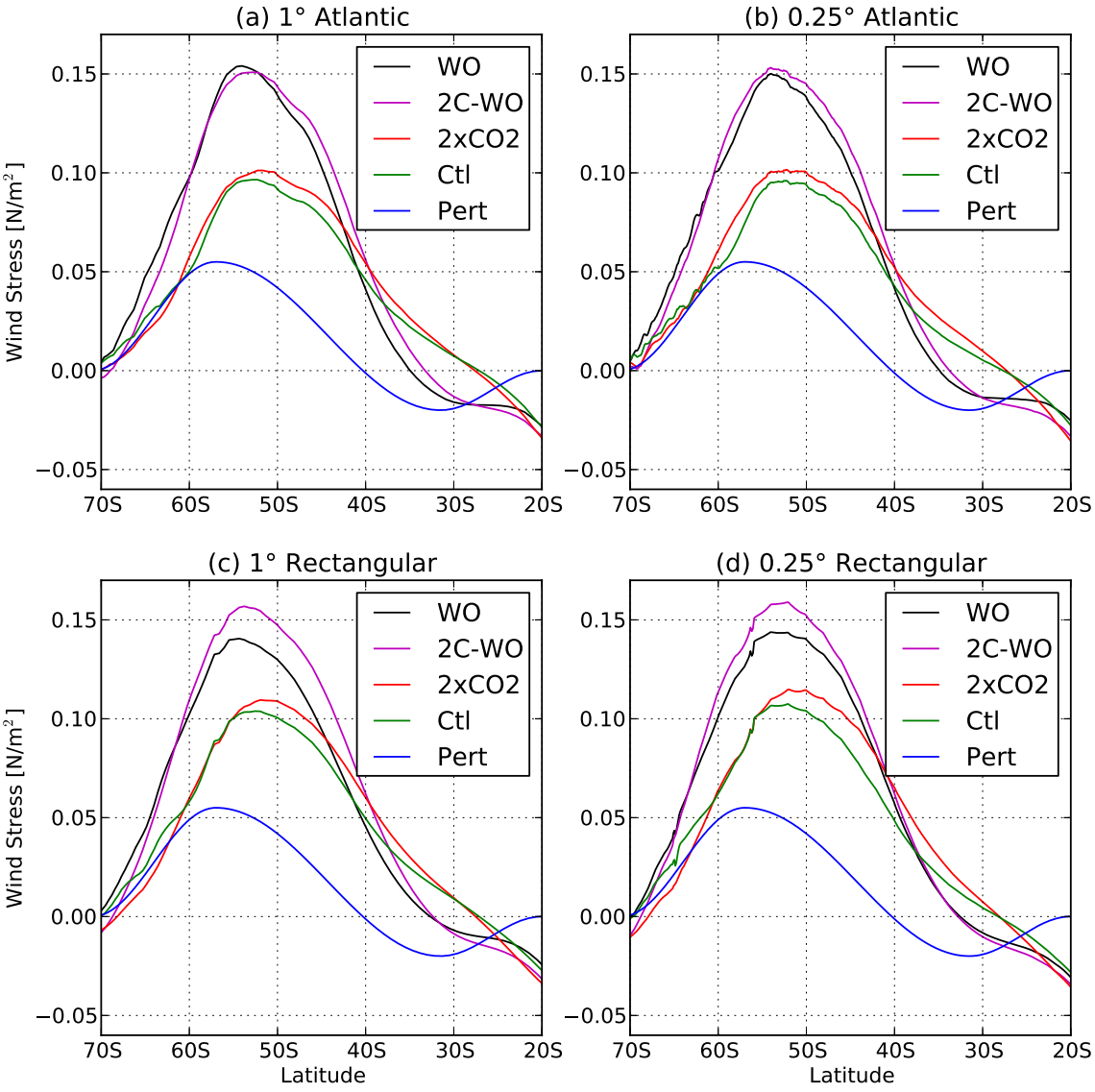

Figure 3.2: Zonal mean wind stress in the SH, averaged over the last 20 years of the control (Ctl), $2\times CO_2$, wind override (WO) and $2\times CO_2$ wind override (2C-WO) experiments, for the (a) 1° Atlantic, (b) 0.25° Atlantic, (c) 1° Rectangular and (d) 0.25° Rectangular models. Also shown is the perturbation pattern (Pert), which is applied as a zonally uniform perturbation of the same magnitude in all models, as described in Section 3.2.3.

3.3 Mean Climate and Circulation

3.3.1 Surface Temperature

The mean sea surface temperature (SST) in the control state is similar across each of the models, as shown in Figure 3.3. SST varies from around 27-28°C about the

Table 3.1: Zonal mean peak position (left 4 columns), and peak stress (right 4 columns) of the SH westerly wind stress in each of the model configurations, showing the control (Ctl), 2×CO_2 (2C), wind override (WO) and 2×CO_2 wind override (2C-WO), averaged over the last 20 years of each simulation.

	Peak Position (°S)				Peak Stress (N m^{-2})			
	Ctl	2C	WO	2C-WO	Ctl	2C	WO	2C-WO
1° Atlantic	52.3	51.6	54.1	52.9	0.097	0.101	0.154	0.151
0.25° Atlantic	52.3	52.3	54.1	54.1	0.096	0.102	0.150	0.153
1° Rectangular	52.6	51.9	54.3	53.8	0.104	0.109	0.141	0.157
0.25° Rectangular	52.1	51.9	54.1	52.1	0.108	0.115	0.144	0.159

equator to -2° C near the poles. SST is increased along the mid latitude western boundaries due to the subtropical gyres transporting warm water polewards. The Southern Ocean SST pattern around 50-60°S is cooler than the corresponding latitudes of the NH, due to the thermal isolation of the ACC. While the topographic features of the Atlantic model create some finer structure in the SST contours, the zonal mean and meridional gradient of SST is similar across the four models.

The zonal mean SST (Figure 3.3e) is relatively insensitive to the bathymetry and resolution changes. In all of the models, SST is largely symmetric through the tropics, and warmer in the mid to high latitudes in the NH than the SH. The Atlantic models are slightly cooler than the Rectangular models through most of the SH, while the 0.25° Atlantic model is slightly warmer from 50-65°N than all of the other models. The observed zonal mean SST in the Atlantic (Locarnini et al., 2013) is significantly warmer, with a difference of around 5°C in the NH midlatitudes, however the Southern Ocean is closer (1-2°C) to observed values.

The spatial structure of sea ice differs significantly between the models, with topographically steered boundary currents playing an important role in setting the distribution and thickness of the sea ice (Figure 3.4). The sea ice thickness contours in the Rectangular models (Figure 3.4c,d) are more zonal in the SH, with ice cover polewards from Drake Passage and increasing towards the southern limit of the domain. Wind forcing pushes ice to accumulate on the eastern side of the gyre, where it is blocked by topography. In the NH of the 1° Rectangular model, sea

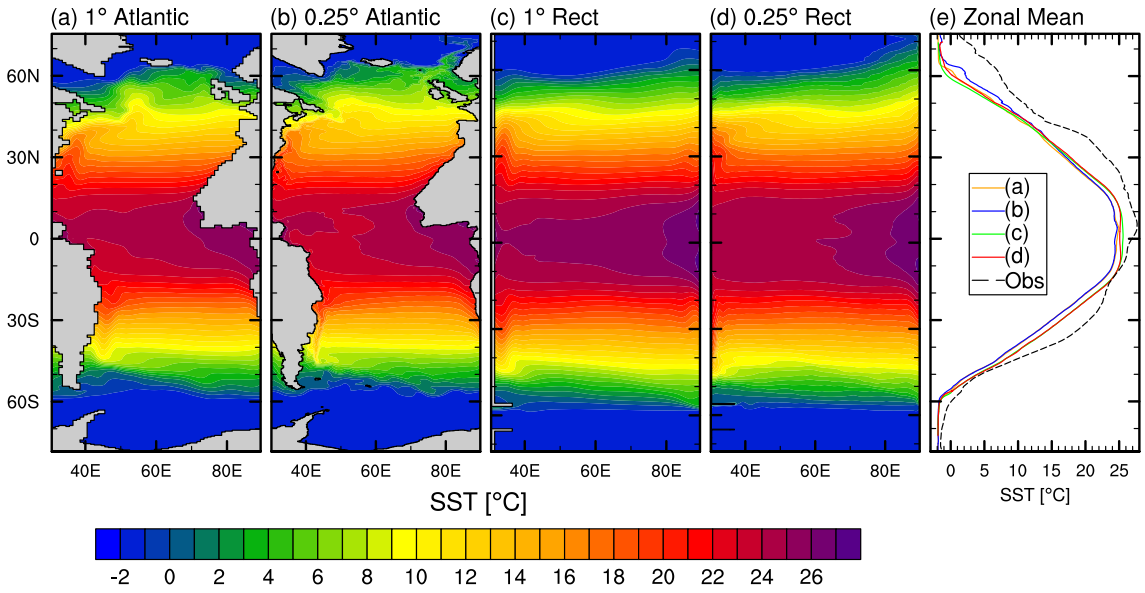

Figure 3.3: Sea surface temperature (SST; °C) averaged over years 71-90 of the control run for the (a) 1° Atlantic model, (b) 0.25° Atlantic model, (c) 1° Rectangular model and (d) 0.25° Rectangular model. (e) Zonal mean of plots (a-d), compared with the zonal mean SST from observations (obs) in the Atlantic basin (Locarnini et al., 2013).

ice is thicker in the north-western corner of the domain and decreases towards the east. This zonal asymmetry is due to the subpolar gyre, which includes a southward flowing western boundary current which expands ice cover in the west. In the 0.25° Rectangular model, the north-eastern corner of the domain is ice free, while the north-western corner is ice-covered poleward of about 60°N.

In the Atlantic models, sea ice accumulates more readily around topographic barriers. There is an increase in ice thickness along the east coast of Greenland and north of Iceland, where topographic barriers protect the sea ice from gyre heat transport. In the SH of the Atlantic models, sea ice is thickest on the east side of the Antarctic Peninsula, around the northward flowing boundary current of the Weddell gyre, in approximate agreement with observations (Figure 3.5). While a subpolar gyre also exists in the Rectangular model, the sea ice follows a different pattern, with the thickest ice trapped in the south-east corner of the domain, as a result of the wind-forced ocean and ice advection.

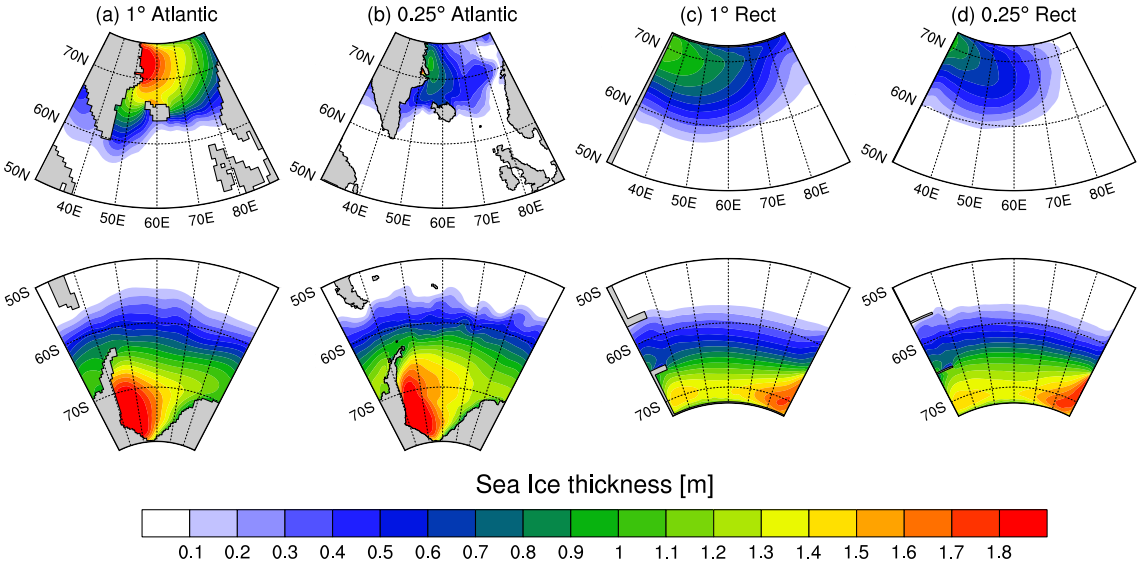

Figure 3.4: Sea ice thickness (m) averaged over years 71-90 of the control run for the (a) 1° Atlantic model, (b) 0.25° Atlantic model, (c) 1° Rectangular model and (d) 0.25° Rectangular model.

Our models all have a greater sea ice extent than the observed annual mean in the Atlantic sector, shown in Figure 3.5. Sea ice exists further equatorward than observations in all of our models. The equatorward bias is partly due to the model design, since there is no Arctic Ocean basin but we tuned the models to have a substantial sea ice extent in both hemispheres in the control runs. The greater sea ice extent is also partly due to the absence of a seasonal cycle, which prevents summer melting. In the SH the pattern of sea ice thickness in the Atlantic models more closely resembles the observed concentration to the east of the Antarctic Peninsula, due to the more realistic structure of the Weddell gyre.

3.3.2 Horizontal Circulation

The differences in the northern subpolar gyre between the models can be seen clearly in the barotropic streamfunction (Figure 3.6). The Rectangular models have a broader subpolar gyre with no topographic constrictions, including an equatorward flowing western boundary current bringing cold water south to around 40°N. By contrast in the Atlantic models the subpolar gyres are more confined by land barriers

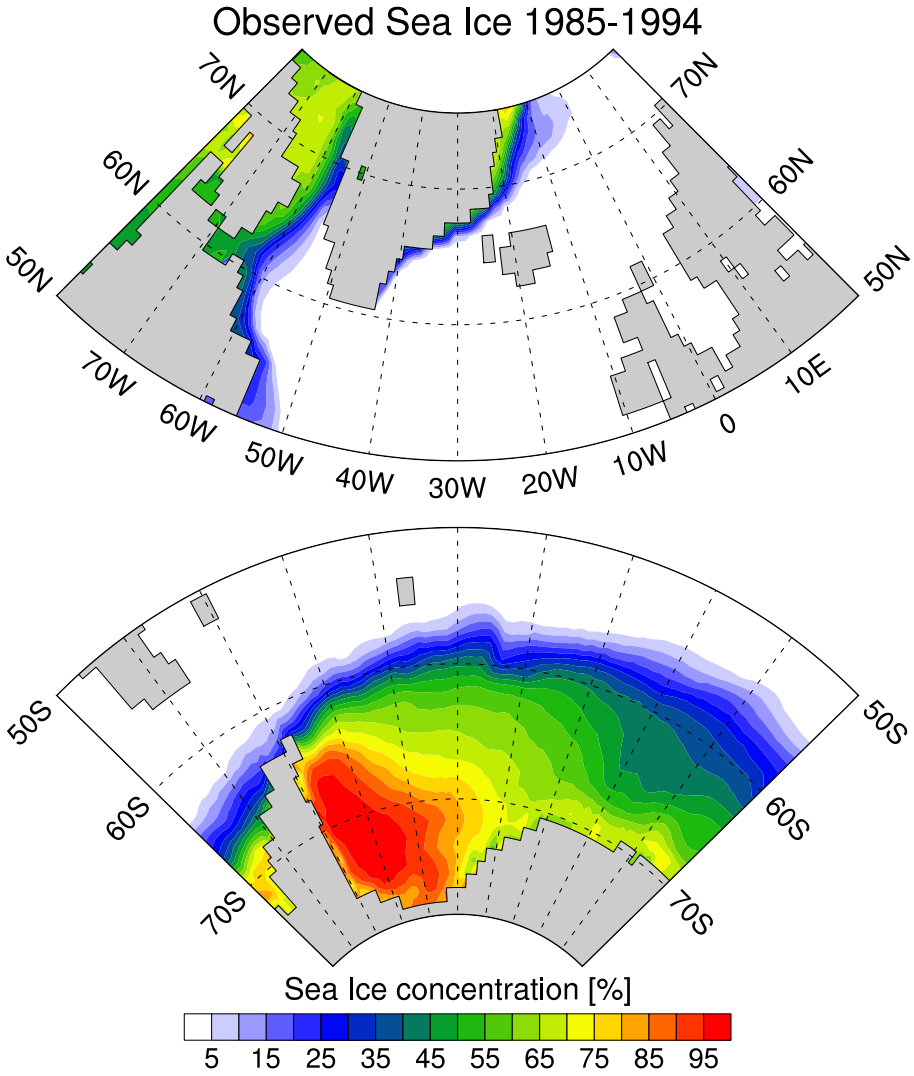

Figure 3.5: Observed sea ice concentration (%) using a 10 year annual mean from 1985-1994 (Hurrell et al., 2008) in the Atlantic sector, using the same latitude limits as in our Atlantic model.

and a shallow sill north of Iceland. Both the Atlantic and Rectangular models have strong Gulf Stream currents associated with the subtropical gyre, so they can efficiently transport subtropical surface waters poleward. We note that the path of the Gulf Stream separates further north than in observations, and does not migrate as far east as expected, due to distortions of the Atlantic bathymetry and coastlines in creating the 60° sector model. This path of the Gulf Stream creates a recirculation off the south east corner of Greenland that is not seen in observations.

Vectors showing the average velocity in the top 500 m are also overlaid in Figure 3.6. The upper level velocity field in the Atlantic model contains a strong northward

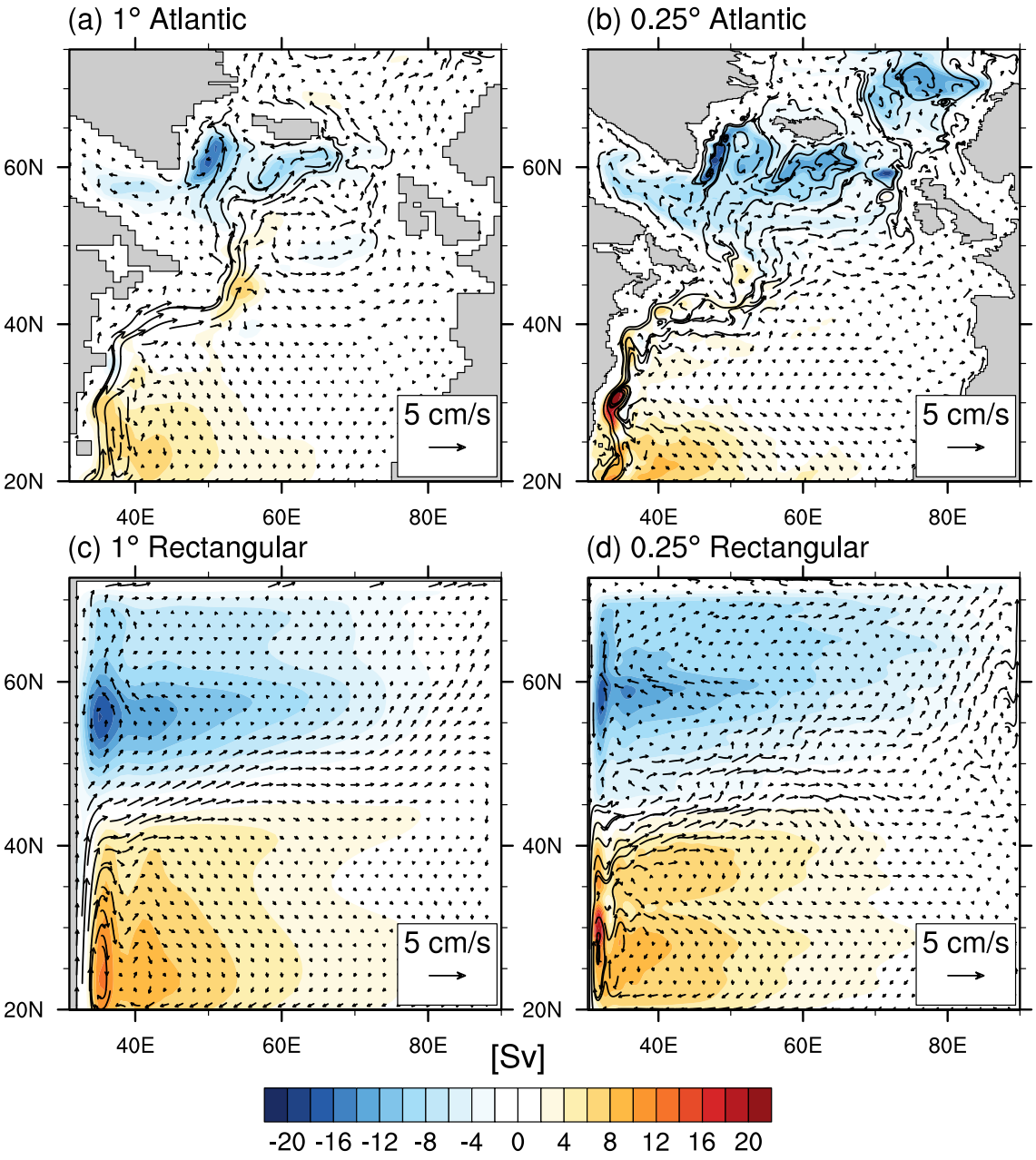

Figure 3.6: Horizontal circulation north of 20°N, showing barotropic streamfunction (2 Sv colour contours), with vectors showing the average velocity (Reference vector: 5 cm/s) in the top 500 m. The data are averaged over years 71-90 of the control run for the (a) 1° Atlantic model, (b) 0.25° Atlantic model, (c) 1° Rectangular model and (d) 0.25° Rectangular model.

flowing western boundary current. However, this boundary current is less evident in the barotropic streamfunction due to an opposing deep western boundary current along the same horizontal path. A southward flowing deep western boundary current is also present in the Rectangular models, but its opposing transport at depth is less aligned with the surface current than in the Atlantic model. In the Rectangular

models, the northward flowing western boundary current separates from the coast at about 45°N, and the subpolar gyre dominates the barotropic streamfunction north of this point.

We also compute a Sverdrup estimate of the maximum transport in the major gyres, by integrating the curl of the wind stress τ

$$\psi = \int_{x_E}^{x} \frac{1}{\rho\beta}(\nabla \times \tau)dx' \tag{3.2}$$

where x_E is the eastern boundary, β is the meridional gradient of the Coriolis parameter and ρ is a reference density. The Sverdrup estimate of transport agrees better with the simulations in the 1° models than the 0.25° models, as shown in Table 3.2. At 1° resolution, with greater viscosity and fewer resolved scales of motion, the Sverdrup estimate captures the first order structure of the gyres, especially in the Rectangular model. In the 1° Atlantic model, the subpolar gyre is less well represented by Sverdrup theory due to enhanced convection off the coast of Iceland, and greater steering of the boundary currents by topography (as found by Spence et al., 2012). However at 0.25° the wind stress curl becomes significantly noisier, due to the influence of fine scale currents which influence the relative velocity stress formulation. The Sverdrup streamfunction thus becomes noisier and provides a less representative picture of the horizontal circulation. A summary of maximum transport values from the major gyres and the ACC is given in Table 3.2, with Sverdrup estimates shown in brackets. The presence of standing eddies in the 0.25° models increases the maximum transport values, especially in the NH subtropical gyres, creating further disagreement with the Sverdrup estimates.

The different boundary currents cause significant changes to the poleward heat transport (PHT), especially near the surface. Transects of PHT in the upper 200 m, integrated from west to east, at 30°N and 60°N are shown in Figure 3.7. For the 1° models, the PHT includes the parameterized eddy heat flux term, whereas in the 0.25° models no parameterization is used. The western boundary currents at 30°N

Table 3.2: Maximum transport values from the subtropical and subpolar gyres and the ACC in each model. The values in brackets show the maximum transport estimated from Sverdrup balance. The ACC transport is the streamfunction difference across Drake Passage, while the Weddell transport is the maximum Weddell gyre value minus the ACC transport. These values were taken from the mean barotropic streamfunction from years 71-90 of each control run.

Sv	1° Rect	1° Atlantic	0.25° Rect	0.25° Atlantic
NH subpol.	18 (16)	17 (11)	17 (17)	20 (15)
NH subtrop.	12 (11)	8 (9)	20 (13)	24 (10)
SH subtrop.	13 (14)	13 (15)	17 (19)	19 (20)
Weddell	17	23	27	29
ACC	85	68	59	124

transport more heat closer to the western boundary at 0.25° resolution compared to 1° resolution. The overall magnitude of PHT is similar between the Atlantic and Rectangular configurations at 30°N. At 60°N, the Atlantic models transport more heat in eastern boundary currents than the Rectangular models, while the 0.25° models again have a greater PHT in their boundary currents. These differences in PHT, shaped by the bathymetry and coastlines, result in reduced sea ice extent (Figure 3.4) in the 0.25° models compared with the 1° models.

3.3.3 Meridional Overturning Circulation

The meridional overturning circulation (MOC), plotted in Figure 3.8 in latitude-density space, exhibits inter-model differences, partly related to the vertical diffusivity schemes chosen for each model, as discussed in Section 3.2.3. The Atlantic models have a stronger NADW cell than the Rectangular models, due to their higher overall vertical diffusivity. Antarctic Bottom Water (AABW) formation is also stronger in the Atlantic models, but its magnitude is more similar between the models. We also include in Figure 3.8c,f the MOC from the Rectangular models where the vertical diffusivity is enhanced to 5×10^{-5} m^2 s^{-1} as in the Atlantic models. With the same vertical diffusivity, the Rectangular models have a similar magnitude of NADW formation as the Atlantic models. However, the AABW cell is relatively insensitive to the vertical diffusivity change. This result suggests that AABW formation is less

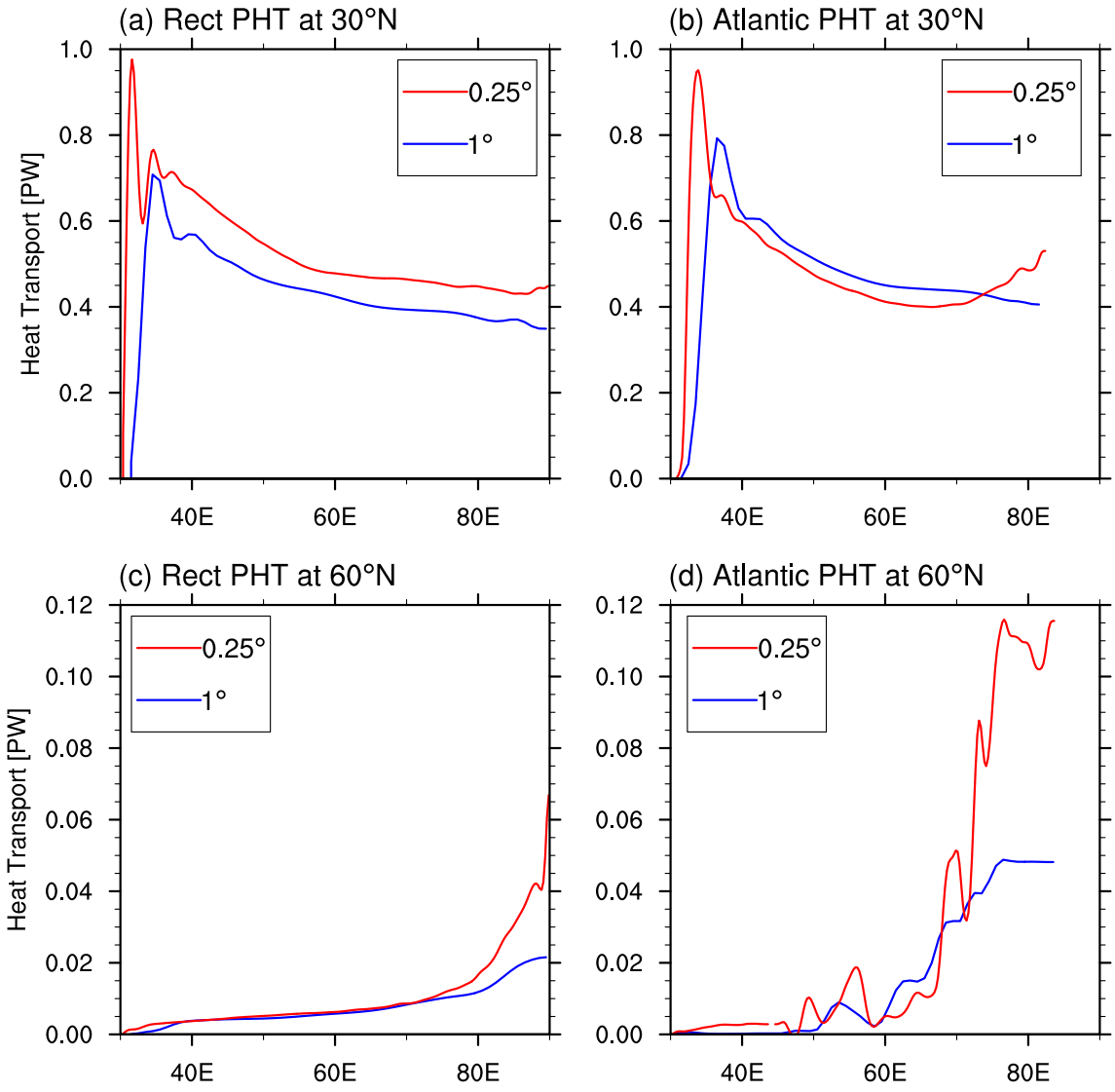

Figure 3.7: Cumulative integral from west to east of poleward heat transport (PHT) in the top 200 m, for the (a) Rectangular models at 30°N, (b) Atlantic models at 30°N, (c) Rectangular models at 60°N and (d) Atlantic models at 60°N. The red curves are from the 0.25° models and the blue curves are from the 1° models.

sensitive to vertical mixing than NADW, and more dependent on surface wind and buoyancy forcing, which are more closely matched between the models.

The lower cell structure is most realistic in the 0.25° Atlantic model, compared with the MOC in global models (e.g. Farneti et al., 2010). The 0.25° Rectangular model also has a stronger lower cell compared with the 1° Rectangular model, though its density range is closer to that of the upper cell than in the Atlantic models. The upper cell also penetrates further southward in the Atlantic models than the

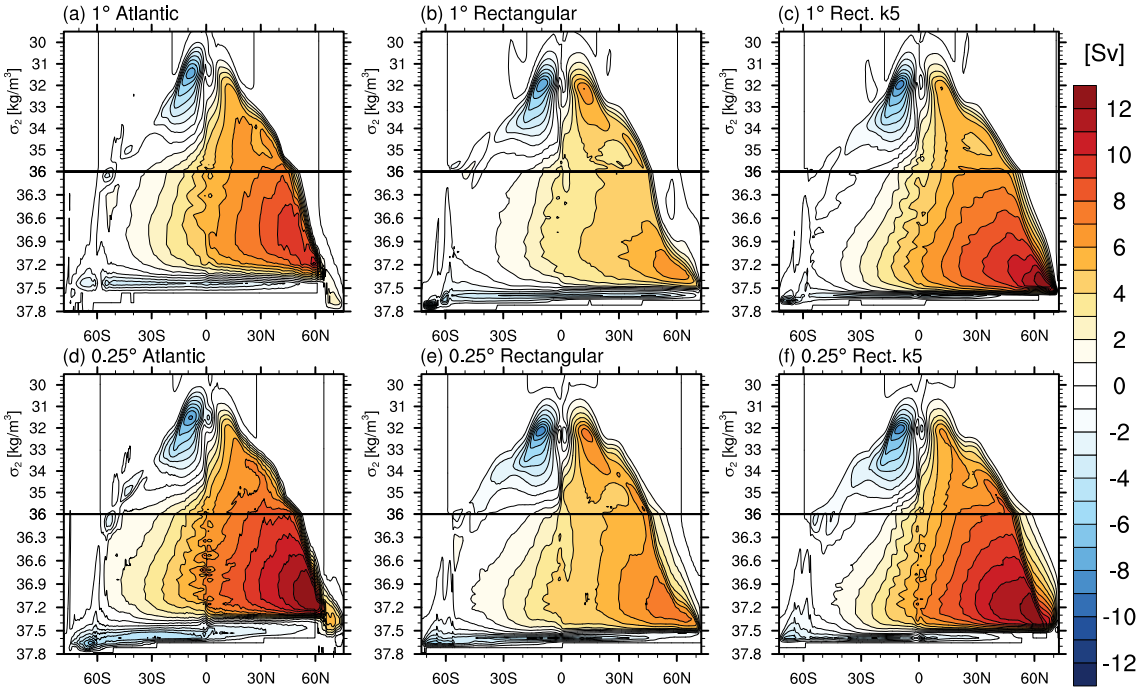

Figure 3.8: Meridional overturning circulation on potential density (σ_2 units) surfaces averaged over years 71-90 of the control run, for the (a), (d) Atlantic, (b), (e) Rectangular and (c), (f) Rectangular models where the vertical diffusivity is set to 5×10^{-5} $m^2 s^{-1}$ as in the Atlantic models. Units are in Sv (1 Sv = 10^9kg s^{-1}) and the contour interval is 1 Sv.

Rectangular models, in line with global model results. These findings suggest that the shelf regions and topographic barriers present in the Atlantic models help to better constrain the deep water formation.

The sinking regions of the models are altered significantly by the presence of land barriers when realistic continental outlines are present. Deep water formation regions are found just south of Iceland in the Atlantic models, as indicated by deep ($\sim$ 1000 m) mixed layers in this region (Figure 3.9). NH Sinking in the Rectangular models occurs mainly along the northern boundary, with some enhancement in the north-eastern corner of the domain. A weaker pattern of sinking along the northern vertical wall also occurs in the Atlantic models. The distribution of deep mixed layers in the NH is similar between the resolutions.

In the SH of the Atlantic models, the sinking regions are greatly shaped by the Antarctic coastline and shelf region. Very deep ($\sim$ 3000 m) mixed layers occur in the

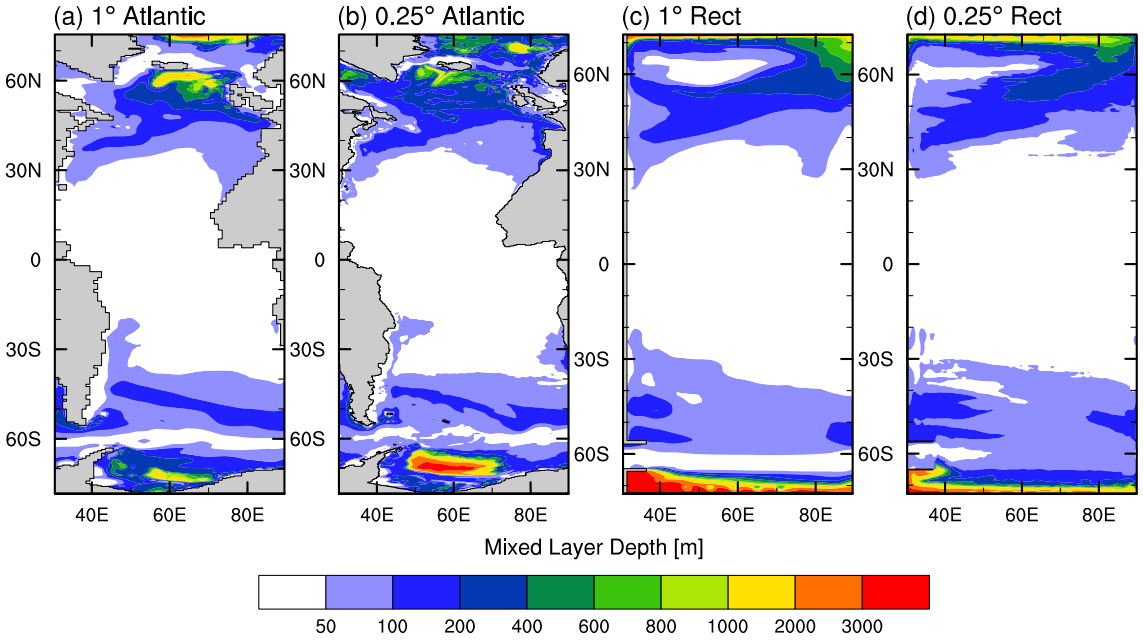

Figure 3.9: Mixed layer depths (m) averaged over years 71-90 of the control run, for the (a) 1° Atlantic model, (b) 0.25° Atlantic model, (c) 1° Rectangular model and (d) 0.25° Rectangular model.

interior of the Weddell Gyre of the 0.25° Atlantic model, whereas in the 1° Atlantic model, the deep sinking regions are shallower (less than 2000 m) and confined to a smaller area. This difference is associated with a stronger AABW cell in the 0.25° Atlantic model. The SH sinking regions in the Rectangular models are more closely confined to the southern sidewall, where very deep mixed layers occur along the entire Antarctic margin.

Potential density referenced to 2000 dbar is shown in Figure 3.10. The 1° Atlantic model has the densest water ($\sigma_2 > 37.8$ kg m^{-3}) in its polar regions, due to the sills at around 60-65°N and 70-75°S. The 0.25° Atlantic model has a similar pattern of relatively dense shelf water, but its magnitude is generally less than 37.8 kg m^{-3}. The boundary between NADW and AABW is approximately marked by the 37.5 kg m^{-3} isopycnal in the 1° Atlantic model, while in the 0.25° Atlantic model and both of the Rectangular models, the boundary is approximately 37.6 kg m s^{-3}. In addition, the Southern Ocean stratification in the 0.25° Atlantic models more closely matches the Rectangular models. The similarity in stratification between

the 0.25° Atlantic model and the Rectangular models is likely due to strong open ocean convection in these models. These three models have large areas of deep convection in the Southern Ocean (shown in Figure 3.9), whereas in the 1° Atlantic model, Southern Ocean mixed layers are not as deep and are constrained to a more southerly extent in the Weddell Sea.

A possible cause of the disagreement in stratification between the 1° and 0.25° Atlantic models may be weaker tracer mixing when eddies are marginally resolved in the 0.25° model. At 1° resolution, stronger mixing across the Southern Ocean from parameterized eddies can lead to a better stratification despite the lower resolution (as in Zhang and Vallis, 2013). Nevertheless, the warming response of the Southern Ocean is relatively insensitive to the change in resolution.

3.3.4 Summary of Mean States

The mean surface temperature and latitudinal distribution in each of the runs are similar between the models. The major difference in surface temperatures relates to the NH sea ice coverage, which is larger at 1° than at 0.25° resolution and is more constrained by topographic features in the Atlantic models. The structure of the gyres and especially the boundary currents are significantly altered when moving from flat bottom to Atlantic bathymetry. The Atlantic bathymetry constricts the extent of the NH subpolar gyre, and shapes the pathway of the Gulf Stream. By contrast in the Rectangular models, the western boundary currents occur mostly in a purely north-south direction, while the gyres have a more barotropic flow structure. These different flow regimes have significant impacts upon the response to radiative and wind forcing perturbations, as we will demonstrate below.

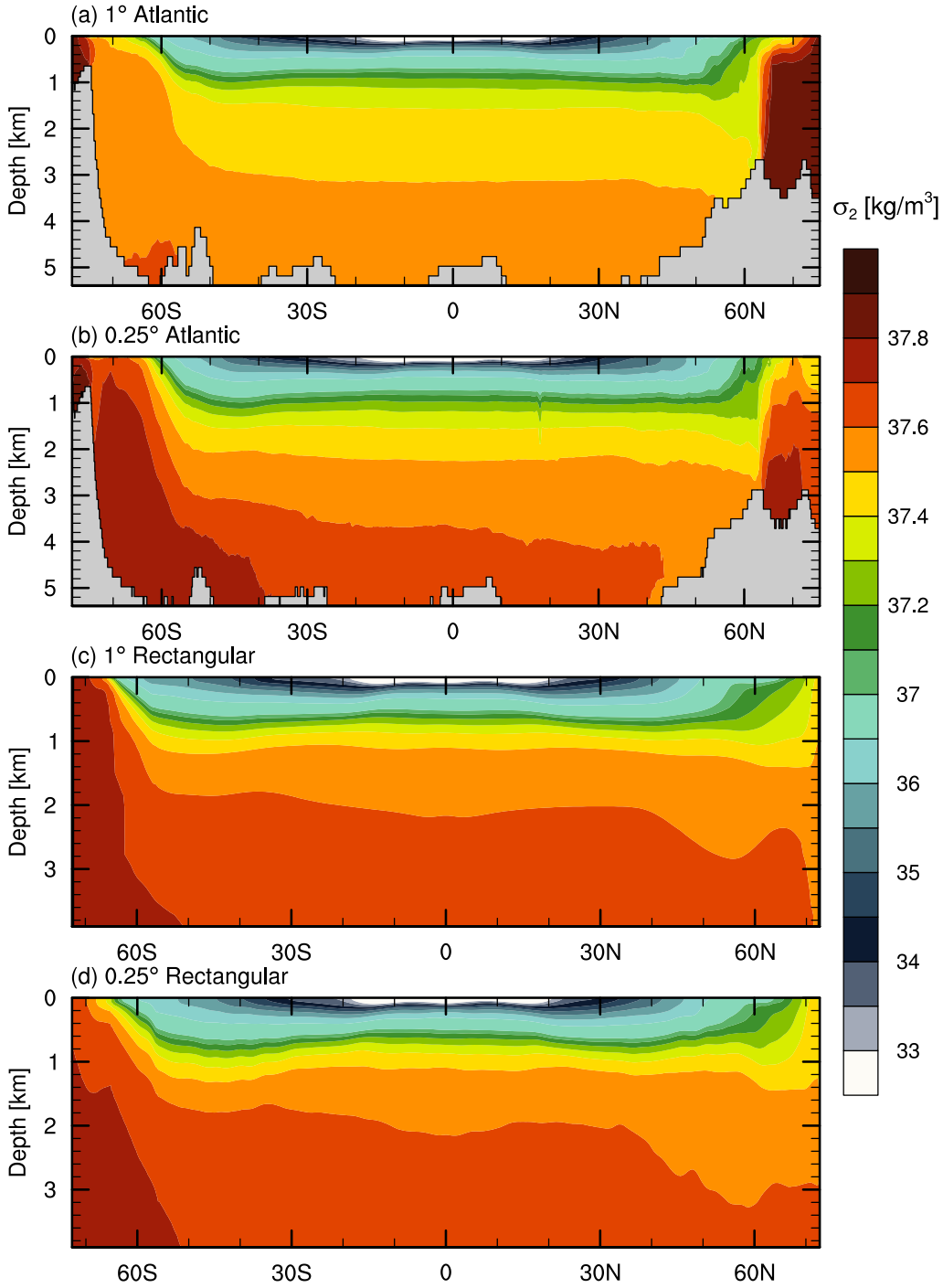

Figure 3.10: Zonally averaged potential density referenced to 2000 dbar in σ_2 units [ρ−1000 kg m^{-3}], averaged over years 71-90 of the control run for the (a) 1° Atlantic, (b) 0.25° Atlantic, (c) 1° Rectangular and (d) 0.25° Rectangular models. Note the colour intervals change from 0.5 to 0.1 kg m^{-3} at 37 kg m^{-3}.

3.4 Climate Response to Radiative and Wind Forcing

We examine the response of each model to forcing changes outlined in Section 3.2.3, designed to represent a 1% per year increase in CO_2 until doubling at year 70, and

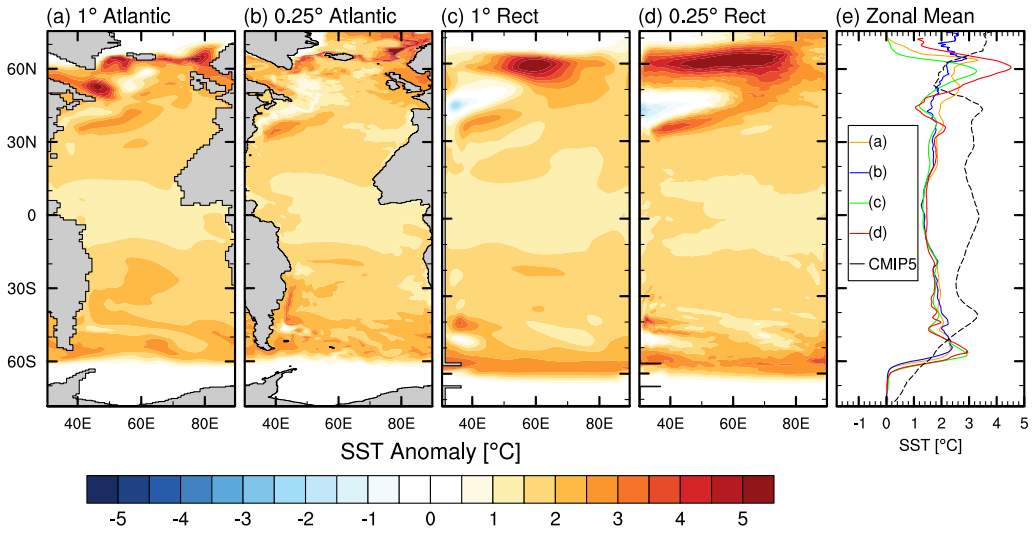

Figure 3.11: SST anomaly in years 71-90 of the $2\times CO_2$ run minus the control run, for the (a) 1° Atlantic model, (b) 0.25° Atlantic model, (c) 1° Rectangular model and (d) 0.25° Rectangular model. (e) Zonal mean of plots (a-d) and the 21st Century warming anomaly in the Atlantic Ocean from the ensemble mean of the RCP8.5 scenario of the CMIP5 models (using the post-processed dataset of Phillips et al., 2014).

linear increase in SH westerly wind forcing over the same period. Results below are shown from the mean of years 71-90 of the $2\times CO_2$ runs, and differenced from the same period of the corresponding control runs.

3.4.1 Surface Warming and Sea Ice Response

The SST warming pattern for each model is shown in Figure 3.11. All of the models have a warming signal of 1-2°C throughout most of the domain, with key differences in the high latitude responses. The 1° Atlantic model has a strong warming response (3-5°C) through the latitudes of 50-65°N, although the persistence of sea ice north of Iceland and near the coast of Greenland suppresses the warming signal to less than 0.5°C north of 65°N. In the 0.25° Atlantic model, the increased warming (>3°C) signal extends to the northern limit of the domain, with nearly all the NH sea ice disappearing in the $2\times CO_2$ run. In both of the Atlantic models, there is no significant region where the SST anomaly indicates cooling.

The Rectangular models show a key difference in the SST anomaly, in that an apparent cooling of 1-2°C appears between 40-50°N on the western edge of the domain. The location of this apparent cooling corresponds to the boundary of the subtropical and subpolar gyres, in particular near the location of the western boundary current separation. At around 60°N and between 50-70°E there is a strong warming signal (up to 5°C) in the 1° Rectangular model, though poleward of 65°N this signal drops to near zero, due to sea ice cover. In the 0.25° Rectangular model, the increased warming (3-5°C) signal extends from 40-80°E and across a larger latitudinal span (50-70°N). The greater extent of warming occurs because there is far less sea ice remaining under warming conditions in the 0.25° Rectangular model.

A comparison of the zonal mean SST warming in each model is shown with the CMIP5 Atlantic Ocean average in Figure 3.11e. All four of our models are exhibit less warming than the CMIP5 average through much of the domain. This difference is larger than the spread between our models, except in the high northern latitudes where major differences in sea ice melting occur. However, the sector geometry of our models is expected to create some significant differences compared with the warming pattern of the CMIP5 global domains.

In the SH, sea ice declines modestly, with a reduction in thickness and overall extent of a similar magnitude in all of the models. SH sea ice contracts poleward by 3.5° and 3.8° latitude in the 1° and 0.25° Atlantic models respectively, and by 4.1° and 4.6° latitude in the 1° and 0.25° Rectangular models. The NH sea ice response is markedly different, as the 0.25° Atlantic and Rectangular models have virtually no sea ice remaining by the end of the warming period, while the 1° Atlantic and Rectangular models remain mostly ice covered north of 65°N. As discussed in Part 2, stronger boundary currents at higher resolution melt the sea ice further in the 0.25° models. The slower, more diffuse, boundary currents in the 1° model are unable to transport as much heat into the polar regions.

3.4.2 Deep Warming

Figure 3.12 shows latitude-depth zonal mean temperature transects in the final 20 years of the $2\times CO_2$ run minus the control run for each model. In the 1° Atlantic model, the greatest patch of warming occurs around 60°N, reaching 1.5 km depth at this latitude. Moving southward to 50°N, this region of enhanced warming shoals to around 600-800 m, and remains confined to the top 500 m southward of 30°N. In the 0.25° model, enhanced warming extends to 1600-2000 m depth from 60°N right up to the northern limit of the domain (75°N). The enhanced deep warming in the northern high latitudes in the 0.25° Atlantic model is due to the greater melting of sea ice, which exposes more surface water in the sinking region to radiative warming.

A Southern Ocean warming signal greater than 0.5°C between 30-60°S extends to around 600-800 m depth in both models, due to the deep mixed layers in this region. Warming greater than 0.1°C generally occurs above the position of the 0°C isotherm of the control run (shown by the black contours in Figure 3.12). The 0°C isotherm approximately corresponds to the maximum level at which NADW penetrates into the deep ocean in these models. In the tropics, there is a warming signal of up to 0.5°C extending down to 1500-2000 m, associated with equatorial upwelling. However tropical warming in the upper 500 m is weaker than that in the mid to high latitudes, due to the stronger stratification.

In the Rectangular models, there are regions of enhanced warming in the high latitudes as seen in the Atlantic models. However, the deep warming signal is less pervasive than in the Atlantic models, due to a shallower penetration of NADW and the lack of shelf regions at high latitudes. These shelf regions sustain a larger region of marginally stable stratification in the Atlantic models compared with the Rectangular models, as seen in the control run temperature contours.

In the 1° Rectangular model, there is a slight cooling signal (less than 0.5°C) between 40-50°N from 400-1000 m depth. In the 0.25° model, the heat uptake at

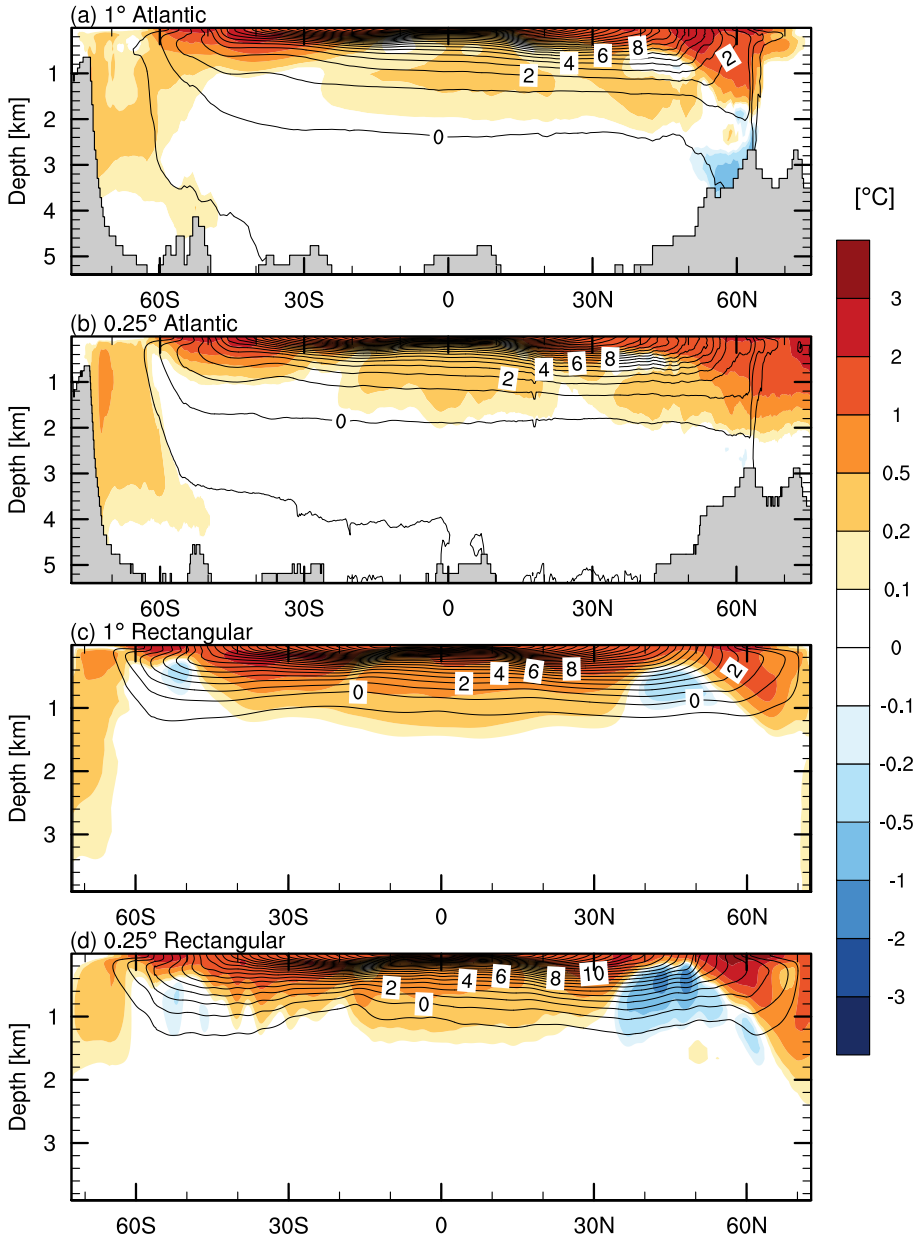

Figure 3.12: Zonal mean temperature anomaly (°C) at depth, with contours of the control run temperature overlaid (1°C interval) in years 71-90 of the $2\times CO_2$ run minus the control run, showing the (a) 1° Atlantic, (b) 0.25° Atlantic, (c) 1° Rectangular and (d) 0.25° Rectangular models. Note the colour intervals become smaller close to zero to highlight warming in the deep layers.

60°N is increased (up to 3°C), but the cooling signal around 40-50°N is also increased (greater than 1°C at some points). The cooling signal occurs around the interface between the warm subtropical and cold subpolar gyres (Figure 3.6), and is likely caused by a southward shift of this interface at the depths of the cooling. Due to the lack of bathymetric constraints in the Rectangular models, the position of the 'Gulf Stream' more easily shifts in response to the warming perturbation, whereas

in the Atlantic models its position is more stable. Southern Ocean heat uptake also follows a different pattern in the Rectangular models than the Atlantic models, with enhanced warming down to 1000 m at around 30-40°S, but shoaling to less than 400 m at 50-60°S.

3.4.3 Meridional Overturning Circulation

The evolution of the NADW and AABW indices during the control and $2\times CO_2$ runs is shown in Figure 3.13. These indices are taken from a 9 year running mean time series of the MOC streamfunction in density coordinates (as plotted in Figure 3.8), and then the maximum absolute value is chosen for each circulation cell. In the $2\times CO_2$ runs there is a clear decrease in AABW formation, which reduces from about 9-10 Sv to 2-3 Sv in both of the 1° models. In the 0.25° models, AABW formation reduces from around 6-7 Sv to 2-3 Sv by the end of the $2\times CO_2$ runs. In contrast NADW formation remains relatively steady in both the 1° and 0.25° models, with a small decrease from around 6 Sv to around 5 Sv in the 1° Rectangular model, while it remains close to its control value of about 12 Sv for the duration of the $2\times CO_2$ run in the 1° Atlantic model. There is a minor decrease in NADW formation in both the 0.25° models.

Most CMIP5 models show a reduction in NADW formation in response to greenhouse warming (Drijfhout et al., 2012), albeit with a wide spread in sensitivity. Our models have a comparatively weak sensitivity of NADW to warming. As discussed in Section 2.3.5, we attribute this weak sensitivity to the strong vertical diffusivity maintaining the thermally indirect AMOC. This sensitivity may be related to the lack of other ocean basins or a fully circumpolar Arctic Ocean, since the Atlantic Ocean heat budget is influenced by thermal forcing from other basins (e.g. Lee et al., 2011). However, we find a shoaling of the NADW cell in response to the warming of surface waters (shown in Figure 2.11). This response is consistent with the global coupled model of Zika et al. (2015), where greenhouse warming significantly weak-

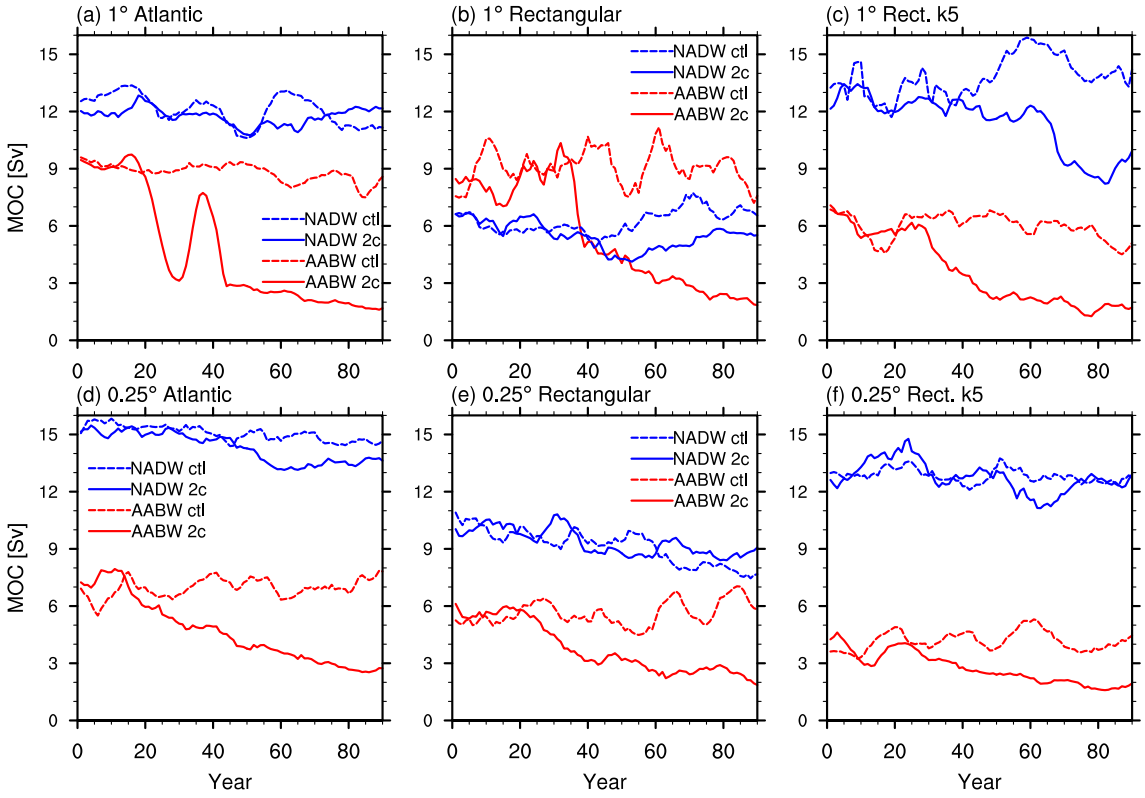

Figure 3.13: Time series of MOC in latitude-density coordinates, showing 9 year running mean indices of North Atlantic Deep Water (NADW; blue) and Antarctic Bottom Water (AABW; red), for the (a), (d) Atlantic, (b), (e) Rectangular and (c), (f) Rectangular models where the vertical diffusivity is set to 5×10^{-5} $m^2 s^{-1}$ as in the Atlantic models. The control runs are shown in dashed curves and the $2\times CO_2$ runs shown in solid curves.

ens the lower cell of the MOC, while the upper cell maintains a similar overturning strength at a shallower depth.

3.4.4 Antarctic Circumpolar Current

The response of Drake Passage (DP) transport to the wind and radiative forcing perturbations is shown in Figure 3.14. In all cases, DP transport declines by more than 20% in the purely radiatively forced $2\times CO_2$ runs. All simulations have a non-zero increase in ACC transport in response to the wind perturbations only, though the sensitivity is significantly greater in the Atlantic models than the Rectangular models. However, in the $2\times CO_2$ wind override runs (blue lines in Figure 3.14),

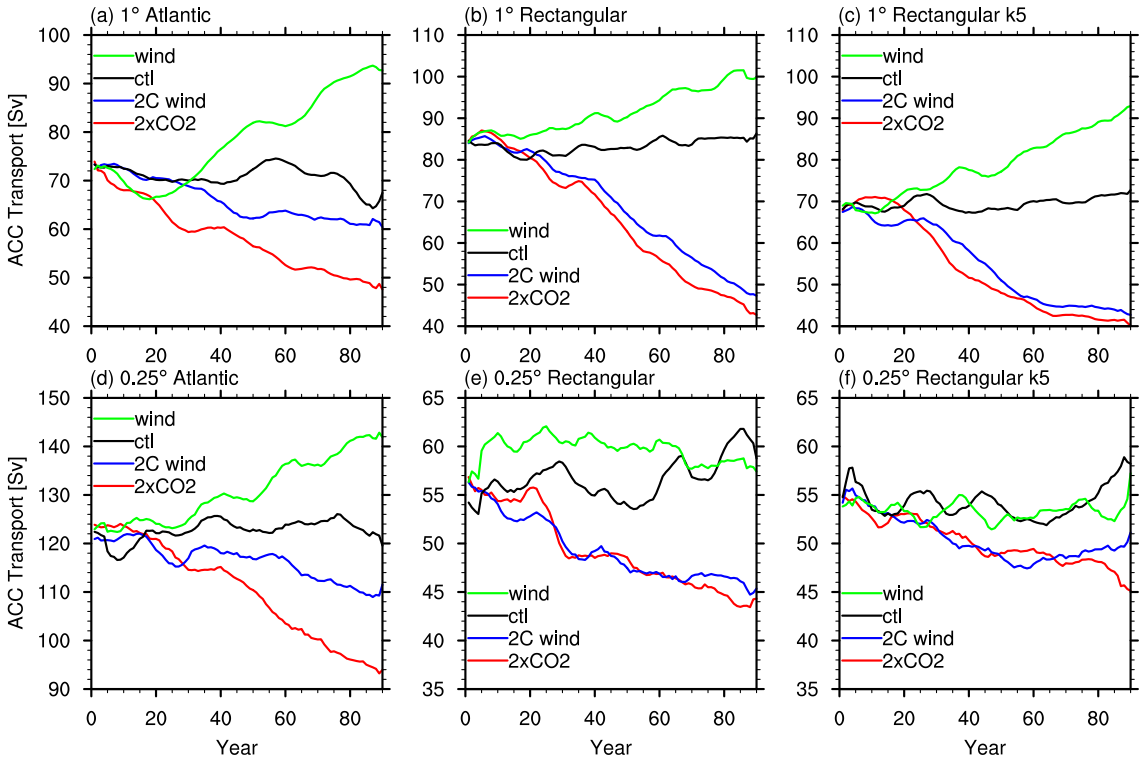

Figure 3.14: Drake Passage transport (Sv) in the (a), (d) Atlantic models, (b), (e) Rectangular models and (c), (f) Rectangular models where the vertical diffusivity is set to 5×10^{-5} m^2s^{-1} as in the Atlantic models. Included are time series for the control experiment (ctl; black), the $2\times CO_2$ experiment (red), the wind override (wind; green) and the $2\times CO_2$ wind override (2C wind; blue). The time series are filtered using a 9 year running mean.

the Atlantic models show significantly higher transport than the $2\times CO_2$ only runs, whereas in the Rectangular models, DP transport declines in the $2\times CO_2$ wind override runs by almost the same amount as in the $2\times CO_2$ runs. The weaker sensitivity to wind forcing in the Rectangular models is robust to the change in vertical diffusivity, as shown in Figure 3.14c,f.

A further observation from Figure 3.14 is that in all of the models, the ACC transport in the $2\times CO_2$ wind override runs is difficult to distinguish from the control runs for the first few decades. This near zero change is due to the combination of a buoyancy forced decrease and a wind forced increase in ACC transport, leading to partial cancellation. Furthermore, natural variability in the ACC transport in both the control and perturbation runs makes the signal harder to detect in the first few decades. A scenario of poleward intensifying winds and radiative surface

warming partly resembles the last several decades of observed trends, with our results broadly agreeing with the satellite-derived near-steady ACC transport over the last two decades (Hogg et al., 2015). Since ACC transport is reduced by warming, and increased by wind stress, it is possible for perturbations of this kind to mask each other, making it difficult to assess the mechanisms governing ACC transport in the absence of a longer period of measurements.

3.5 Discussion

We have shown that including realistic ocean bathymetry and coastlines in a sector climate model causes important changes to the ocean circulation that are pertinent to climatic feedbacks. Although the mean climate state at the surface and in the deep ocean are similar between the configurations, the circulation differences and associated changes in sea ice cause major changes to the warming patterns in the $2\times CO_2$ runs. The warming signal in the high northern latitudes of the Atlantic models is positive nearly everywhere. At the same latitudes of the Rectangular models, there is both a warming signal and an apparent cooling caused by a shift in the gyre interface, leading to an overall lower asymmetry in the 1° Rectangular model. However, in the 0.25° Rectangular model, the net warming signal is larger than in the 0.25 ° Atlantic model, despite a similar apparent cooling patch as in the 1° Rectangular model.

Many ocean model studies have employed sector configurations similar to our Rectangular model, with little or no complexity in the bathymetry or coastlines. Such models normally possess a climate state analogous to the real climate system, and many are based on the Atlantic basin with a Southern Ocean circumpolar channel. Our results suggest that these sector models may be improved by including realistic bathymetry and coastlines, and that the strength of the gyres are strongly influenced by terrain features.

The subpolar gyre is particularly affected by topography in the North Atlantic, due to the land-masses of Canada, Greenland and Iceland, and the shallower bathymetry in this region. These features significantly affect the pathways of boundary currents and thereby the heat transported northward by the gyres. With topography present, the NH subtropical gyre and the associated Gulf Stream are significantly stronger than the subpolar gyre and its southward flowing boundary current. Without topography included, the subtropical and subpolar gyres have similar flow structure and heat transport.

Owing to these boundary current differences, sea ice is strongly influenced by the bathymetry and coastlines of the model. Embayments and shelf regions present in the Atlantic models enable sea ice to form more readily and persist in response to increased anthropogenic forcing. The structure of boundary currents is also shaped by the bathymetry, both at the surface and in the deep ocean. Since the boundary currents greatly influence the sea ice distribution and its melting response, the boundary current pathways have a strong influence on the ocean's response to greenhouse warming. These bathymetric effects show that flat bottom rectangular ocean models may have markedly different sensitivities to forcing compared with realistic global models.

The higher sensitivity of ACC transport to wind forcing in the Atlantic models may be due to the presence of a barotropic free mode mechanism. This barotropic free mode occurs where the ACC aligns with circumpolar contours of f/H, as occurs close to the Antarctic Peninsula. Hughes et al. (1999) showed that the depth-integrated circumpolar flow can be accelerated by an eastward wind stress perturbation along these f/H contours. Zika et al. (2013a) found that the ACC transport is sensitive to an eastward wind stress perturbation along the Antarctic coast. Furthermore, wind forcing along the ACC core forces both a baroclinic transport leading to enhanced eddy kinetic energy, and a barotropic acceleration of the ACC along f/H contours (Langlais et al., 2015).

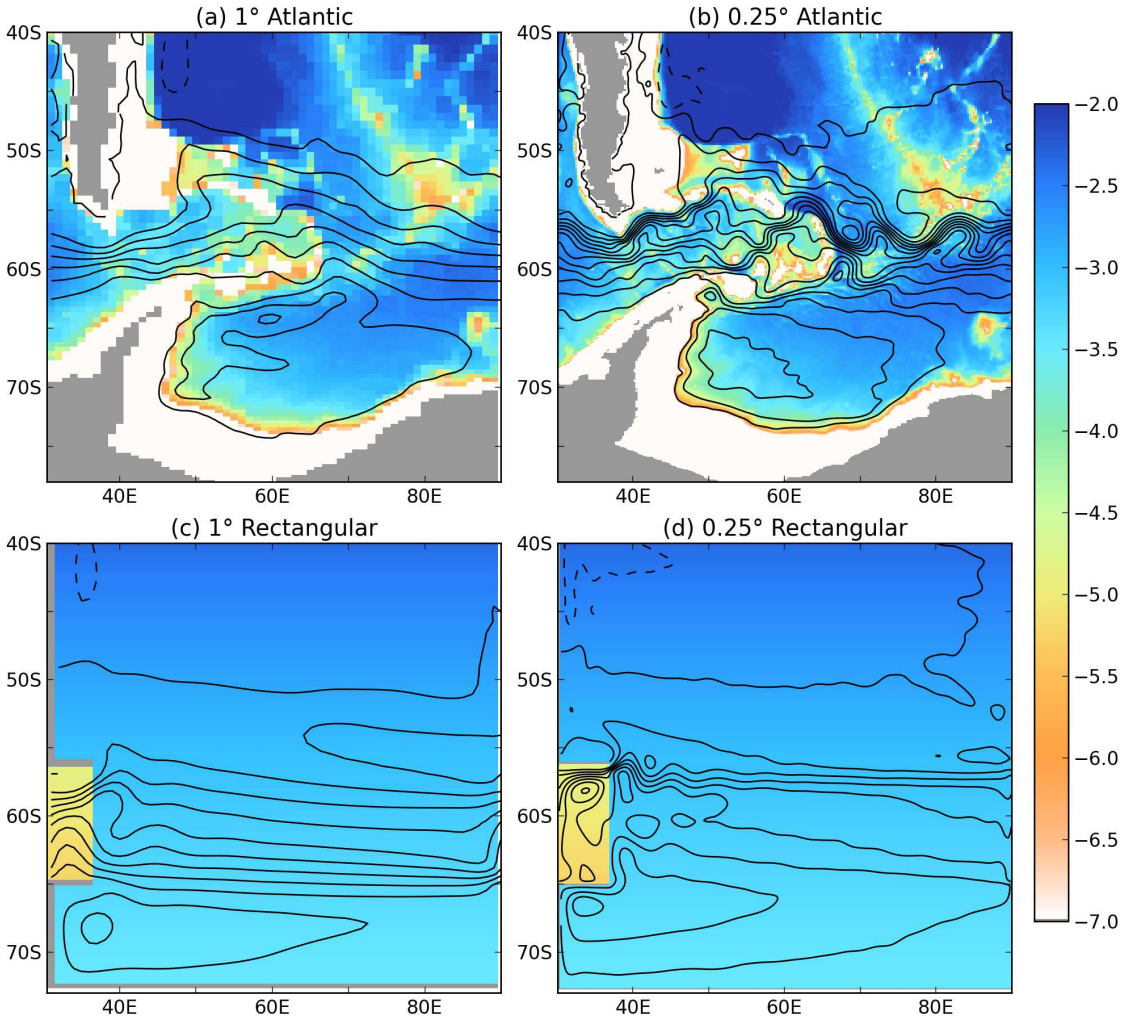

Figure 3.15: Colours showing f/H (10^{-8} s^{-1}m^{-1}), where f is the Coriolis parameter and H is the ocean depth, and contours of barotropic streamfunction (10 Sv interval; negative dashed) overlaid for the (a) 1° Atlantic, (b) 0.25° Atlantic, (c) 1° Rectangular and (d) 0.25° Rectangular models.

The differences in Southern Ocean f/H contours between the models are illustrated in Figure 3.15. In the Rectangular model, H is a constant except for a step change in the DP sill, meaning the free mode mechanism is absent. The reduced sensitivity of circumpolar transport to wind forcing in the Rectangular models at both resolutions suggests that the details of bathymetry have an important influence on the sensitivity of the ACC to surface forcing, as in Langlais et al. (2015). The decline in DP transport in response to surface warming is consistent with recent idealized studies in which surface buoyancy forcing has a strong control over ACC transport (Hogg, 2010; Shakespeare and Hogg, 2012).

Both the Rectangular model and the Atlantic model have a higher asymmetry of warming when the ocean resolution is eddy-permitting than coarse. This enhanced asymmetry is caused primarily by stronger boundary currents transporting more heat northwards in the NH at higher resolution. The eddy component of poleward heat transport is smaller than the mean flow component at most latitudes, regardless of the resolution. The poleward heat transport of the mean flow, especially in the boundary currents, is significantly increased at higher resolution. In the Southern Ocean we do not find major differences in eddy heat transport between the Rectangular and Atlantic models, or major sensitivity to the resolution change. The parameterized eddy heat flux at 1°, and the explicit (partially resolved) eddy heat flux at 0.25° contribute a similar amount of poleward heat transport in the models considered here.

3.6 Conclusion

We have shown here that including realistic bathymetry and continental outlines in a sector climate model can cause important changes to the ocean circulation when compared with an idealized flat bottom model. The structure of the gyres and boundary currents are significantly altered by coastlines and bathymetry constrictions in the Atlantic model, and these changes have major impacts on the magnitude and distribution of heat fluxes and sea ice. Although the mean climate state of the models is similar, circulation differences alter the response to greenhouse warming, especially in the North Atlantic, where localized cooling emerges in the Rectangular model but not in the Atlantic model. At eddy-permitting (0.25°) resolution, both the Rectangular and Atlantic models have a higher asymmetry of warming, with greater melting of sea ice compared with the equivalent models at coarse (1°) resolution. The Atlantic models have higher ACC transport sensitivity to Southern Ocean wind stress perturbations than the Rectangular models, which is likely due to the topographically constrained free mode of ACC transport.

Concluding Remarks

This thesis has examined the influence of the ocean circulation on the interhemispheric asymmetry of global warming, using several different model approaches. Previous work suggested that the ocean contributes a substantial portion of the asymmetry in SST warming by limiting poleward heat transport in the Southern Ocean, and enhancing poleward heat transport in the NH subtropical and subpolar gyres. Here we used new model simulations including a novel Atlantic-only configuration with realistic topography to isolate the ocean's contribution to this asymmetry, firstly by blocking the Drake Passage throughflow, and secondly by removing the asymmetry of land-masses between the hemispheres. We further examined changes to the asymmetry when moving from coarse to eddy-permitting ocean resolution, and the impact of including realistic bathymetry within an idealized sector climate model. These methods have allowed us to disentangle the ocean's contribution to the asymmetry from the land-ocean warming contrast, which also causes faster warming in the NH. We briefly summarise the main findings of the thesis below, and finish with recommendations for future research.

Summary of Findings

The interhemispheric temperature asymmetry was enhanced at eddy-permitting ocean resolution compared with coarse resolution, both in control runs and in $2\times CO_2$ warming scenarios. This result was shown to be robust to changes in the model bathymetry, and was found in both an Atlantic-like sector model and a flat bottom rectangular model. The higher SST asymmetry at eddy-permitting resolution was primarily due to faster, less viscous boundary currents in the mid to high northern

latitudes. These better-resolved boundary currents transported more heat into the sea ice region, thereby reducing sea ice extent in the NH and enhancing melting in the $2\times CO_2$ scenarios. By contrast, the SH surface warming was relatively insensitive to the change in resolution, with similar heat transport across the Southern Ocean by parameterized versus explicit eddies. Imposing a poleward shift and intensification of the SH westerly winds also increased the warming asymmetry, by enhancing upwelling of deep water in the Southern Ocean, and increasing Antarctic Bottom Water formation. Radiative forcing increased the temperature asymmetry more than the wind forcing perturbations, however these perturbations increased the temperature asymmetry when applied both separately and together.

The Antarctic Circumpolar Current (ACC) was found to have a significant impact upon the interhemispheric asymmetry of SST warming in a coarse resolution global climate model. When the ACC was blocked by a Drake Passage land barrier, the SST warming asymmetry was significantly reduced. The reduced SST asymmetry was due to greater ocean heat transport towards Antarctica in the presence of a gyre, resulting in a near total loss of Antarctic sea ice. Without Antarctic sea ice, the Southern Ocean warmed significantly more in response to an increase in greenhouse gas forcing, especially in the Pacific sector and around the Antarctic Peninsula. There was no significant change in SAT warming asymmetry with Drake Passage closed. The lack of change to SAT warming asymmetry suggests that other mechanisms such as land surface warming and compensating atmospheric heat transport are more dominant in setting the SAT warming asymmetry.

The impact of realistic Atlantic bathymetry in an idealized sector climate model was further examined, and compared with a flat bottom rectangular model. The Atlantic and rectangular models had similar surface climates, but bathymetry caused important changes to the sensitivity to forcing. Bathymetry strongly constrains the pathways of the North Atlantic gyres and their associated boundary currents. When bathymetry is absent, a larger subpolar gyre and stronger southward boundary

current exists, and the position of the gyres can move more freely in response to wind forcing, as they are not constrained by f/H contours. These shifts in the gyre boundaries create a local cooling region in the NH mid-latitudes under radiative forcing scenarios. By contrast, no significant cooling region was found when more realistic Atlantic bathymetry is incorporated. The horizontal circulation is greatly enhanced in the deep ocean without bathymetry, leading to a more barotropic kinetic energy profile. The more realistic Atlantic models show greater sensitivity of ACC transport to enhanced Southern Ocean winds than the rectangular models, due to a topographically constrained free mode mechanism not present in the idealized rectangular models. The pathways of motion, shaped by bathymetry, thus control sensitivity of the circulation to external forcing.

The models used in this thesis, both coarse and eddy-permitting, have insufficient resolution to fully resolve mesoscale ocean eddies. A resolution of no larger than 0.1° is required to resolve mesoscale eddies at midlatitudes. This may have an important impact on the dynamical response of the Southern Ocean, where eddy dynamics play a primary role in the setting the isopycnal slope and hence the thermal gradient across the Southern Ocean. It therefore remains an important area of future research to investigate the asymmetry of ocean warming at higher resolution than was possible in this thesis. Nevertheless, we expect our findings of enhanced boundary current heat transport in the eddy-permitting regime to be highly relevant to evolving climate models moving from coarse to finer resolution.

Recommendations for Future Research

1. An eddy-resolving ICCM with Atlantic bathymetry

Given the substantial changes found moving from coarse to eddy-permitting ocean resolution, a logical progression of this work would be to extend the Intermediate

Complexity Coupled Model (ICCM) configuration to the eddy-resolving regime, using 0.1° ocean resolution. The Atlantic bathymetry would need to be re-generated at the higher resolution, from either satellite-derived topography or an equivalent resolution ocean model, as in Snow et al. (2015). The parameters governing the vertical diffusion and sea ice albedo would need to be re-examined in an eddy-resolving version, since these settings had an important influence on the sea-ice distribution and ultimately the melting in response to greenhouse forcing.

A further consideration in developing a 0.1° ICCM is whether to include a seasonal cycle, which has an important influence on sea ice formation and melting. We decided not to use a seasonal cycle in our experiments, to keep the modelling framework more closely aligned with Farneti and Vallis (2009). Furthermore, the optical depth profile of the atmosphere, which is a proxy for water vapour radiation effects, was not designed to vary seasonally. These limitations could be overcome by using a full complexity atmosphere, which could still be implemented in the sector domain. Such an atmosphere would be more computationally expensive, but would still be far less expensive than the eddy-resolving ocean component of a global coupled model.

2. Interhemispheric Asymmetry of Warming in an Aquaplanet Model

Another means of removing the landmass asymmetry is to remove all land from the model, except for some strategically placed coastlines to create an asymmetric ocean circulation. In the ICCM used here, the ocean domain could simply be extended to a 120° sector, although this would roughly double the computational expense of the model at 0.25° or 0.1° resolution. Alternatively, the ocean and atmosphere could be extended to a global domain with either no land or very idealized continents. This kind of aquaplanet framework was previously used by Enderton and Marshall (2009) to explore equilibrium solutions, but one could also apply warming perturbations

within such a model. One advantage of using an aquaplanet framework is that the SAT is more closely determined by SST throughout the domain. This closer correspondence may give rise to greater feedbacks in the atmosphere response to asymmetric SST warming patterns, especially in the thermal wind balance and its associated westerly winds.

3. Interhemispheric Asymmetry of Warming in a High Resolution Ocean-Only Model

Although our work exclusively used coupled models, the ocean's asymmetric warming pattern could also be examined within an ocean-only model with a uniform surface heat flux perturbation as in Marshall et al. (2014, 2015). They used a 1° ocean model, however our results suggest that if this work were extended to incorporate horizontal resolutions at, say, 0.25° or 0.1° there may be other important differences in the warming asymmetry. Modelling groups are heavily investing resources into developing eddy-resolving coupled climate models (e.g. Kirtman et al., 2012; Griffies et al., 2015), however there remain large overheads in coupling a high resolution ocean to a high resolution atmosphere. Imposing a uniform heat flux within a high-resolution ocean-only model is an efficient means of testing how an eddy-resolving coupled climate model might produce its own SST warming patterns.

Appendix A
Ice-atmosphere feedbacks dominate the response of the climate system to Drake Passage closure

This appendix contains a reformatted version of the manuscript:

England, M. H., **D. K. Hutchinson**, A. Santoso and W. P. Sijp, 2015. Ice-atmosphere feedbacks dominate the response of the climate system to Drake Passage closure. *Journal of Climate*, submitted.

My contributions to this paper total approximately 35%. I configured and ran all transient experiments. The lead author designed the analyses and wrote the first draft of the paper. I generated figures A.1 to A.9 and calculated all metrics used in the paper. I also contributed significantly to iterations of the text and analyses. The third author contributed via the model control experiment and generated figure A.10. The fourth author contributed via the paleoclimate interpretations and paleoclimate literature. Only the lead author and myself were involved in writing the manuscript.

Abstract

The response of the global climate system to Drake Passage (DP) closure is examined using a fully coupled ocean-atmosphere-ice model. Unlike most previous studies, a full three-dimensional atmospheric general circulation model is included with a complete hydrological cycle and a freely evolving wind field, as well as a coupled dynamic-thermodynamic sea-ice module. Upon DP closure the initial response is found to be consistent with previous ocean-only and intermediate complexity climate model studies, with an expansion and invigoration of the Antarctic meridional overturning, along with a slowdown in North Atlantic Deep Water (NADW) production. This results in a dominance of Southern Ocean poleward geostrophic flow and Antarctic sinking when DP is closed. However, within just a decade of DP closure, the increased southward heat transport has melted back a substantial fraction of Antarctic sea-ice. At the same time the polar oceans warm by 4-6 °C on the zonal mean, and the maximum strength of the Southern Hemisphere westerlies weaken by $\simeq$10%. These effects, not captured in models without ice and atmosphere feedbacks, combine to force Antarctic Bottom Water (AABW) to warm and freshen, to the point that this water mass becomes less dense than NADW. This leads to a marked contraction of the Antarctic overturning, allowing NADW to ventilate the abyssal ocean once more. Poleward heat transport settles back to very similar values as seen in the unperturbed DP open case. Yet remarkably, the equilibrium climate in the closed DP configuration retains a strong Southern Hemisphere warming, similar to past studies with no dynamic atmosphere. However, here it is ocean-atmosphere-ice feedbacks, primarily the ice-albedo feedback and partly the weakened mid-latitude jet, not a vigorous southern sinking, that maintain the warm polar oceans. This demonstrates that DP closure can drive a hemisphere-scale warming with polar amplification, without the presence of any vigorous Southern Hemisphere overturning circulation. Indeed DP closure leads to warming that is sufficient over the West Antarctic Ice Sheet region to inhibit ice sheet growth. This highlights the impor-

tance of the DP gap, Antarctic sea-ice and the associated ice-albedo feedback in maintaining the present-day glacial state over Antarctica.

A.1 Introduction

The land-mass geometry around Antarctica has varied substantially over the past 100 million years, with a Southern Ocean gateway only established about 30 Myr ago (Barker and Burrell, 1977; Stickley et al., 2004) once both modern-day Australia and South America broke away from Antarctica. It is still debated to what extent the establishment of a circumpolar Southern Ocean influences global climate. While model (Toggweiler and Bjornsson, 2000; Sijp et al., 2009, and references therein) and paleoclimate (e.g. Kennett, 1977) evidence suggests that the opening of a Southern Ocean gateway could have contributed to the glaciation of Antarctica, other work argues for a weaker effect (Livermore et al., 2005; Huber and Nof, 2006). Fundamental ocean physics dictates that when the Southern Ocean gateway is open, no net meridional geostrophic flow can cross the Drake Passage gap (Toggweiler and Samuels, 1995). This constraint can yield significant differences in the ocean thermohaline circulation in model experiments wherein the same basic configuration is run with, and without, a Drake Passage gap. An open gap also enables the establishment of an Antarctic Circumpolar Current (ACC), which can lead to thermal isolation of Antarctica. Most studies have hitherto focused on the meridional overturning circulation and ACC response to changes in a Southern Ocean gateway. Here we will show how important ice-albedo feedbacks can dominate the climate response to the establishment of a Southern Ocean gateway.

The pioneering paper of Gill and Bryan (1971) was the first to demonstrate the fundamental role of the Drake Passage (DP) gap in controlling global ocean circulation. Beyond the obvious non-existence of a circumpolar current, Gill and Bryan (1971) showed that closure of the DP gap, and therefore the provision of a

western boundary, also enables net meridional geostrophic flow across the Southern Ocean, something that is impossible in today's climate with the absence of zonal land boundaries. In Gill and Bryan (1971) the resultant overturning circulation without a DP gap becomes dominated by a vast Southern sinking cell, characterized by enhanced poleward heat transport to the south, warmed upper ocean temperatures around Antarctica, and greatly enhanced production rates of the model equivalent of Antarctic Bottom Water (AABW). While Gill and Bryan (1971) performed their experiments within a simplified Southern Hemisphere sector model, excluding interactions with the Northern Hemisphere, similar results are obtained when global ocean models are used (e.g. Cox, 1989; England, 1993; Toggweiler and Samuels, 1995). These global models further suggest a suppression of North Atlantic Deep Water (NADW) due to the vigor and northward penetration of the strong Southern sinking cell when DP is closed.

In addition to the above, several other studies have explored the ocean circulation response to opening and closing the Drake Passage, and most have incorporated either ocean-only models (e.g. England, 1993; Toggweiler and Samuels, 1995) or ocean models coupled to simplified atmospheric models (e.g. Nong et al., 2000; Toggweiler and Bjornsson, 2000; Sijp and England, 2004; Sijp et al., 2009). In all of these past studies the mechanism invoked to explain the climate response to DP opening is focused on the meridional overturning circulation, and specifically the dominance of a vigorous global-scale Southern Ocean cell when DP is closed, transporting a large amount of heat poleward; versus the present-day configuration of a circumpolar flow that isolates Antarctica, inhibiting meridional geostrophic flow across the DP gap. This difference in the MOC yields a substantially colder Antarctica when the DP is open compared to when DP is closed. Yet these studies employ models wherein either no or only limited atmospheric feedbacks and hydrological cycle are resolved, and so questions remain as to the applicability of these results to the real world. Here we will undertake coupled climate experiments aimed at investigating the role of the Southern Ocean gateway in global climate, in isolation of

other factors such as orbital cycles and atmospheric CO_2, but importantly including a full dynamic atmosphere coupled to ocean-sea-ice and land surface models.

There have been only a few studies of the DP effect undertaken using a coupled climate model. For example Part 1 examines the role of the Drake Passage in generating the well-known interhemispheric warming asymmetry found in response to increasing greenhouse forcing. They attribute part of this asymmetry to the thermal isolation of Antarctica facilitated by the ACC. However when models are configured using solar, land-mass, and CO_2 values typical of the Eocene-Oligocene era, the ACC is not necessarily established immediately upon opening a southern gateway (Lefebvre et al., 2012; Hill et al., 2013). Furthermore, the precise model configuration of the Drake Passage geometry adopted for the Eocene-Oligocene boundary in the Cenozoic can influence the results (e.g. Zhang et al., 2010). A more recent study is that of Yang et al. (2014) which examines the role of Panama seaway on the DP effect. They found that with an open Panama seaway which was inferred prior to 14 million years ago, the DP effect was found to be more dramatic. Our focus here however is not on a paleoclimatic reconstruction of the events that took place upon gateway opening across the Eocene-Oligocene boundary. As in Part 1, our interest is in the climate dynamics, feedbacks, and processes that define the role of the DP gap in the modern-day climate system, as this might have implications for future patterns of global warming. For this reason we do not configure the model for any paleoclimate simulations; instead adopting a modern-day configuration. Whilst prior studies tend to primarily focus on the equilibrium response, here we closely examine the transient evolution of key climatic features to provide more insights on the associated dynamics of the DP effect.

Past work exploring the Drake Passage effect in the modern-day climate system has identified both the lack of an ACC and changes in the meridional overturning circulation as key drivers of Antarctic warming when DP is closed. In this study, employing a full-coupled climate model, we will show that despite an initial invig-

oration of a global-scale Southern Ocean cell when DP is closed, with AABW production reaching almost 50 Sv, this rapidly decays back to typical modern-day (DP open) values. In fact our two model simulations in coupled mode, one with and one without a DP gap, yield remarkably similar poleward heat transport fields at most southern latitudes. Yet the climate response when DP is closed is characterized by a much warmer SH climate; this turns out to be largely the result of an ice-albedo amplifying feedback wherein reduced Antarctic sea-ice enables a warmer upper ocean, which inhibits ice regrowth. We further show that a DP closed geometry leads to a reduction in the subpolar westerly winds over the Southern Ocean, further enabling a warm polar ocean to persist despite minimal change in the Antarctic meridional overturning circulation.

A.2 Climate Model and Experimental Design

This study employs the Commonwealth Scientific and Industrial Research Organisation Mark-3L (CSIRO Mk3L) coupled climate model, comprising fully interactive ocean, atmosphere, land-surface and sea-ice sub-models (Phipps et al., 2011, 2013). The version used here is that of Santoso et al. (2012) which includes an improved representation of the geometry in the Indonesian seaway. The model was designed specifically for millennial-scale climate simulations and has been shown to simulate various aspects of the climate system with a good degree of fidelity (e.g. Santoso et al., 2011, 2012). Of particular relevance to this study is the model's ability to capture a correct representation of Antarctic sea-ice coverage, extent, and seasonality. In this regard, average maximum September sea-ice extent in the model (18.0×10^6 km^2) fits well within the observed range during 1979–2006 ($17.5 - 18.9 \times 10^6$ km^2, Cavalieri and Parkinson, 2008). Furthermore, in both model and observations, very little of this sea-ice is multi-year, with only on average 3.0×10^6 km^2 remaining during summer, again well within the range of $2.5 - 3.8 \times 10^6$ km^2 found in observations (Cavalieri and Parkinson, 2008).

The atmospheric model is of resolution 5.6° longitude × 3.2° latitude, with 18 vertical levels. It resolves full annual and diurnal cycles, and includes a cumulus convection scheme based on the UK Meteorological Office scheme (Gregory and Rowntree, 1990) coupled to the prognostic cloud scheme of Rotstayn (2000). The sea-ice model includes dynamics and thermodynamics as described in O'Farrell (1998). The land surface model is an enhanced version of the soil-canopy scheme of Kowalczyk et al. (1994) with static vegetation and land surface properties.

The ocean model code is the GFDL Modular Ocean Model, with a resolution of 2.8° longitude × 1.6° latitude and 21 geopotential levels, increasing in thickness with depth. The vertical diffusivity varies as the inverse of the Brunt-Väisälä frequency, with a minimum value set at 3×10^{-5} m^2 s^{-1}, except in the top 80 m where this value is increased to between 1.5×10^{-4} and 2×10^{-3} m^2 s^{-1} to simulate the effects of mixing by surface winds. Convective mixing is parameterized by increasing the diffusivity to 100 m^2 s^{-1} whenever static instability arises. The model implements the scheme of Gent and McWilliams (1990, hereafter GM) and Gent et al. (1995) for transport of tracers by mesoscale eddies. The eddy diffusivity is set to 600 m^2 s^{-1} in the deep ocean, but is reduced towards zero in the upper layers as required by continuity. The above diffusivity values are within the range of observed estimates (e.g. Cisewski et al., 2005). The model parameters above are chosen to achieve an optimum simulation of the global climate and to minimize numerical instabilities across model experiments. The coupled model is forced with an atmospheric CO_2 concentration fixed at the pre-industrial level of 280 ppm. No flux adjustment has been applied in this study.

While the ocean model resolution for millennial-scale simulations is insufficient to resolve eddies, inclusion of the GM eddy-induced advection scheme approximates the eddy heat transport response when the ACC is established in a Drake Passage open configuration. This occurs in response to the adjustment of isopycnal surfaces upon establishment of the ACC, with GM mixing transporting heat poleward

via isopycnal layer thickness diffusion. This parameterizes the poleward transport of heat due to eddies in the presence of a mid-latitude jet like the ACC. Hence, while eddies are not explicitly resolved by the model, their impact on poleward heat transport is parameterized to capture the richer eddy fluxes present in a DP open configuration compared to when the DP is closed.

Two main simulations are investigated in this study. The first experiment uses a standard modern-day land-mass configuration (DP_{open}), and the second includes the addition of a land bridge to close the Drake Passage gateway (DP_{clsd}). In all other ways the two experiment configurations are identical - our focus here is thus on the role of a Southern Ocean gateway in the modern day climate. In terms of model spin-up and equilibration, a DP_{open} configuration was initially integrated 1500-years under pre-industrial atmospheric CO_2 concentrations of 280 ppm. Using this equilibrated climate state as the initial conditions, the two different simulations were then integrated a further 2000 years. Thus both the DP_{clsd} and DP_{open} experiments employ the same initial conditions, with the added benefit that we can track the transient response of the climate system to Drake Passage closure in the DP_{clsd} experiment. The mean state comparisons shown in this study are taken from the end of the respective 2000 year integrations, although it is noted that all fields in the DP_{open} experiment are largely identical at the end of this 2000 year integration when compared to the initial conditions.

In the results presented here, the DP open case will be taken to be the control experiment, with the DP closed climate investigated as a transient response initialized from the open DP case. Previous coupled climate studies examining an open and closed DP configuration have focused on the equilibrated steady-state climates. Here, both the transient response to a closure of the Drake Passage and the final steady-state DP closed climate will be described in relation to their difference from the modern-day DP open geometry. As noted above the goal of these experiments is not an attempt to reconstruct past paleoclimatic conditions from the Eocene era

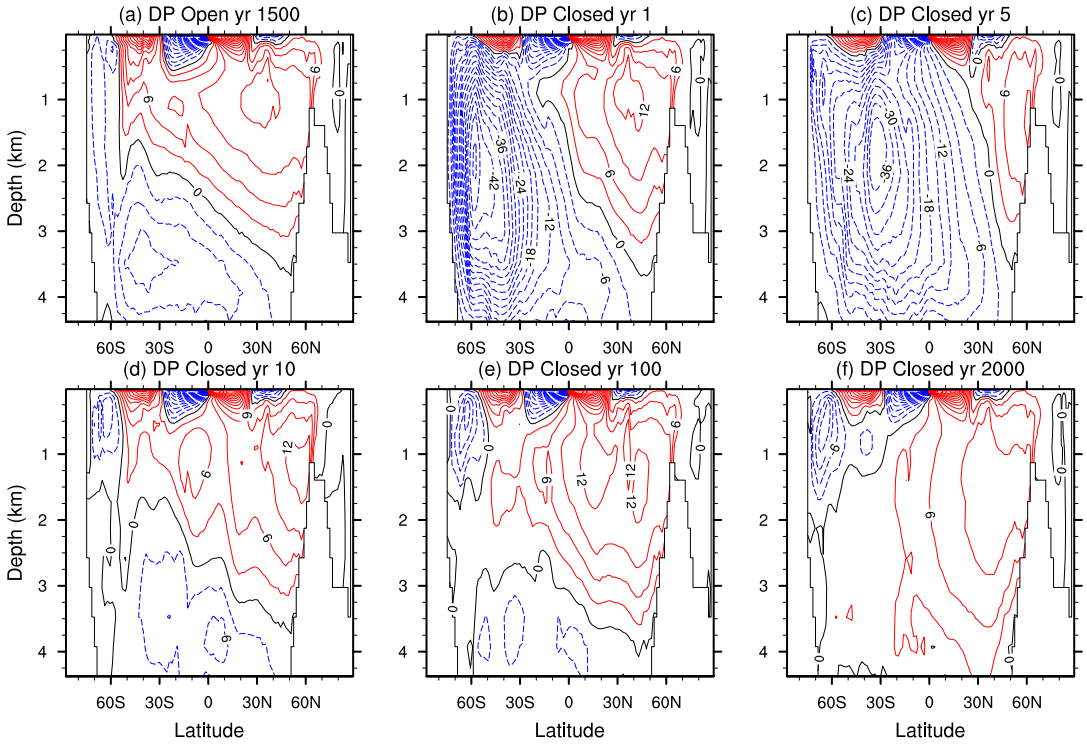

Figure A.1: Global ocean meridional overturning circulation (MOC, Sv) in (a) DP_{open} (equilibrated at Year 1500) and in the DP_{clsd} experiments in (b) Year 1 (c) Year 5 (d) Year 10 and (e) Year 100. Also shown is (f) the equilibrated DP_{clsd} MOC in Year 2000. In all plots, MOC is shown as the annual average apart from the equilibrated panels (a), (f) where a decade-long mean is shown. Contour interval is 3 Sv ($1\ Sv = 10^6\ m^3\ s^{-1}$), red contours denote positive values (clockwise circulation), blue contours denote negative values (anticlockwise circulation), and black is the zero contour.

with closed DP and Tasman seaways and different greenhouse gas concentrations and orbital parameters. Rather, we aim to examine the climate processes controlling Southern Hemisphere climate in each configuration, to gain insight into the dynamics regulating Antarctic and Southern Ocean climate in relation to the DP throughflow.

A.3 Results

A.3.1 Meridional Overturning Circulation

The meridional overturning circulation (MOC) in DP_{open} and in the transient response to closing DP is summarized in Figs. A.1 and A.2. A standard pre-industrial MOC is simulated in the DP_{open} experiment, with 14.8 Sv NADW overturning, 5.9 Sv of AABW production, and an abyssal cell of strength 12.3 Sv (Fig. A.1a). Within a year of closing DP, however, a vigorous interhemispheric Southern Ocean overturning cell has been established (Figs. A.1b, A.2), peaking at 46.1 Sv and characterized by intense bottom water production and global ventilation of the abyssal oceans from the south. This pattern is typical of that seen in previous model studies using simplified atmospheres and/or ocean-only models to investigate the climate response to DP closure. Within a decade this southern cell has largely suppressed NADW formation, with the Southern Ocean abyssal waters upwelling throughout the world's oceans, and the North Atlantic cell contracting to a weakened overturning confined within the Atlantic basin (Fig. A.1c). However, even at this stage the Southern cell has weakened in amplitude, with the sinking adjacent to Antarctica a small fraction of its peak strength at Year 1. By Year 50 the Southern Ocean overturning cell has weakened from its peak of 46.1 Sv down to 10.1 Sv, shoaling to just 1000-m depth, and NADW production has recovered to its DP_{open} value of 14.8 Sv, once again exiting into the Southern Ocean (Fig. A.1d). From around year 100 until full equilibration, NADW overturning persists at a strength of 9-17 Sv with a mean of 12.5 Sv, eventually ventilating the global oceans at all depths below 1500-m, while the Southern cell becomes confined to the upper near-Antarctic region (Fig. A.1f). Thus in marked contrast to previous ocean-only and ICCM studies, no interhemispheric abyssal cell of Southern Ocean origin is captured in the equilibrated DP_{clsd} experiment. Instead, the atmosphere-ocean-ice system has adjusted to closing DP in such a way to yield substantially warmer and lighter surface waters

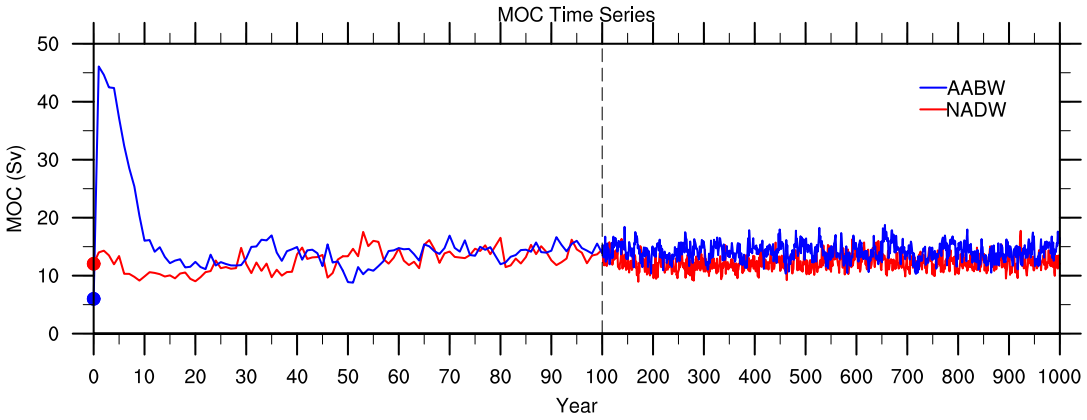

Figure A.2: Meridional overturning circulation (Sv) time series of the maximum overturning rate in the North Atlantic Deep Water (NADW) and Antarctic Bottom Water (AABW) cells, respectively. Note the two time-axis intervals differ between Years 0-100 and Years 100-1000.

around Antarctica.

While the time-series of MOC strength reveals that southern Antarctic overturning remains on average higher than NADW production throughout much of the simulation (Fig. A.2), the AABW metric is tracking a shallow confined cell that no longer reaches the abyssal oceans by the time of equilibration (Fig. A.1f). In contrast NADW ventilates the deep and abyssal layers in the equilibrated DP_{clsd} experiments. This is again in marked contrast to previous ocean-only and ICCM studies.

A.3.2 Deep Water-Masses

To investigate this further an analysis of the transient response in high-latitude water-mass properties is summarized in Figs. A.3 and A.4. Fig. A.3 shows the evolution of volume-weighted average $T - S$ values in Antarctic and North Atlantic waters in the regions of deep and bottom water mass formation, sampled at the 1000-2000 m depth range to directly evaluate the interhemispheric difference in deep water properties. Fig. A.4 shows latitude-depth zonal mean sections of temperature, salinity and potential density differences between the two experiments (DP_{clsd} minus DP_{open}) at years 10, 100, and 2000. Initially, with DP open, Antarctic

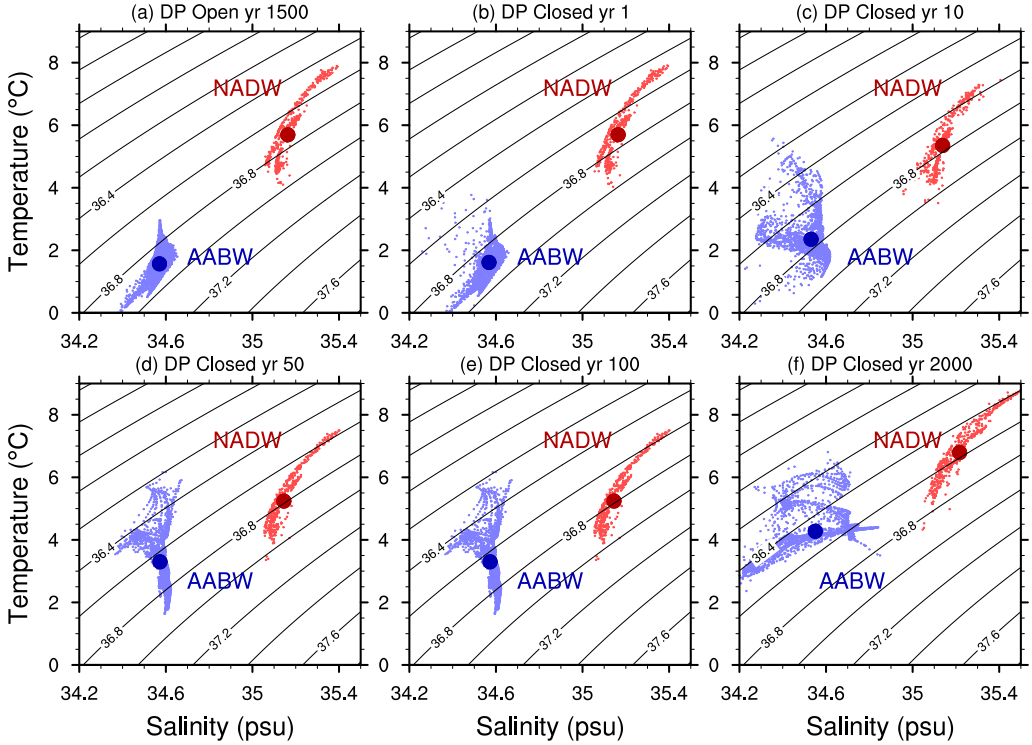

Figure A.3: Volume-weighted average and scatterplot of individual interior temperature-salinity ($T - S$) values for the NADW and AABW regions for Year 1500 of experiment $\mathrm{DP}_{\mathrm{open}}$ (i.e. the $\mathrm{DP}_{\mathrm{clsd}}$ initial conditions) and in $\mathrm{DP}_{\mathrm{clsd}}$ during years 1, 10, 50, 100, and 2000. The $\mathrm{DP}_{\mathrm{clsd}}$ $T - S$ values are in equilibrium by Year 2000. The $T - S$ values are shown for the respective source water regions at 1000-2000 m depth in the Antarctic south of 60°S and in the North Atlantic between 45°N and 60°N. BLUE = Antarctic and RED = North Atlantic waters. Individual values are shown as small dots and the volume-weighted mean as large dots. Overlaid are contours of constant density referenced to 2000-m depth (σ_2; in kg m^{-3}).

deep waters are much colder, fresher, and denser than their North Atlantic counterparts (Fig. A.3a). The higher density of Antarctic surface waters when DP is initially closed is the reason that a vigorous full depth overturning cell develops in the south, dominating the global ocean circulation (Fig. A.1b,c). This can occur in $\mathrm{DP}_{\mathrm{clsd}}$ (and not $\mathrm{DP}_{\mathrm{open}}$) because the land bridge across the DP gap allows meridional geostrophic flow to traverse the Southern Ocean poleward. Once DP is closed, however, the Antarctic surface waters begin to warm and to a lesser extent freshen (Fig. A.4, left hand panels) in response to increased poleward heat transport and ice melt, gradually becoming less dense as the model integration proceeds (Figs. A.3 and A.4). Eventually, the Antarctic upper and deep waters become less dense than the corresponding waters in the North Atlantic, triggering a contraction in the

vigorous Southern Ocean meridional cell. Yet despite the contraction in this cell, and the abatement in the poleward heat transport anomalies first seen when DP is closed, Antarctic surface waters remain substantially warmer in DP_{clsd} compared to DP_{open} (Fig. A.4, top panels). We will see that this is linked to a near absence of Antarctic sea-ice in the DP_{clsd} experiment, leading to a reduction in the ice-albedo over the region, and much warmer SST around the polar Southern Ocean in the closed DP experiment. The mid-latitude jet also weakens in response to the ice-free Antarctic waters, leading to further surface warming and freshening in the ocean as both northward Ekman transport and evaporative fluxes weaken (Sen Gupta and England, 2006; Thompson et al., 2011). While a warming response in Southern Ocean SST to DP closure is similar to previous ocean-only and intermediate complexity climate models, the mechanism obtained here is entirely different; relying on ice-albedo and wind feedback processes as will be further described below.

A.3.3 Poleward Heat Transport

The poleward heat transport response to closing Drake Passage closely reflects changes in the MOC; namely, a rapid invigoration of the transport of heat southward when the Antarctic overturning cell is at full strength, peaking at 2.4 PW in the first decade, followed by a multi-decadal recovery toward values more typical of the unperturbed DP_{open} experiment (Fig. A.5). At peak change in Year 4, the heat transport across the Southern Ocean at around 60°S has increased more than four-fold – from 0.35 PW (DP_{open}) to 1.50 PW (DP_{clsd}). The southward heat transport in the subtropics is also profoundly altered by DP closure; increasing from 0.7 PW (DP_{open}) to 2.3 PW (DP_{clsd}) at 30°S by Year 10 (Fig. A.5a). Yet as the simulation progresses, the meridional heat transport rapidly returns toward the initial conditions of DP_{open}. By the time of equilibration, the poleward heat transport is almost identical between the two DP experiments at almost all latitudes (Fig. A.5a), apart from changes in the latitude band of the ACC, where DP_{clsd} heat transport remains

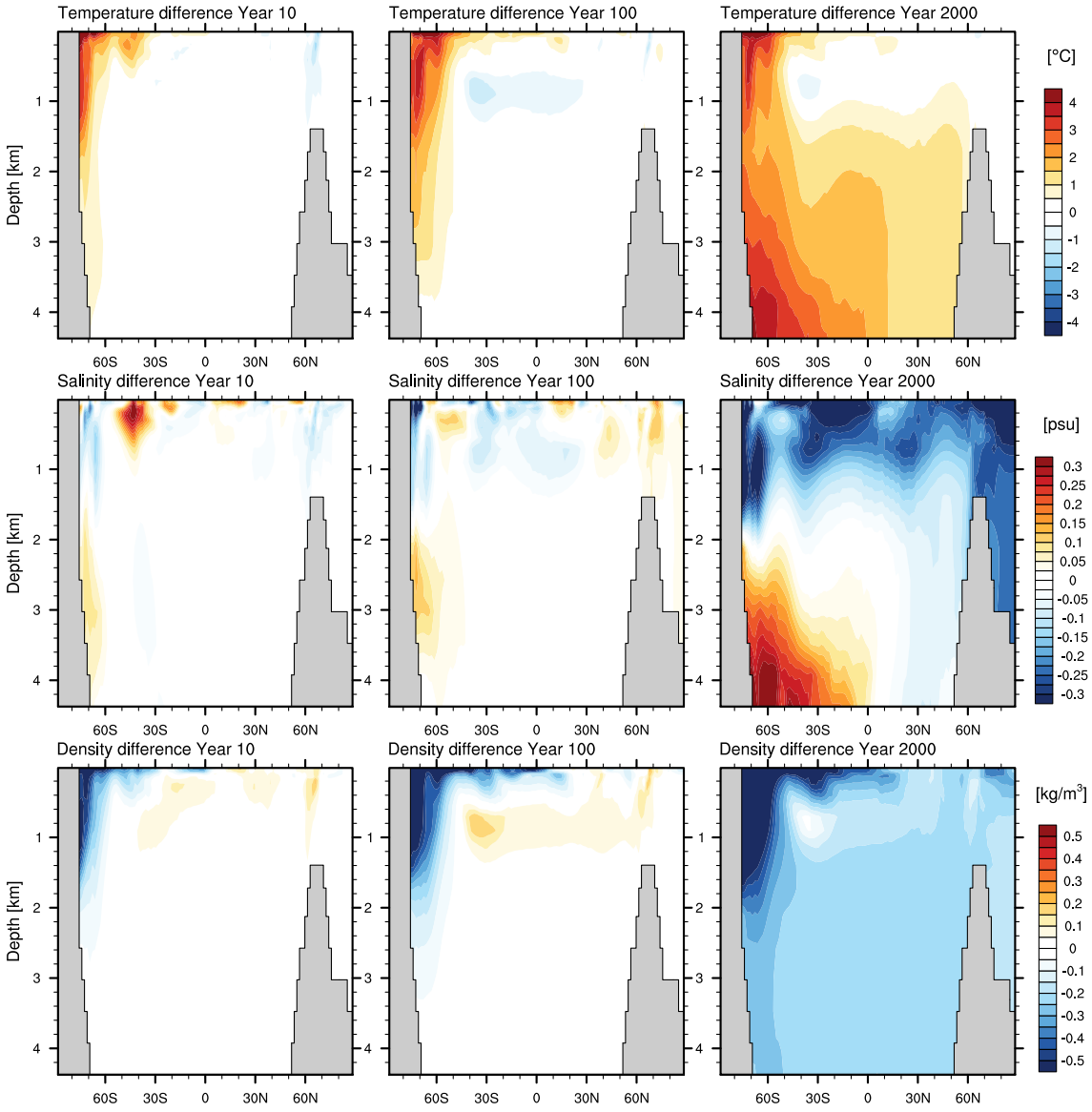

Figure A.4: Latitude-depth global zonal mean differences in temperature, salinity and potential density between the two experiments (DP_{clsd} minus DP_{open}) at years 10, 100, and 2000.

higher than in DP_{open} by around 0.25 PW. This modest increase in heat transport across the Southern Ocean is consistent with the suppressed ACC and the weakened atmospheric mid-latitude jet in DP_{clsd} (see Section 3A.3.5), which act in concert to enable more subtropical heat to reach the Antarctic margin via increased poleward geostrophic flow and reduced northward Ekman transport, respectively. In contrast at all other latitudes there is virtually no difference in the poleward heat transport between the two experiments.

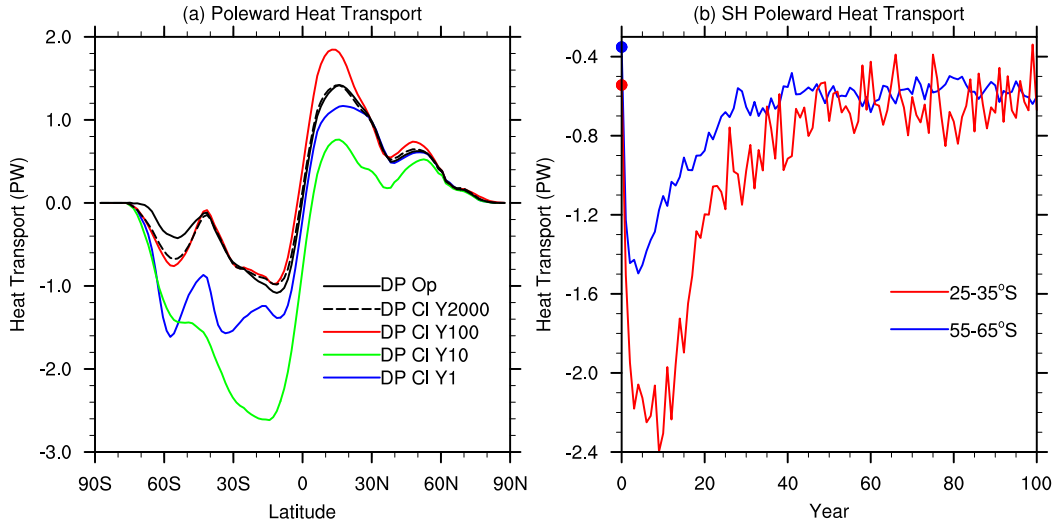

Figure A.5: (a) Poleward heat transport in PW (1 PW = 10^{15} Watts) in DP_{open} (equilibrated, Year 1500) and in DP_{clsd} in Years 1, 10, 100, and also equilibrated (Year 2000). (b) Time-series of poleward heat transport averaged across the latitude bands $25-35°S$ and $55-65°S$ for model years 0 - 100 in DP_{clsd}, with initial conditions highlighted (DP_{open}). Quasi-steady states persist in PHT after Year 100.

A.3.4 Antarctic Sea-Ice

The massive initial change in poleward heat transport upon closing Drake Passage has a significant impact on the Antarctic sea-ice distribution. Snapshots of the maximum Antarctic sea-ice extent along with a time-series of area-integrated net Antarctic sea-ice volume reveal a rapid melting of Southern Hemisphere sea-ice within the first decade of DP closure (Fig. A.6). Unlike the meridional overturning and poleward heat transport, however, which largely recover to DP_{open} values within a century, the sea-ice never recovers from the climatic disruption caused by DP closure. In particular, in DP_{clsd}, Antarctic sea-ice is almost entirely absent in summertime, and has only very limited coverage in winter: just some 2×10^6 km^2 when DP is closed compared to 18×10^6 km^2 when DP is open (the Antarctic continent, for comparative purposes, is $\simeq 14 \times 10^6$ km^2 in area). Thus the wintertime sea-ice extent in DP_{clsd} is around 30% less than the summertime sea-ice extent in DP_{open}. This remarkable difference in sea-ice between the experiments has a profound impact on the ice albedo effect around Antarctica, and in turn on hemisphere and global-scale climate, as described further below.

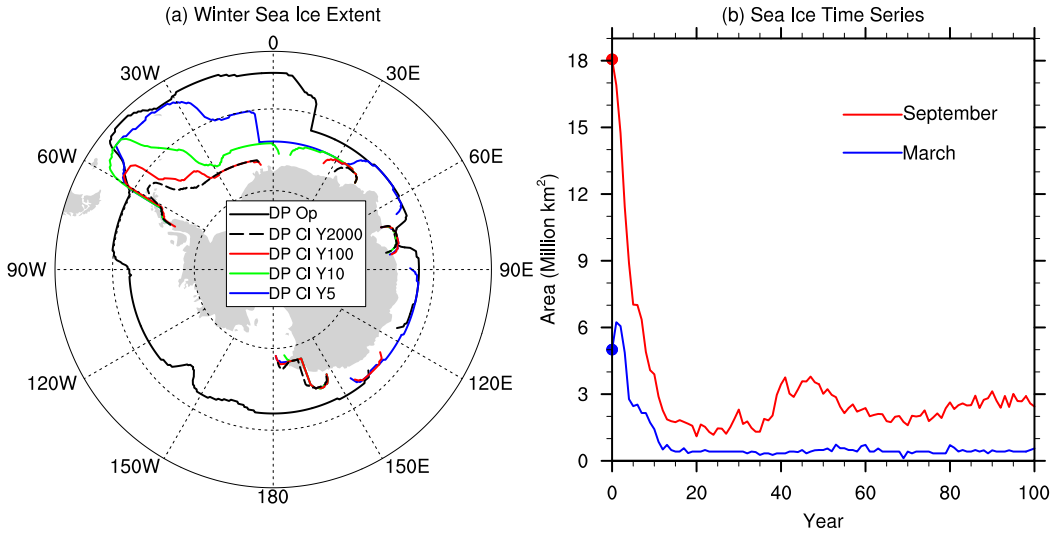

Figure A.6: (a) Wintertime Antarctic sea-ice extent in DP_{open} (equilibrated) and in DP_{clsd} in Years 5, 10, 100, and also equilibrated (Year 2000). Wintertime Antarctic sea-ice extent is defined as where the concentration first reaches a fraction of 0.15. (d) Time-series of net March and September Antarctic sea-ice extent ($\times 10^6$ km^2) in Years 0-100, defined as the total area of sea-ice with concentration greater than 0.15. Quasi-steady states persist in total sea-ice extent after Year 100.

The rapidity of sea-ice decline in the coupled model in response to DP closure is easy to understand when considering that, as in observations, very little of the total Antarctic sea-ice coverage in DP_{open} comprises multi-year ice: specifically only 3.0×10^6 km^2 of the wintertime maximum of 18.0×10^6 km^2 persists from one year to the next. This enables a rapid response of sea-ice to the sudden warming generated by enhanced poleward heat transport when DP is closed.

A.3.5 Equilibrium Climate Response

Here we describe the final climatic state attained when DP is closed compared to DP_{open}. Fig. A.7 shows the annual-mean surface air temperature differences between the equilibrium climates of DP_{clsd} and DP_{open}. The differences are calculated between the 10-year averaged climate states attained at the end of the respective model experiments. Overlaid in green contours is the wintertime maximum sea-ice extent in DP_{clsd} and DP_{open}. In response to DP closure the Southern Hemisphere climate warms considerably, particularly in regions where considerable sea-ice melt has

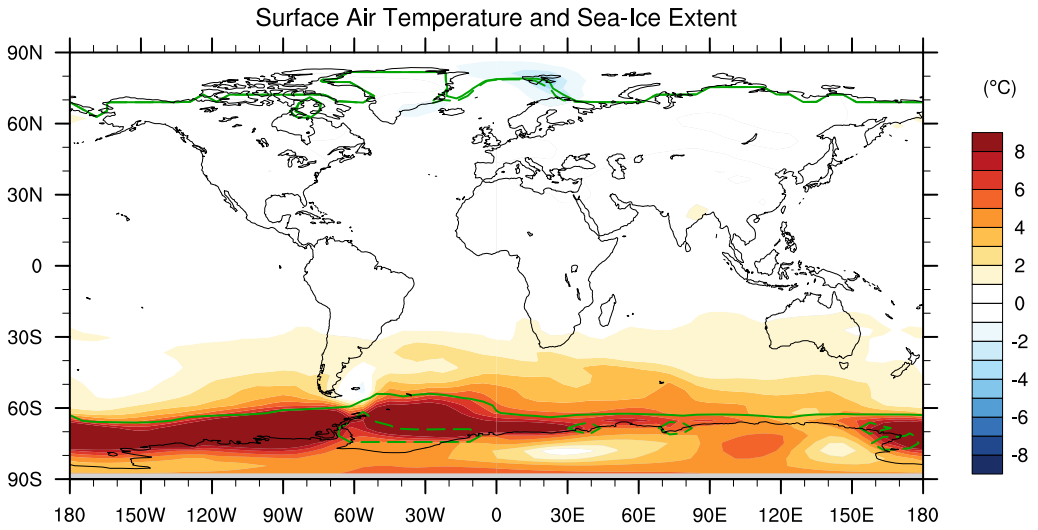

Figure A.7: Difference in annual-mean surface air temperature (°C) between the steady state climates of DP_{clsd} minus DP_{open}. Contours of the sea-ice extent in DP_{clsd} (dashed) and DP_{open} (solid) are overlaid in green.

occurred. For example, zonally averaged between 60-70°S, the mean SAT anomaly reaches 7.1°C in the annual average, as high as 9.1°C in the cold season (September), and 5.6°C in March. The higher wintertime warming is a result of the much greater differences in sea-ice coverage in the cold season compared to the warm season (Fig. A.6b, A.7) when sea-ice coverage is already low in both experiments. This occurs because of the massive seasonal retreat of Antarctic sea-ice during summer in the present-day climate, so that both experiments have relatively limited sea-ice coverage during the warm season.

Changes in oceanic sea surface temperatures (Fig. A.8a) reflect the changes seen in surface air temperatures, with significant warming across much of the Southern Ocean. Surface salinity, in contrast, shows regions of both freshening and increased salinity (Fig. A.8b), which reflects changes in circulation, sea-ice melt, and rates of evaporation minus precipitation (E-P). Overall, precipitation increases around the Antarctic coastline apart from in the Amundsen-Bellingshausen sector (not shown), and decreases just north of this latitude band. These changes translate to non-uniform salinity differences of the same overall pattern. The barotropic streamfunction in experiment DP_{clsd} is overlaid for reference in Fig. A.8b, revealing a marked intensification and equatorward expansion of the Weddell Gyre (54 Sv and reaching

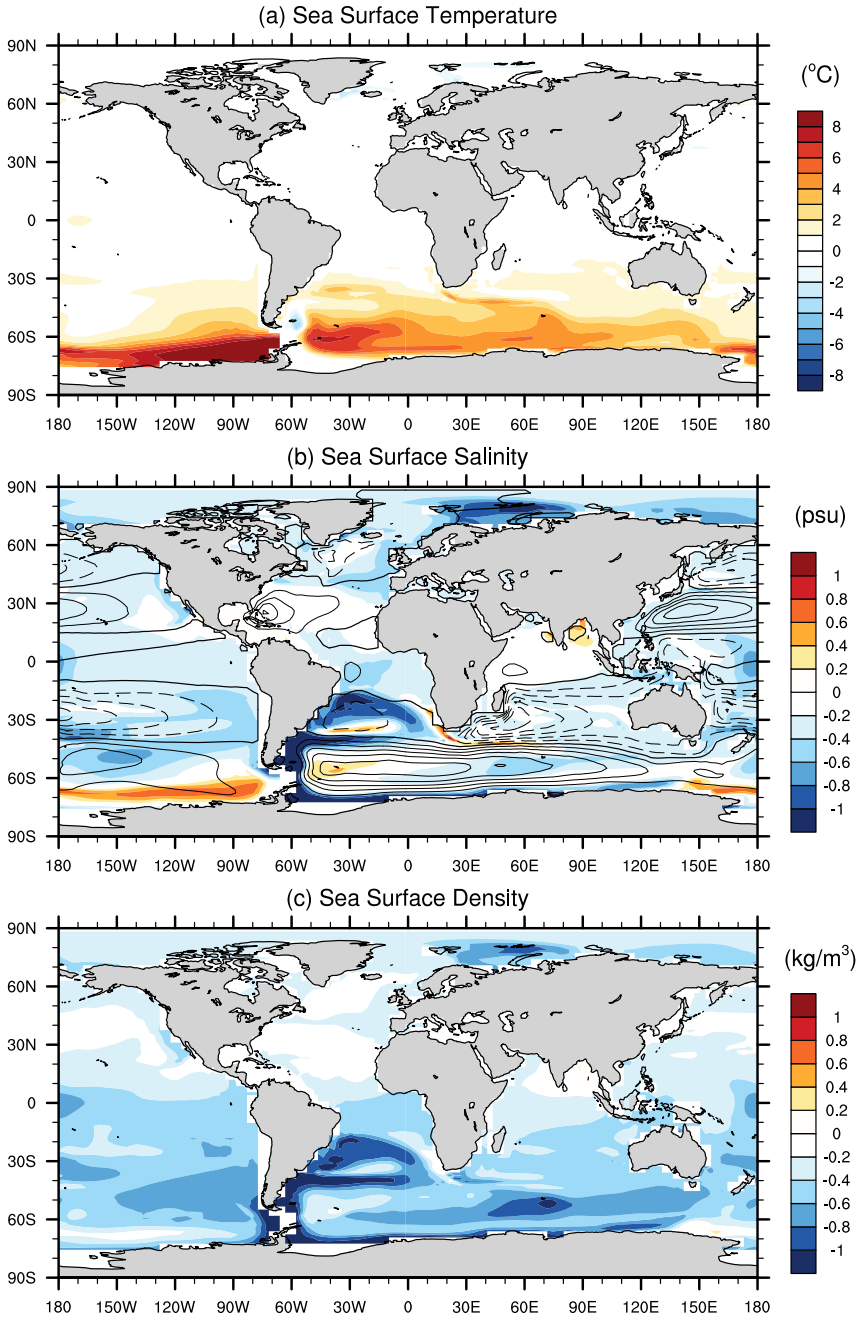

Figure A.8: Differences in annual-mean surface ocean properties between the steady state climates of DP_{clsd} minus DP_{open}: (a) sea surface temperature (°C), (b) sea surface salinity, and (c) sea surface density (kg m^{-3}). In (b), the horizontal transport streamfunction is overlaid from the DP_{clsd} experiment (contour interval is 10 Sv, 1 Sv = 10^6 m^3 s^{-1}); with flow direction counter-clockwise for dashed contours and clockwise for solid contours.

to approximately 39°S in DP_{clsd} compared to 33 Sv and only reaching north to 49°S in DP_{open}). These circulation changes further decrease salinity in the South Atlantic sector as the Weddell Gyre transports fresh polar waters northward in the DP closed configuration.

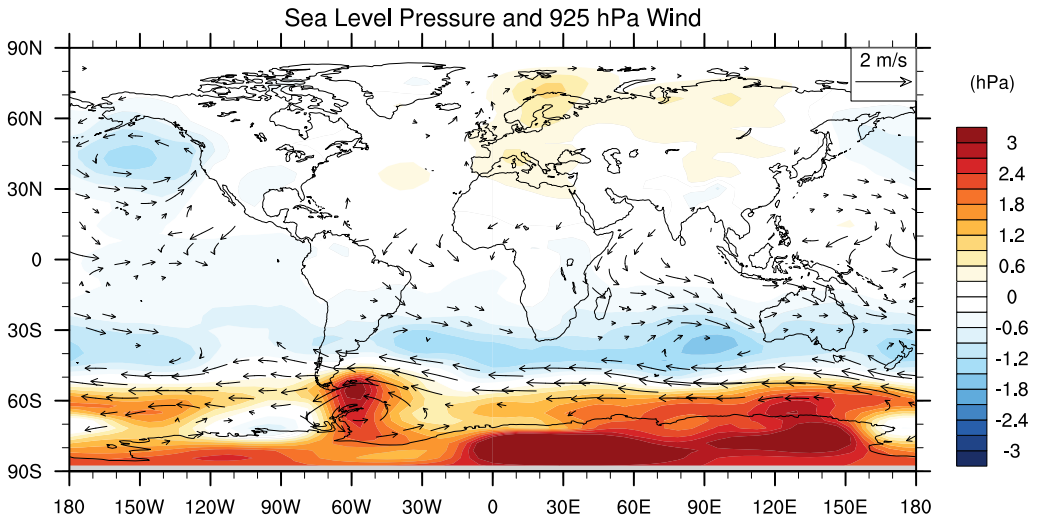

Figure A.9: Difference in sea level pressure (hPa) and 925 hPa wind vectors between the steady state climates of DP_{clsd} minus DP_{open}. Wind vector differences of magnitude 0.2 m/s or less are not shown, revealing the weakening of the westerly winds over the Southern Ocean in DP_{clsd}.

Sea surface density decreases almost everywhere in the Southern Ocean in response to DP closure (Fig. A.8c). This demonstrates that despite some isolated regions of increased surface salinity (Fig. A.8b), warming in these regions dominates salinity changes in relation to the net surface buoyancy response to DP closure. This increase in surface buoyancy across much of the Southern Ocean explains the marked contraction in the vigorous southern sinking cell first triggered by DP closure.

Significant atmospheric circulation changes can also be seen when comparing experiment DP_{clsd} to DP_{open}, particularly over the southern mid-latitudes. Fig. A.9 shows the 925 hPa wind and atmospheric sea-level pressure (SLP) differences between the experiments, revealing that the mid-latitude jet is substantially weaker in experiment DP_{clsd}. This is related to a significant negative trend in the Southern Annular Mode, with higher SLP over much of Antarctica and over the oceans poleward of 60°S, and a band of decreased SLP centered near 30°S (Fig. A.9). These SLP changes are a result of the reduced meridional temperature gradient across the latitudes of the jet, with warming strongest at high southern latitudes when DP is closed. This results in a $\simeq$10% reduction in the maximum zonal mean strength of the mid-latitude westerly winds. At other latitudes of the westerlies the weakening

can be even stronger, up to 25% zonal mean slowdown for example at around 53°S. The weaker westerlies drive a reduction in equatorward Ekman transport of cold, fresh Subantarctic surface waters, leading to further warming at these latitudes, and in some regions, higher salinities. The weakened mid-latitude jet is also associated with reduced storminess and cloud cover (not shown), leading to further surface ocean warming. In this way, both sea-ice albedo effects as well as atmospheric feedbacks lead to a substantial warming of the Southern Ocean in response to closure of the Drake Passage.

A.4 Discussion and conclusions

We have shown that the global climate response to Drake Passage closure can yield a significant Southern Hemisphere warming without requiring a corresponding invigoration of the Antarctic overturning circulation and poleward transport of heat across the DP gap. This is in marked contrast to previous studies using ocean-only and intermediate complexity climate models. Furthermore, this heating is achieved without any change in atmospheric greenhouse gas concentrations or planetary orbital parameters. Rather, the Southern Hemisphere warming comes about apparently due to a melt-back in Antarctic sea-ice when DP is closed, and the associated reduced surface albedo over the region. In addition, a weakened mid-latitude jet results from the reduced meridional temperature gradient across the Southern Ocean, which leads to further warming of Subantarctic surface waters. These processes combine to leave annual average Southern Hemisphere air temperatures around $5-8$°C higher around the Antarctic margin.

The warming around Antarctica when DP is closed is particularly significant over the West Antarctic Ice Sheet (WAIS) region (Fig. A.7). Comparing the location of the wintertime contours of 0°C surface air temperature reveals a marked contraction of sub-freezing air around the continent in $\mathrm{DP}_{\mathrm{clsd}}$ (Fig. A.10). While

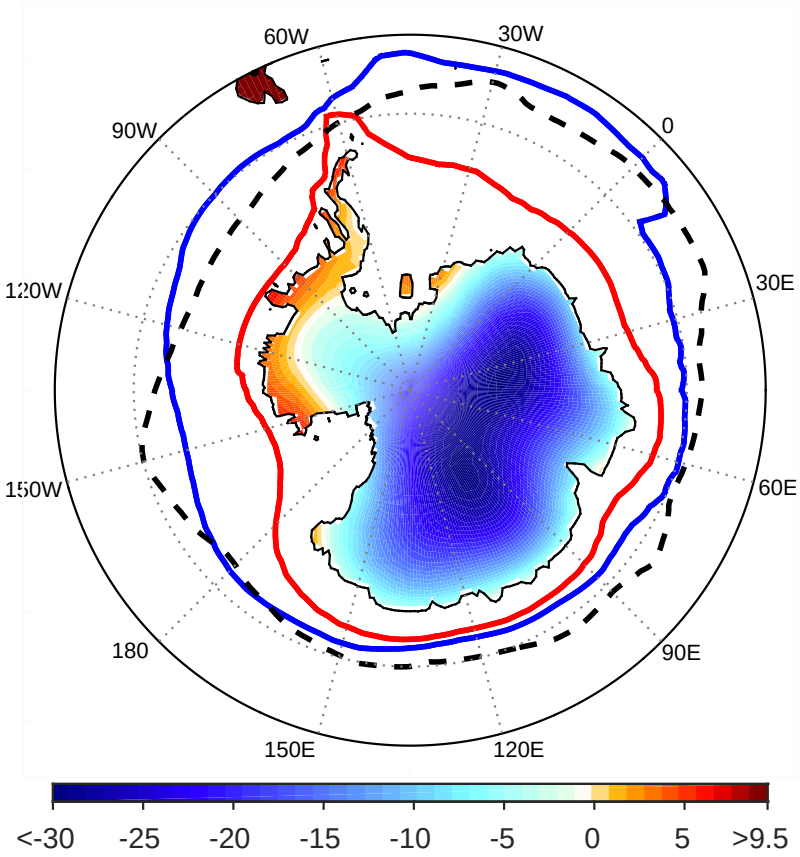

Figure A.10: Summertime (January) surface air temperature in DP_{clsd} shown as colour shading; temperatures above freezing point ($> 0°C$) are indicated in shades of orange and red. Overlaid is the location of the wintertime (July average) contours of 0°C surface air temperature in DP_{clsd} (red), DP_{open} (blue), and observed (black dashed). Observations are taken from the 20th Century Reanalysis Version 2, averaged over 1959-2012.

the winter season might dominate the amount of precipitation falling as snow, the long-term build up of ice sheets requires retention of accumulated snow and ice over summer. Summertime air temperatures are thus critical for determining whether an ice cap can build up over Antarctica. Colour shading in Fig. A.10 reveals that over the Antarctic Peninsula and WAIS regions in DP_{clsd}, there are large areas where summertime surface air temperature is $1 - 3°C$ above freezing point, potentially too warm to retain any ice build up over summer. In contrast in DP_{open} these regions remain sub-freezing throughout summer. In addition, oceanic temperatures adjacent to the WAIS are substantially colder, by up to 8°C, in DP_{open} compared to DP_{clsd} (Fig. A.8a); meaning that a DP open configuration is far more likely to accommodate ice shelves and a marine-grounded ice sheet in this region compared

to DP closed. The SST and SAT response to DP opening thus has potential implications for Cenozoic cooling of Antarctica, and the growth of land-ice and ice shelves during this time. In particular, opening of DP may have contributed to glacier formation and the build-up of a marine-grounded ice sheet during the Oligocene-Eocene boundary, particularly over the Antarctic Peninsula and WAIS regions.

While the steady-state global climate incorporating a closed Southern Ocean gateway largely owes its warmth to the ice-albedo feedback and the associated reduced midlatitude jet, the transient adjustment upon closing DP is rather different. Closing the Drake Passage initially leads to a dramatic expansion and strengthening of the Antarctic Bottom Water cell and a rapid contraction of the North Atlantic thermohaline circulation, consistent with previous ocean-only and intermediate complexity climate models. Then, within a decade of DP closure, the increased southward heat transport by the Antarctic cell has all but melted away Antarctic sea-ice. This forces near-Antarctic $T - S$ values to both warm and freshen, becoming less dense than North Atlantic Deep Water. This leads to a collapse of the Southern Ocean cell, and a return to an ocean state characterized by a confined Antarctic overturning cell and a NADW formation rate typical of the present-day climate. Poleward heat transport becomes very similar between the equilibrated DP open and DP closed cases, yet remarkably, the climate retains a strong Southern Hemisphere warming. As above, in steady state it is primarily ice-albedo and atmospheric feedbacks, not a vigorous southern sinking cell, that keep the polar oceans warm. Ultimately, DP closure can drive a hemisphere-scale warming with polar amplification, without the presence of any vigorous Southern Hemisphere overturning circulation. This suggests that the present-day glacial climate over Antarctica could be facilitated as much by the presence of sea-ice around the polar continent as it is by the thermal isolation provided by the Antarctic Circumpolar Current. This could have ramifications for global warming; namely, if Antarctic sea-ice melts significantly, ice-albedo feedbacks could drive further atmospheric warming, with peak amplitude in the region of the Antarctic ice shelves and where the Antarctic

ice sheets feed into the Southern Ocean.

Bibliography

Barker, P. F. and J. Burrell, 1977: The opening of Drake Passage. *Mar. Geol.*, **25**, 15–34, doi:10.1016/0025-3227(77)90045-7.

Barnes, E. A. and L. Polvani, 2013: Response of the midlatitude jets, and of their variability, to increased greenhouse gases in the CMIP5 models. *J. Climate*, **26**, 7117–7135, doi:10.1175/JCLI-D-12-00536.1.

Blunden, J. and D. S. Arndt, 2014: State of the climate in 2013. *Bull. Amer. Meteor. Soc.*, **95**, S1–S279, doi:10.1175/2014BAMSStateoftheClimate.1.

Böning, C. W., A. Dispert, M. Visbeck, S. R. Rintoul, and F. U. Schwarzkopf, 2008: The response of the Antarctic Circumpolar Current to recent climate change. *Nature Geosci.*, **1**, 864–869, doi:10.1038/ngeo362.

Bonjean, F. and G. S. E. Lagerloef, 2002: Diagnostic Model and Analysis of the Surface Currents in the Tropical Pacific Ocean. *J. Phys. Oceanogr.*, **32**, 2938–2954, doi:10.1175/1520-0485(2002)032<2938:DMAAOT>2.0.CO;2.

Bracegirdle, T. J., E. Shuckburgh, J.-B. Sallee, Z. Wang, A. J. S. Meijers, N. Bruneau, T. Phillips, and L. J. Wilcox, 2013: Assessment of surface winds over the Atlantic, Indian, and Pacific Ocean sectors of the Southern Ocean in CMIP5 models: historical bias, forcing response, and state dependence. *J. Geophys. Res. Atmos.*, **118**, 547–562, doi:10.1002/jgrd.50153.

Bryan, F. O., P. R. Gent, and R. Tomas, 2014: Can Southern Ocean eddy effects be parameterized in climate models? *J. Climate*, **27**, 411–425, doi:10.1175/JCLI-D-12-00759.1.

Bryan, K. and L. J. Lewis, 1979: A water mass model of the World Ocean. *J. Geophys. Res.*, **84**, 2503–2517, doi:10.1029/JC084iC05p02503.

Bryan, K., S. Manabe, and M. J. Spelman, 1988: Interhemispheric Asymmetry in the Transient Response of a Coupled Ocean-Atmosphere Model to a CO2 Forcing. *J. Phys. Oceanogr.*, **18**, 851–867, doi:10.1175/1520-0485(1988)018<0851:IAITTR>2.0.CO;2.

Butler, A. H., D. W. J. Thompson, and R. Heikes, 2010: The steady-state atmospheric circulation response to climate change-like thermal forcings in a simple general circulation model. *J. Climate*, **23**, 3474–3496, doi:10.1175/2010JCLI3228.1.

Byrne, M. P. and P. A. O'Gorman, 2013: Land-Ocean Warming Contrast over a Wide Range of Climates: Convective Quasi-Equilibrium Theory and Idealized Simulations. *J. Climate*, **26**, 4000–4016, doi:10.1175/JCLI-D-12-00262.1.

Cavalieri, D. J. and C. L. Parkinson, 2008: Antarctic sea ice variability and trends, 19792006. *J. Geophys. Res.*, **113**, C07 004, doi:10.1029/2007JC004564.

Cisewski, B., V. H. Strass, and H. Prandke, 2005: Upper-ocean vertical mixing in the Antarctic Polar Front Zone. *Deep Sea Res. II*, **52**, 1087–1108, doi:10.1016/j.dsr2.2005.01.010.

Collins, M., et al., 2013: Long-term climate change: projections, commitments and irreversibility. *Climate Change 2013: The Physical Science Basis. Contribution of Working Group I to the Fifth Assessment Report of the Intergovernmental Panel on Climate Change*, 1029–1136.

Cox, M. D., 1989: An Idealized Model of the World Ocean. Part I: The Global-Scale Water Masses. *J. Phys. Oceanogr.*, **19**, 1730–1752, doi:10.1175/1520-0485(1989)019<1730:AIMOTW>2.0.CO;2.

Delworth, T. L. and F. Zeng, 2008: Simulated impact of altered Southern Hemisphere winds on the Atlantic Meridional Overturning Circulation. *Geophys. Res. Lett.*, **35**, L20 708, doi:10.1029/2008GL035166.

Delworth, T. L., et al., 2012: Simulated climate and climate change in the GFDL CM2.5 high-resolution coupled climate model. *J. Climate*, **25**, 2755–2781, doi:10.1175/JCLI-D-11-00316.1.

Downes, S. M. and A. M. Hogg, 2013: Southern Ocean Circulation and Eddy Compensation in CMIP5 Models. *J. Climate*, **26**, 7198–7220, doi:10.1175/JCLI-D-12-00504.1.

Drijfhout, S., G. J. van Oldenborgh, and A. Cimatoribus, 2012: Is a Decline of AMOC Causing the Warming Hole above the North Atlantic in Observed and Modeled Warming Patterns? *J. Climate*, **25**, 8373–8379, doi:10.1175/JCLI-D-12-00490.1.

Dufresne, J.-L., J. Quaas, O. Boucher, S. Denvil, and L. Fairhead, 2005: Contrasts in the effects on climate of anthropogenic sulfate aerosols between the 20th and the 21st century. *Geophys. Res. Lett.*, **32**, L21 703, doi:10.1029/2005GL023619.

Enderton, D. and J. Marshall, 2009: Explorations of Atmosphere-Ocean-Ice Climates on an Aquaplanet and Their Meridional Energy Transports. *J. Atmos. Sci.*, **66**, 1593–1611, doi:10.1175/2008JAS2680.1.

England, M. H., 1993: Representing the Global-Scale Water Masses in Ocean General Circulation Models. *J. Phys. Oceanogr.*, **23**, 1523–1552, doi:10.1175/1520-0485(1993)023<1523:RTGSWM>2.0.CO;2.

Farneti, R., T. L. Delworth, A. J. Rosati, S. M. Griffies, and F. Zeng, 2010: The role of mesoscale eddies in the rectification of the Southern Ocean response to climate change. *J. Phys. Oceanogr.*, **40**, 1539–1557, doi:10.1175/2010JPO4353.1.

Farneti, R. and P. R. Gent, 2011: The effects of the eddy-induced advection coefficient in a coarse-resolution coupled climate model. *Ocean Model.*, **39**, 135–145, doi:10.1016/j.ocemod.2011.02.005.

Farneti, R. and G. K. Vallis, 2009: An intermediate complexity climate model (ICCMp1) based on the GFDL flexible modelling system. *Geosci. Mod. Dev.*, **2**, 73–88, doi:10.5194/gmd-2-73-2009.

Farneti, R. and G. K. Vallis, 2011: Mechanisms of interdecadal climate variability and the role of ocean-atmosphere coupling. *Climate Dyn.*, **36**, 289–308, doi:10.1007/s00382-009-0674-9.

Flato, G. M. and G. J. Boer, 2001: Warming asymmetry in climate change simulations. *Geophys. Res. Lett.*, **28**, 195, doi:10.1029/2000GL012121.

Fox-Kemper, B., R. Ferrari, and R. Hallberg, 2008: Parameterization of Mixed Layer Eddies. Part I: Theory and Diagnosis. *J. Phys. Oceanogr.*, **38**, 1145–1165, doi:10.1175/2007JPO3792.1.

Friedman, A. R., Y.-T. Hwang, J. C. H. Chiang, and D. M. W. Frierson, 2013: Interhemispheric temperature asymmetry over the Twentieth Century and in future projections. *J. Climate*, **26**, 5419–5433, doi:10.1175/JCLI-D-12-00525.1.

Frierson, D. M. W., I. M. Held, and P. Zurita-Gotor, 2006: A gray-radiation aquaplanet moist GCM. Part I: Static stability and eddy scale. *J. Atmos. Sci.*, **63**, 2548–2566, doi:10.1175/JAS3753.1.

Fučkar, N. S., S.-P. Xie, R. Farneti, E. A. Maroon, and D. M. W. Frierson, 2013: Influence of the Extratropical Ocean Circulation on the Intertropical Convergence Zone in an Idealized Coupled General Circulation Model. *J. Climate*, **26**, 4612–4629, doi:10.1175/JCLI-D-12-00294.1.

Gent, P. R. and J. C. McWilliams, 1990: Isopycnal Mixing in Ocean Circulation Models. *J. Phys. Oceanogr.*, **20**, 150–155, doi:10.1175/1520-0485(1990)020<0150:IMIOCM>2.0.CO;2.

Gent, P. R., J. Willebrand, T. J. McDougall, and J. C. McWilliams, 1995: Parameterizing Eddy-Induced Tracer Transports in Ocean Circulation Models. *J. Phys. Oceanogr.*, **25**, 463–474, doi:10.1175/1520-0485(1995)025<0463:PEITTI>2.0.CO;2.

Gill, A. E. and K. Bryan, 1971: Effects of geometry on the circulation of a three-dimensional southern-hemisphere ocean model. *Deep Sea Res.*, **18**, 685–721, doi:10.1016/0011-7471(71)90086-6.

Gregory, D. and P. R. Rowntree, 1990: A Mass Flux Convection Scheme with Representation of Cloud Ensemble Characteristics and Stability-Dependent Closure. *Mon. Wea. Rev.*, **118**, 1483–1506, doi:10.1175/1520-0493(1990)118<1483:AMFCSW>2.0.CO;2.

Griffies, S. M., 1998: The Gent-McWilliams Skew Flux. *J. Phys. Oceanogr.*, **28**, 831–841, doi:10.1175/1520-0485(1998)028<0831:TGMSF>2.0.CO;2.

Griffies, S. M., 2012: *Elements of the Modular Ocean Model (MOM), GFDL Ocean Group Technical Report No. 7* . NOAA Geophysical Fluid Dynamics Laboratory, 618 pp.

Griffies, S. M. and R. W. Hallberg, 2000: Biharmonic Friction with a Smagorinsky-Like Viscosity for Use in Large-Scale Eddy-Permitting Ocean Models. *Mon. Weather Rev.*, **128**, 2935–2946, doi:10.1175/1520-0493(2000)128<2935:BFWASL>2.0.CO;2.

Griffies, S. M., et al., 2009: Coordinated Ocean-ice Reference Experiments (COREs). *Ocean Model.*, **26**, 1–46, doi:10.1016/j.ocemod.2008.08.007.

Griffies, S. M., et al., 2015: Impacts on Ocean Heat from Transient Mesoscale Eddies in a Hierarchy of Climate Models. *J. Climate*, **28**, 952–977, doi:10.1175/JCLI-D-14-00353.1.

Hallberg, R. and A. Gnanadesikan, 2006: The Role of Eddies in Determining the Structure and Response of the Wind-Driven Southern Hemisphere Overturning:

Results from the Modeling Eddies in the Southern Ocean (MESO) Project. *J. Phys. Oceanogr.*, **36**, 2232–2252, doi:10.1175/JPO2980.1.

Hill, D. J., A. M. Haywood, P. J. Valdes, J. E. Francis, D. J. Lunt, B. S. Wade, and V. C. Bowman, 2013: Paleogeographic controls on the onset of the Antarctic circumpolar current. *Geophys. Res. Lett.*, **40**, 5199–5204, doi:10.1002/grl.50941.

Hogg, A. M., 2010: An Antarctic Circumpolar Current driven by surface buoyancy forcing. *Geophys. Res. Lett.*, **37**, L23 601, doi:10.1029/2010GL044777.

Hogg, A. M., M. P. Meredith, D. P. Chambers, E. P. Abrahamsen, C. W. Hughes, and A. K. Morrison, 2015: Recent trends in the Southern Ocean eddy field. *J. Geophys. Res. Oc.*, **120**, 257–267, doi:10.1002/2014JC010470.

Hogg, A. M. and D. R. Munday, 2014: Does the sensitivity of Southern Ocean circulation depend upon bathymetric details? *Phil. Trans. R. Soc. A*, **372**, 20130 050, doi:10.1098/rsta.2013.0050.

Huber, M. and D. Nof, 2006: The ocean circulation in the southern hemisphere and its climatic impacts in the Eocene. *Palaeogeogr. Palaeoclimatol. Palaeoecol.*, **231**, 9–28, doi:10.1016/j.palaeo.2005.07.037.

Hughes, C. W., M. P. Meredith, and K. J. Heywood, 1999: Wind-Driven Transport Fluctuations through Drake Passage: A Southern Mode. *J. Phys. Oceanogr.*, **29**, 1971–1992, doi:10.1175/1520-0485(1999)029<1971:WDTFTD>2.0.CO;2.

Hurrell, J. W., J. J. Hack, D. Shea, J. M. Caron, and J. Rosinski, 2008: A New Sea Surface Temperature and Sea Ice Boundary Dataset for the Community Atmosphere Model. *J. Climate*, **21**, 5145–5153, doi:10.1175/2008JCLI2292.1.

Jackett, D. R., T. J. McDougall, R. Feistel, D. G. Wright, and S. M. Griffies, 2006: Algorithms for Density, Potential Temperature, Conservative Temperature, and the Freezing Temperature of Seawater. *J. Atmos. Oceanic Technol.*, **23**, 1709–1728, doi:10.1175/JTECH1946.1.

Jones, D. C., T. Ito, and N. S. Lovenduski, 2011: The transient response of the Southern Ocean pycnocline to changing atmospheric winds. *Geophys. Res. Lett.*, **38**, 2–6, doi:10.1029/2011GL048145.

Kennett, J. P., 1977: Cenozoic Evolution of Antarctic Glaciation, the Circum-Antarctic Ocean, and Their Impact on Global Paleoceanography. *J. Geophys. Res.*, **82**, 3843–3860, doi:10.1029/JC082i027p03843.

Kidston, J. and E. P. Gerber, 2010: Intermodel variability of the poleward shift of the austral jet stream in the CMIP3 integrations linked to biases in 20th century climatology. *Geophys. Res. Lett.*, **37**, L09 708, doi:10.1029/2010GL042873.

Kirtman, B. P., et al., 2012: Impact of ocean model resolution on CCSM climate simulations. *Climate Dyn.*, **39**, 1303–1328, doi:10.1007/s00382-012-1500-3.

Kowalczyk, E. A., J. R. Garratt, and P. B. Krummel, 1994: *Implementation of a soil-canopy scheme into the CSIRO GCM – regional aspects of the model response*. Technical Report 32, CSIRO Division of Atmospheric Research, Victoria, Australia, 59 pp.

Langlais, C. E., S. R. Rintoul, and J. D. Zika, 2015: Sensitivity of Antarctic Circumpolar Current Transport and Eddy Activity to Wind Patterns in the Southern Ocean. *J. Phys. Oceanogr.*, **45**, 1051–1067, doi:10.1175/JPO-D-14-0053.1.

Large, W. G., J. C. McWilliams, and S. C. Doney, 1994: Oceanic vertical mixing: A review and a model with a nonlocal boundary layer parameterization. *Rev. Geophys.*, **32**, 363–403, doi:10.1029/94RG01872.

Lee, H.-C., A. Rosati, and M. J. Spelman, 2006: Barotropic tidal mixing effects in a coupled climate model: Oceanic conditions in the Northern Atlantic. *Ocean Model.*, **11**, 464–477, doi:10.1016/j.ocemod.2005.03.003.

Lee, S.-K., W. Park, E. van Sebille, M. O. Baringer, C. Wang, D. B. Enfield, S. G. Yeager, and B. P. Kirtman, 2011: What caused the significant increase in Atlantic

Ocean heat content since the mid-20th century? *Geophys. Res. Lett.*, **38**, L17 607, doi:10.1029/2011GL048856.

Lefebvre, V., Y. Donnadieu, P. Sepulchre, D. Swingedouw, and Z.-S. Zhang, 2012: Deciphering the role of southern gateways and carbon dioxide on the onset of the Antarctic Circumpolar Current. *Paleoceanography*, **27**, PA4201, doi: 10.1029/2012PA002345.

Levitus, S., et al., 2012: World ocean heat content and thermosteric sea level change (0–2000 m), 1955–2010. *Geophys. Res. Lett.*, **39**, L10 603, doi: 10.1029/2012GL051106.

Lévy, M., P. Klein, A.-M. Tréguier, D. Iovino, G. Madec, S. Masson, and K. Takahashi, 2010: Modifications of gyre circulation by sub-mesoscale physics. *Ocean Modell.*, **34**, 1 – 15, doi:10.1016/j.ocemod.2010.04.001.

Livermore, R., A. Nankivell, G. Eagles, and P. Morris, 2005: Paleogene opening of Drake Passage. *Earth and Planetary Science Letters*, **236**, 459–470, doi: 10.1016/j.epsl.2005.03.027.

Locarnini, R. A., A. V. Mishonov, J. I. Antonov, T. P. Boyer, H. E. Garcia, O. K. Baranova, M. M. Zweng, and D. R. Johnson, 2010: World Ocean Atlas 2009, Volume 1: Temperature. S. Levitus, Ed. NOAA Atlas NESDIS 68, U.S. Government Printing Office, Washington, D.C., 184 pp.

Locarnini, R. A., et al., 2013: World Ocean Atlas 2013, Volume 1: Temperature. S. Levitus, Ed., A. Mishonov technical editor, NOAA Atlas NESDIS 73.

Manabe, S., J. Ploshay, and N.-C. Lau, 2011: Seasonal Variation of Surface Temperature Change during the Last Several Decades. *J. Climate*, **24**, 3817–3821, doi:10.1175/JCLI-D-11-00129.1.

Manabe, S., R. J. Stouffer, M. J. Spelman, and K. Bryan, 1991: Transient Responses of a Coupled Ocean-Atmosphere Model to Gradual Changes of Atmospheric

CO2. Part I. Annual Mean Response. *J. Climate*, **4**, 785–818, doi:10.1175/1520-0442(1991)004<0785:TROACO>2.0.CO;2.

Marshall, J., K. C. Armour, J. R. Scott, Y. Kostov, U. Hausmann, D. Ferreira, T. G. Shepherd, and C. M. Bitz, 2014: The ocean's role in polar climate change: asymmetric Arctic and Antarctic responses to greenhouse gas and ozone forcing. *Phil. Trans. R. Soc. A*, **372**, 20130 040, doi:10.1098/rsta.2013.0040.

Marshall, J., J. R. Scott, K. C. Armour, J.-M. Campin, M. Kelley, and A. Romanou, 2015: The ocean's role in the transient response of climate to abrupt greenhouse gas forcing. *Climate Dyn.*, **44**, 2287–2299, doi:10.1007/s00382-014-2308-0.

Marzocchi, A., J. J.-M. Hirschi, N. P. Holliday, S. A. Cunningham, A. T. Blaker, and A. C. Coward, 2015: The North Atlantic subpolar circulation in an eddy-resolving global ocean model. *J. Marine Systems*, **142**, 126–143, doi:10.1016/j.jmarsys.2014.10.007.

Meehl, G., et al., 2007: *Global Climate Projections. In: Climate Change 2007: The Physical Science Basis. Contribution of Working Group I to the Fourth Assessment Report of the Intergovernmental Panel on Climate Change.* Cambridge University Press, 570 pp.

Meredith, M. and A. Hogg, 2006: Circumpolar response of Southern Ocean eddy activity to a change in the Southern Annular Mode. *Geophys. Res. Lett.*, **33**, L16 608, doi:10.1029/2006GL026499.

Meredith, M. P., et al., 2011: Sustained Monitoring Of The Southern Ocean At Drake Passage: Past Achievements And Future Priorities. *Rev. Geophys.*, **49**, RG4005, doi:10.1029/2010RG000348.

Morice, C. P., J. J. Kennedy, N. A. Rayner, and P. D. Jones, 2012: Quantifying uncertainties in global and regional temperature change using an ensemble of observational estimates: The HadCRUT4 data set. *J. Geophys. Res.*, **117**, D08 101, doi:10.1029/2011JD017187.

Morrison, A. K. and A. M. Hogg, 2013: On the relationship between Southern Ocean overturning and ACC transport. *J. Phys. Oceanogr.*, **43**, 140–148, doi: 10.1175/JPO-D-12-057.1.

Morrison, A. K., O. A. Saenko, A. M. Hogg, and P. Spence, 2013: The role of vertical eddy flux in Southern Ocean heat uptake. *Geophys. Res. Lett.*, **40**, 5445–5450, doi:10.1002/2013GL057706.

Munday, D. R., H. L. Johnson, and D. P. Marshall, 2013: Eddy saturation of equilibrated circumpolar currents. *J. Phys. Oceanogr.*, **43**, 507–532, doi:10.1175/JPO-D-12-095.1.

Myhre, G., et al., 2013: Anthropogenic and natural radiative forcing. *Climate Change 2013: The Physical Science Basis. Contribution of Working Group I to the Fifth Assessment Report of the Intergovernmental Panel on Climate Change*, 658–740.

Nakicenovic, N. and R. Swart, (Eds.) , 2000: *Special Report on Emissions Scenarios. A Special Report of Working Group III of the Intergovernmental Panel on Climate Change IPCC*. Cambridge University Press, 570 pp.

National Geophysical Data Center, 2006: 2-minute gridded global relief data (ETOPO2v2). U.S. Department of Commerce, National Oceanic and Atmospheric Administration, http://www.ngdc.noaa.gov/mgg/fliers/06mgg01.html.

Nong, G. T., R. G. Najjar, D. Seidov, and W. H. Peterson, 2000: Simulation of ocean temperature change due to the opening of Drake Passage. *Geophys. Res. Lett.*, **27**, 2689–2692, doi:10.1029/1999GL011072.

O'Farrell, S. P., 1998: Investigation of the dynamic sea ice component of a coupled atmosphere-sea ice general circulation model. *J. Geophys. Res.*, **103**, 15 751–15 782, doi:10.1029/98JC00815.

Phillips, A. S., C. Deser, and J. Fasullo, 2014: Evaluating Modes of Variability in Climate Models. *EOS*, **95**, 453–455, doi:10.1002/2014EO490002.

Phipps, S. J., 2010: *The CSIRO Mk3L climate system model v1.2*. Technical Report, Antarctic Climate and Ecosystems Cooperative Research Centre, Hobart, Tasmania, Australia, 121 pp.

Phipps, S. J., L. D. Rotstayn, H. B. Gordon, J. L. Roberts, A. C. Hirst, and W. F. Budd, 2011: The CSIRO Mk3L climate system model version 1.0 Part 1: Description and evaluation. *Geoscientific Model Development*, **4**, 483–509, doi: 10.5194/gmd-4-483-2011.

Phipps, S. J., et al., 2013: Paleoclimate Data-Model Comparison and the Role of Climate Forcings over the Past 1500 Years. *J. Climate*, **26**, 6915–6936, doi: 10.1175/JCLI-D-12-00108.1.

Pierrehumbert, R. T., 2010: *Principles of planetary climate*. Cambridge University Press, 688 pp.

Polvani, L. M. and P. J. Kushner, 2002: Tropospheric response to stratospheric perturbations in a relatively simple general circulation model. *Geophys. Res. Lett.*, **29**, 14–18, doi:10.1029/2001GL014284.

Rahmstorf, S. and M. H. England, 1997: Influence of Southern Hemisphere Winds on North Atlantic Deep Water Flow. *J. Phys. Oceanogr.*, **27**, 2040–2054, doi: 10.1175/1520-0485(1997)027<2040:IOSHWO>2.0.CO;2.

Risien, C. M. and D. B. Chelton, 2008: A global climatology of surface wind and wind stress fields from eight years of QuikSCAT scatterometer data. *J. Phys. Oceanogr.*, **38**, 2379–2413, doi:10.1175/2008JPO3881.1.

Rotstayn, L. D., 2000: On the "tuning" of autoconversion parameterizations in climate models. *J. Geophys. Res.*, **105**, 15 495–15 507, doi:10.1029/2000JD900129.

Santoso, A., W. Cai, M. H. England, and S. J. Phipps, 2011: The Role of the Indonesian Throughflow on ENSO Dynamics in a Coupled Climate Model. *J. Climate*, **24**, 585–601, doi:10.1175/2010JCLI3745.1.

Santoso, A., M. H. England, and W. Cai, 2012: Impact of Indo-Pacific Feedback Interactions on ENSO Dynamics Diagnosed Using Ensemble Climate Simulations. *J. Climate*, **25**, 7743–7763, doi:10.1175/JCLI-D-11-00287.1.

Sen Gupta, A. and M. H. England, 2006: Coupled Ocean–Atmosphere–Ice Response to Variations in the Southern Annular Mode. *J. Climate*, **19**, 4457–4486, doi:10.1175/JCLI3843.1.

Sen Gupta, A., A. Santoso, A. S. Taschetto, C. C. Ummenhofer, J. Trevena, and M. H. England, 2009: Projected Changes to the Southern Hemisphere Ocean and Sea Ice in the IPCC AR4 Climate Models. *J. Climate*, **22**, 3047–3078, doi:10.1175/2008JCLI2827.1.

Shakespeare, C. J. and A. M. Hogg, 2012: An analytical model of the response of the meridional overturning circulation to changes in wind and buoyancy forcing. *J. Phys. Oceanogr.*, **42**, 1270–1287, doi:10.1175/JPO-D-11-0198.1.

Sijp, W. P. and M. H. England, 2004: Effect of the Drake Passage Throughflow on Global Climate. *J. Phys. Oceanogr.*, **34**, 1254–1266, doi:10.1175/1520-0485(2004)034<1254:EOTDPT>2.0.CO;2.

Sijp, W. P., M. H. England, and J. R. Toggweiler, 2009: Effect of Ocean Gateway Changes under Greenhouse Warmth. *J. Climate*, **22**, 6639–6652, doi:10.1175/2009JCLI3003.1.

Simmons, H. L., S. R. Jayne, L. C. Laurent, and A. J. Weaver, 2004: Tidally driven mixing in a numerical model of the ocean general circulation. *Ocean Model.*, **6**, 245–263, doi:10.1016/S1463-5003(03)00011-8.

Simpkins, G. R., L. M. Ciasto, D. W. J. Thompson, and M. H. England, 2012: Seasonal Relationships between Large-Scale Climate Variability and Antarctic Sea Ice Concentration. *J. Climate*, **25**, 5451–5469, doi:10.1175/JCLI-D-11-00367.1.

Sinha, B., A. T. Blaker, J. J.-M. Hirschi, S. Bonham, M. Brand, S. Josey, R. S.

Smith, and J. Marotzke, 2012: Mountain ranges favour vigorous Atlantic meridional overturning. *Geophys. Res. Lett.*, **39**, L02 705, doi:10.1029/2011GL050485.

Snow, K., A. M. Hogg, S. M. Downes, B. M. Sloyan, M. L. Bates, and S. M. Griffies, 2015: Sensitivity of abyssal water masses to overflow parameterisations. *Ocean Model.*, **89**, 84–103, doi:10.1016/j.ocemod.2015.03.004.

Spence, J. P., M. Eby, and A. J. Weaver, 2008: The Sensitivity of the Atlantic Meridional Overturning Circulation to Freshwater Forcing at Eddy-Permitting Resolutions. *J. Climate*, **21**, 2697–2710, doi:10.1175/2007JCLI2103.1.

Spence, P., O. A. Saenko, W. Sijp, and M. H. England, 2012: The Role of Bottom Pressure Torques on the Interior Pathways of North Atlantic Deep Water. *J. Phys. Oceanogr.*, **42**, 110–125, doi:10.1175/2011JPO4584.1.

Spence, P., O. A. Saenko, W. Sijp, and M. H. England, 2013: North Atlantic climate response to Lake Agassiz drainage at coarse and ocean eddy-permitting resolutions. *J. Climate*, **26**, 2651–2667, doi:10.1175/JCLI-D-11-00683.1.

Stickley, C. E., et al., 2004: Timing and nature of the deepening of the Tasmanian Gateway. *Paleoceanography*, **19**, PA4027, doi:10.1029/2004PA001022.

Stouffer, R. J., S. Manabe, and K. Bryan, 1989: Interhemispheric asymmetry in climate response to a gradual increase of atmospheric CO2. *Nature*, **342**, 660–662.

Straub, D. N., 1993: On the transport and angular momentum balance of channel models of the Antarctic Circumpolar Current. *J. Phys. Oceanogr.*, **23**, 776–782, doi:10.1175/1520-0485(1993)023<0776:OTTAAM>2.0.CO;2.

Sutton, R. T., B. Dong, and J. M. Gregory, 2007: Land/sea warming ratio in response to climate change: IPCC AR4 model results and comparison with observations. *Geophys. Res. Lett.*, **34**, L02 701, doi:10.1029/2006GL028164.

Thompson, D. W. J., S. Solomon, P. J. Kushner, M. H. England, K. M. Grise, and D. J. Karoly, 2011: Signatures of the Antarctic ozone hole in Southern Hemisphere surface climate change. *Nature Geosci.*, **4**, 741–749, doi:10.1038/ngeo1296.

Toggweiler, J. R. and H. Bjornsson, 2000: Drake Passage and palaeoclimate. *J. Quat. Sci.*, **15**, 319–328, doi:10.1002/1099-1417(200005)15:4<319::AID-JQS545>3.0.CO;2-C.

Toggweiler, J. R. and B. Samuels, 1995: Effect of Drake Passage on the global thermohaline circulation. *Deep Sea Res. I*, **42**, 477–500, doi:10.1016/0967-0637(95)00012-U.

Toggweiler, J. R. and B. Samuels, 1998: On the Ocean's Large-Scale Circulation near the Limit of No Vertical Mixing. *J. Phys. Oceanogr.*, **28**, 1832–1852, doi:10.1175/1520-0485(1998)028<1832:OTOSLS>2.0.CO;2.

Treguier, A. M., J. Deshayes, C. Lique, R. Dussin, and J. M. Molines, 2012: Eddy contributions to the meridional transport of salt in the North Atlantic. *J. Geophys. Res. Oc.*, **117**, C05 010, doi:10.1029/2012JC007927.

Wang, M. and J. E. Overland, 2009: A sea ice free summer Arctic within 30 years? *Geophys. Res. Lett.*, **36**, 2–6, doi:10.1029/2009GL037820.

Wang, W.-C., X.-Z. Liang, M. Dudek, D. Pollard, and S. Thompson, 1995: Atmospheric ozone as a climate gas. *Atmos. Res.*, **37**, 247–256, doi:10.1016/0169-8095(94)00080-W.

Weaver, A. J. and E. S. Sarachik, 1990: On the importance of vertical resolution in certain ocean general circulation models. *J. Phys. Oceanogr.*, **20**, 600–609, doi:10.1175/1520-0485(1990)020<0600:OTIOVR>2.0.CO;2.

Wolfe, C. L. and P. Cessi, 2009: Overturning Circulation in an Eddy-Resolving Model: The Effect of the Pole-to-Pole Temperature Gradient. *J. Phys. Oceanogr.*, **39**, 125–142, doi:10.1175/2008JPO3991.1.

Wolfe, C. L. and P. Cessi, 2011: The Adiabatic Pole-to-Pole Overturning Circulation. *J. Phys. Oceanogr.*, **41**, 1795–1810, doi:10.1175/2011JPO4570.1.

Yang, S., E. Galbraith, and J. Palter, 2014: Coupled climate impacts of the Drake Passage and the Panama Seaway. *Climate Dyn.*, **43**, 37–52, doi:10.1007/s00382-013-1809-6.

Zhang, Y. and G. K. Vallis, 2013: Ocean heat uptake in eddying and non-eddying ocean circulation models in a warming climate. *J. Phys. Oceanogr.*, **43**, 2211–2229, doi:10.1175/JPO-D-12-078.1.

Zhang, Z.-S., Q. Yan, and H.-J. Wang, 2010: Has the Drake Passage Played an Essential Role in the Cenozoic Cooling? *Atmos. Oc. Sci. Lett.*, **3**, 288–292.

Zika, J. D., F. Laliberté, L. R. Mudryk, W. P. Sijp, and A. J. G. Nurser, 2015: Changes in ocean vertical heat transport with global warming. *Geophys. Res. Lett.*, **42**, 4940–4948, doi:10.1002/2015GL064156.

Zika, J. D., J. Le Sommer, C. O. Dufour, A. Naveira-Garabato, and A. Blaker, 2013a: Acceleration of the Antarctic Circumpolar Current by Wind Stress along the Coast of Antarctica. *J. Phys. Oceanogr.*, **43**, 2772–2784, doi:10.1175/JPO-D-13-091.1.

Zika, J. D., W. P. Sijp, and M. H. England, 2013b: Vertical Heat Transport by Ocean Circulation and the Role of Mechanical and Haline Forcing. *J. Phys. Oceanogr.*, **43**, 2095–2112, doi:10.1175/JPO-D-12-0179.1.

Appendix B
Published Articles

Copies of the following articles in their published formats are included hereafter.

Hutchinson, D. K., M. H. England, A. Santoso and A. McC. Hogg, 2013. Interhemispheric asymmetry in transient global warming: The role of Drake Passage. *Geophysical Research Letters*, **40**, 1587-1593, doi:10.1002/grl.50341

Hutchinson, D. K., M. H. England, A. McC. Hogg and K. Snow, 2015. Interhemispheric asymmetry of warming in an eddy permitting coupled sector model. *Journal of Climate*, **28**, 7385-7406. doi:10.1175/JCLI-D-15-0014.1

Interhemispheric asymmetry in transient global warming: The role of Drake Passage

David K. Hutchinson,[1,2] Matthew H. England,[1,2] Agus Santoso,[1,2] and Andrew McC. Hogg[2,3]

Received 1 January 2013; revised 7 March 2013; accepted 7 March 2013; published 29 April 2013.

[1] Climate models predict that the Northern Hemisphere (NH) will warm faster than the Southern Hemisphere (SH) in response to increasing greenhouse gases, and observations show that this trend has already begun to occur. This interhemispheric asymmetry has largely been attributed to land-ocean differences between the hemispheres and Arctic sea ice melt, while the role of ocean currents in setting this asymmetry is less well understood. This study isolates the impact of an open Southern Ocean gateway upon the interhemispheric asymmetry in transient global warming by forcing a fully coupled climate model with an increasing CO_2 scenario with and without a land bridge across Drake Passage (DP). It is found that over the transient warming period, the NH-SH surface warming asymmetry is reduced in the DP closed case, by approximately 41% for sea surface temperature and approximately 6% for surface air temperature. In the DP open case, sea ice extent is far greater in the SH than in the DP closed case, whereas the sea ice response to warming in the NH is insensitive to whether or not DP is closed. These results illustrate that part of the interhemispheric asymmetry in surface warming is due to the Antarctic Circumpolar Current (ACC) thermally isolating Antarctica. The ACC limits ocean heat transport across the DP latitudes and allows a much greater coverage of sea ice in the Southern Ocean than would be the case in the absence of a circumpolar ocean.
Citation: Hutchinson, D. K., M. H. England, A. Santoso, and A. M. Hogg (2013), Interhemispheric asymmetry in transient global warming: The role of Drake Passage, *Geophys. Res. Lett.*, *40*, 1587–1593, doi:10.1002/grl.50341.

1. Introduction

[2] Global climate models show a strong interhemispheric asymmetry in the transient response of surface air temperature (SAT) to CO_2, with the Northern Hemisphere (NH) warming considerably faster than the Southern Hemisphere (SH) [*Meehl et al*., 2007]. This result has been well established through several decades of climate modeling [e.g., *Bryan et al*., 1988; *Manabe et al*., 1991; *Flato and Boer*, 2001] and has been found to be largely attributed to the greater coverage of ocean in the SH, yielding a higher effective heat capacity of the SH compared to the NH. Higher evaporative cooling over the oceans implies that warming is more rapid over land, further enhancing the interhemispheric asymmetry independently of ocean circulation differences. Yet ocean circulation differs markedly across the hemispheres, with the land mass geometry enabling a circumpolar flow around Antarctica, which could impact the warming response to rising greenhouse gases. This study focuses on the role of an open Southern Ocean gateway in regulating the hemisphere-scale response to global warming in a coupled climate model.

[3] Observations of warming in recent decades have confirmed that this warming asymmetry has already begun to occur. The HADCRUT4 data set [*Morice et al.*, 2012] has shown a steady trend from 1980 onward exhibiting much faster warming in the NH compared to the SH. Furthermore, the spatial pattern of SAT warming in the last 2 decades is broadly consistent with earlier global climate model predictions [*Manabe et al.*, 2011]. Observations of ocean warming have also indicated greater warming of sea surface temperature (SST) in the NH compared to the SH, though the magnitude of asymmetry is somewhat less than that in the SAT [*Levitus et al*., 2012]. *Levitus et al*.'s [2012] data also indicate that the ocean heat uptake and its asymmetry toward greater NH warming are largest in the Atlantic Ocean. The Pacific and Indian Oceans make smaller contributions to the net interhemispheric asymmetry. *Lee et al.* [2011] used simulations of 20th century warming to show that the North Atlantic Ocean heat content increase is more dependent on remote heating of the global ocean than local heating of the Atlantic. This result suggests that advection of heat into the North Atlantic by ocean currents is playing a major role in setting the asymmetry of SST warming.

[4] A further cause of warming asymmetry is the difference in polar climates. Antarctic sea ice trends have been nonuniform in recent decades, with a decline west of the Antarctic Peninsula and growth over the Ross Sea region [*Simpkins et al.*, 2012]. By contrast, seasonal melting of Arctic sea ice appears to be accelerating [*Wang and Overland*, 2009], allowing a strong ice-albedo positive feedback that exacerbates the warming and thus the asymmetry between hemispheres. Sea ice can also alter the polar warming response by insulating the air from warmer ocean temperatures below the ice.

[5] There are several additional factors which may influence the interhemispheric asymmetry of global warming. Sulfate aerosols are expected to cool the NH more than the SH [*Dufresne et al.*, 2005] and therefore reduce the warming

All supporting information may be found in the online version of this article.

[1]Climate Change Research Center, University of New South Wales, Sydney, New South Wales, Australia.
[2]ARC Centre of Excellence for Climate Systems Science, Sydney, New South Wales, Australia.
[3]Research School of Earth Sciences, Australian National University, Canberra, Australian Capital Territory, Australia.

Corresponding author: D. K. Hutchinson, Climate Change Research Center, Level 4 Mathews Building, University of New South Wales, Sydney 2052, NSW, Australia. (david.hutchinson@unsw.edu.au)

0094-8276/13/10.1002/grl.50341

asymmetry. Ozone may also play a role in the asymmetry, as the anthropogenic ozone hole has caused a trend toward the high-index polarity of the Southern Annular Mode [*Thompson et al.*, 2011], contributing to cooling over high southern latitudes. In the present study, no aerosols are included, and ozone concentrations are prescribed from observations and fixed in time [*Wang et al.*, 1995]; thus, we focus on ocean heat transport and heat capacity effects on the asymmetry, and the specific role of the Drake Passage (DP) gap.

[6] The Antarctic Circumpolar Current (ACC) provides a further possible mechanism for slowing global warming at high southern latitudes. The vigorous re-entrant flow of the ACC prevents any net upper ocean meridional geostrophic flow across DP, causing Antarctica to be 3–4°C cooler than it would otherwise be if DP were closed [*Toggweiler and Bjornsson*, 2000; *Sijp and England*, 2004]. Although the impacts of the ACC upon the climate have been investigated previously in ocean-only models [*Cox*, 1989; *Toggweiler and Samuels*, 1995], in intermediate complexity climate models [*Sijp and England*, 2004; *Sijp et al.*, 2009], and in idealized continental geometries [*Enderton and Marshall*, 2009], the DP effect has not been explored in a coupled climate model with realistic continental geometry. Here we investigate the hypothesis that the ocean, and particularly the ACC, plays a major role in controlling the interhemispheric asymmetry during transient global warming. We compare climate simulations with an open and closed DP under transient warming to demonstrate the influence of the ACC on this interhemispheric asymmetry.

2. Climate Model and Experimental Design

[7] This study implements the Commonwealth Scientific and Industrial Research Organisation Mark version 3L climate model (CSIRO Mk3L) Earth system model, comprising fully interactive ocean, atmosphere, land, and sea ice submodels [*Phipps*, 2010]. CSIRO Mk3L is designed for millennial climate simulations with ocean model resolution of 1.6° latitude × 2.8° longitude × 21 levels, and atmospheric model resolution of 3.2° latitude × 5.6° longitude × 18 pressure levels. The version used in this study includes an updated configuration of the Indonesian Archipelago as implemented by *Santoso et al.* [2012].

[8] Two sets of six-member ensemble simulations were run. The first set uses the standard coastline configuration, and the second set includes an extra land bridge to close the Drake Passage (DP), referred to respectively as the DP_{open} and DP_{clsd} simulations. The land bridge reduces the ocean surface area of the SH by only 0.2% and therefore makes negligible *direct* change to hemisphere-averaged surface properties such as albedo and heat capacity. Indirect changes can occur, for example, via differing sea ice distributions across the hemispheres. The DP_{open} simulations were initiated from a 2500 year pre-industrial control simulation with an atmospheric CO_2 concentration of 280 ppm. The DP_{clsd} control simulation was also initiated from this run at year 1500 and equilibrated for a further 2000 years with the DP land bridge included. A six-member ensemble was generated at the end of each control run, using the model restart configuration at the end of six consecutive years. Each ensemble member was then perturbed with increasing atmospheric CO_2 concentration following the Special Report on Emission Scenarios A2 forcing scenario [*Nakicenovic and Swart*, 2000] from nominal year 1781 until 2100. From the year 2100 onward, CO_2 was held fixed at 856 ppm.

[9] The control simulations and warming experiments were initially conducted with and without flux adjustments in single-member experiments. The flux adjustments were set in order to restore the DP_{open} simulation toward a modern climatology in the control state. The same set of flux adjustments were applied to the DP_{clsd} simulation for comparison. While the flux adjustments improved the climatology of the DP_{open} simulation, they produced spurious trends in the warming scenarios of the DP_{clsd} simulation. Since the DP_{clsd} simulation has a very different ocean circulation in the SH, the flux adjustments derived from the DP_{open} simulation restored the DP_{clsd} simulation toward a different mean state. Ensemble simulations were therefore run without flux adjustments to ensure a physically meaningful comparison between the two sets of simulations; their results are presented here.

3. Results

3.1. Interhemispheric Asymmetry

[10] The interhemispheric asymmetry in temperature anomaly (defined as the NH minus SH mean temperature anomaly) is plotted in Figure 1a, showing the SAT and SST asymmetry for both ensembles over the period 1781–2300. The SST asymmetry is higher in the DP_{open} ensemble than the DP_{clsd} ensemble, with an average asymmetry of 0.37°C from 2081-2100 in the DP_{open} ensemble, compared to 0.22°C in the DP_{clsd} ensemble. Using a bootstrap resampling method to obtain a 95% confidence interval, the SST asymmetry ensembles become statistically different from year 2072 onwards, marked by the vertical dashed line in Figure 1a. The asymmetry is mainly due to the reduced warming around the coast of Antarctica when DP is open (Figure 2c).

[11] [12] The spatial pattern and magnitude of asymmetry in SAT is more robust across the two ensembles (Figure 3); from 2081 to 2100, SAT asymmetry is 0.82°C in the DP_{open} ensemble compared to 0.77°C in the DP_{clsd} ensemble. The SAT asymmetry is thus more robust to the change induced by closing DP, suggesting that the differences in surface heat capacity and land-ocean effects are dominant in setting the SAT asymmetry. Nevertheless, the SAT asymmetry is reduced by 6% compared to the DP_{open} case, while the SST asymmetry is reduced by 41% compared to the DP_{open} case.

3.2. Surface Warming

[13] In the transient warming runs, SST anomalies around Antarctica remain considerably cooler in the DP_{open} ensemble over the Ross Sea and South Pacific sectors (Figure 2). The slower warming of SST around DP and in the Pacific sector of the Southern Ocean is likely due to the thermal isolation created by the ACC. There is also a region of enhanced warming in the Weddell Gyre to the east of DP, which warms faster in the DP_{open} ensemble. This region is associated with enhanced sea ice melt (Figure S1g in the auxiliary material). When DP is closed, this warmer region of the Weddell Gyre is spread across a larger area by the enhanced subpolar gyre that forms in the absence of the DP throughflow. The SST anomalies in the Arctic Ocean are very similar in both ensembles, showing relatively weak warming over most of the Arctic due to persistent sea ice

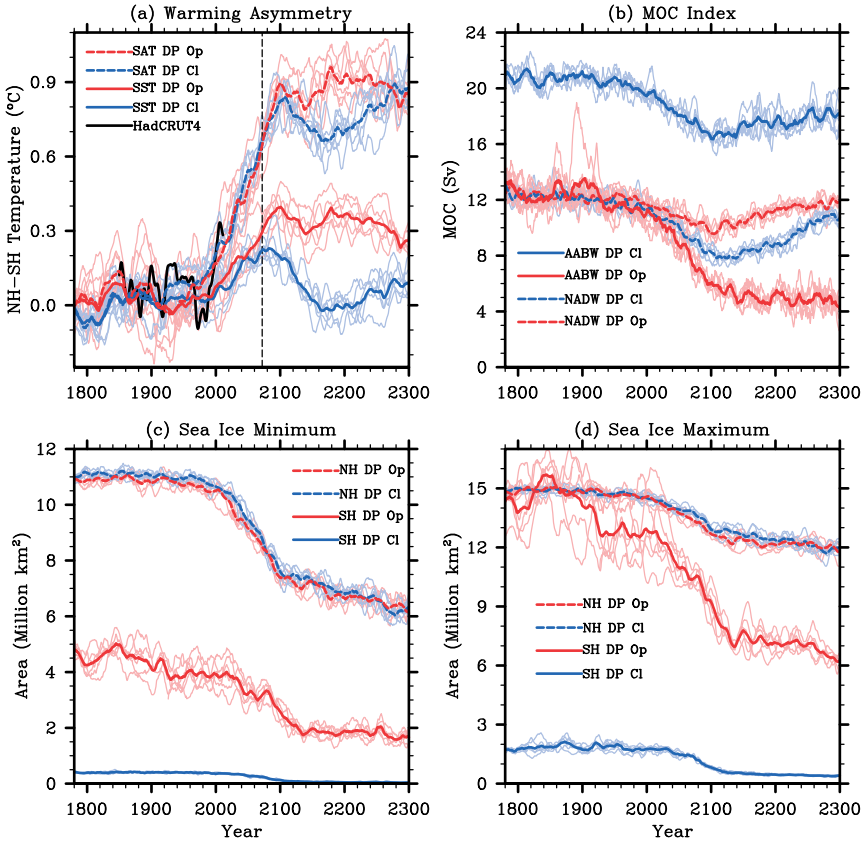

Figure 1. (a) Northern Hemisphere-Southern Hemisphere (NH-SH) temperature anomaly relative to the pre-industrial 100 year mean, showing the asymmetry in surface air temperature (SAT) anomalies (dashed lines), sea surface temperature (SST) anomalies (solid lines), and the HadCRUT4 observational data set [*Morice et al.*, 2012]. The vertical dashed line marks the year after which the SST asymmetry trends become statistically different. (b) Meridional overturning circulation (MOC) index calculated as the annual mean formation of Antarctic Bottom Water (AABW) (solid lines) and North Atlantic Deep Water (NADW) (dashed lines); (c) sea ice minimum extent, measured as the area where sea ice concentration is greater than 0.15 (NH—dashed lines, SH—solid lines); (d) as in Figure 1c but the sea ice maximum. In all plots, the bold lines represent ensemble means, and the fine lighter colored lines are the ensemble members. All model trends have been filtered using an 11 year running average.

coverage. There is also a localized region of very strong warming between Svalbard and Scandinavia, associated with sea ice melt. This "hotspot" is present in both ensembles and therefore appears to have little dependence on the DP changes in this experiment.

[14] The SAT changes show a similar pattern of polar amplification to that typical of International Panel on Climate Change (IPCC) AR4 simulations [*Meehl et al.*, 2007]. Figure 3 shows the SAT ensemble mean anomaly during 2081–2100 relative to the pre-industrial 100 year mean, as in Figure 2. Both ensembles show amplified warming in the high latitudes of the NH, especially in the Arctic, and stronger warming over land than ocean. SAT changes over the ocean reflect the SST patterns in most regions, except in the Arctic where there is little change in SST but a large increase in SAT. The SAT trends over the Arctic are broadly consistent with IPCC AR4 projections *Meehl et al.* [2007], while the SST warming in the Arctic is limited by persistent sea ice coverage, discussed further in section 3.4.

3.3. Deep Warming and Overturning Changes

[15] Figure 4 shows the zonally averaged ocean temperature anomaly for each ensemble, plotted as a function of latitude and depth during 2081–2100 relative to the pre-industrial 100 year mean. In the DP_{open} ensemble (Figure 4a), Southern Ocean warming is substantially weaker, especially adjacent to the coast of Antarctica. In the DP_{clsd} ensemble (Figure 4b), ocean warming persists through to the highest latitudes of the Southern Ocean, extending to approximately 1500 m depth. There is a reversal of this trend below 1500 m depth, with the DP_{open} ensemble warming more than the DP_{clsd} ensemble. This warming at depth can be explained by the shallower penetration of AABW in the DP_{clsd} ensemble, discussed below.

[16] [17] The meridional overturning circulation (MOC) streamfunction, calculated in density coordinates and reprojected back to latitude-depth space, during 2081–2100 is overlaid on the temperature anomalies in Figures 4a and 4b, with the difference in streamfunctions shown in Figure 4c. The rate of Antarctic Bottom Water (AABW) formation is higher in the DP_{clsd} ensemble; however, its density is reduced due to the warmer Antarctic climate. The lower density of the AABW mass causes it to penetrate to shallower depths, and the NADW mass becomes the dominant source of the abyssal ocean in this case. In the DP_{open} ensemble, by contrast, the AABW mass dominates the abyssal ocean.

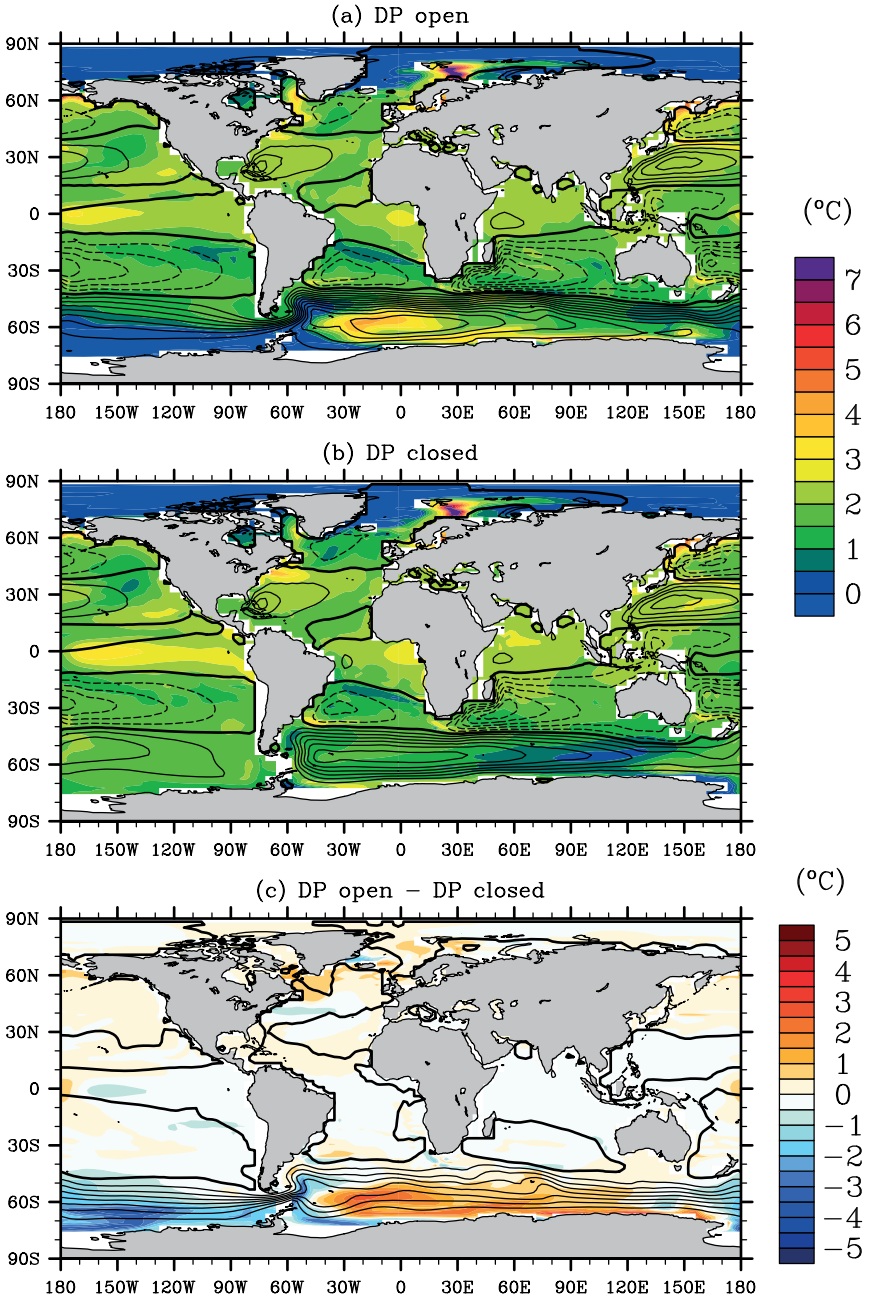

Figure 2. Sea surface temperature (SST) ensemble mean anomaly (colored contours) during 2081–2100 relative to the final 100 years of the pre-industrial simulation for (a) DP_{open}, (b) DP_{clsd}, and (c) the difference $DP_{open} - DP_{clsd}$. The respective barotropic streamfunctions during 2081–2100 are overlaid (black contours) on Figures 2a–2b, and the difference in streamfunctions is overlaid on Figure 2c. The streamfunction contour interval is 10 Sv, solid lines are positive, dashed lines are negative, and the zero contour is bold.

Therefore, AABW ventilation can more rapidly transfer any surface warming signal to the deep Southern Ocean in the DP_{open} ensemble, as seen in Figure 4c.

[18] [19] Figure 1b shows a time series of NADW and AABW formation, calculated from the MOC streamfunction in latitude-density coordinates. The domain of the water masses is defined as having potential density of $\sigma_2 >$ 35 kg m^{-3}, and poleward of 50°N and 50°S for NADW and AABW, respectively. Weakening of AABW relative to NADW formation in the DP_{open} ensemble slows the advection of heat across the DP latitudes. By contrast, the steady formation of AABW in the DP_{clsd} ensemble allows the high latitude Southern Ocean to warm more rapidly in that experiment set.

[20] [21] It is worth noting that the NADW formation is very similar between the two control simulations and does not appear to depend strongly on the DP throughflow, in contrast to previous studies that used models with idealized continental geometries [e.g., *Toggweiler and Bjornsson*, 2000; *Enderton and Marshall*, 2009] or a noninteractive atmosphere [*Sijp and England*, 2004]. The realistic landmass with topography and the fully interactive atmosphere

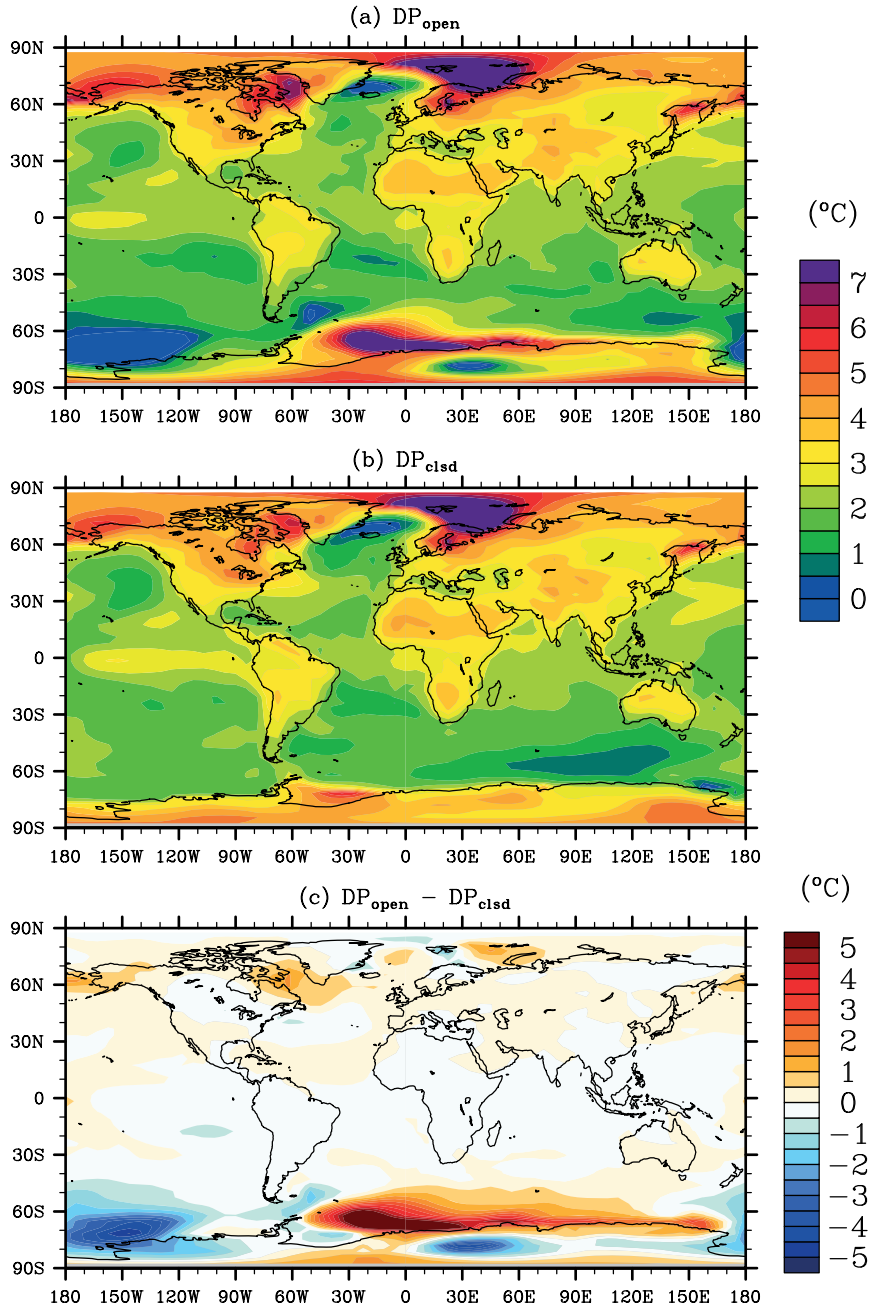

Figure 3. Surface air temperature anomaly during 2081–2100 relative to pre-industrial 100 year mean for (a) DP_{open}, (b) DP_{clsd}, and (c) the difference $DP_{open} - DP_{clsd}$.

in our model, complete with a hydrological cycle, appear to play an important role in regulating the heat and freshwater budgets of the Atlantic MOC [*Sinha et al.*, 2012]. Nonetheless, our result is consistent with *Rahmstorf and England* [1997], who showed that the rate of NADW formation is much less sensitive to Southern Ocean wind forcing when atmospheric thermal feedbacks are included.

3.4. Sea Ice Changes

[22] Differences in the Southern Ocean SST response of the two ensemble sets are strongly linked to sea ice patterns. The sea ice minima for both the NH and SH, measured respectively as the September and March sea ice extent (the area where sea ice concentration exceeds 0.15) are shown in Figure 1c. In the DP_{open} ensemble, the Arctic sea ice minimum is 11.0 M km^2 in pre-industrial conditions and declines to approximately 7.8 M km^2 by 2081–2100. The DP_{clsd} ensemble shows a similar trend, covering 11.1 M km^2 in pre-industrial conditions and declining to 8.0 M km^2 by 2081–2100. The Arctic sea ice maxima (Figure 1d) show a weaker decline over the same period, from 15.0 M to 13.0 M km^2 in the DP_{open} ensemble and 14.9 M to 13.3 M km^2 in the DP_{clsd} ensemble. Although the initial extent of the sea ice minimum is larger than satellite estimates (8.2 M km^2 for the 1980–1999 average), the magnitude of the decline in these simulations is consistent with IPCC AR4 projections [Figure 10.13 of *Meehl et al.*, 2007].

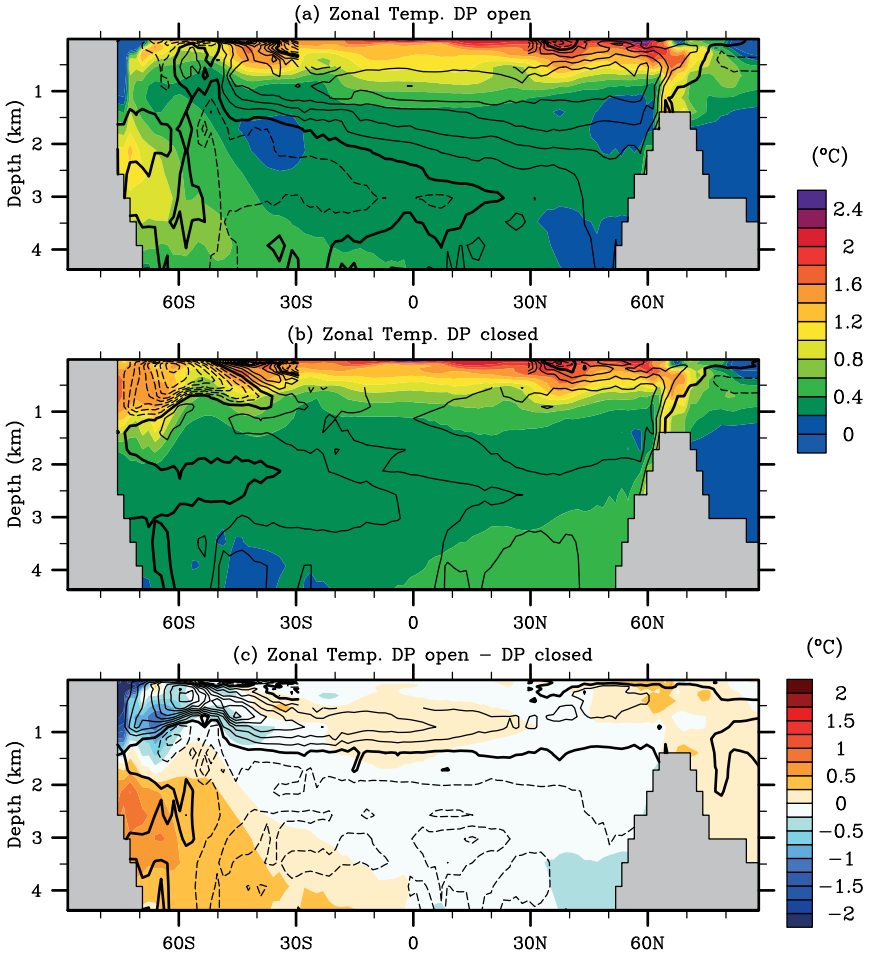

Figure 4. Zonal-averaged ocean temperature anomaly (colored contours) during 2081–2100 relative to pre-industrial 100 year mean, for (a) DP_{open}, (b) DP_{clsd}, and (c) $DP_{open} - DP_{clsd}$. The meridional overturning circulation during 2081–2100, calculated in density coordinates and reprojected back to latitude-depth space, is shown in black contours (2 Sv interval; solid lines are positive, dashed lines are negative, and the zero contour is bold). The tropical overturning cells are masked out in the domain ±30° latitude and < 500 m depth in order to show the near surface temperature trend.

[23] In the DP_{open} ensemble, there is a substantial coverage of SH sea ice, and though it decreases over the warming period, there remains a substantial coverage providing insulation to the sea surface despite ongoing global warming. The SH sea ice maximum declines from a pre-industrial level of 14.6 M to 9.7 M km^2 by 2081–2100, and the minimum declines from 4.4 M to 2.9 M km^2 over the same period, consistent with *Meehl et al.* [2007]. By contrast, the DP_{clsd} ensemble begins with almost no SH sea ice even in winter, with a pre-industrial maximum of 1.8 M km^2 declining to 1.0 M km^2 by 2081–2100, and a minimum declining from 0.4 M to 0.2 M km^2 over the same period.

[24] Recent observations show that Arctic sea ice is melting more rapidly than IPCC AR4 projections [*Wang and Overland*, 2009], and therefore, warming of SST in the Arctic is likely to be higher than our model suggests. Thus, our model may underestimate the asymmetry of warming in SST due to a weak trend in the Arctic. Nevertheless, the trends in Arctic sea ice are very similar between the DP_{open} and DP_{clsd} ensembles, and therefore, our experiments can still isolate the impact of the ACC on the warming asymmetry. For further details of the sea ice trends discussed here, polar stereographic plots of pre-industrial and late 21st century sea ice concentration for both ensemble sets can be found in Figure S1 for the SH and Figure S2 for the NH.

[25] The sea ice differences indicate that when the ACC is replaced by polar gyres in the presence of a land bridge, the increased advection of heat into the far Southern Ocean prevents much of the present day sea ice from forming. The sea ice coverage that forms when the ACC is present shields the subpolar Southern Ocean from substantial radiative forcing, thus slowing the warming response of the SH sufficiently to increase the interhemispheric asymmetry of both SST and SAT.

4. Summary and Conclusions

[26] The results presented here have further implications for detecting a CO_2 warming footprint in observed temperature trends. By comparing two sets of ensemble global warming simulations with an open and a closed DP, we demonstrate the importance of the ACC in limiting the rate of warming in the Southern Ocean. This effect would not be captured in climate models with simplified representations of the ocean, such as a uniform slab ocean or an aquaplanet. Furthermore, given the faster rate of warming in the NH and

the lower proportion of observations available in the high southern latitudes, care needs to be taken when inferring global trends from an asymmetric set of observations.

[27] This study has demonstrated the importance of the ACC in determining the climate response to global warming and highlights the need to improve its representation in climate models. While the impact of the DP has been analyzed in ocean-only, intermediate complexity and idealized coupled climate models, this study is the first to demonstrate its impact in a fully coupled climate model with realistic continents and a complete representation of the hydrological cycle. The present model relies upon subgrid scale eddy parameterizations; however, the Southern Ocean climate may respond differently when eddies are explicitly resolved [*Hallberg and Gnanadesikan*, 2006]. Investigating the interhemispheric asymmetry of global warming in eddy-permitting and eddy-resolving models will be the focus of a follow-up study.

[28] Transient global warming experiments with the DP closed reveal that a significant fraction of warming asymmetry in SST can be attributed to the thermal isolation provided the ACC. The ACC enables a much greater presence of sea ice and reduced poleward heat transport in the SH, causing the Southern Ocean as a whole to warm more slowly in response to strong CO_2 forcing. Previous discussions of the interhemispheric asymmetry have emphasized the role of heat capacity differences between the hemispheres, heat uptake in the deep mixed layers of the Southern Ocean, and ice-albedo feedback in the Arctic. This study has shown that the ACC provides a further mechanism to slow global warming in the high southern latitudes, contributing to a substantial proportion of the asymmetry compared to the scenario of a blocked circumpolar flow around the Southern Hemisphere.

[29] **Acknowledgments.** This work was supported by the Australian Research Council, including the ARC Centre of Excellence in Climate System Science, and an award under the Merit Allocation Scheme on the NCI National Facility at the ANU.

References

Bryan, K., S. Manabe, and M. J. Spelman (1988), Interhemispheric asymmetry in the transient response of a coupled ocean-atmosphere model to a CO_2 forcing, *J. Phys. Oceanogr.*, *18*(6), 851–867, doi:10.1175/1520-0485(1988)018<0851:IAITTR>2.0.CO;2.

Cox, M. D. (1989), An idealized model of the world ocean. Part I: The global-scale water masses, *J. Phys. Oceanogr.*, *19* (11), 1730–1752, doi:10.1175/1520-0485(1989)019<1730:AIMOTW>2.0.CO;2.

Dufresne, J.-L., J. Quaas, O. Boucher, S. Denvil, and L. Fairhead (2005), Contrasts in the effects on climate of anthropogenic sulfate aerosols between the 20th and the 21st century, *Geophys. Res. Lett.*, *32* (21), L21703, doi:10.1029/2005GL023619.

Enderton, D., and J. Marshall (2009), Explorations of atmosphere–ocean–ice climates on an aquaplanet and their meridional energy transports, *J. Atmos. Sci.*, *66*(6), 1593–1611, doi:10.1175/2008JAS2680.1.

Flato, G. M., and G. J. Boer (2001), Warming asymmetry in climate change simulations, *Geophys. Res. Lett.*, *28* (1), 195, doi: 10.1029/2000GL012121.

Hallberg, R., and A. Gnanadesikan (2006), The role of eddies in determining the structure and response of the wind-driven Southern Hemisphere overturning: Results from the modeling eddies in the Southern Ocean (MESO) project, *J. Phys. Oceanogr.*, *36*(12), 2232–2252, doi:10.1175/JPO2980.1.

Lee, S.-K., W. Park, E. van Sebille, M. O. Baringer, C. Wang, D. B. Enfield, S. G. Yeager, and B. P. Kirtman (2011), What caused the significant increase in Atlantic Ocean heat content since the mid-20th century?, *Geophys. Res. Lett.*, *38*(17), 1–6, doi:10.1029/2011GL048856.

Levitus, S., et al. (2012), World ocean heat content and thermosteric sea level change (0–2000 m), 1955–2010, *Geophys. Res. Lett.*, *39*(10), 1–5, doi:10.1029/2012GL051106.

Manabe, S., R. J. Stouffer, M. J. Spelman, and K. Bryan (1991), Transient responses of a coupled ocean-atmosphere model to gradual changes of atmospheric CO_2. Part I. Annual mean response, *J. Clim.*, *4*(8), 785–818, doi:10.1175/1520-0442(1991)004<0785:TROACO>2.0.CO;2.

Manabe, S., J. Ploshay, and N.-C. Lau (2011), Seasonal variation of surface temperature change during the last several decades, *J. Clim.*, *24*(15), 3817–3821, doi:10.1175/JCLI-D-11-00129.1.

Meehl, G., et al. (2007), *Global Climate Projections. In: Climate Change 2007: The Physical Science Basis. Contribution of Working Group I to the Fourth Assessment Report of the Intergovernmental Panel on Climate Change,* pp. 747–845, Cambridge University Press, Cambridge, U.K.

Morice, C. P., J. J. Kennedy, N. A. Rayner, and P. D. Jones (2012), Quantifying uncertainties in global and regional temperature change using an ensemble of observational estimates: The HadCRUT4 data set, *J. Geophys. Res.*, *117*(D8), 1–22, doi:10.1029/2011JD017187.

Nakicenovic, N., and R. Swart (eds.) (2000), *Special Report on Emissions Scenarios. A Special Report of Working Group III of the Intergovernmental Panel on Climate Change IPCC,* 570 pp., Cambridge University Press, Cambridge, U.K.

Phipps, S. J., (2010), The CSIRO Mk3L climate system model v1.2, 121pp., *Technical Report*, Antarctic Climate and Ecosystems Cooperative Research Centre, Hobart, Tasmania, Australia.

Rahmstorf, S., and M. H. England (1997), Influence of Southern Hemisphere winds on North Atlantic deep water flow, *J. Phys. Oceanogr.*, *27*(9), 2040–2054, doi:10.1175/1520-0485(1997)027<2040:IOSHWO>2.0.CO;2.

Santoso, A., M. H. England, and W. Cai (2012), Impact of Indo-Pacific feedback interactions on ENSO dynamics diagnosed using ensemble climate simulations, *J. Clim.*, *25*(21), 7743–7763, doi:10.1175/JCLI-D-11-00287.1.

Sijp, W. P., and M. H. England (2004), Effect of the Drake Passage throughflow on global climate, *J. Phys. Oceanogr.*, *34*(5), 1254–1266, doi:10.1175/1520-0485(2004)034<1254:EOTDPT>2.0.CO;2.

Sijp, W. P., M. H. England, and J. R. Toggweiler (2009), Effect of ocean gateway changes under greenhouse warmth, *J. Clim.*, *22*(24), 6639–6652, doi:10.1175/2009JCLI3003.1.

Simpkins, G. R., L. M. Ciasto, D. W. J. Thompson, and M. H. England (2012), Seasonal relationships between large-scale climate variability and Antarctic sea ice concentration, *J. Clim.*, *25*(16), 5451–5469, doi:10.1175/JCLI-D-11-00367.1.

Sinha, B., A. T. Blaker, J. J.-M. Hirschi, S. Bonham, M. Brand, S. Josey, R. S. Smith, and J. Marotzke (2012), Mountain ranges favour vigorous Atlantic meridional overturning, *Geophys. Res. Lett.*, *39*(2), 1–7, doi:10.1029/2011GL050485.

Thompson, D. W. J., S. Solomon, P. J. Kushner, M. H. England, K. M. Grise, and D. J. Karoly (2011), Signatures of the Antarctic ozone hole in Southern Hemisphere surface climate change, *Nature Geosci.*, *4*(11), 741–749, doi:10.1038/ngeo1296.

Toggweiler, J. R., and H. Bjornsson (2000), Drake Passage and palaeoclimate, *J. Quat. Sci.*, *15* (4), 319–328, doi:10.1002/1099-1417(200005)15:4<319::AID-JQS545>3.0.CO ;2-C.

Toggweiler, J. R., and B. Samuels (1995), Effect of Drake Passage on the global thermohaline circulation, *Deep Sea Res. I*, *42*(4), 477–500, doi:10.1016/0967-0637(95)00012-U.

Wang, M., and J. E. Overland (2009), A sea ice free summer Arctic within 30 years?, *Geophys. Res. Lett.*, *36*(7), 2–6, doi:10.1029/2009GL037820.

Wang, W.-C., X.-Z. Liang, M. Dudek, D. Pollard, and S. Thompson (1995), Atmospheric ozone as a climate gas, *Atmos. Res.*, *37*(1-3), 247–256, doi:10.1016/0169-8095(94)00080-W.

Interhemispheric Asymmetry of Warming in an Eddy-Permitting Coupled Sector Model

DAVID K. HUTCHINSON* AND MATTHEW H. ENGLAND

Climate Change Research Centre, University of New South Wales, and ARC Centre of Excellence for Climate Systems Science, Sydney, Australia

ANDREW M. HOGG AND KATE SNOW

Research School of Earth Sciences, Australian National University, and ARC Centre of Excellence for Climate Systems Science, Canberra, Australia

(Manuscript received 22 December 2014, in final form 21 June 2015)

ABSTRACT

Climate model projections and observations show a faster rate of warming in the Northern Hemisphere (NH) than the Southern Hemisphere (SH). This asymmetry is partly due to faster rates of warming over the land than the ocean, and partly due to the ocean circulation redistributing heat toward the NH. This study examines the interhemispheric warming asymmetry in an intermediate complexity coupled climate model with eddy-permitting (0.25°) ocean resolution, and results are compared with a similar model with coarse (1°) ocean resolution. The models use a pole-to-pole 60° wide sector domain in the ocean and a 120° wide sector in the atmosphere, with Atlantic-like bathymetry and a simple land model. There is a larger high-latitude ocean temperature asymmetry in the 0.25° model compared with the 1° model, both in equilibrated control runs and in response to greenhouse warming. The larger warming asymmetry is caused by greater melting of NH sea ice in the 0.25° model, associated with faster, less viscous boundary currents transporting heat northward. The SH sea ice and heat transport response is relatively insensitive to the resolution change, since the eddy heat transport differences between the models are small compared with the mean flow heat transport. When a wind shift and intensification is applied in these warming scenarios, the warming asymmetry is further enhanced, with greater upwelling of cool water in the Southern Ocean and enhanced warming in the NH. Surface air temperatures show a substantial but lesser degree of high-latitude warming asymmetry, reflecting the sea surface warming patterns over the ocean but warming more symmetrically over the land regions.

1. Introduction

Global climate models predict greater warming in the Northern Hemisphere (NH) than the Southern Hemisphere (SH) over the twenty-first century in response to increasing greenhouse gases (Friedman et al. 2013). Observations of sea surface temperature (SST) warming show a high degree of interhemispheric asymmetry (Morice et al. 2012), which is reflected in the rapid melting of Arctic sea ice in contrast to a lack of melting of Antarctic sea ice (Blunden and Arndt 2014). This asymmetry has long been established (Stouffer et al. 1989; Manabe et al. 1991; Flato and Boer 2001) and is due in large part to differences in the land surface area of each hemisphere, since the NH is 39% land covered while the SH is only 19% (National Geophysical Data Center 2006). The ocean's large heat capacity and its high evaporative cooling imply that it should warm more slowly than the land surface (Sutton et al. 2007; Byrne and O'Gorman 2013) and thus create a warming asymmetry. The asymmetry is reinforced by the Antarctic Circumpolar Current (Hutchinson et al. 2013), which limits ocean heat transport toward the high southern latitudes.

Marshall et al. (2014, 2015) recently argued that much of the asymmetry of SST warming predicted in models from phase 5 of the Coupled Model Intercomparison

* Current affiliation: Bolin Centre for Climate Research, Stockholm University, Stockholm, Sweden.

Corresponding author address: David Hutchinson, Bolin Centre for Climate Research, Stockholm University, 10691 Stockholm, Sweden.
E-mail: david.hutchinson@geo.su.se

DOI: 10.1175/JCLI-D-15-0014.1

Project (CMIP5) can be explained by ocean circulation. They applied a globally uniform warming flux of $4\,W\,m^{-2}$ over a 100-yr simulation using a global ocean-only model and found a global SST anomaly pattern with striking similarity to the CMIP5 average. It therefore seems likely that the interhemispheric asymmetry of warming is caused in large part by both ocean circulation and faster warming over land. Marshall et al. (2014) also found that ozone forcing causes a temporary cooling of the Southern Ocean due to wind-driven upwelling, whereas in the latter half of the twenty-first century stronger wind forcing creates warming in the Southern Ocean. This transient cooling trend may be enhanced at eddy-permitting ocean resolution (Morrison et al. 2013) due to the fast response of the vertical eddy heat flux induced by stronger winds.

Global climate models suitable for equilibrium integrations remain restricted to the resolution of parameterized ocean eddies, on the order of 1° resolution as in most of the CMIP5 models. There is a growing body of evidence that permitting or resolving eddies will alter the climate's response to atmospheric forcing (Farneti et al. 2010; Spence et al. 2013; Zhang and Vallis 2013). Furthermore, key oceanic processes that regulate Earth's climate, such as western boundary currents and interocean exchange, are better resolved in high-resolution ocean models. Thus we are motivated to examine the impact of a higher-resolution ocean model on the interhemispheric asymmetry of warming, since the response of eddies, stronger boundary currents, and sea ice may depend upon resolution.

Recent progress has been made in simulating a fully coupled climate system at high resolution for greater than 100 years, allowing $2\times CO_2$ warming experiments at 0.25° resolution in the eddy-permitting regime (Delworth et al. 2012) and at 0.1° resolution in the eddy-resolving regime (Kirtman et al. 2012; Bryan et al. 2014; Griffies et al. 2015). These cutting-edge simulations have come at a high computational expense and were not tuned to the same degree as their low-resolution equivalents, nor were they run to equilibrium. Yet, the higher-resolution models have shown climate states strikingly different from their lower-resolution counterparts, raising questions about how these differences can be explained or reconciled between resolutions.

A key difference highlighted by these high-resolution simulations is the sea ice climatology. Kirtman et al. (2012) found a lower sea ice concentration and coverage in the NH at 0.1° resolution than the 1° model, which had a more realistic sea ice climatology. SH sea ice coverage was very similar between the resolutions, leading to a greater degree of asymmetry between the polar climates at high resolution. By contrast, the Delworth et al. (2012) model showed a greater coverage of sea ice at 0.25° resolution. However, parameter changes such as zero prescribed background vertical diffusion and increased ice albedo may have weakened the meridional overturning circulation (MOC) and increased sea ice extent.

A recent ocean-only study (Zhang and Vallis 2013) examined differences in the MOC between coarse, eddy-permitting, and eddy-resolving resolutions (2°, 0.25°, and 0.125°, respectively). They found a decreased heat transport across the Southern Ocean in the eddy-permitting model, resulting in overly steep isopycnals and a weaker Antarctic Bottom Water (AABW) cell. By contrast, the eddy-resolving simulation had a more realistic stratification and lower overturning cell, as did the coarse model. However, their domain was a flat-bottomed 60° pole-to-pole sector, with idealized temperature forcing and uniform salinity. Our study examines resolution dependence in a similar domain; however, we include realistic bathymetry and couple the ocean with sea ice, atmosphere, and land components.

While pole-to-pole sector domains are often used in ocean models to make higher-resolution modeling more tractable, the same approach is less common in coupled models of the climate system, where global dynamics are important. One climate model that uses a sector configuration is the intermediate complexity climate model (ICCM) of Farneti and Vallis (2009), with a 60° wide sector ocean coupled to a 120° sector atmosphere. This model was designed as a fast-running coarse-resolution climate model to explore a wide range of parameters (Farneti and Vallis 2011), but it also provides a useful framework for reducing the computational load in a high-resolution coupled climate model. A further benefit is that it allows a comparison between ocean-only sector models (e.g., Zhang and Vallis 2013) and fully coupled climate models that cannot be easily adapted to sector domains.

In this study we use different configurations of the Farneti and Vallis (2009) ICCM to explore the gap between ocean-only sector models and global coupled climate models, at two different horizontal ocean model resolutions. This configuration allows us to simulate the ocean at eddy-permitting (0.25°) resolution for 500-yr control runs, enabling a lower degree of drift than many global climate models at this resolution. We compare our results to a coarse-resolution 1° model, with parameterized eddies. We investigate the impact of resolution on the interhemispheric temperature asymmetry and its response to greenhouse warming. We further examine the impact of a poleward shift and intensification of the SH westerly winds on the asymmetry.

2. Climate model and experiments

a. Model description

The experiments presented here use the intermediate complexity climate model developed by Farneti and Vallis (2009) with several modifications outlined below. The ocean component is the Modular Ocean Model (MOM) version 5.0.2 (Griffies 2012), in a 60° wide sector domain, spanning from 78°S to 75°N. The ocean is simulated at two different resolutions, 1° and 0.25° longitudinal spacing, using a Mercator grid refinement in the latitudinal spacing. Both resolutions use z^* vertical coordinates with 50 levels to a depth of 5500 m and varying vertical resolution from 10 m at the surface to 210 m at depth.

The ocean coastlines and bathymetry use a modified Atlantic-like topography, derived from a realistic global ocean model, as described in Snow et al. (2015). The bathymetry is constructed via dilation and contraction of terrain contained within two piecewise linear boundaries to fit a 60° wide sector. The boundaries are chosen to be mainly over land bordering the Atlantic Ocean, producing sidewalls everywhere except for a zonally unbounded channel through Drake Passage to allow a flow analogous to the Antarctic Circumpolar Current (ACC). The sea ice model is the Sea Ice Simulator in the standard MOM distribution, and uses the same horizontal grid as the ocean model.

The atmosphere is a B-grid dynamical model, spanning a 120° sector and latitudes from 84°S to 84°N, with a horizontal resolution of 2° latitude × 2° longitude and seven vertical levels. The atmosphere employs a simplified gray radiation model, with no seasonal or diurnal cycle, and no explicit greenhouse gas or cloud schemes. Outside of the ocean sector, a simple land model is coupled to the atmosphere. As described in Farneti and Vallis (2009), the land model uses a "bucket" soil water scheme, with constant values of water availability and heat capacity. When precipitation exceeds the water capacity, idealized rivers redistribute runoff back into the ocean using a basin map. This scheme allows closure of the water budget within the coupled model. There is no orography, and all precipitated water stays in liquid form. Coupling of the model components is implemented through the Geophysical Fluid Dynamics Laboratory Flexible Modeling System. A schematic diagram of the ICCM sector domain can be found in Fig. 1 of Farneti and Vallis (2009).

The different horizontal resolutions allow a comparison of coupled climate simulations between parameterized and permitted ocean eddies. In the 1° model, we use the Gent and McWilliams (1990) eddy parameterization as implemented by Griffies (1998), using a constant coefficient of 600 $m^2 s^{-1}$, while in the 0.25° model no eddy parameterization is used. In the mixed layer at both resolutions, we use the submesoscale eddy parameterization of Fox-Kemper et al. (2008) and the K profile parameterization (KPP) boundary layer mixing scheme of Large et al. (1994). We use the interior gravity wave–induced mixing scheme of Simmons et al. (2004) and the coastal tide mixing scheme of Lee et al. (2006). The background vertical diffusivity is set to 5×10^{-5} $m^2 s^{-1}$, which is higher than estimates from observations, but forces an overturning circulation similar in magnitude to that of the global ocean (section 3e). For a discussion on the sensitivity of the ICCM to vertical diffusivity, see Farneti and Vallis (2009).

b. Calibration of radiative forcing

Because of the gray radiation scheme used in the ICCM, no explicit representation of greenhouse gases is possible. To emulate the effects of increasing greenhouse gases, we adjust the infrared optical depth as a proxy for greenhouse gas radiative forcing. The model contains an analytic profile of longwave optical depth (Frierson et al. 2006), where the dimensionless surface optical depth τ_0 is given by

$$\tau_0 = \tau_{0e} + (\tau_{0p} - \tau_{0e}) \sin^2(\theta), \tag{1}$$

where $\tau_{0e} = 6.0$ and $\tau_{0p} = 1.5$ are the surface values at the equator and pole, respectively, and θ is the latitude. The vertical structure of optical depth is given by

$$\tau = \tau_0 \left[f_l \left(\frac{p}{p_s} \right) + (1 - f_l) \left(\frac{p}{p_s} \right)^4 \right], \tag{2}$$

where p and p_s are the pressure at the model level and the surface respectively, and $f_l = 0.1$ is a parameter that allows shorter relaxation times in the stratosphere.

This optical depth profile is designed to represent the greenhouse effect of water vapor in the atmosphere, which is strongest in the tropics, decreases toward the poles, and decays rapidly with height (Frierson et al. 2006). We implemented radiative forcing by increasing τ_{0e} and τ_{0p} in proportion to their original values, which keeps the shape of the optical depth profile the same. The rationale for this choice is that although greenhouse gases cause global radiative forcing, the water vapor feedback follows a similar profile to the original distribution.

To achieve the equivalent radiative forcing of a $2\times CO_2$ scenario, we calibrated the optical depth parameters to give an increase in radiative forcing of 8 W m^{-2}. This value was chosen to represent 4 W m^{-2} of direct radiative forcing from doubling CO_2 concentration, plus a further 4 W m^{-2} to represent the water vapor

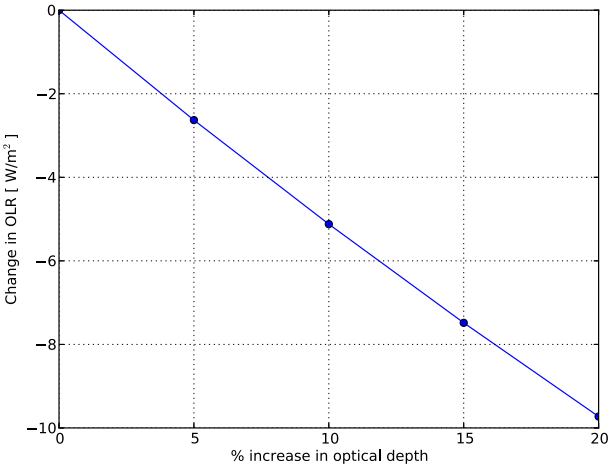

FIG. 1. Calibration of the optical depth parameter to achieve a radiative forcing of 8 W m^{-2}. The drop in OLR after 1 day is approximately equal to the radiative forcing of the optical depth change.

feedback (Myhre et al. 2013), which would otherwise be missing in this model. To calibrate this forcing, a set of five perturbation tests were initiated from a spun-up state and run for 1 day with increases in the optical depth of 0%, 5%, 10%, 15%, and 20%. In each case, the global mean outgoing longwave radiation (OLR) was computed and the anomaly from the 0% case is shown in Fig. 1. The near-instantaneous deficit in OLR approximately equals the radiative forcing from the optical depth change (e.g., Pierrehumbert 2010). The percentage change associated with an 8 W m^{-2} forcing was found to be 16.2% using linear regression. Finally, to emulate a 1% per year increase in CO_2, the optical depth was increased by 0.215% per year, so that it reached the $2\times CO_2$ value of 16.2% at year 70, after which it was held fixed.

c. *Wind stress forcing*

The default configuration of the ICCM yields midlatitude westerly winds that are nearly symmetric about the equator, being too weak in the Southern Hemisphere and with an equatorward bias compared with observations (Farneti and Vallis 2009). This wind stress profile was partially corrected in this model by adjusting the land surface roughness in the SH. A shorter roughness length results in a lower drag coefficient, as given by Eqs. (12)–(14) of Frierson et al. (2006). We used a land surface roughness length of $z_0 = 0.1$ m everywhere in the domain, except between the latitudes of 40° to 70°S where the roughness length was lowered to $z_0 = 1.0 \times 10^{-4}$ m. This adjustment yielded a more realistic position and strength of the SH surface westerly winds, although the peak magnitude is still lower than observed values. The improved wind stress profile is shown in Fig. 2a, compared with the default symmetric profile and an observational dataset.

In the warming experiments presented here, we found that the midlatitude SH westerly wind stress peak increased by 5% and 6% in the 1° and 0.25° models respectively. In the 1° model the peak location shifted equatorward from 52.3° to 51.6°S, while in the 0.25° model the peak location remained steady at 52.3°S. This evolution does not agree with the poleward wind shift found in most global climate model projections (Barnes and Polvani 2013). The difference is partly due to the gray radiation scheme employed here, which does not include ozone or an explicit representation of greenhouse gases. Ozone depletion and CO_2 forcing can both cause cooling of the polar stratosphere, which in turn leads to a poleward shift of the westerly winds (Polvani and Kushner 2002; Barnes and Polvani 2013). These effects are not captured by the radiative forcing method we have used to emulate a CO_2 perturbation in the troposphere. Nevertheless, there remains uncertainty over the relative roles of greenhouse gases and ozone in the observed and projected poleward shift of the westerly winds (Kidston and Gerber 2010; Thompson et al. 2011). It is therefore useful to examine warming scenarios both with and without a poleward shift and intensification of the westerly winds.

To simulate the impact of a poleward shift of the westerly winds on the ocean circulation, we apply a correction to the wind stress field as shown in Figs. 2b and 2c. This correction is referred to as a ''wind override'' and consists of a perturbation in the Southern Hemisphere only, with a zonally uniform pattern, which increases the peak zonal mean wind stress from approximately 0.1 to 0.15 N m^{-2} [a similar perturbation to that in Delworth and Zeng (2008)]. The wind override is applied both with and without radiative forcing. In the 1° model, the wind override shifts the wind stress peak southward from 52.3° to 54.1°S in the control case, and from 51.6° to 52.9°S in the $2\times CO_2$ case. In the 0.25° model, the wind stress peak shifts from 52.3° to 54.1°S in both the control and $2\times CO_2$ cases. The position of the wind stress maximum cannot be explicitly controlled, since the winds are freely evolving. However, the wind override experiments provide a much larger change to the Southern Ocean wind stress than the differences between the control and $2\times CO_2$ runs, as shown in Figs. 2b and 2c.

d. *Summary of experiments*

The 1° model was equilibrated for 1000 years after the model parameters were finalized. The ocean temperature and salinity restart file at year 500 was interpolated

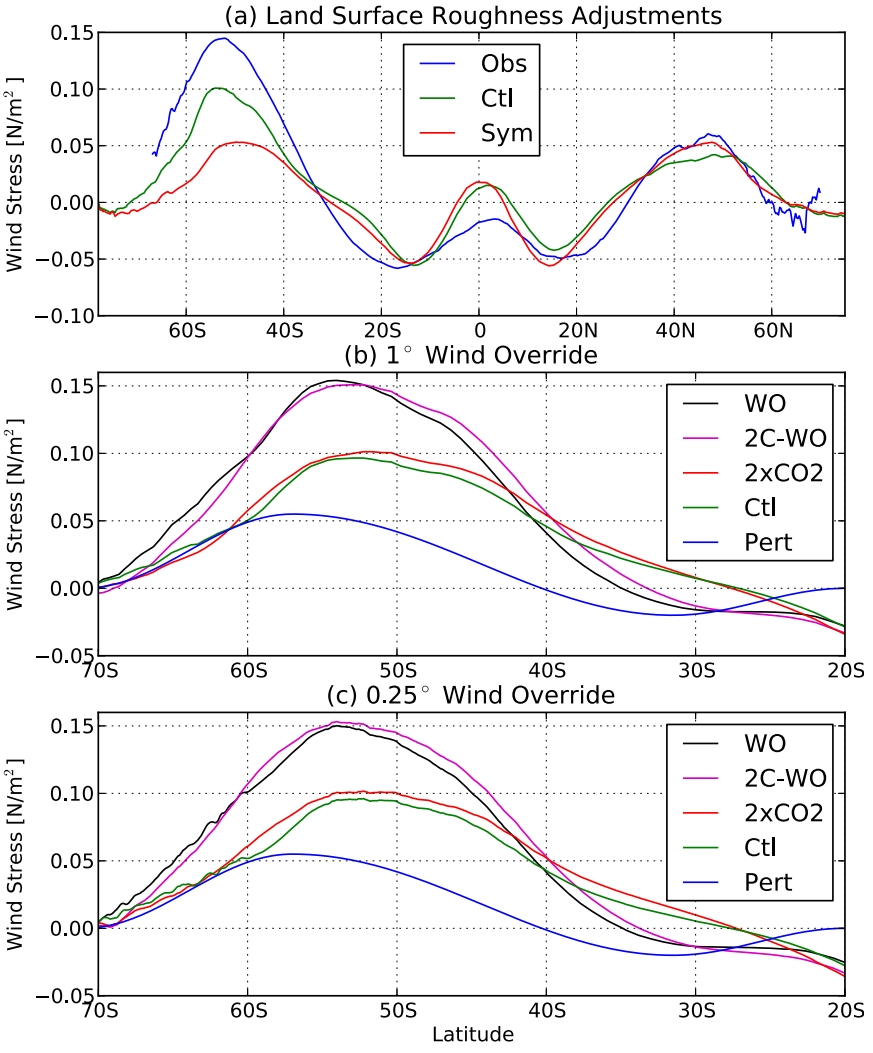

FIG. 2. (a) Zonal mean wind stress (N m^{-2}) comparison between the observational dataset of Risien and Chelton (2008) (blue), the default ICCM wind stress (red), and the wind stress with land surface roughness adjustments (green). (b) Zonal mean wind stress in the 1° Control, 2×CO_2, wind override (WO), and 2×CO_2 wind override (2C-WO) experiments, with the perturbation pattern (Pert) from year 70 onward. (c) As in (b), but for the 0.25° model. The experiment definitions are given in section 2d.

onto the 0.25° grid and spun up from zero velocity for a further 500 years. These equilibrated states were used to initiate perturbation experiments and parallel control runs. In each case we subtract the control run from the perturbation run to remove model drift.

We present four experiments at each resolution, and define shorthand for these experiments below. All experiments are initiated from the same equilibrated state, and run for 90 years: 1) Control (no perturbation); 2) 2×CO_2: where our equivalent CO_2 was increased by 1% per year until doubling at year 70 and then held fixed; 3) wind override: a wind shift and intensification perturbation, with a linearly increasing magnitude until year 70 and then held fixed; and 4) 2×CO_2 wind override: combined perturbations of the 2×CO_2 and wind override experiments. We add the prefix 1° or 0.25° to this shorthand to denote the ocean model resolution.

3. Warming response

a. *Control climates*

The control states of both the 1° and 0.25° models have a substantial interhemispheric temperature asymmetry. The land–ocean ratio is very similar between the hemispheres; the NH and SH are 61% and 59% land

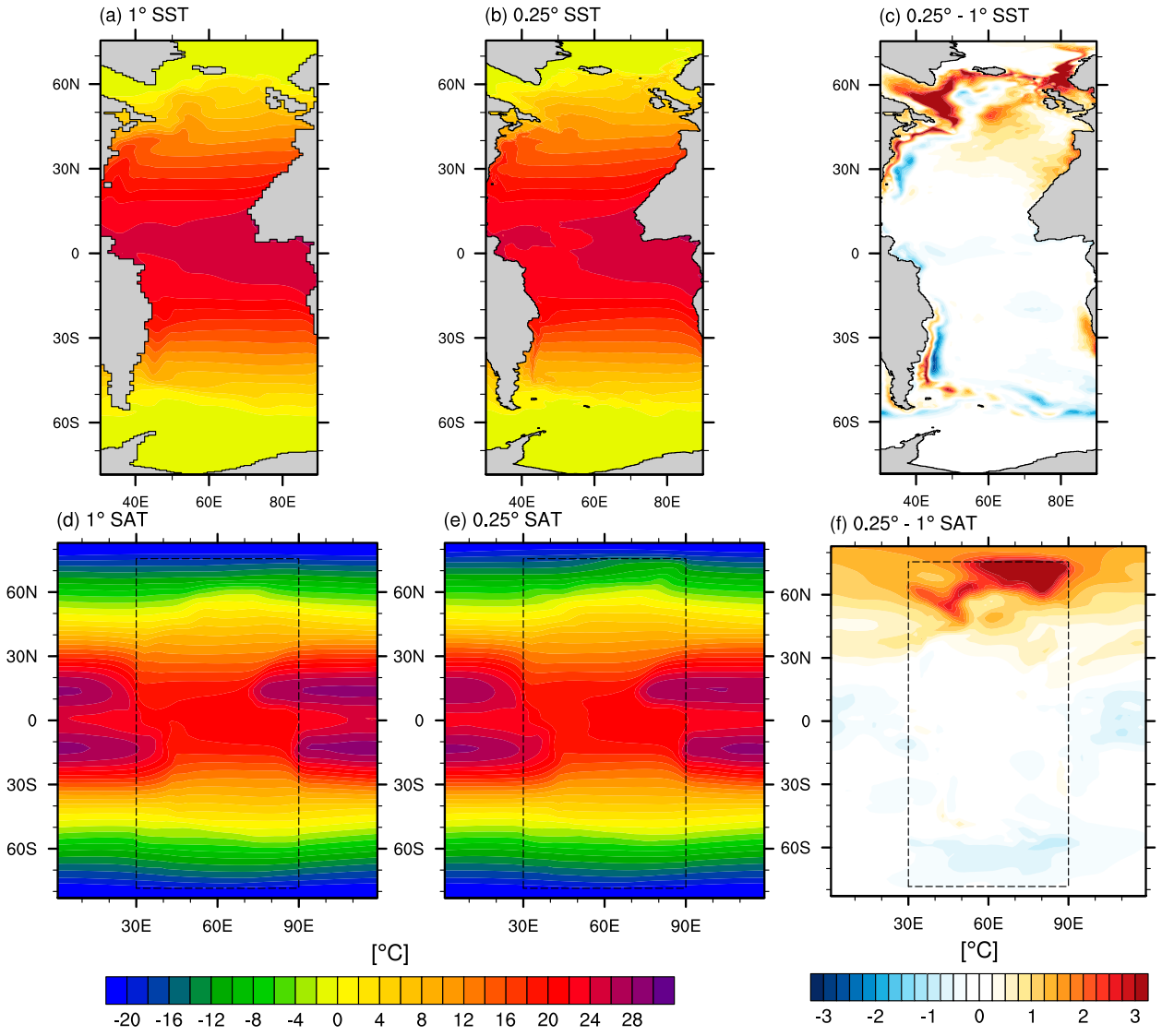

FIG. 3. Control run climates, showing sea surface temperature (SST; °C) in the (a) 1° model and (b) 0.25° model, and (c) difference 0.25° − 1°; and surface air temperature (SAT; °C) in the (d) 1° model and (e) 0.25° model, and (f) difference 0.25° − 1°. The ocean domain is denoted by the dashed box in (d)–(f).

covered respectively. The land distribution and the largely symmetric atmosphere forcing ensure that the ocean circulation is the key mechanism that creates the asymmetry. The interhemispheric temperature (NH − SH) difference is 2.19°C and 1.25°C for SST and surface air temperature (SAT) respectively in the 1° control run, and 2.72° and 1.95°C for SST and SAT in the 0.25° control run. This asymmetry compares with an interhemispheric SST difference of 3.63°C from an observational climatology (Locarnini et al. 2010).

A comparison of the control run surface climates is shown in Fig. 3. There is a significant increase in the interhemispheric temperature asymmetry when moving from 1° to 0.25° ocean resolution. The difference is greatest in the northern high latitudes, where warmer SST penetrates farther toward the poles. The SAT difference is greatest over the northern edge of the ocean basin, but there is also a warmer SAT over the mid- and high-latitude land regions. The Southern Hemisphere SST and SAT are more similar between the resolutions. These differences are closely linked to sea ice differences between the models, which are discussed in section 3c. The asymmetries we present in the perturbation runs are in addition to a substantial asymmetry in the mean state.

b. *Surface and deep warming*

Both the 1° and the 0.25° simulations show a strong asymmetry of warming in the Atlantic configuration.

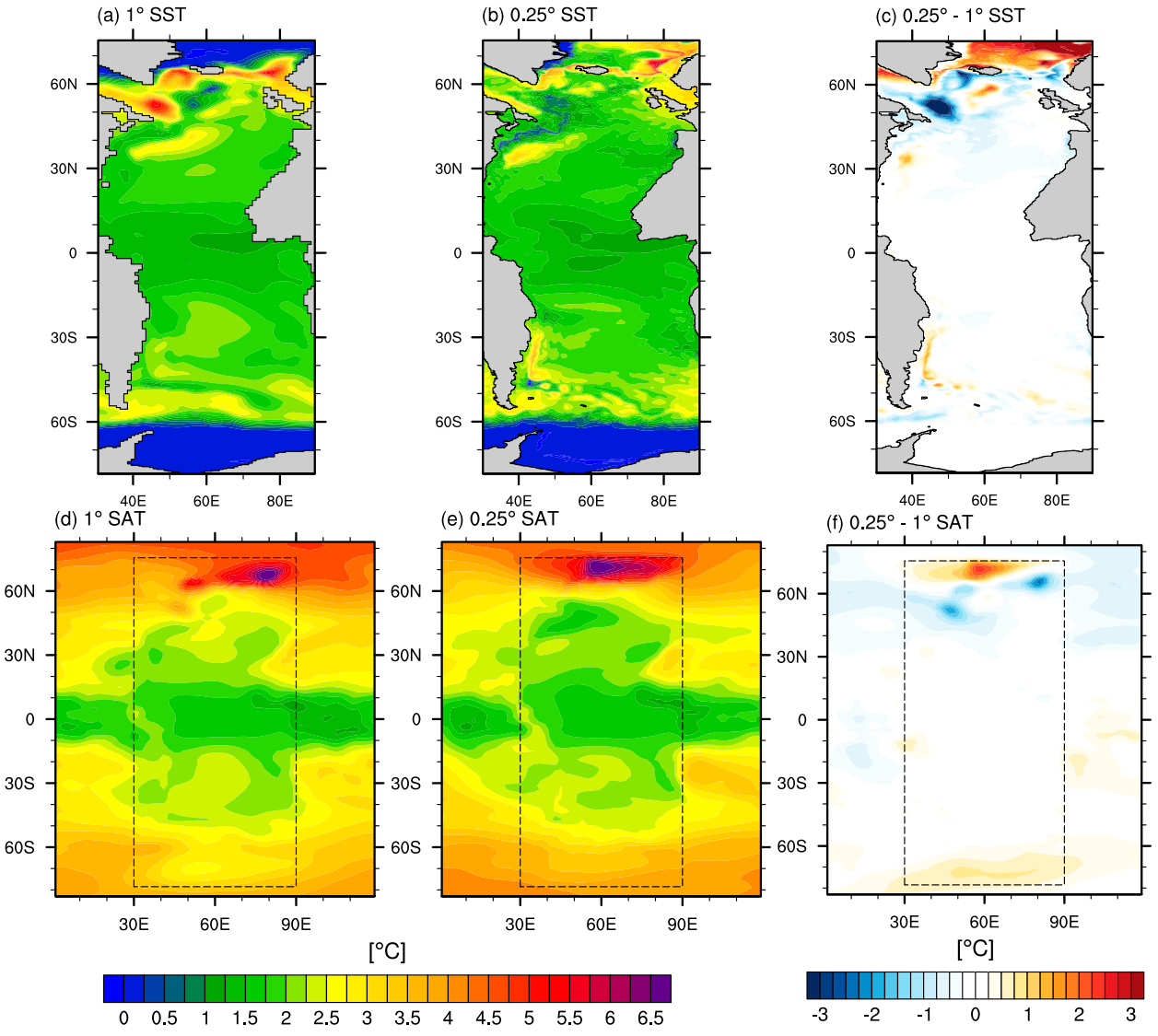

FIG. 4. SST anomaly (°C) in the (a) 1° model, (b) 0.25° model, and (c) the difference; and SAT anomaly (°C) in the (d) 1° model, (e) 0.25° model, and (f) the difference. The anomaly is the average from years 71–90 of the $2\times CO_2$ run, minus the same period from the control run. The ocean domain is indicated by the dashed box in (d)–(f).

Figure 4 shows the SST and SAT anomaly pattern in years 71–90 of the $2\times CO_2$ run, differenced from the same period of the control run. In the 1° model there is a region around 60°N where SST warms by up to 5°C (Fig. 4a). This warming is associated with a high rate of melting of Arctic sea ice. North of approximately 65°N there is a region of suppressed warming, where sea ice persists in the $2\times CO_2$ state. The 0.25° SST (Fig. 4b) shows a similar pattern of warming in most regions, except that the warming extends throughout nearly all of the North Atlantic. The patterns of SST warming project strongly onto the northern high-latitude SAT warming patterns (Figs. 4d,e). SAT warming is enhanced over the Arctic in the 0.25° model compared with the 1° model, due to the greater sea ice melting and high-latitude SST warming. Differences in SST and SAT warming between the resolutions are shown in Figs. 4c and 4f.

The Antarctic warming is markedly lower than the Arctic warming in both simulations. Sea ice melt in the SH is relatively low through the $2\times CO_2$ runs and there is very little (~0.1°C) warming of SST poleward of 60°S in either scenario. There remains polar amplification of the SH SAT warming pattern; however, its magnitude is 3°C lower over the Southern Ocean than the over the NH ocean at the same latitudes. The SH

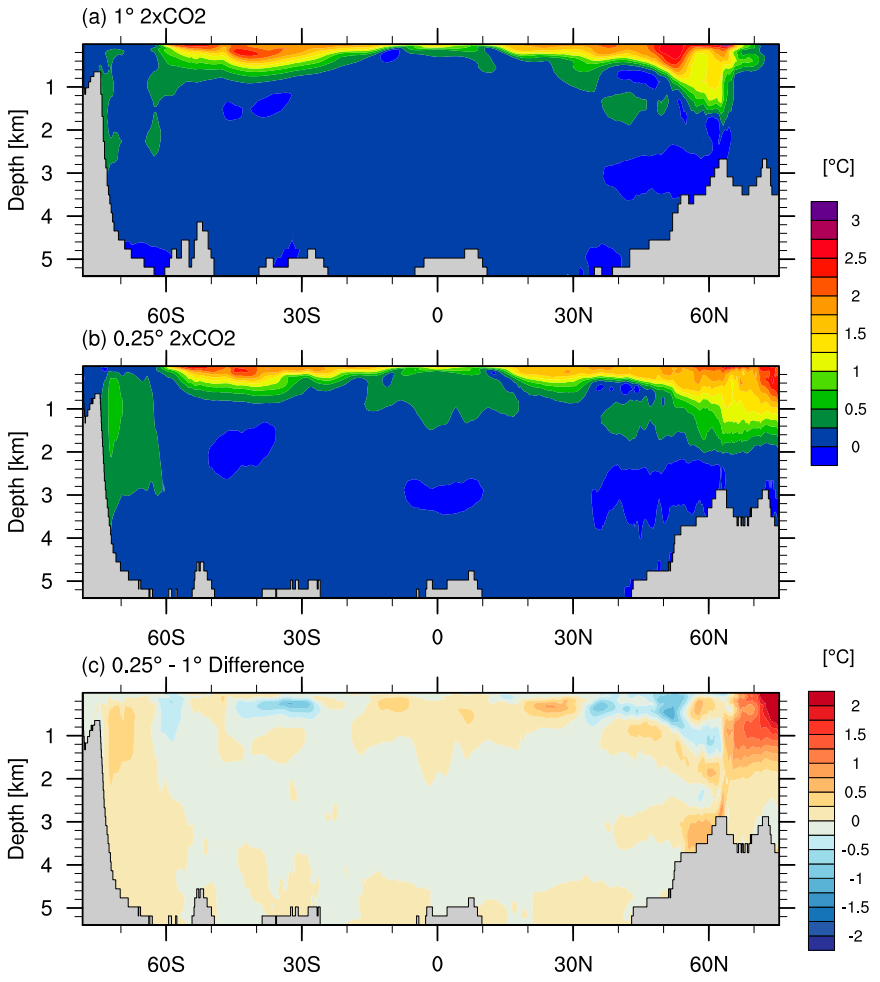

FIG. 5. Zonal mean temperature anomaly (°C) in the (a) 1° and (b) 0.25° 2×CO_2 runs, and (c) the difference (0.25° − 1°). The anomaly is the average from years 71–90 of the 2×CO_2 run, minus the same period from the control run.

warming pattern is relatively insensitive to the change in resolution. This result suggests that the parameterized and permitted eddy regimes perform similarly well in simulating the surface warming of the Southern Ocean.

The zonal mean temperature anomaly at depth in each of the models is shown in Fig. 5. The warming anomaly is generally less than 0.5°C below the top 1 km, except in the northern high-latitude deep water formation region. The enhanced warming in the northern high latitudes extends to the edge of the domain in the 0.25° model, whereas in the 1° model the warming signal becomes weaker north of 65°N. In addition, there is a stronger warming signal in the top 500 m at around 50°–55°N in the 1° model, associated with the melting of sea ice at lower latitudes in this model. Deep warming south of 60°S is slightly stronger in the 0.25° model, but is generally less than 0.5°C at all depths.

c. *Sea ice response*

The sea ice climatology is sensitive to the change in resolution (Fig. 6). In the 1° model, the NH sea ice is thicker and covers a greater area than in the 0.25° model in the control simulation. By contrast, the SH sea ice distribution and thickness is similar at both resolutions, with a moderate melt back of SH sea ice at the end of the 2×CO_2 run. By the end of the 2×CO_2 run, NH sea ice in the 0.25° model melts almost completely (Fig. 6d). This in turn leads to increased radiative forcing of the high-latitude ocean and a larger SST response. In contrast, NH sea ice in the 1° model melts to a lesser extent (Fig. 6b), and most of the ocean north of 65°N remains covered by ice. The NH sea ice extent at the end of the 1° 2×CO_2 run is similar to that of the 0.25° control run.

Because of the major role sea ice plays in the asymmetric warming response, additional experiments are

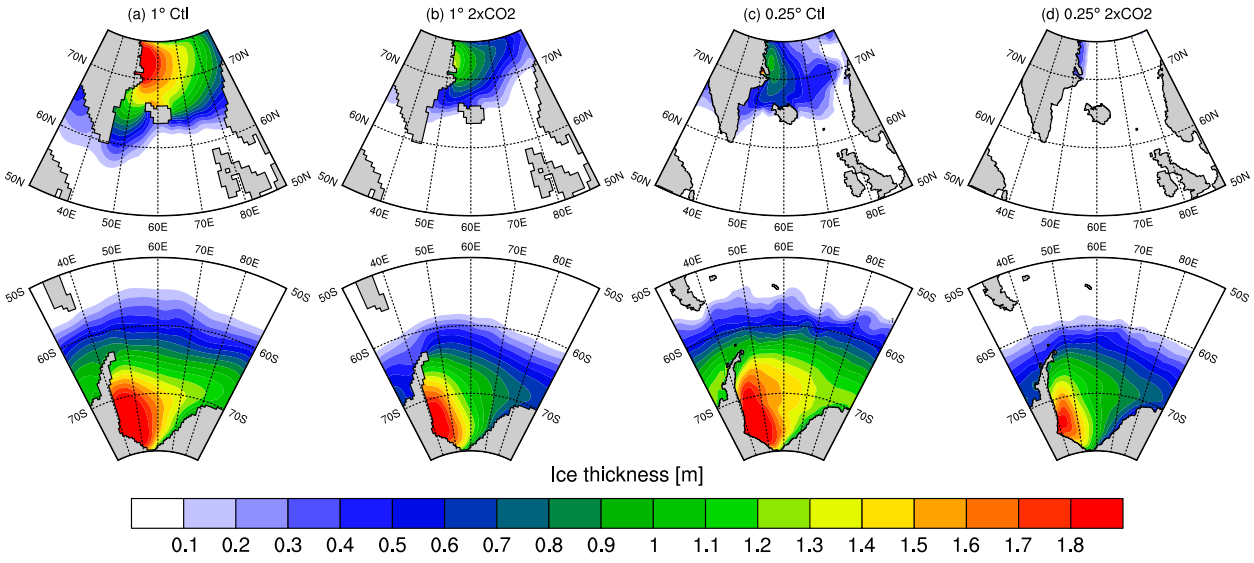

FIG. 6. Sea ice thickness (m) in the (a) 1° control run, (b) 1° 2×CO_2 run, (c) 0.25° control run, and (d) 0.25° 2×CO_2 run averaged over years 71–90.

performed in an attempt to decouple the feedback from ice melting. In these experiments, sea ice from the control run is output at monthly resolution for the 90-yr period analyzed here, and additional runs based on the control and 2×CO_2 runs are performed in which sea ice is restored toward the control run sea ice evolution. This restoring perturbs the circulation of both runs, with North Atlantic Deep Water (NADW) and AABW formation weakening due to the altered fluxes at their formation regions. Figure 7 shows the SST warming response of the ice-restored 2×CO_2 run minus the ice-restored control run. We also show the difference between the 2×CO_2 warming anomaly (shown in Fig. 4) and the ice restored 2×CO_2 anomaly.

With sea ice restoring, the polar warming of SST is greatly damped, especially in the NH. In the region of the Gulf Stream, there is a cooling of up to 2°C (Figs. 7a,b), which is likely due to a large reduction of NADW formation in the ice restored warming run. The strong warming signal poleward of 50°N in the 2×CO_2 run largely disappears. In the SH, the warming signal is also damped by the ice restoring, but since the change in SH sea ice extent is much smaller, the SH warming signal is less perturbed by the ice restoring. Away from the ice region, the warming signal is largely unchanged, with around 1.5°C warming of SST between 40°N and 40°S.

The ice-restoring results contrast with Marshall et al. (2014, 2015), who found a strong SST asymmetry in warming simulations where sea ice was not allowed to melt. However, they used an ocean-only model in which sea ice was held fixed, and equilibrated their model in that state. Our configuration differs in that sea ice continues to evolve and is simultaneously restored toward a control state. In our model, the restoring damps any warming that is advected into the ice region, and greater warming results in stronger damping. Nevertheless, the ice restoring results confirm that sea ice melting is of first-order importance in setting the high-latitude asymmetry. We argue that the heat transported by warm boundary currents is the underlying cause of asymmetry between the NH and SH sea ice responses.

d. Boundary currents

The Southern Ocean's response to external forcing is expected to change at higher resolution, due to effects such as eddy compensation and eddy saturation (Farneti et al. 2010; Morrison and Hogg 2013; Munday et al. 2013). However, we find that the Southern Ocean SST and sea ice respond similarly between the resolutions. Rather than transient eddy effects, our results suggest that better resolution of the mean boundary currents causes the greatest change. Figure 8 shows 20-yr averages of the ocean surface speed in the North Atlantic region for the (a) 1° and (b) 0.25° model control runs. In the 0.25° model, the boundary currents are faster on average and more tightly confined to the edge of the basins, while in the 1° simulation they are broader, slower, and more viscous. These boundary currents penetrate farther north in the high latitudes of the domain in the 0.25° model, bringing warm water farther into the ice region and enhancing sea ice melt.

Figure 8c shows a comparison of surface currents with observations, using the 1993–2014 mean from the 1/3°

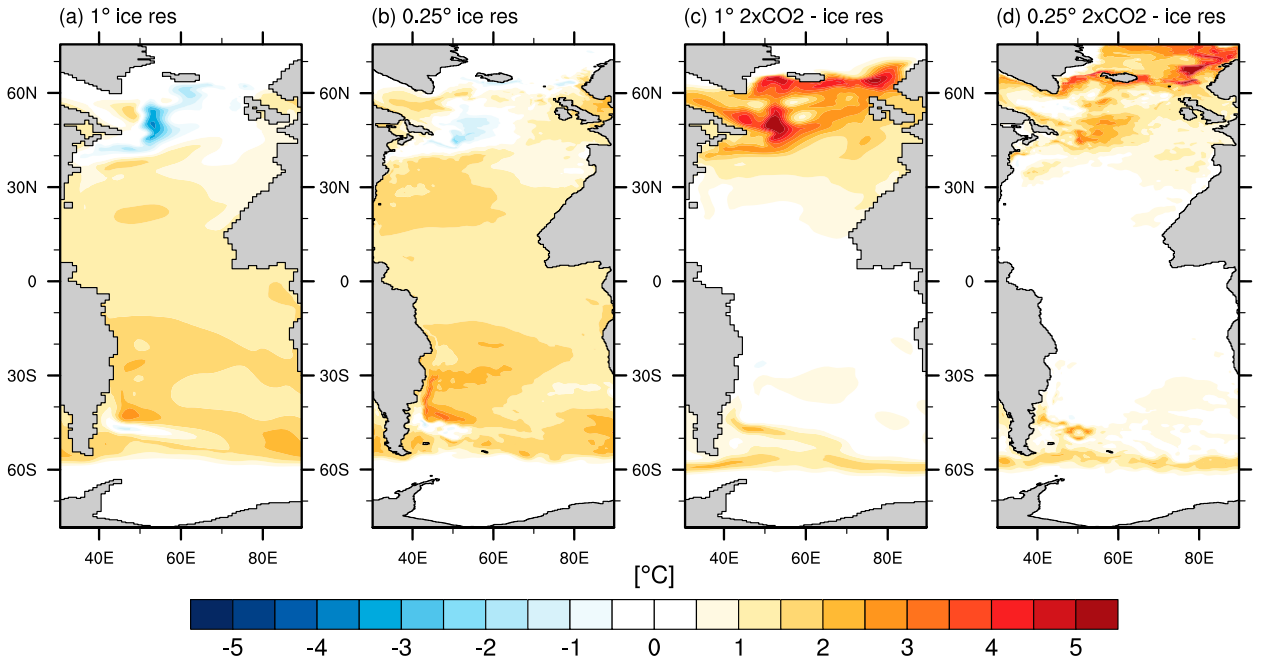

FIG. 7. SST anomalies (°C) from the (a) 1° and (b) 0.25° ice-restored warming runs, and the difference between the SST anomaly of the $2\times CO_2$ runs (Figs. 4a,b) minus the ice-restored warming runs in (a) and (b) for the (c) 1° and (d) 0.25° models.

resolution Ocean Surface Current Analyses–Real time (OSCAR) dataset (Bonjean and Lagerloef 2002). These observations demonstrate the greater fidelity of the 0.25° model velocities, although some features such as the boundary currents around the south of Greenland and the Labrador Sea are still weaker than observed values. We compare the poleward heat transport (PHT) of the boundary currents between the resolutions by calculating cumulative integrals of PHT from west to east at 30° and 60°N, in the top 200 m (Fig. 8d). These integrals reveal that the western boundary current at 30°N has a larger peak value of PHT in the 0.25° model (0.95 PW) than the 1° model (0.79 PW), and that the heat transported by the eastern boundary currents is larger in the 0.25° model at both 30° and 60°N.

e. *Meridional overturning circulation*

The meridional overturning circulation in the control and $2\times CO_2$ runs is shown for both models in Fig. 9. The MOC has been computed online in latitude–density coordinates, and then reprojected to latitude–depth coordinates. This method removes the Deacon cell component of the MOC to give a clearer picture of the residual circulation. The structure of the MOC is similar between the simulations, however the magnitude of overturning in both the North Atlantic Deep Water cell and the Antarctic Bottom Water cell are greater in the 0.25° model. In the control runs, NADW penetrates deeper in the 1° model than the 0.25° model (about 2.5 km compared with 1.5 km). This deeper penetration occurs at around 60°N, before returning to less than 2 km southward of 50°N. In the $2\times CO_2$ runs, NADW formation shoals in both the 1° and 0.25° models, as shown in the MOC difference plots of Figs. 9c and 9f.

In the 1° model the peak value of NADW formation is 12.0 Sv (1 Sv $\equiv 10^6\,m^3\,s^{-1}$) in the control and remains steady at the same value in the $2\times CO_2$ run, while in the 0.25° model NADW weakens from 15.0 to 13.5 Sv in the $2\times CO_2$ run. The sensitivity of NADW formation to warming is weaker than in most CMIP5 models (Drijfhout et al. 2012), although there is considerable intermodel spread across the CMIP5 ensemble. The weak sensitivity in our model may be due to the strong vertical diffusion maintaining this cell (discussed in section 2a) or to the lack of other ocean basins, since the Atlantic Ocean heat budget is influenced by thermal forcing from other basins (e.g., Lee et al. 2011). Unlike NADW, there is a strong decrease in AABW, from 8.8 to 1.9 Sv in the 1° model and from 6.9 Sv to 2.7 Sv in the 0.25° model. There is also an increase in Southern Ocean upwelling of NADW in the $2\times CO_2$ run.

The MOC plots presented in Fig. 9 have been filtered to reduce noise near the equator. Without this filtering, the MOC contained small cells of 1–2 Sv of alternating orientation within a few degrees of the equator. These alternating cells are sensitive to the number of density bins used in the online overturning diagnostic

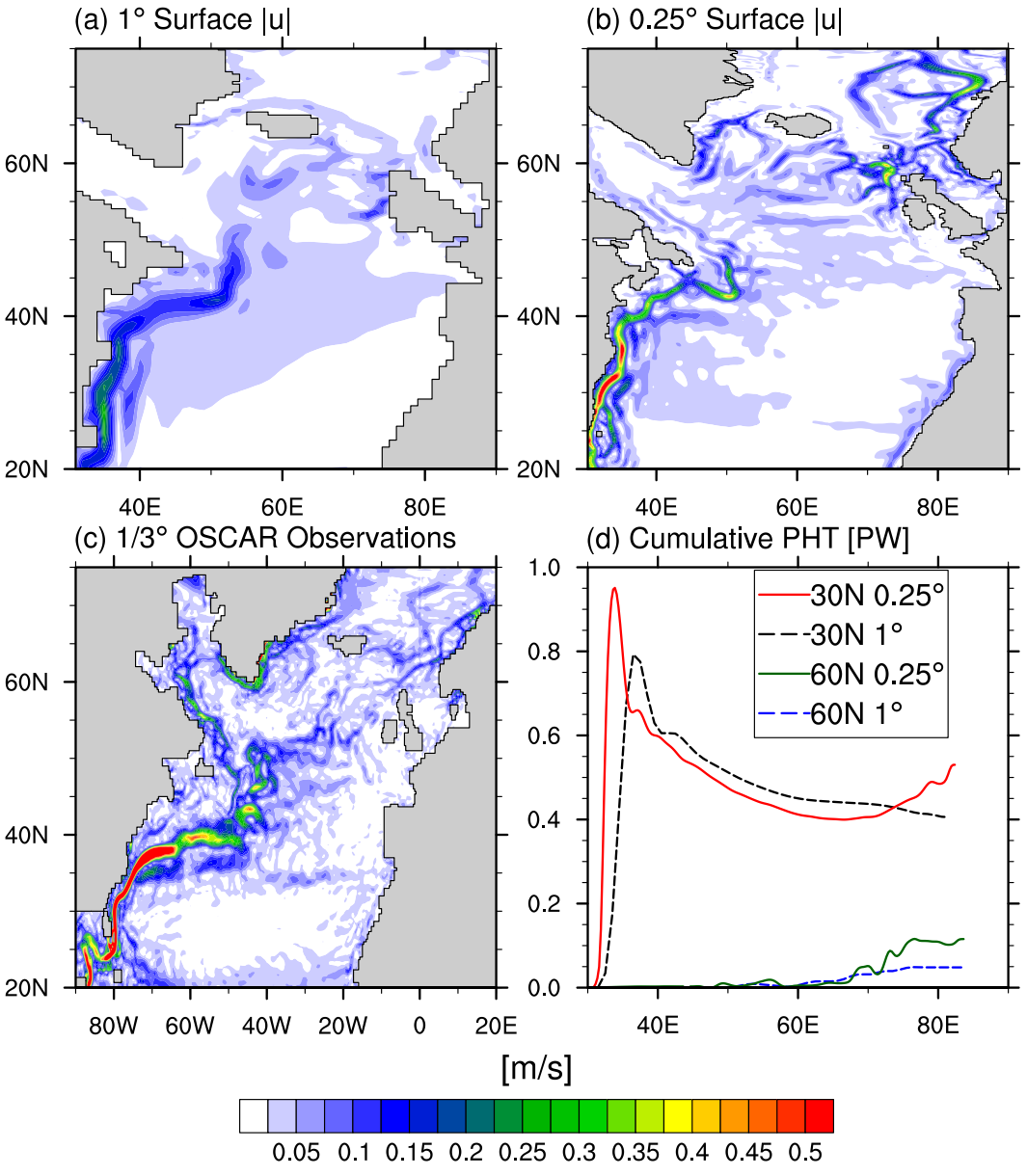

FIG. 8. 20-yr mean surface speed ($m\,s^{-1}$) in the North Atlantic for the (a) 1° control, (b) 0.25° control run, and (c) 1/3° OSCAR observations of surface currents, showing the 22-yr mean from 5-daily observations from 1993–2014 (Bonjean and Lagerloef 2002). Grid points in (c) were masked out if more than half the time steps were missing. (d) Cumulative integrals from west to east of poleward heat transport (PW) in the top 200 m, at 30°N (red: 0.25°, black dashed: 1°) and 60°N (green: 0.25°, blue dashed: 1°) for each model.

calculation. We use 160 density bins compared with only 50 vertical levels in the model, in order to better resolve the AABW cell, whereas the apparent noise is reduced when only 80 bins are used. We applied a three-point mean filter along the density coordinate within ±20° latitude, between the density bins corresponding to depths of approximately 200 to 3000 m. The cells may be partly due to weak computational upwelling modes as in Weaver and Sarachik (1990), since the vertical velocities are relatively high about the equator and there is no enhancement of the horizontal or vertical viscosity in this region. The noise might be reduced either by imposing a higher viscosity about the equator or by enhancing the vertical resolution. Several recent studies have also found sharp gradients in the MOC near the equator at eddy-permitting or -resolving resolution (Farneti et al. 2010; Delworth et al. 2012; Zhang and Vallis 2013). Since this study is mainly focused on the

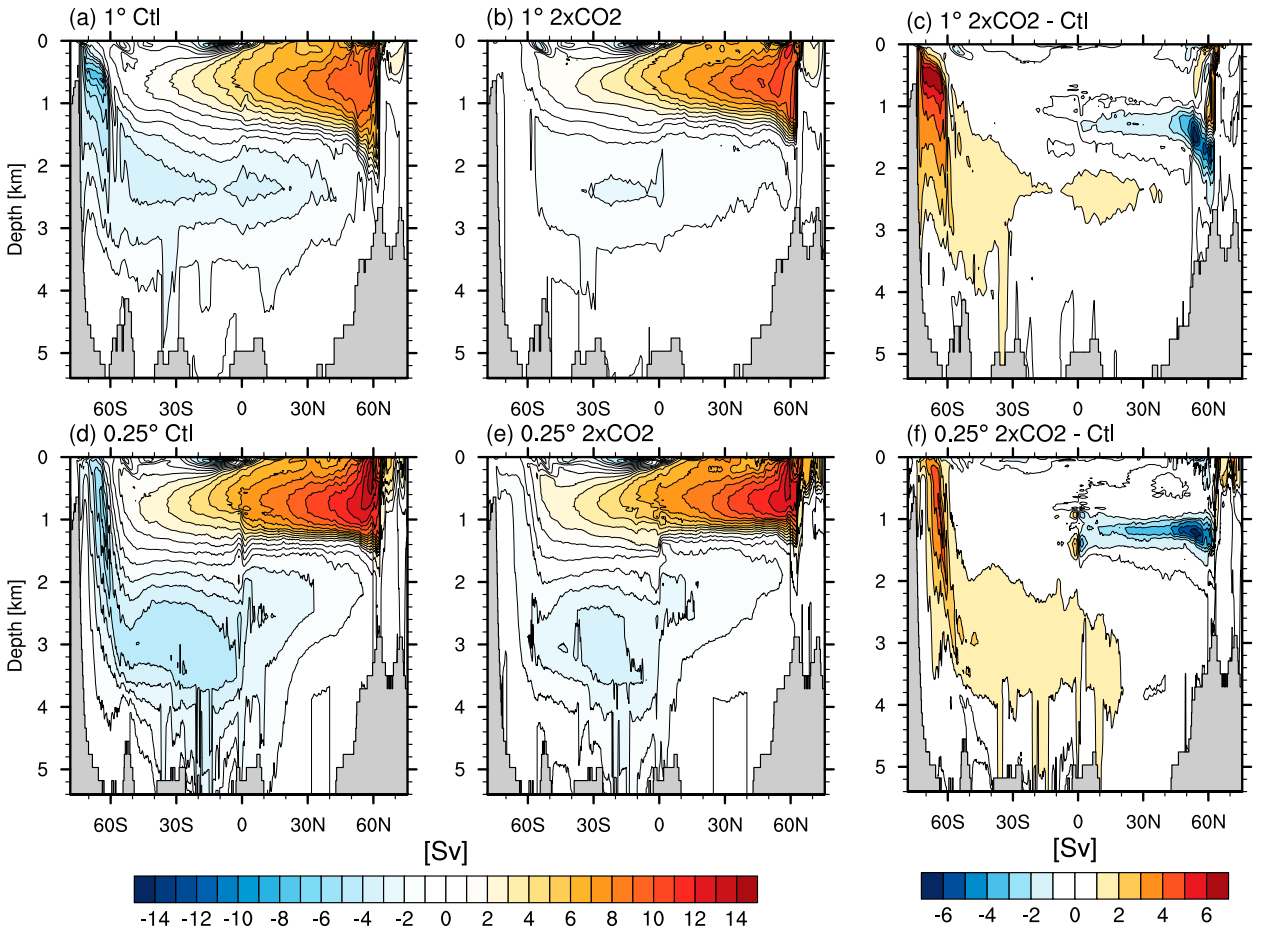

FIG. 9. Meridional overturning circulation (1-Sv contours) in the 1° model for the (a) control run and (b) $2\times CO_2$ run, and (c) the difference $2\times CO_2$ − control; and in the 0.25° model for the (d) control run, (e) $2\times CO_2$ run, and (f) the difference $2\times CO_2$ − control. The circulation is calculated online in latitude–density coordinates and reprojected to latitude–depth space.

high-latitude response of the climate, the MOC presented here is suitable for this purpose.

f. Poleward heat transport

Poleward heat transport for the atmosphere and ocean is shown in Fig. 10, with the atmosphere and ocean components marked as AHT and OHT respectively. In the control simulations of both models, the total PHT is greater in the NH (peak of 1.7–1.8 PW) than in the SH (peak of 1.4–1.5 PW). The OHT is strongly northward in the NH (0.5–0.6 PW) and slightly southward (<0.1 PW) in the SH. The AHT partly compensates for this difference in OHT, as the AHT is about 0.2 PW stronger in the SH than the NH. This compensation is not total, implying that OHT is a major factor in the asymmetry of the control climate.

In the $2\times CO_2$ runs, the asymmetry in OHT increases at both resolutions, as shown in Figs. 10c and 10d. The change in OHT is positive at all latitudes in the 1° model and almost all latitudes in the 0.25° model. The AHT change in the $2\times CO_2$ run is of opposite sign and greater magnitude in the SH. The peak changes in PHT in the 1° model are 0.07 PW in the NH and −0.04 PW in the SH, whereas in the 0.25° model the peak changes are 0.06 PW in the NH and −0.06 PW in the SH. Thus the overall asymmetry in PHT increases in the 1° model but remains steady in the 0.25° model in response to radiative forcing.

Ocean poleward heat transport is decomposed into its mean and eddy components in Fig. 11. In the 1° model, eddy heat transport is smaller than the mean flow component throughout most of the ocean. It is only in the Southern Ocean from about 50°–60°S that the eddy component is comparable in size to the advective component. In the NH midlatitudes there is also a local maximum of poleward eddy heat flux, but it is small compared to the advective component in that region.

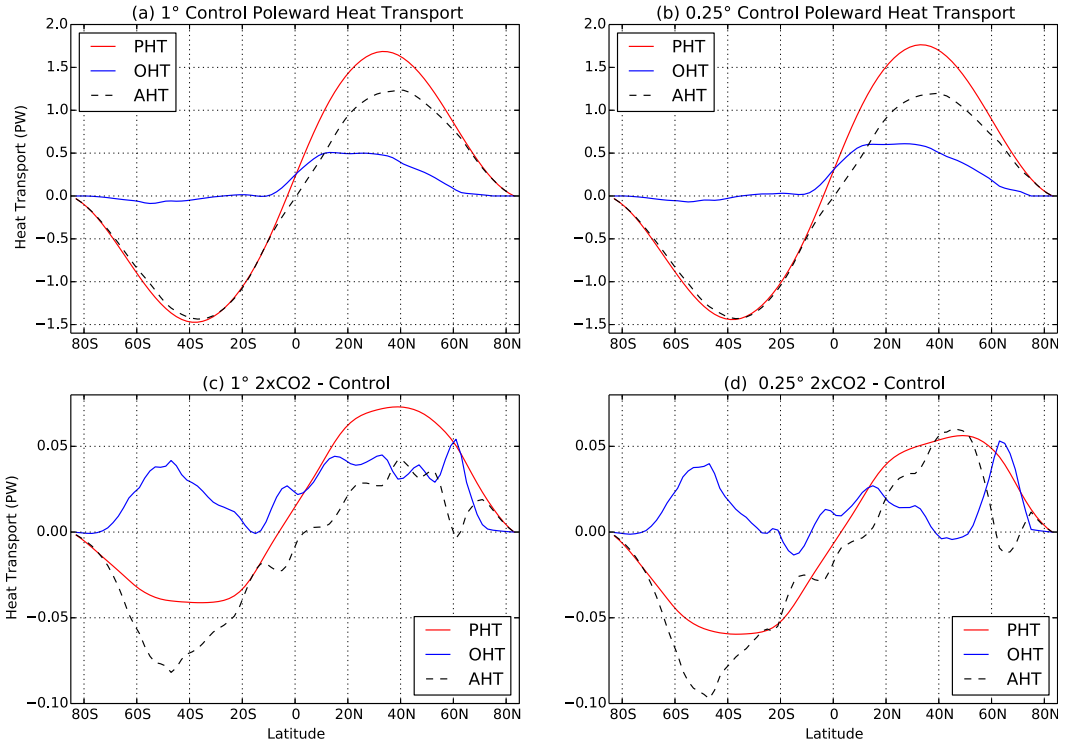

FIG. 10. Poleward heat transport (PW) in the (a) 1° and (b) 0.25° control runs showing the total (PHT; red), ocean component (OHT; blue) and atmosphere component (AHT; black dashed). The difference between the $2\times CO_2$ run and the control run is shown for the (c) 1° model and (d) 0.25° model.

The 0.25° model has explicit (albeit partially resolved) eddy heat fluxes and no eddy parameterization, so we derive the eddy heat transport from the velocity and temperature fields directly. We calculate the mean heat transport from the annual average and the eddy component from the residual anomaly transport calculated from 5-day averages of temperature and velocity. This decomposition treats standing eddies and jets as part of the mean flow, and only the transient eddies contribute to the eddy heat flux. Eddy heat transport in the 0.25° model is similar to that of the 1° model, except in the tropical band within ±15° latitude. Outside this region, eddy heat transport in the 0.25° is generally smaller in magnitude than the 1° model, and follows a similar latitudinal structure. Although our model does not fully resolve eddies, these results are consistent with Bryan et al. (2014), who found that the main differences in heat transport between their coarse and eddy-resolving models were due to the mean flow rather than transient eddies. The increase in OHT in both simulations consists mainly of the mean flow.

The key difference in OHT between the simulations is in the northern middle to high latitudes. The overall pattern of OHT is similar at both resolutions, while its peak value, centered around 10°–30°N, is approximately 0.1 PW higher in the 0.25° model than the 1° model. The OHT in the 1° model is close to zero (<0.01 PW) northward of about 65°N, whereas it remains above 0.05 PW up to around 71°N in the 0.25° model, and only falls to near-zero values at the edge of the domain. These differences in the high-latitude OHT are largely due to stronger boundary currents at the higher resolution, which result in considerable differences in the sea ice climatology.

4. Wind override response

In this section we present the results of experiments with a transient wind override applied. Although several previous studies have applied a wind perturbation as a step change (Delworth and Zeng 2008; Marshall et al. 2014), we aim to emulate the effects of a transient change to the wind field. The perturbation patterns are linearly increased from year 1 to year 70 and held fixed thereafter, in line with the transient increase in radiative forcing applied over the same period. The perturbation pattern is shown with the zonal wind stress from the control and $2\times CO_2$ runs in Figs. 2b and 2c.

a. Surface and deep warming

We show the SST anomaly induced by the wind override both with and without the $2\times CO_2$ radiative

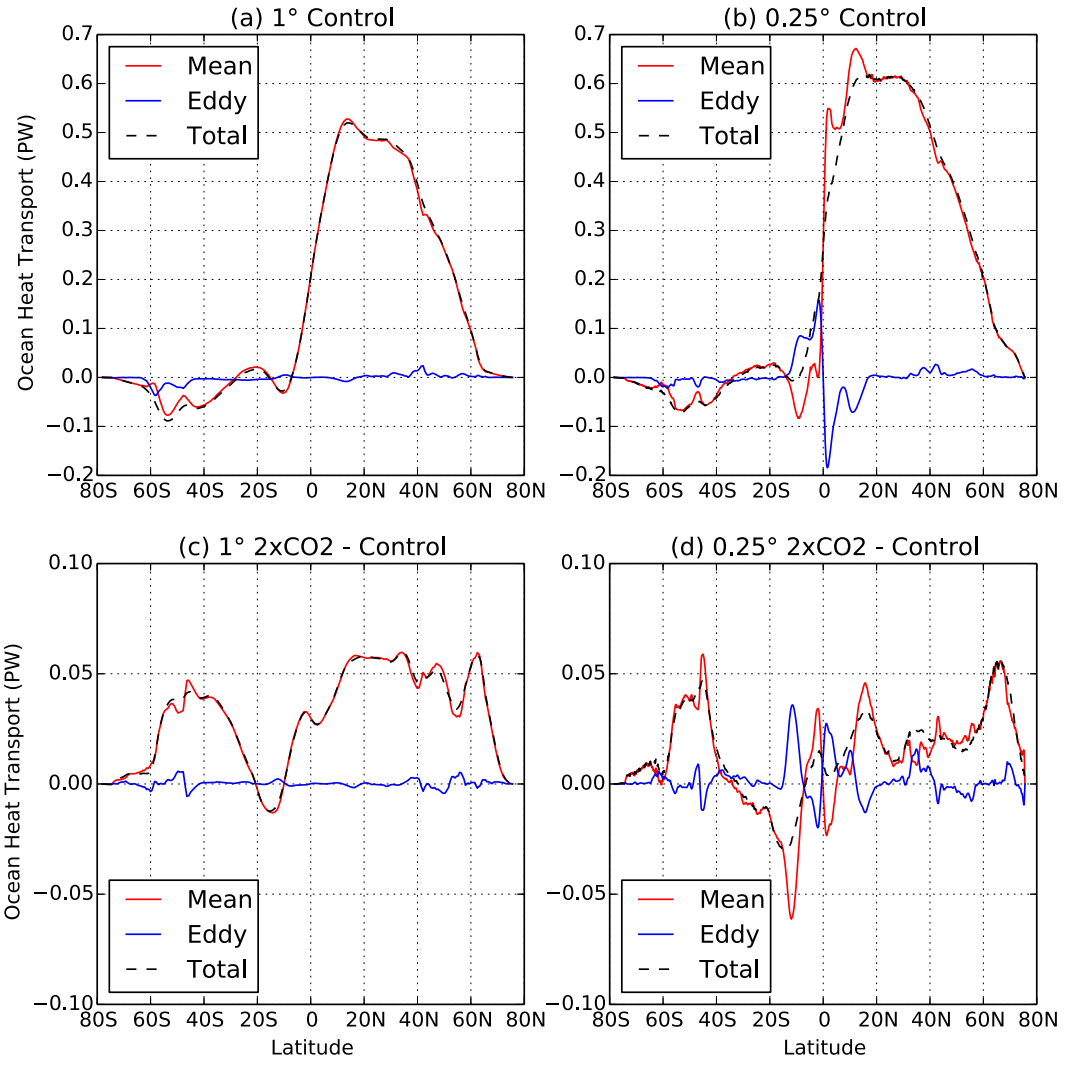

FIG. 11. The ocean poleward heat transport (OHT; PW) for the (a) 1° control and (b) 0.25° control runs, showing the total (black dashed), the mean flow component (red) and the eddy component (blue). The difference between the $2\times CO_2$ run and the control run is shown for the (c) 1° model and (d) 0.25° model.

forcing in Fig. 12. In the wind override run, there is a clear warming trend through most of the North Atlantic, especially around 50°–60°N. In the SH midlatitudes, there are both positive and negative signals. There is a cooling trend along the western boundary current of the SH subtropical gyre, and a warming trend on the southern edge of this boundary current. These trends are likely due to the intensification and southward shift of the gyre in response to the wind override. The warming signal at the southern edge of the boundary current extends east into the interior of the basin, due to the ACC transporting the warmer water eastward. There is also a cooling signal in the southeastern corner of the domain, which we attribute to greater upwelling and Ekman transport in the Southern Ocean, bringing deep water to the surface and exporting cool water northward.

In the $2\times CO_2$ wind override runs, the pattern is similar to that of the wind override runs, with warming of the North Atlantic and similar alternate signal trends in the SH. The main differences in the $2\times CO_2$ wind override runs are that the NH warming perturbation (compared to the $2\times CO_2$ run) is weaker and the SH cooling trend is stronger. There appears to be a larger region of the Southern Ocean that is cooled by enhanced Ekman transport, and the warming trend in the NH high latitudes is reduced. However, the wind override increases the temperature asymmetry both with and without radiative forcing. Sea ice thickness decreases near the Antarctic Peninsula and near the northern boundary of the domain

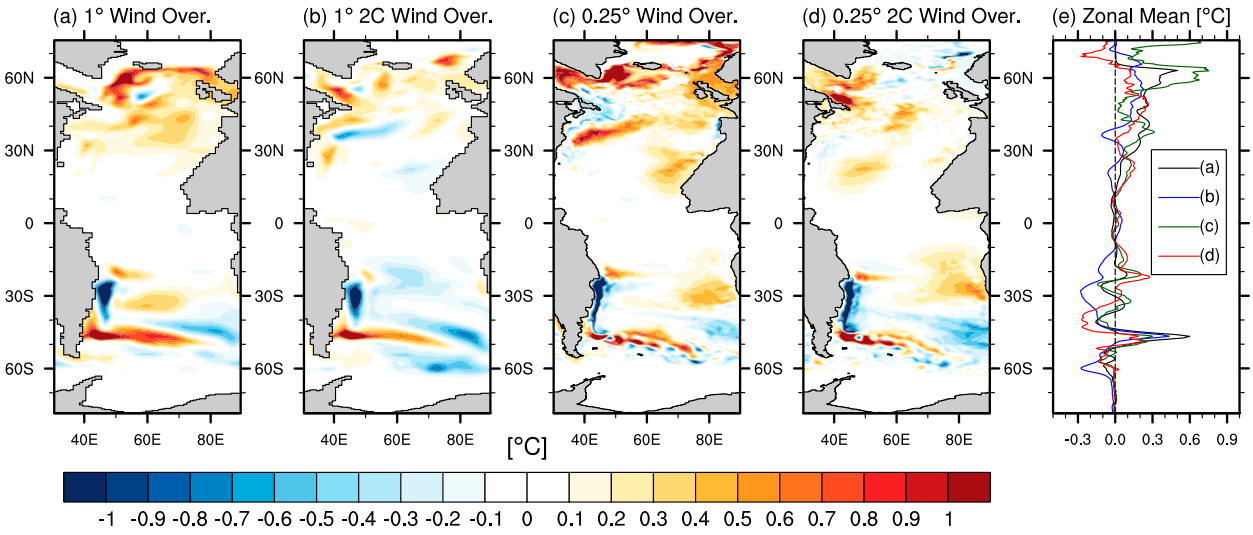

FIG. 12. Additional SST anomaly (°C) in years 71–90 in the 1° model for the (a) wind override and (b) $2\times CO_2$ wind override, and in the 0.25° model for the (c) wind override and (d) $2\times CO_2$ wind override. In (a) and (c), the control run temperature has been subtracted, while in (b) and (d) the $2\times CO_2$ temperature has been subtracted. (e) Zonal mean of (a)–(d).

in the wind override runs. These changes mainly occur away from the ice edge, so that sea ice extent remains similar to the control and $2\times CO_2$ runs (not shown).

The zonal mean temperature anomaly at depth induced by the wind override is shown in Fig. 13, with the anomalies in plots derived in the same manner as in Fig. 12. In the 1° cases, there is a strong cooling signature in the top 1 km from 50° to 60°S, of order 1°C in the wind override and 0.5°C in the $2\times CO_2$ wind override run. This cooling is likely due to the enhanced upwelling and northward export of cooler water. Poleward of 50°S there is a weaker cooling trend extending to full depth. The North Atlantic shows a warming trend mainly in the top 1 km, which is stronger in the wind override run but also present in the $2\times CO_2$ wind override run. Most of the ocean below 1 km north of 40°S warms slightly (0°–0.1°C), which is likely due to an increase in Southern Ocean upwelling (section 4b).

The 0.25° model shows similar patterns of high-latitude deep warming to the 1° model. The North Atlantic warms in the top 1 km, and the Southern Ocean cools throughout the ocean depth poleward of 60°S. The cooling signal in the top 1 km of the Southern Ocean is weaker than in the 1° model. This weakening may be due to partial eddy compensation in the 0.25° model, while the effect is weaker in the 1° model. In the $2\times CO_2$ run, there is a reduced deep warming in the top 1 km north of 65°N, which is also reflected in the SST response (Fig. 12).

b. *Meridional overturning circulation*

The MOC in the wind override runs is shown in Fig. 14, reprojected from latitude–density space into latitude–depth space as in Fig. 9. The 1° wind override run has an enhanced AABW cell compared with the control run with an increase of about 5.5 Sv in peak magnitude south of 55°S. In the $2\times CO_2$ wind override run, AABW formation is reduced but remains 0.7 Sv stronger than in the $2\times CO_2$ run. In the 0.25° wind override run, AABW formation is enhanced by 1.5 Sv compared with the control run, while in the $2\times CO_2$ wind override run AABW weakens, but is approximately 0.4 Sv stronger than in the $2\times CO_2$ run. AABW formation is therefore less sensitive to the wind override in our eddy-permitting model than in the parameterized eddy regime.

The increase in AABW in the 1° model is likely a result of Ekman transport increasing the isopycnal slope, combined with enhanced upwelling of the lower cell of the MOC, consistent with Delworth and Zeng (2008). The reduced sensitivity of AABW formation in the 0.25° model may be due to eddy compensation, whereby the northward Ekman transport induced by the wind override is partially compensated by a southward eddy-induced transport. In the 1° model we do not employ a spatially variable eddy parameterization, which can enhance eddy compensation in coarse-resolution models (Farneti and Gent 2011). Despite this difference, the surface temperature anomaly patterns in response to the wind override are similar between the resolutions.

NADW is enhanced in the wind override runs but retains a similar magnitude and structure. In the 1° wind override run, NADW peak magnitude north of 45°N is 1.2 Sv stronger than in the control run, whereas in the

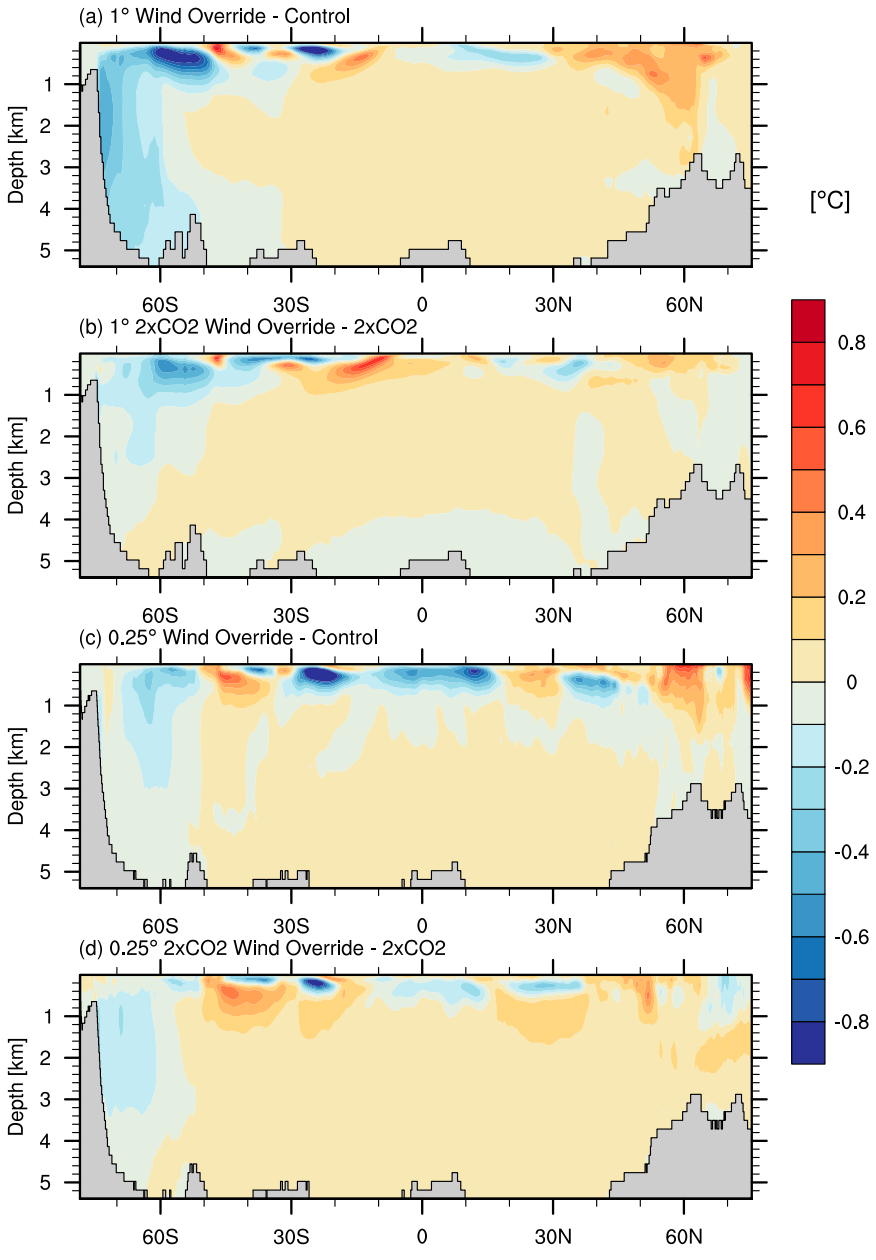

FIG. 13. Zonal mean temperature anomaly (°C) in the 1° model for the (a) wind override and (b) $2\times CO_2$ wind override and in the 0.25° model for the (c) wind override and (d) $2\times CO_2$ wind override. In (a) and (c) the control run temperature has been subtracted while in (b) and (d) the $2\times CO_2$ run temperature has been subtracted.

$2\times CO_2$ wind override run it is 0.1 Sv weaker than in the $2\times CO_2$ run. In the 0.25° wind override run, NADW peak magnitude is 0.6 Sv stronger than in the control run, while in the $2\times CO_2$ wind override run it is 0.5 Sv stronger than in the $2\times CO_2$ run. When the MOC is measured in latitude–depth space (not shown), NADW formation is about 1 Sv stronger in the wind override runs than in the control and $2\times CO_2$ runs, and the Southern Ocean Deacon cell is enhanced by about 2 Sv. The strengthening of NADW formation and enhanced Southern Ocean upwelling causes some of the enhanced warming asymmetry in the wind override runs.

c. *Summary of asymmetry*

We derive indices of the interhemispheric temperature asymmetry by taking the hemisphere mean

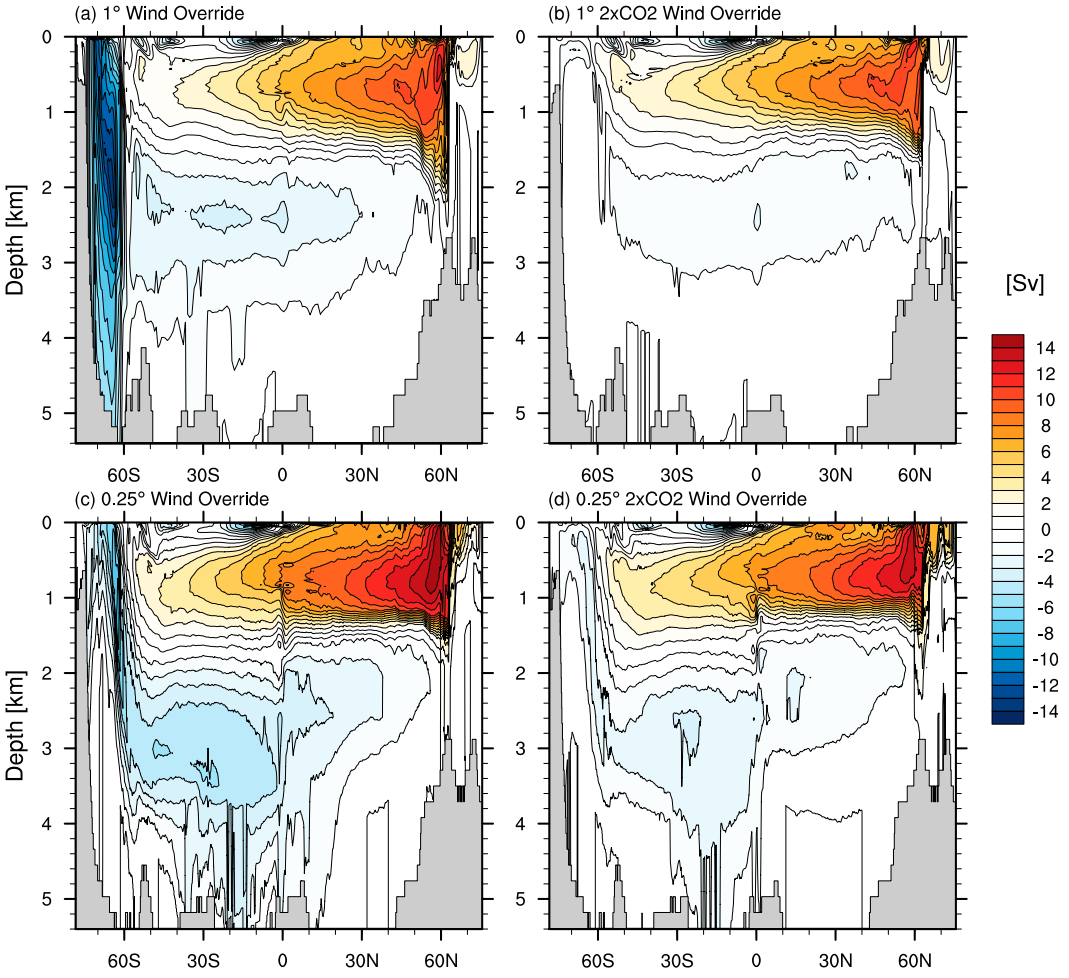

FIG. 14. Meridional overturning circulation (1-Sv contours) in latitude–density coordinates, reprojected into latitude–depth coordinates, showing the 1° model in the (a) wind override and (b) $2\times CO_2$ wind override runs, and the 0.25° model in the (c) wind override and (d) $2\times CO_2$ wind override runs.

temperature difference, and the ±45°-to-pole and ±60°-to-pole mean differences, for SST and SAT. Time series of the ±45°-to-pole and ±60°-to-pole indices are plotted in Fig. 15, showing a strong warming asymmetry in the high-latitude SST response at both resolutions. There is also a strong asymmetry in SAT warming at high latitudes in the 1° case, but less so in the 0.25° case. The smaller signal of high-latitude SAT asymmetry is likely due to the near-symmetric landmasses, and the compensation of atmospheric poleward heat transport against the increased ocean poleward heat transport. Each of these indices has had the corresponding control run index subtracted, and the result filtered using a 9-yr running average, to focus on the low-frequency signal. The hemisphere-wide asymmetry (not shown) is weaker, since the tropical warming response is largely symmetric and covers a larger surface area than the ±45°-to-pole region.

To summarize these indices, the time-averaged temperature asymmetry indices from the control and perturbation runs are shown in Fig. 16. The radiative forcing and wind override both increase the asymmetry in the high-latitude warming, while radiative forcing has a significantly larger effect than the wind override. These indices also highlight the major interhemispheric temperature asymmetries in the control runs, which are larger in the 0.25° model than in the 1° model.

5. Discussion

In all of the experiments presented here, we find a strong interhemispheric asymmetry in high-latitude warming. In this model the land–ocean ratio is approximately the same at all latitudes, and the atmospheric forcing is largely symmetric, due to the simplified gray radiation scheme. Thus the primary source of

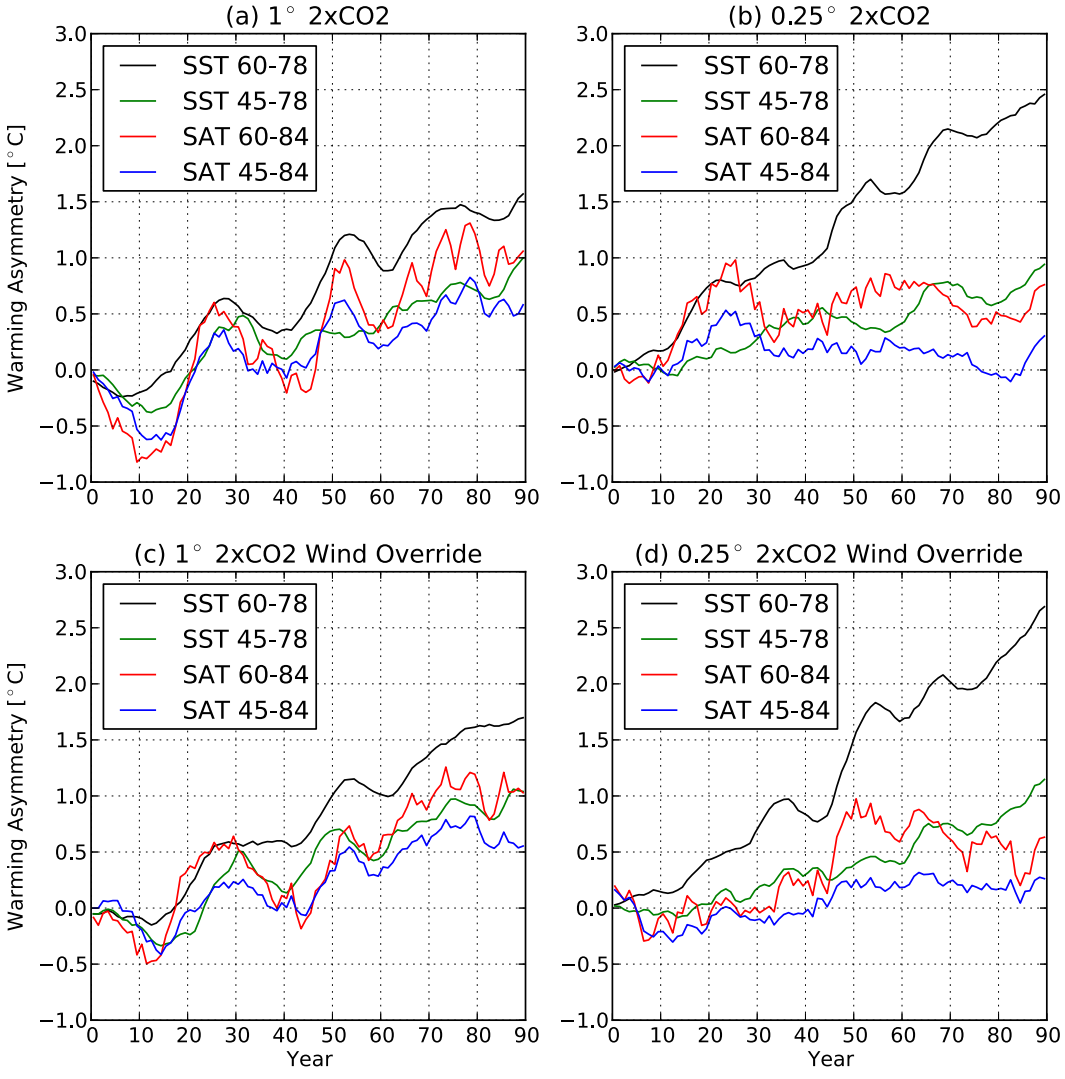

FIG. 15. Warming asymmetry (°C) showing the 45°–pole and 60°–pole mean difference for SST and SAT in the (a) 1° 2×CO_2 run, (b) 0.25° 2×CO_2 run, (c) 1° 2×CO_2 wind override run, and (d) 0.25° 2×CO_2 wind override run. In each case the control run has been subtracted, and the time series then filtered using a 9-yr running mean.

asymmetry is the existence of an ACC in the Southern Ocean, versus the gyre circulation in the NH. We infer that the asymmetry of warming in this model is governed by ocean circulation. This result agrees with the findings of Marshall et al. (2014), who found that most of the interhemispheric asymmetry of SST warming predicted in CMIP5 models can be explained by the ocean circulation redistributing a uniform heat flux perturbation.

One of the aims of this study was to establish whether the inclusion of explicit eddy heat fluxes, especially in the Southern Ocean, would substantially change the pattern of warming found in the coarse-resolution model. We found that poleward eddy heat fluxes were generally small compared to the mean flow, and that the Southern Ocean warming pattern was not sensitive to the resolution change. While our model does not fully resolve eddies, the insensitivity of heat fluxes in the Southern Ocean to the resolution change is consistent with the eddy-resolving model of Bryan et al. (2014). However, we did find a substantial sensitivity to resolution in the heat fluxes of boundary currents. The 0.25° simulations had stronger warming and sea ice melt in the North Atlantic, which was likely caused by higher velocities and better resolved boundary currents.

The stronger boundary currents in the 0.25° model created a large difference in the NH sea ice response. We found that in the eddy-permitting regime, NH sea ice was thinner and covered a smaller area in the control simulations, and melted almost completely by the end of the 2×CO_2 run. By contrast in the 1° model, NH sea ice

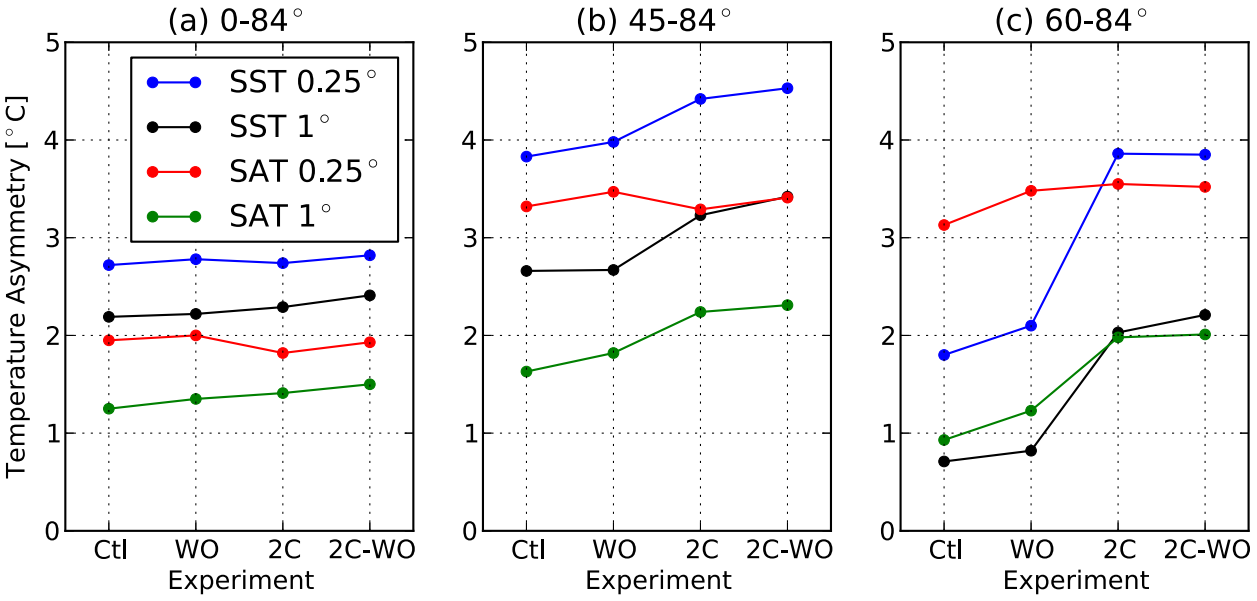

FIG. 16. Temperature asymmetry (°C) indices for (a) 0°–84°, (b) 45°–84°, and (c) 60°–84° latitude, showing SST and SAT at each resolution. Abbreviations for the experiments are Ctl: control, WO: wind override, 2C: 2×CO_2, and 2C-WO: 2×CO_2 wind override. The control run was averaged over the full 90 years, while the perturbation runs were averaged for the last 20 years only.

covered a larger area in the control runs, and a substantial amount of ice remained at the end of the 2×CO_2 run. The SH sea ice was greater in extent and thickness and exhibited less melting in response to radiative forcing. This result was robust across the different resolutions, suggesting that the SH climate response was well captured at the coarser resolution. The resolution sensitivity of sea ice between our 1° and 0.25° models is similar to that found in an eddy-resolving coupled climate model (Kirtman et al. 2012; Bryan et al. 2014), where the decline in Arctic sea ice was greater in the 0.1° model compared with a 1° resolution ocean model, but there was little dependence on resolution of the SH sea ice response.

Sea ice differences between the resolutions could perhaps be reduced by tuning the sea ice albedo. For example Delworth et al. (2012) raised the ice albedo and lowered the vertical diffusion when moving from coarse to eddy-permitting ocean resolution to obtain a more realistic sea ice climatology. While this kind of tuning might have made the NH sea ice extent more comparable between our 1° and 0.25° models, such a change would likely increase the SH sea ice extent, thereby creating a new disparity between the resolutions. Our study is focused on processes that differ between the resolutions, rather than obtaining the most realistic climatology, so tuning of the ice albedo and vertical diffusion are beyond the scope of this study.

Our model allows us to compare warming scenarios both with and without a poleward shift of the westerly winds, due to the nearly steady position of the westerly winds under radiative forcing perturbations. Adding a wind shift and intensification to the model leads to cooling of the surface Southern Ocean and warming of the North Atlantic [consistent with the findings of Toggweiler and Samuels (1998), Delworth and Zeng (2008), and Sijp and England (2009)], leading to an overall greater magnitude of interhemispheric warming asymmetry. The wind override causes a larger change in temperature asymmetry when no radiative forcing is applied. In particular, AABW formation is substantially increased when the wind override is applied to the control state, but in the 2×CO_2 state AABW weakens both with and without the wind override.

This wind stress profile in the ICCM contrasts with that of Enderton and Marshall (2009), who used an aquaplanet model with narrow land barriers to simulate the effect of a Drake Passage throughflow in an otherwise symmetric world. In their case, having an open Drake Passage versus a closed basin created a stronger and more poleward SH westerly wind stress and a significant reduction in surface air temperature. However, in their aquaplanet model the SAT closely mirrors the SST at all locations, and therefore the thermal wind balance of the atmosphere is strongly constrained by lower SST in the SH high latitudes. Our model's SAT is also influenced by the land surface, which has limited interhemispheric asymmetry and allows the atmosphere temperature to be more symmetric than in the Enderton and Marshall (2009) model.

There remain uncertainties over how the westerly wind position will evolve, despite the consistent poleward shift found in CMIP5 projections (Barnes and Polvani 2013). Idealized atmosphere experiments (Butler et al. 2010) show that tropical warming and polar stratospheric cooling tend to shift the jets poleward, while polar surface warming shifts the jets equatorward. Furthermore, models with an equatorward bias of the westerly winds in their control state have a greater poleward shift under warming scenarios (Kidston and Gerber 2010). Our results imply that the future evolution of the SH westerly wind position will have a significant impact on the interhemispheric asymmetry of warming.

When applying our results to the global climate system, several caveats must be considered. First, there is no seasonal cycle in our model, which has an important influence on sea ice dynamics. Although our goal was to examine the long-term annual mean climate response, we do not know whether a seasonally varying model with otherwise similar forcing would yield the same results in its annual mean. However, the similarities in sea ice evolution between our model and the Kirtman et al. (2012) model support our annual-mean forcing as a useful coupled model scenario. Our results show that predictions of the ocean–sea ice response to rising CO_2 may change substantially as models move to finer resolution. Given the apparent underestimation of NH sea ice melting in CMIP5 models compared with observations (Collins et al. 2013), improving the resolution of the ocean and sea ice components of climate models may help to improve their NH sea ice predictions.

The simplified gray radiation scheme used in our atmosphere model provides some limitation, since the water vapor in the model is hard-wired through the optical depth profile. However, this scheme significantly reduces the computational expense of the atmosphere component of the model. This model does not include ozone or aerosols; however, the wind override scenarios provide an analog of the poleward shift of the SH westerly winds due to ozone depletion (Thompson et al. 2011). Finally, the domain of the model has only one ocean basin and an ACC-like channel, which pushes our warming results to be more Atlantic-like. The global ocean also comprises the Pacific and Indian Ocean basins with no northern deep sinking regions, which reduces the asymmetry of meridional heat transport from the overturning circulation compared with a one basin model. Nonetheless we propose that the processes leading to asymmetry of warming in our model are relevant to the global climate system, even if the signal is stronger than expected in a global setting.

6. Conclusions

We have shown that the ocean circulation causes a substantial proportion of the interhemispheric temperature asymmetry, both in the control runs and in $2\times CO_2$ warming experiments. In this model the land–ocean ratio and atmosphere forcing are similar between the hemispheres, so the asymmetry cannot be due to faster warming over land. Yet the ocean geometry is fundamentally asymmetric, with a zonally unbounded channel in the SH midlatitudes and sidewalls everywhere in the NH. The high-latitude warming asymmetry is enhanced when moving from 1° to 0.25° ocean resolution, due to reduced sea ice cover and faster melting in the Arctic region. This major difference in sea ice response appears to be caused by enhanced boundary currents at the eddy-permitting resolution; most of the poleward heat transport in the ocean model is carried by the mean flow rather than transient eddies. By contrast the Southern Ocean poleward heat transport and Antarctic sea ice cover appear to be insensitive to the resolution change. As in the NH, the mean flow dominates the poleward heat transport rather than transient eddies, in both the eddy-permitting model and the parameterized eddy model. When a poleward wind shift and intensification is added to this warming scenario, the warming asymmetry is enhanced and Southern Ocean warming suppressed. The wind override enhances the upper limb of the MOC, leading to greater subduction of heat in the NH and more upwelling of cool deep water in the SH. The asymmetry caused by doubling CO_2 is greater in magnitude than that caused by the wind override, but both perturbations increase the asymmetry when imposed both separately and together.

Acknowledgments. Thanks to Marshall Ward for model setup and software support, Riccardo Farneti for code and assistance in setting up the ICCM, and Steve Sherwood for advice on radiative forcing. This research was undertaken with the assistance of resources provided at the NCI National Facility systems at the Australian National University through the National Computational Merit Allocation Scheme supported by the Australian Government. This project was supported by the Australian Research Council, including support from an ARC Laureate Fellowship (FL100100214) and an ARC Future Fellowship (FT120100842). The authors thank three anonymous reviewers for constructive comments, which helped to improve the manuscript.

REFERENCES

Barnes, E. A., and L. Polvani, 2013: Response of the midlatitude jets, and of their variability, to increased greenhouse gases in

the CMIP5 models. *J. Climate,* **26,** 7117–7135, doi:10.1175/JCLI-D-12-00536.1.

Blunden, J., and D. S. Arndt, 2014: State of the climate in 2013. *Bull. Amer. Meteor. Soc.,* **95,** S1–S279, doi:10.1175/2014BAMSStateoftheClimate.1.

Bonjean, F., and G. S. E. Lagerloef, 2002: Diagnostic model and analysis of the surface currents in the tropical Pacific Ocean. *J. Phys. Oceanogr.,* **32,** 2938–2954, doi:10.1175/1520-0485(2002)032<2938:DMAAOT>2.0.CO;2.

Bryan, F. O., P. R. Gent, and R. Tomas, 2014: Can Southern Ocean eddy effects be parameterized in climate models? *J. Climate,* **27,** 411–425, doi:10.1175/JCLI-D-12-00759.1.

Butler, A. H., D. W. J. Thompson, and R. Heikes, 2010: The steady-state atmospheric circulation response to climate change–like thermal forcings in a simple general circulation model. *J. Climate,* **23,** 3474–3496, doi:10.1175/2010JCLI3228.1.

Byrne, M. P., and P. A. O'Gorman, 2013: Land–ocean warming contrast over a wide range of climates: Convective quasi-equilibrium theory and idealized simulations. *J. Climate,* **26,** 4000–4016, doi:10.1175/JCLI-D-12-00262.1.

Collins, M., and Coauthors, 2013: Long-term climate change: Projections, commitments and irreversibility. *Climate Change 2013: The Physical Science Basis,* T. F. Stocker et al., Eds., Cambridge University Press, 1029–1136.

Delworth, T. L., and F. Zeng, 2008: Simulated impact of altered Southern Hemisphere winds on the Atlantic meridional overturning circulation. *Geophys. Res. Lett.,* **35,** L20708, doi:10.1029/2008GL035166.

——, and Coauthors, 2012: Simulated climate and climate change in the GFDL CM2.5 high-resolution coupled climate model. *J. Climate,* **25,** 2755–2781, doi:10.1175/JCLI-D-11-00316.1.

Drijfhout, S., G. J. van Oldenborgh, and A. Cimatoribus, 2012: Is a decline of AMOC causing the warming hole above the North Atlantic in observed and modeled warming patterns? *J. Climate,* **25,** 8373–8379, doi:10.1175/JCLI-D-12-00490.1.

Enderton, D., and J. Marshall, 2009: Explorations of atmosphere–ocean–ice climates on an aquaplanet and their meridional energy transports. *J. Atmos. Sci.,* **66,** 1593–1611, doi:10.1175/2008JAS2680.1.

Farneti, R., and G. K. Vallis, 2009: An intermediate complexity climate model (ICCMp1) based on the GFDL flexible modelling system. *Geosci. Model Dev.,* **2,** 73–88, doi:10.5194/gmd-2-73-2009.

——, and P. R. Gent, 2011: The effects of the eddy-induced advection coefficient in a coarse-resolution coupled climate model. *Ocean Modell.,* **39,** 135–145, doi:10.1016/j.ocemod.2011.02.005.

——, and G. K. Vallis, 2011: Mechanisms of interdecadal climate variability and the role of ocean–atmosphere coupling. *Climate Dyn.,* **36,** 289–308, doi:10.1007/s00382-009-0674-9.

——, T. L. Delworth, A. J. Rosati, S. M. Griffies, and F. Zeng, 2010: The role of mesoscale eddies in the rectification of the Southern Ocean response to climate change. *J. Phys. Oceanogr.,* **40,** 1539–1557, doi:10.1175/2010JPO4353.1.

Flato, G. M., and G. J. Boer, 2001: Warming asymmetry in climate change simulations. *Geophys. Res. Lett.,* **28,** 195–198, doi:10.1029/2000GL012121.

Fox-Kemper, B., R. Ferrari, and R. Hallberg, 2008: Parameterization of mixed layer eddies. Part I: Theory and diagnosis. *J. Phys. Oceanogr.,* **38,** 1145–1165, doi:10.1175/2007JPO3792.1.

Friedman, A. R., Y.-T. Hwang, J. C. H. Chiang, and D. M. W. Frierson, 2013: Interhemispheric temperature asymmetry over the twentieth century and in future projections. *J. Climate,* **26,** 5419–5433, doi:10.1175/JCLI-D-12-00525.1.

Frierson, D. M. W., I. M. Held, and P. Zurita-Gotor, 2006: A gray-radiation aquaplanet moist GCM. Part I: Static stability and eddy scale. *J. Atmos. Sci.,* **63,** 2548–2566, doi:10.1175/JAS3753.1.

Gent, P. R., and J. C. McWilliams, 1990: Isopycnal mixing in ocean circulation models. *J. Phys. Oceanogr.,* **20,** 150–155, doi:10.1175/1520-0485(1990)020<0150:IMIOCM>2.0.CO;2.

Griffies, S. M., 1998: The Gent–McWilliams skew flux. *J. Phys. Oceanogr.,* **28,** 831–841, doi:10.1175/1520-0485(1998)028<0831:TGMSF>2.0.CO;2.

——, 2012: Elements of the Modular Ocean Model (MOM). GFDL Ocean Group Tech. Rep. 7, NOAA Geophysical Fluid Dynamics Laboratory, 618 pp.

——, and Coauthors, 2015: Impacts on ocean heat from transient mesoscale eddies in a hierarchy of climate models. *J. Climate,* **28,** 952–977, doi:10.1175/JCLI-D-14-00353.1.

Hutchinson, D. K., M. H. England, A. Santoso, and A. M. Hogg, 2013: Interhemispheric asymmetry in transient global warming: The role of Drake Passage. *Geophys. Res. Lett.,* **40,** 1587–1593, doi:10.1002/grl.50341.

Kidston, J., and E. P. Gerber, 2010: Intermodel variability of the poleward shift of the austral jet stream in the CMIP3 integrations linked to biases in 20th century climatology. *Geophys. Res. Lett.,* **37,** L09708, doi:10.1029/2010GL042873.

Kirtman, B. P., and Coauthors, 2012: Impact of ocean model resolution on CCSM climate simulations. *Climate Dyn.,* **39,** 1303–1328, doi:10.1007/s00382-012-1500-3.

Large, W. G., J. C. McWilliams, and S. C. Doney, 1994: Oceanic vertical mixing: A review and a model with a nonlocal boundary layer parameterization. *Rev. Geophys.,* **32,** 363–403, doi:10.1029/94RG01872.

Lee, H.-C., A. Rosati, and M. J. Spelman, 2006: Barotropic tidal mixing effects in a coupled climate model: Oceanic conditions in the northern Atlantic. *Ocean Modell.,* **11,** 464–477, doi:10.1016/j.ocemod.2005.03.003.

Lee, S.-K., W. Park, E. van Sebille, M. O. Baringer, C. Wang, D. B. Enfield, S. G. Yeager, and B. P. Kirtman, 2011: What caused the significant increase in Atlantic Ocean heat content since the mid-20th century? *Geophys. Res. Lett.,* **38,** L17607, doi:10.1029/2011GL048856.

Locarnini, R. A., A. V. Mishonov, J. I. Antonov, T. P. Boyer, H. E. Garcia, O. K. Baranova, M. M. Zweng, and D. R. Johnson, 2010: *Temperature*. Vol. 1, *World Ocean Atlas 2009,* NOAA Atlas NESDIS 68, 184 pp.

Manabe, S., R. J. Stouffer, M. J. Spelman, and K. Bryan, 1991: Transient responses of a coupled ocean–atmosphere model to gradual changes of atmospheric CO_2. Part I. Annual mean response. *J. Climate,* **4,** 785–818, doi:10.1175/1520-0442(1991)004<0785:TROACO>2.0.CO;2.

Marshall, J., K. C. Armour, J. R. Scott, Y. Kostov, U. Hausmann, D. Ferreira, T. G. Shepherd, and C. M. Bitz, 2014: The ocean's role in polar climate change: Asymmetric Arctic and Antarctic responses to greenhouse gas and ozone forcing. *Philos. Trans. Roy. Soc.,* **372A,** 20130040, doi:10.1098/rsta.2013.0040.

——, J. R. Scott, K. C. Armour, J.-M. Campin, M. Kelley, and A. Romanou, 2015: The ocean's role in the transient response of climate to abrupt greenhouse gas forcing. *Climate Dyn.,* **44,** 2287–2299, doi:10.1007/s00382-014-2308-0.

Morice, C. P., J. J. Kennedy, N. A. Rayner, and P. D. Jones, 2012: Quantifying uncertainties in global and regional temperature change using an ensemble of observational estimates: The HadCRUT4 data set. *J. Geophys. Res.,* **117,** D08101, doi:10.1029/2011JD017187.

Morrison, A. K., and A. M. Hogg, 2013: On the relationship between Southern Ocean overturning and ACC transport. *J. Phys. Oceanogr.,* **43,** 140–148, doi:10.1175/JPO-D-12-057.1.

——, O. A. Saenko, A. M. Hogg, and P. Spence, 2013: The role of vertical eddy flux in Southern Ocean heat uptake. *Geophys. Res. Lett.,* **40,** 5445–5450, doi:10.1002/2013GL057706.

Munday, D. R., H. L. Johnson, and D. P. Marshall, 2013: Eddy saturation of equilibrated circumpolar currents. *J. Phys. Oceanogr.,* **43,** 507–532, doi:10.1175/JPO-D-12-095.1.

Myhre, G., and Coauthors, 2013: Anthropogenic and natural radiative forcing. *Climate Change 2013: The Physical Science Basis,* T. F. Stocker et al., Eds., Cambridge University Press, 658–740.

National Geophysical Data Center, 2006: 2-minute gridded global relief data (ETOPO2v2). U.S. Department of Commerce, NOAA. [Available online at http://www.ngdc.noaa.gov/mgg/fliers/06mgg01.html.]

Pierrehumbert, R. T., 2010: *Principles of Planetary Climate.* Cambridge University Press, 688 pp.

Polvani, L. M., and P. J. Kushner, 2002: Tropospheric response to stratospheric perturbations in a relatively simple general circulation model. *Geophys. Res. Lett.,* **29,** 14–18, doi:10.1029/2001GL014284.

Risien, C. M., and D. B. Chelton, 2008: A global climatology of surface wind and wind stress fields from eight years of QuikSCAT scatterometer data. *J. Phys. Oceanogr.,* **38,** 2379–2413, doi:10.1175/2008JPO3881.1.

Sijp, W. P., and M. H. England, 2009: Southern Hemisphere westerly wind control over the ocean's thermohaline circulation. *J. Climate,* **22,** 1277–1286, doi:10.1175/2008JCLI2310.1.

Simmons, H. L., S. R. Jayne, L. C. Laurent, and A. J. Weaver, 2004: Tidally driven mixing in a numerical model of the ocean general circulation. *Ocean Modell.,* **6,** 245–263, doi:10.1016/S1463-5003(03)00011-8.

Snow, K., A. M. Hogg, S. M. Downes, B. M. Sloyan, M. L. Bates, and S. M. Griffies, 2015: Sensitivity of abyssal water masses to overflow parameterisations. *Ocean Modell.,* **89,** 84–103, doi:10.1016/j.ocemod.2015.03.004.

Spence, P., O. A. Saenko, W. Sijp, and M. H. England, 2013: North Atlantic climate response to Lake Agassiz drainage at coarse and ocean eddy-permitting resolutions. *J. Climate,* **26,** 2651–2667, doi:10.1175/JCLI-D-11-00683.1.

Stouffer, R. J., S. Manabe, and K. Bryan, 1989: Interhemispheric asymmetry in climate response to a gradual increase of atmospheric CO_2. *Nature,* **342,** 660–662, doi:10.1038/342660a0.

Sutton, R. T., B. Dong, and J. M. Gregory, 2007: Land/sea warming ratio in response to climate change: IPCC AR4 model results and comparison with observations. *Geophys. Res. Lett.,* **34,** L02701, doi:10.1029/2006GL028164.

Thompson, D. W. J., S. Solomon, P. J. Kushner, M. H. England, K. M. Grise, and D. J. Karoly, 2011: Signatures of the Antarctic ozone hole in Southern Hemisphere surface climate change. *Nat. Geosci.,* **4,** 741–749, doi:10.1038/ngeo1296.

Toggweiler, J. R., and B. Samuels, 1998: On the ocean's large-scale circulation near the limit of no vertical mixing. *J. Phys. Oceanogr.,* **28,** 1832–1852, doi:10.1175/1520-0485(1998)028<1832:OTOSLS>2.0.CO;2.

Weaver, A. J., and E. S. Sarachik, 1990: On the importance of vertical resolution in certain ocean general circulation models. *J. Phys. Oceanogr.,* **20,** 600–609, doi:10.1175/1520-0485(1990)020<0600:OTIOVR>2.0.CO;2.

Zhang, Y., and G. K. Vallis, 2013: Ocean heat uptake in eddying and non-eddying ocean circulation models in a warming climate. *J. Phys. Oceanogr.,* **43,** 2211–2229, doi:10.1175/JPO-D-12-078.1.